ELECTRON TRANSFER AT DNA-MODIFIED ELECTRODES

THESIS BY

DONATO MARINO CERES

In Partial Fulfillment of the Requirements

for the Degree of

Doctor of Philosophy

California Institute of Technology

Pasadena, California

2006

(Defended May 18, 2006)

ACKNOWLEDGEMENTS

My experience at Caltech has been probably the most important of my life. During these six years I have grown not only intellectually but also, and especially, as a human being. Along my journey in the sunny California I have interacted with many people and each one of them gave me a small piece of their wisdom that I will carry with me for the rest of my life. I will be eternally grateful to all of them for what I am and what I will be.

My journey started in 1998 during a visit in Israel (I really hope that one day this beautiful corner of the world will resolve its conflicts, preserving the so-fascinating poly-cultural identity that makes it such a wonderful place), where for the first time I heard of DNA and like for many others, I fell in love with its beauty. Although I didn't know what DNA really was, I decided that I wanted to work with it and understand it more. In very broken English, I sent an email to Dr. Jacqueline Barton asking if it was possible to finish my master's in her laboratory. It took less than 24 hours to receive her answer. Already then I understood how much passion and enthusiasm Jackie has for research. I then decided to leave the old world and follow the "American dream".

I am extremely grateful to Jackie for allowing me to come and work in her group. She has been a terrific mentor and it has been a pleasure and an honor working for and with her. Through her enthusiasm she taught me to be positive about research, to always look at the big picture without getting lost in small details (although details are important sometimes), and at the same time to be very critical. I have seen my self maturing and becoming a more responsible scientist. Thank you, Jackie!

The first people I have interacted with were Dr. Elizabeth and Dr. Michael Hill Boon. Liz taught me the basic concepts of the research and, with extreme patience, she helped me get oriented in a completely new environment. Thank you so much: I would not have made it without your help, Liz. Mike was and still is extremely helpful, having taught me the basic of chemistry and electrochemistry. Mike, Liz, and I had a lot of fun at

Occidental College, doing experiments all night long because we needed to have them done by the next day. I will not ever forget those moments. Mike, moreover, is a very good friend, always available to talk and listen if I have a problem and willing to lend a hand if I need it. Thank you, Mike, you are very special.

Along my path at Caltech, I have met many great people from which I have learned a lot. I feel honored to have overlapped with such great researchers and friends. I am indebted to Dr. Melanie O'Neill for having shared with me her time here. I will always have wonderful memories of our trips to gorgeous places all over California. I have learned a lot from her and become a better person. Thank you, Melanie! I also have to thank all my lab mates, who have been so kind and helpful on many occasions and always open to talk, discuss, argue, and teach me new things. The dynamic in the group is extremely unique. Very nice and intelligent people, apparently, like to aggregate.

I also want to thank the Lucky Baldwin's crowd. At Lucky's I have met very interesting and diverse people, each extremely open to talk about life problems, have fun, and listen. I have to thank them for having accepted me so naturally and kindly. It is rare to find such a combination in one place at the same time, but Lucky's must be a little magic!

Finally, I want to thank the most important persons in my life: my family. I want to thank my brother Gerardo, sister Isabella, brother-in-law Mauro, and sister-in-law Roberta for being so kind and generous with me every time I went back to Switzerland to visit. I envy them for having beautiful families and the most adorable kids ever: Christel, Chiara, Elisa, and Adam. I am quite sure I have made my mother Ida and father Donato proud of me by becoming a Doctor but this is probably only a small consolation for them; I have been away for so long. I owe them every thing I have and am. They will always be for me a model of life and love. Thank you!

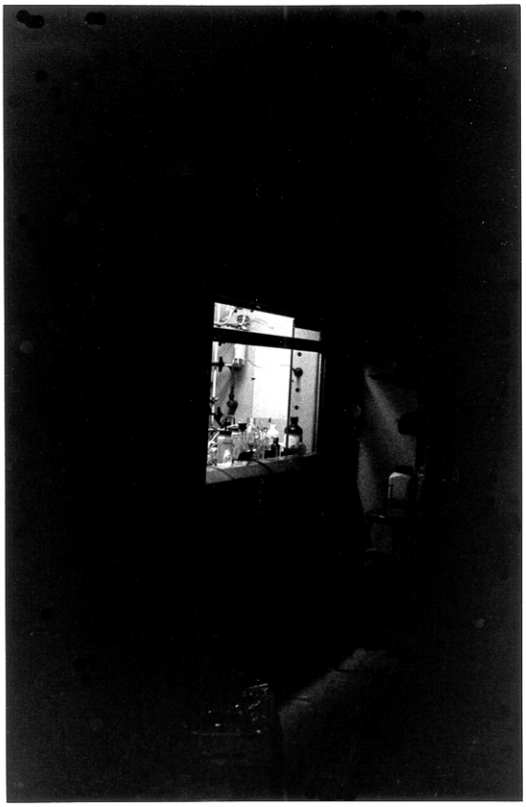

ABSTRACT

The DNA π stack provides an efficient pathway for transport of electron and electron holes. Ground-state electron transport is furthermore extremely sensitive to subtle DNA structural perturbations, such as a single base mismatch, that alter π-stacking. As a result, DNA-modified electrodes have allowed the development of highly sensitive diagnostic devices for the detection of base mismatches, lesions, and mutations. We have been able to apply DNA-mediated charge transduction, using a methylene blue/ferricyanide electrocatalytic cycle, in a DNA chip format for the detection of a single base mismatches at a microelectrode. Electrocatalysis is detected at DNA-modified electrodes down to 40 μm electrode in diameter, where 10^8 DNA molecules are responsible for the electron transduction. This exquisite sensitivity both for mismatch detection irrespective of sequence context and to a small number of molecules is an important requisite for the development of a device able to detect multiple genetic variations in the absence of DNA amplification.

We have also investigated in detail the electrochemical properties of DNA films. DNA is a highly charged molecule and, when self-assembled on a gold surface in a dense array, its properties are similar to those of polyelectrolyte films. We have found that the structure of the DNA film is sensitive to ion concentration and identity. Variations of the electrostatic potential across the film can sensitively affect both thermodynamics and kinetics of redox reporters incorporated in the film. Methylene blue reduction in the DNA film occurs via a two electron, one proton process. The Pourbaix diagram is linear in the case of a monovalent anionic buffer, while it is curved in phosphate buffer. Electron transfer kinetics are also affected by the relative concentration of divalent anions: at low pH the film is compressed in the linker portion and the rate of electron transfer is faster. Based on this understanding of the electrostatic balance inside the DNA film, a new analytical tool

for monitoring hybridization events on gold surfaces has been developed using electrochemical impedance spectroscopy of ferricyanide.

In order to explore the electron transport properties of DNA films mechanistically scanning tunneling microscopy (STM) has also been employed. These experiments provide a first opportunity to examine DNA conductivity under physiological conditions. These STM experiments on DNA films show that DNA, when perpendicularly oriented with respect to the surface, is coupled to the STM tip and the local density of states contribute to the measured tunneling current. At positive biases, when the surface is positive, the DNA is tilted towards the surface and as a result decoupled from the tip; the DNA appears "transparent" and the underlying surface instead is imaged. Also important is the integrity of the base stack. When the percentage of DNA duplexes containing a single base mismatch in the film is increased, the conductivity of the film decreases. The STM tip, being held at a constant current, approaches the DNA film until, at a critical mismatch content, the tip must penetrate the film and image resolution is lost. The current versus voltage characteristic of the DNA film has furthermore been determined through a new scanning tunneling spectroscopic technique that provides highly stable and reproducible measurements. We find that DNA duplex films under physiological conditions exhibit negative differential resistance, which is a feature that is typical of resonant electron tunneling via energetically localized molecular orbitals. This observation provides an experimental evidence for the existence of localized states within the DNA HOMO-LUMO gap that can be responsible for the ground state electron transport observed in electrochemical experiments.

TABLE OF CONTENTS

LIST OF FIGURES

Chapter 1 DNA-MEDIATED CHARGE TRANSPORT

1.1 Introduction

The discovery of the DNA double helix in 1953 defines a historical landmark.[1] Since then, scientists have always been fascinated by its elegant structure and began to wonder whether the particular arrangement of the four bases was hiding an intrinsic function, in addition to carrying the hereditary information. In 1962, Eley and Spivey noted structural the similarity between the DNA helix and graphite and postulated the possibility that DNA may also function as a charge mediator. At that time, however, they did not know if this function would have any biological relevance. There have been an enormous number of experiments trying to harness DNA structure and function for practical purposes, such as molecular electronics or DNA computing, but only very recently are we starting to discover biological context for charge transport (CT) in the double helix. Nevertheless, there is still a lot to be done.

DNA is composed of an array of heterocyclic aromatic base pairs, stacked at a distance of 3.4 Å, wrapped within a negatively charged sugar-phosphate backbone (Figure 1-1).[2] Because the bases are in close proximity, in van der Waals contact, the π orbitals strongly interact with each other, generating an electronic coupling that is a fundamental requirement for the conductivity of all π systems. However, unlike solid state π systems, DNA is a highly dynamic molecule whose structure is constantly modulated by the close interaction of water molecules and counterions on the picosecond to millisecond time scale.[3-9] Motion of the bases also modulates the π-π interaction (π-stack) and therefore the electronic coupling necessary for CT to occur. CT rate is thus gated by the DNA structural conformational dynamics.[10]

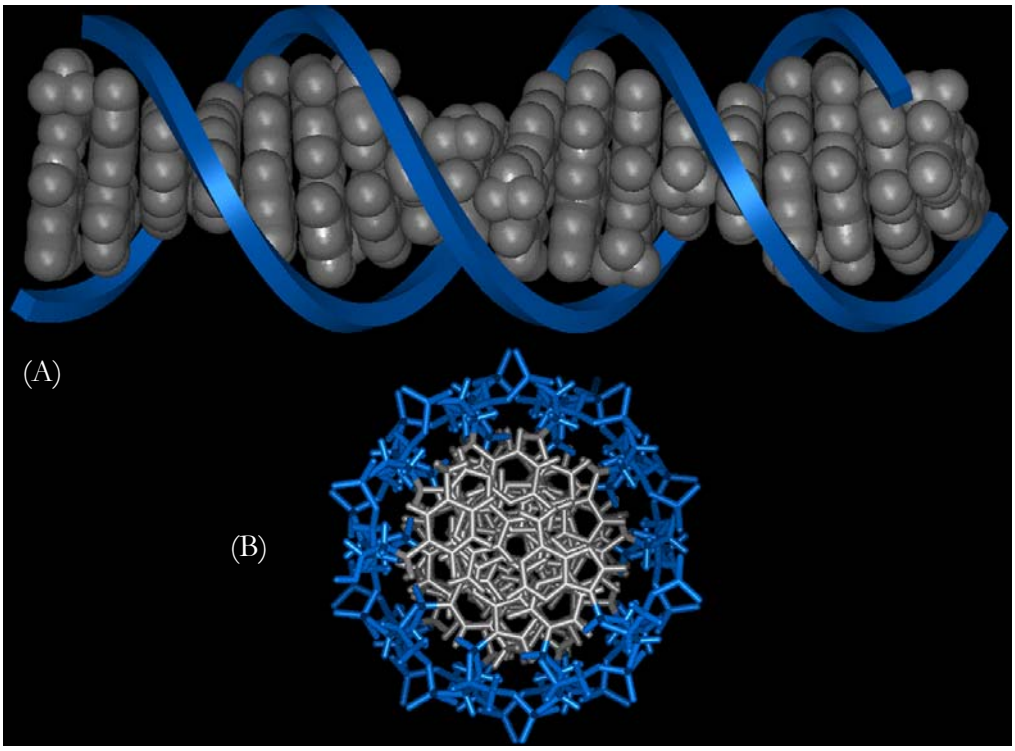

Figure 1-1: The π-stack of the double helical DNA. The π-stack of DNA bases in the double helix viewed along the helix axis (A), and down the helix (B). In this idealized model of B-DNA the stack of heterocyclic aromatic bases pairs is distinctly visible within the sugar-phosphate backbone (schematized by ribbons).

Perhaps the easiest approach for testing the ability of DNA to mediate charge is to directly measure its conductivity. Placing a single DNA molecule between two tiny electrodes and measuring the current vs. voltage characteristic sounds like a very appealing experiment. Early attempts to measure the conductivity of DNA molecules, however, resulted in a significantly wide spectrum of classifications: from wide band-gap semiconductor,[11] to superconductor,[12] and everything in between.[13, 14] The origin of this large discrepancy of experimental results resides in the fact that DNA, under conditions required for such experiments, is not structurally characterized in highly dehydrated conditions, in direct contact with metal electrodes, and at extreme low temperatures and high voltages. Taking all these facts into consideration, it is not surprising that these attempts to measure DNA conductivity only produced inconsistent results.

1.2 Experimental Approaches to Studies of DNA-Mediated CT

In our laboratory, we are exploring DNA-mediated CT via three distinct strategic paths: spectroscopical, biochemical, and electrochemical. Albeit they are very different techniques, they all rely on well-structurally characterized DNA molecules under physiological conditions. In general they utilize redox probes that allow the quantitation of the extent of CT, i.e. yields, rates, and distance dependence. These include metallointercalators, organic intercalators, and modified bases, which are all readily incorporated in DNA duplexes. An important feature that distinguishes our probes from those employed in other laboratories is their strong interaction with the DNA π-stack, making them electronically well coupled (Figure 1-2).

Our first spectroscopical approach is the one that historically showed that DNA can mediate charge, which initiated a very long-lasting debate on DNA CT. The first example of photoinduced DNA-mediated CT was observed between two polypyridyl metal complexes, where the luminescence rate of $Ru(phen)_3^{2+}$ (phen = 9,10-phenantroline) was highly quenched in the presence of tris(phen) complexes of Co(III) and Rh(III) in a DNA-mediated fashion.[15, 16] Subsequently, we have investigated CT between $Ru(phen)(bpy')(dppz)^{2+}$ (where bpy = 2,2'-bipyridine and dppz=dipyridophenazine) and $Rh(phi)_2bpy'$ (where phi = phenanthrequinone diimine)[17-20] or ethidium (Et)[21] (Figures 1-3 and 1-4) tethered to DNA. We found with Et that the CT reaction occurs much faster than the time scale of the instrumentation ($>10^{-10}$ s) and with a very shallow distance dependence. Moreover, an intervening mismatch, which causes a local disruption of the π-stack, decreased the CT yield, corroborating the idea that the pathway for CT is not via the sugar backbone but rather the π-stack.

Biochemical investigations of CT in DNA have mainly involved the photochemical reaction between an intercalator and a guanine doublet (GG). These types of studies rely

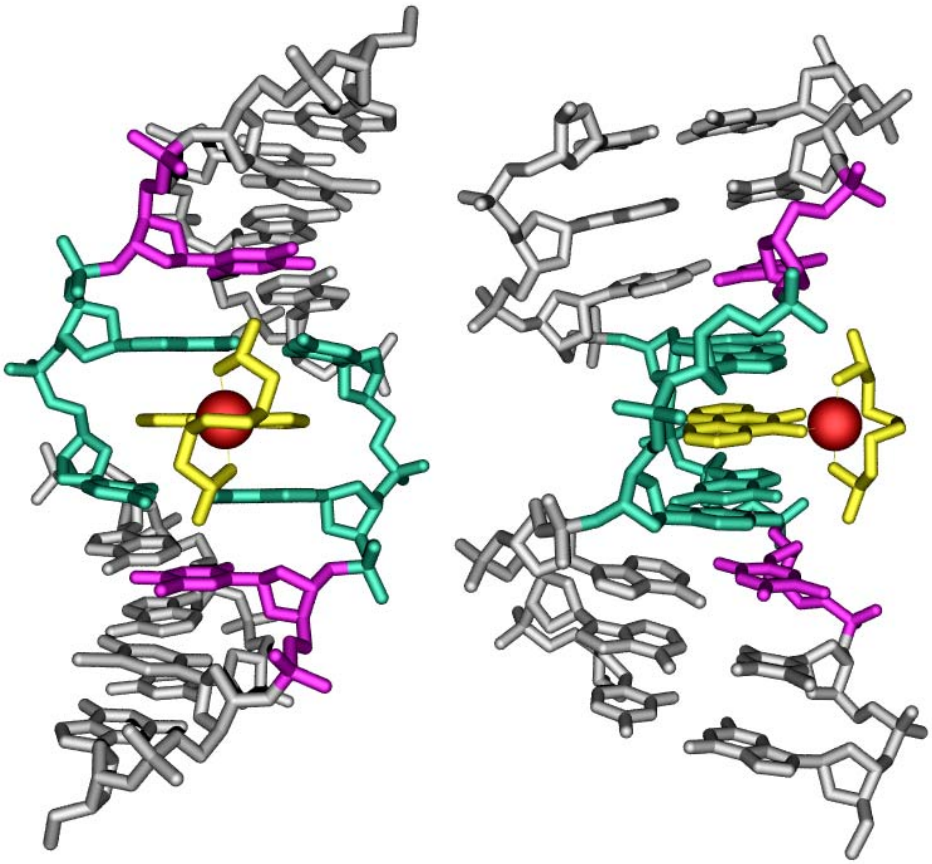

Figure 1-2: A 1.4 Å crystal structure of the intercalating phi ligands in the case of D-a-[Rh(R,R-dimethyltrien)phi]$^{3+}$ with a DNA octamer. The intercalator is inserted as an additional DNA base step with minimal perturbation of DNA p-stack. (pdb:454D)

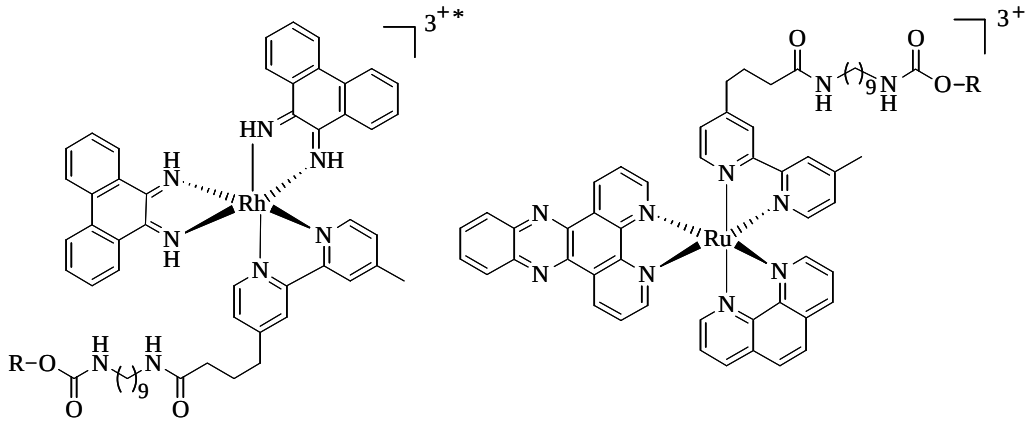

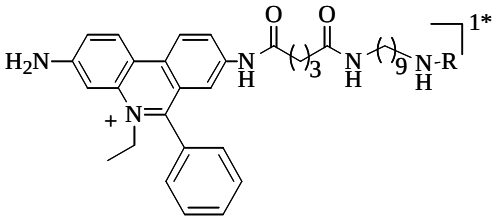

Ethidium

Figure 1-3: Chemical structure of some of the photooxidants that have been used in DNA CT studies.

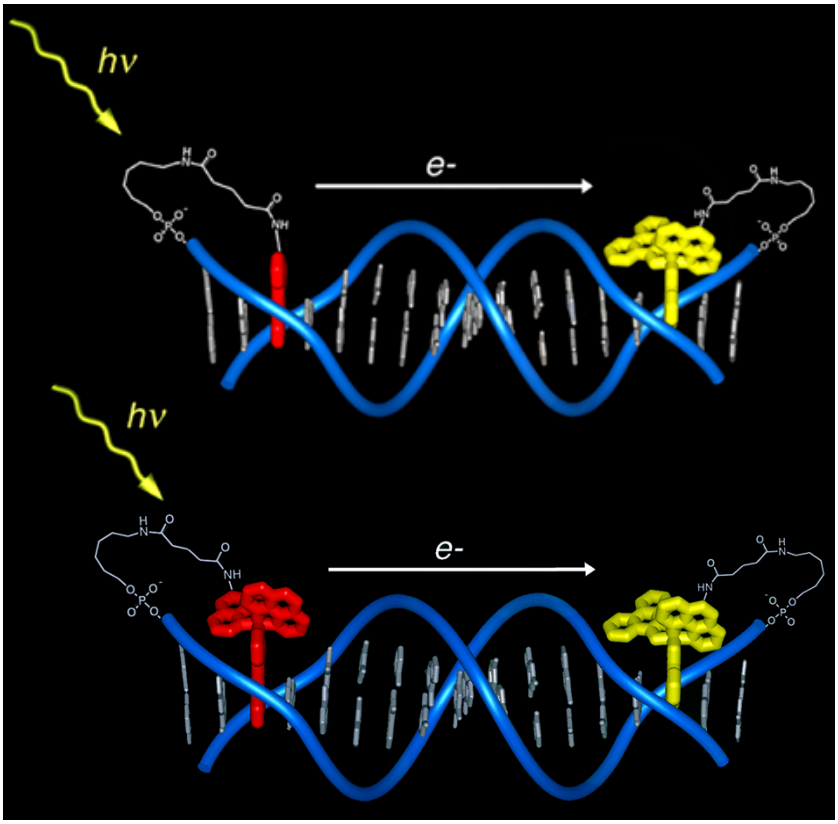

Figure 1-4: Charge transfer occurs through the DNA π-stack and is strongly dependent on minor base stack perturbations. Photoinduced electron transfer is observed from the tethered intercalated ethidium to a rhodium intercalator or rhodium to ruthenium bound to DNA up to 30 Å away. The efficiency of electron transfer is drastically reduced in the presence of a single base-pair mismatch.

on the fact that G has the lowest oxidation potential of all four bases[22] and when adjacent to another G, its potential is even lower.[23] When an electron hole resides on a GG there is high chance that it might react with water or oxygen causing permanent oxidation damage, which can be visualized by gel electrophoresis. *Ab initio* calculations have shown that the HOMO is mainly localized on the 5'-G of a GG.[24] We have experimentally observed that upon irradiation of an intercalating photooxidant covalently bound to the DNA, permanent damage consistently occurs at the 5'-G. Hence, the selective oxidation of 5'-G has become essentially a signature of DNA-mediated CT. Biochemical studies of DNA-mediated CT allowed the investigation of the distance dependence of CT yields[25-28] and first showed that permanent DNA damage might occur *in vivo* via long range CT.[29]

CT reactions between an intercalator and a DNA base have also been investigated by spectroscopy. CT between covalently bound Et and a modified base, 7-deazaguanine (zG), exhibited a reaction on the femtosecond time scale and a very shallow distance dependence that was sensitive to intervening sequence and mismatches.[30, 31] These experiments strongly suggested that the dynamical motion of the DNA, and in particular the repositioning of Et orientation inside the DNA, might gate the reaction. It became clearer that DNA dynamics is very important for efficient CT yield and rate. To further investigate the role DNA base dynamics might have on CT reactions, we studied the fluorescence quenching of 2-aminopurine (Ap) both by steady state fluorescence and femtosecond spectroscopy (Figure 1-5).[10, 32-34] In these experiments, we investigated the direct CT between two bases, Ap and G, avoiding the problem of intercalator stacking and coupling and thus interrogating specifically the role of base dynamics. We have found that CT is indeed gated by the motion of the bases, where CT yields and rates are essentially reflecting the probability and the motion time scale of achieving a so-called CT active conformation, respectively. $\pi-\pi$ interactions are modulated by the motion of the bases in such a way that the orbital can delocalize and propagate over a certain number of bases in a sequence-dependent fashion.

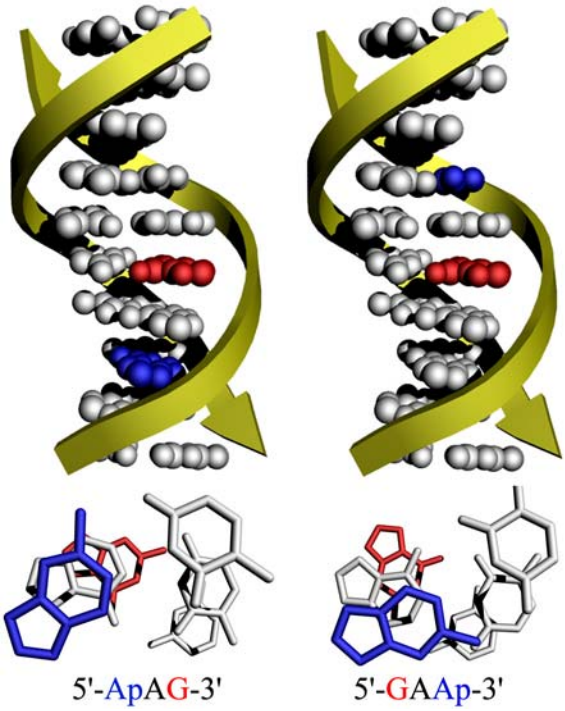

Figure 1-5: DNA assemblies used to study the directional asymmetry of the base-base CT. CT is more facile in the 5' to 3' direction.

1.3 Mechanistic Considerations

Mechanistic models regarding DNA CT have varied tremendously over the course of the last decade, as experimental results have continuously changed the phenomenological landscape. An obvious starting point was the analogy with the σ-system in proteins,[35] but that was quickly proven to be erroneous. As a consequence of experiments where CT yields were correlated in some way to the redox potential of the photooxidant, theoreticians started to think that the relative energy of the bases in the bridge might actually play a role in the CT process. A model has been suggested whereby CT occurred by the interplay of tunneling (often called "superexchange" as it describes a tunneling process that goes beyond a typical electron tunneling distance) through high energy bases (As and Ts) and bridge occupancy at low energy sites, such as Gs.[36, 37] Although this multistep hopping was the only model accepted by physicists, perhaps because it was easy to describe, it could not rationalize all experimental evidences. For instance, this model was not able to predict the modulation of the yield of G oxidation observed when the ionic distribution around the DNA was systematically varied or distal/proximal oxidation ratios were greater than one.[38] Gradually, however, scientists started considering DNA more like a molecule in its own environment.

Polaron-like hopping[39] between G residues was a first attempt to describe the distortion of the DNA as a means for charge migration, but it implies that the injected charge was the cause of such a distortion. However, we have shown with fluorescence quenching of Ap by G that charge injection alone is affected by the DNA sequence *before* the charge is injected.[40] This implied that the electronic coupling along the π-stack is already pre-determined by the DNA sequence and its environment; Ap fluorescence quenching turned out only to probe the probability for CT. How can the electronic coupling be communicated along the DNA? Once again, this theoretical question has been answered by an experimental result. Systematic studies on the distance dependence of Ap

fluorescence quenching exhibited an oscillatory behavior, revealing for the first time a new special feature of the DNA molecule.[40] In order to explain these observations, we have proposed a model based on the formation of delocalized domains (extended π orbitals) that are formed when the DNA bases are in a particular configuration and can propagate fast along the DNA gated by the global dynamical motion (Figure 1-6). Very recently, additional evidence, supporting the idea that this stacking interaction modulates also the energetics of the DNA (compared to those of bases measured as monomers), came from the investigation of kinetic hole traps, such as N^4-cyclopropylcytosine (cpC) and N^2-cyclopropylguanine (cpG).[41, 42] Consistent observation of comparable oxidations of high-energy pyrimidines (cpC) and low-energy purines (cpG) suggests that the DNA bases are strongly coupled with each other causing the energetic of single bases to be modulated by interactions with near neighbors.

To date, there is no rigorous model that is able to describe and predict these last findings, but we are slowing moving towards a unified theory that involves principally the fast DNA dynamics, which is able to modulate electronic coupling among bases and redox partners, and alter the electronic structure of the DNA compared to those of the isolated nucleotides. A revised model of the polaron[43] also seems able to describe these phenomena in principle, but the debate now appears to be more semantic rather than conceptual.

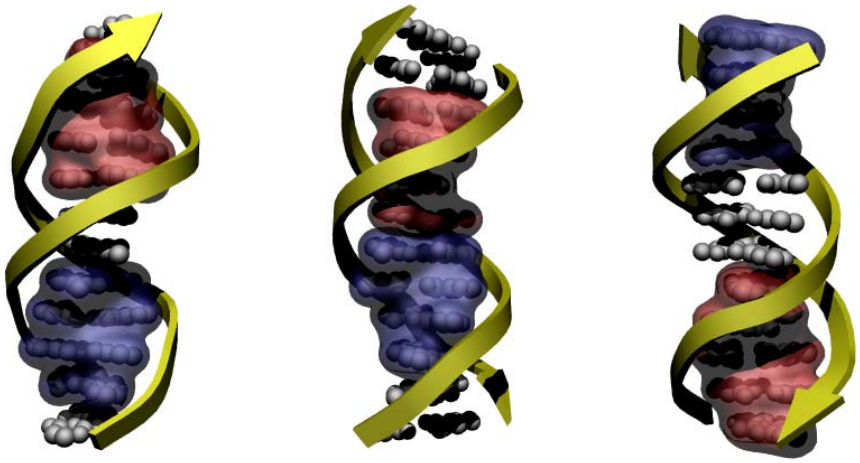

(A) (B) (B)

Figure 1-6: Model for CT through delocalized domains. (A) An electron hole injected into the DNA delocalized domain (blue domain) can propagate along the DNA. (B) Radical motion is gated by conformational changes that can produce overlap between adjacent domains (B) allowing the charge to migrate into another domain (C).

1.4 Electron Transfer at DNA-Modified Electrodes

DNA-mediated electron transfer (ET) at modified electrodes was first studied as a possible alternative to the investigation of DNA CT in solution. Although metallointercalators have been tested on DNA-modified surfaces, organic intercalators are mainly used as probes in electrochemical investigations. The two intercalators that have been shown to be the most proficient for probing ET at DNA films are methylene blue (MB) and daunomycin (DM). MB is a three-ringed heterocycle which binds to DNA with a relatively high binding constant ($K \sim 10^6\ M^{-1}$).[44-47] Its redox potential is conveniently situated at approximately 0 V vs. NHE and its reduction appears to be reversible. DM is a redox active antitumor agent[48] that can likewise be reversibly reduced at about -0.4 V vs. NHE. The major advantage of DM is its ability to be readily cross-linked to the exocyclic amine of G in the presence of formaldehyde.[49] Moreover, the DNA-DM adducts are a well defined system also because they have been crystallographically characterized (Figure 1-7).[50] Unfortunately, however, DM-DNA linkages are not very inherently stable[51] and the two-electron reduction seems to be responsible for the breakage of the glycosidic bond, which holds the redox moiety to the sugar.[52-54] Nevertheless, DM was stable enough to provide important insights about DNA ET.

First investigations of DNA ET at a modified gold electrode involved the reversible reduction of micromolar concentration of MB.[55] We have found that the binding affinity of MB to the surface-bound DNA was not different from that in solution. The stoichiometry was consistent with the intercalation of about one MB per duplex, as a consequence of the tight packing of the DNA on the surface. Thus, MB is expected to bind at the top of the film, indicating that long-range DNA-mediated ET was responsible for the observed electrochemical signal. In order to further corroborate the DNA-mediated character of the ET, we also prepared DNA films containing DM crosslinked to

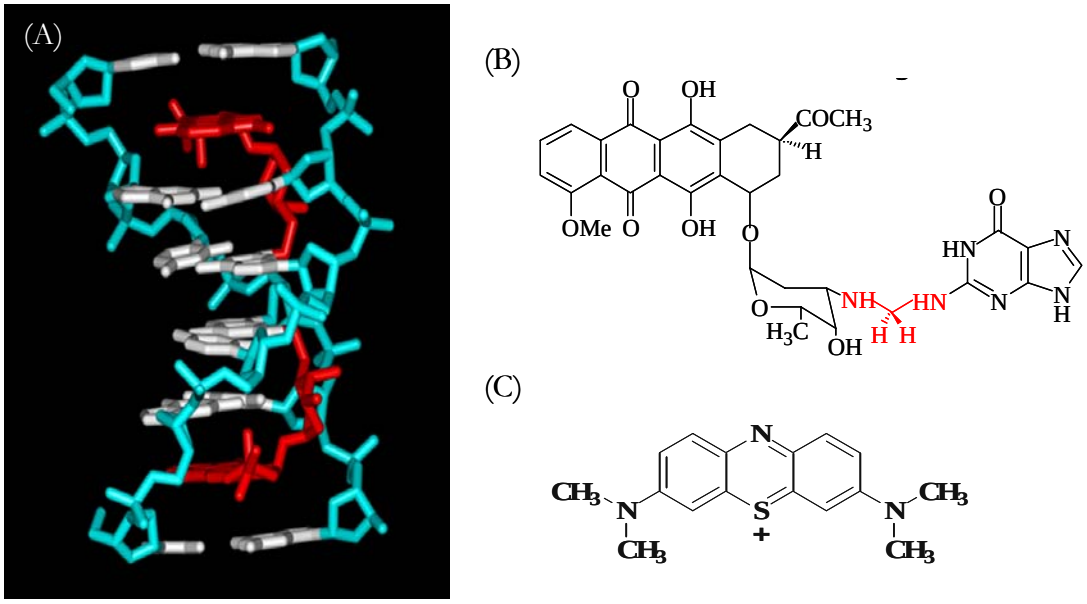

Figure 1-7: Crystal structure of DM crosslinked to the exocyclic amine of a G residue. (B) Chemical structure of the DM-G crosslinking and (C) MB.

G residues specifically positioned in the duplex.[56] Remarkably, an ET rate constant of about 100 s^{-1} was consistently observed regardless of the position of DM in the duplex. Comparable rates have been measured for redox probes attached to alkane-thiol films,[57] suggesting that the actual rate-limiting step was the linker portion of the film, the actual ET in DNA being much faster. Moreover, we observed that the incorporation of a single base mismatch between the gold surface and the DM crosslinking site completely turned off the electrochemical response (Figure 1-8). This confirmed that the pathway for ET was indeed through the DNA base stack. It also showed that, like in solution experiments, electronic perturbations of the π-stack can sensibly modulate the ET in DNA films. However, DNA-mediated ET did not display the same sequence sensitivity as in solution experiments,[58] perhaps as a consequence of the tight packing of the film that limits the sequence dependent DNA flexibility.

Only one model has been proposed in an attempt to describe ET in DNA films.[59] The mechanism for ET through DNA films is perhaps substantially different from CT in solution, albeit the similarity with solution-phase experiments, but an understanding of both aspects of the same molecule must provide complementary insights. Photoinduced CT with metallointercalators occurs at energies that are on the order of a few eV higher than the ground state ET in DNA films. If we consider the energetics of the bridge comparable to the isolated bases, the reduction potential of MB and DM are significantly below the DNA bridge (for example for thymine $E^{0/-}$ ~ -1.1 V vs. NHE)[60] and thermal accessibility at those energies is improbable. Still, we have observed efficient ET through DNA films over distances of 5 to 10 nm where the rate limiting step is seemingly tunneling through the significantly shorter (1.5 nm) linker.[56, 61]

The only model that has been proposed to date is based on the analogy that DNA films might have with ionic crystals,[59] where ET through the films is due to ionic conductivity. In this model, longitudinal polarization of the film upon application of a bias

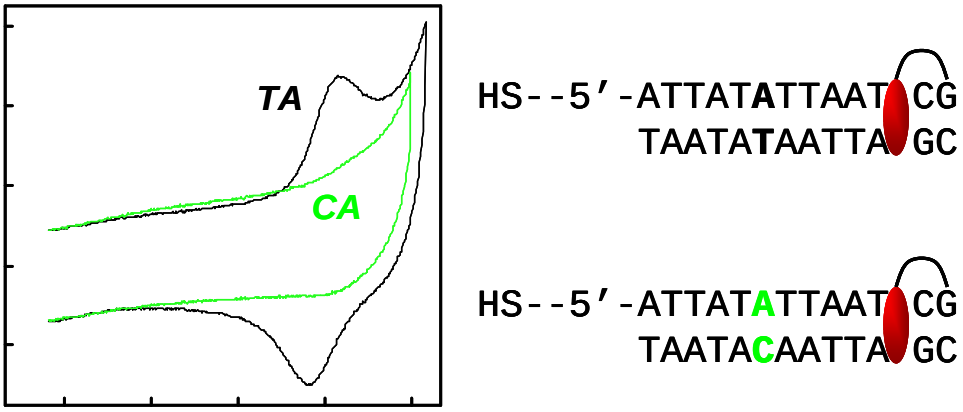

Figure 1-8: Mismatch detection at DNA-modified surfaces. Electrochemical reduction of DM crosslinked to a specific G residue in the duplex produces a clear electrochemical signal (TA) when the DNA is fully base paried, while the signal is drastically turned off in the presence of an intervening mismatch (CA).

potential seems to be facilitated by the counterions associated with the negatively charged backbone. The increase of the longitudinal polarizability along the DNA axis was invoked to explain the increase of the electron mean free path along the DNA helices. Because we have already established that the electron path in the DNA is through the π-stack, polarizability of π orbitals along the DNA axis is highly unlikely. In the context of the formation of delocalized domains, however, it is possible that the rigidity imposed by the tightness in DNA films might facilitate the formation of more extended well-coupled π-stacked arrays, inducing an anisotropic (longitudinal) conductivity of well-ordered DNA molecules.

Effective occupancy of the DNA bridge by the electrons requires the introduction of a more sophisticated model. Electrochemical measurements of ET at DNA-modified electrodes strongly suggest that the DNA bridge is indeed occupied at energies that are in close proximity to the Fermi level of the gold electrode. To date, there is no understanding of the actual electronic structure of DNA, especially in the stacked conformation. Quantum mechanical calculations of simple stacked aromatic molecules have shown that the band structure can change dramatically depending on several factors, such as the number of monomers, the relative distance, and orientation.[62] The appearance of energy states in the HOMO-LUMO gap as well as formation of indirect band gaps are well-known phenomena. However, none of these considerations has been applied to the DNA electronic structure. Recent theoretical works have shown that the band gap in G stacks is substantially lowered by their relative position and that structural distortions may indeed induce formation of partial delocalized electron states.[63]

In this Thesis, we investigate the existence of energetically localized states that might be responsible for the observed electrochemical behavior. In Chapter 2, we investigate the sensitivity of the DNA-mediated ET to local electronic perturbations, such as a mismatch. We also apply this technology for the construction of a miniaturized DNA chip for the diagnosis of genetic mutations. We investigate the electrochemical behavior of

DNA films in the presence of redox active intercalators, such as MB, and charged cationic and anionic metal complexes, in particular ruthenium hexamine ($Ru(NH_3)_6^{3+}$) and ferricyanide

($Fe(CN)_6^{3-}$) in Chapter 3. DNA films are polyelectrolyte films and their electrochemical behavior is highly affected by the electrostatic interaction caused by the ionic environment. It is important to understand the extent of this interaction in order to interpret the behavior of redox probes at DNA modified electrodes. In Chapter 4, we directly investigate the existence of localized states in DNA films by *in situ* scanning tunneling microscopy and spectroscopy. Finally, in the appendix of the Thesis, we present an overview of electrochemical techniques for the measurement of electrode kinetics. The techniques are revised and expanded in particular for the electrochemical analysis of localized states.

1.5 References

1. Eley, D. D.; Spivey, D. I., Semiconductivity of Organic Substances .9. Nucleic Acid in Dry State. *Transactions of the Faraday Society* **1962,** 58, (470), 411-415.
2. Saenger, W., *Principles of Nucleic Acid Structure*. Springer: New York, 1984.
3. Borer, P. N.; Laplante, S. R.; Kumar, A.; Zanatta, N.; Martin, A.; Hakkinen, A.; Levy, G. C., C-13-Nmr Relaxation in 3 DNA Oligonucleotide Duplexes: Model-Free Analysis of Internal and Overall Motion. *Biochemistry* **1994,** 33, (9), 2441-2450.
4. Brauns, E. B.; Murphy, C. J.; Berg, M. A., Local dynamics in DNA by temperature-dependent Stokes shifts of an intercalated dye. *Journal of the American Chemical Society* **1998,** 120, (10), 2449-2456.
5. Cheatham, T. E.; Kollman, P. A., Molecular dynamics simulation of nucleic acids. *Annual Review of Physical Chemistry* **2000,** 51, 435-471.
6. Georghiou, S.; Bradrick, T. D.; Philippetis, A.; Beechem, J. M., Large-amplitude picosecond anisotropy decay of the intrinsic fluorescence of double-stranded DNA. *Biophysical Journal* **1996,** 70, (4), 1909-1922.
7. Giudice, E.; Lavery, R., Simulations of nucleic acids and their complexes. *Accounts of Chemical Research* **2002,** 35, (6), 350-357.
8. Liang, Z. C.; Freed, J. H.; Keyes, R. S.; Bobst, A. M., An electron spin resonance study of DNA dynamics using the slowly relaxing local structure model. *Journal of Physical Chemistry B* **2000,** 104, (22), 5372-5381.
9. Nordlund, T. M.; Andersson, S.; Nilsson, L.; Rigler, R.; Graslund, A.; McLaughlin, L. W., Structure and Dynamics of a Fluorescent DNA Oligomer Containing the Ecori Recognition Sequence: Fluorescence, Molecular-Dynamics, and Nmr-Studies. *Biochemistry* **1989,** 28, (23), 9095-9103.

10. O'Neill, M. A.; Becker, H. C.; Wan, C. Z.; Barton, J. K.; Zewail, A. H., Ultrafast dynamics in DNA-mediated electron transfer: Base gating and the role of temperature. *Angewandte Chemie-International Edition* **2003,** 42, (47), 5896-5900.

11. Porath, D.; Bezryadin, A.; de Vries, S.; Dekker, C., Direct measurement of electrical transport through DNA molecules. *Nature* **2000,** 403, (6770), 635-638.

12. Kasumov, A. Y.; Kociak, M.; Gueron, S.; Reulet, B.; Volkov, V. T.; Klinov, D. V.; Bouchiat, H., Proximity-induced superconductivity in DNA. *Science* **2001,** 291, (5502), 280-282.

13. Fink, H. W.; Schonenberger, C., Electrical conduction through DNA molecules. *Nature* **1999,** 398, (6726), 407-410.

14. Okahata, Y.; Kobayashi, T.; Tanaka, K.; Shimomura, M., Anisotropic electric conductivity in an aligned DNA cast film. *Journal of the American Chemical Society* **1998,** 120, (24), 6165-6166.

15. Barton, J. K.; Kumar, C. V.; Turro, N. J., DNA-Mediated Photoelectron Transfer-Reactions. *Journal of the American Chemical Society* **1986,** 108, (20), 6391-6393.

16. Purugganan, M. D.; Kumar, C. V.; Turro, N. J.; Barton, J. K., Accelerated Electron-Transfer between Metal-Complexes Mediated by DNA. *Science* **1988,** 241, (4873), 1645-1649.

17. Arkin, M. R.; Stemp, E. D. A.; Holmlin, R. E.; Barton, J. K.; Hormann, A.; Olson, E. J. C.; Barbara, P. F., Rates of DNA-mediated electron transfer between metallointercalators. *Science* **1996,** 273, (5274), 475-480.

18. Arkin, M. R.; Stemp, E. D. A.; Turro, C.; Turro, N. J.; Barton, J. K., Luminescence quenching in supramolecular systems: A comparison of DNA- and SDS micelle-mediated photoinduced electron transfer between metal complexes. *Journal of the American Chemical Society* **1996,** 118, (9), 2267-2274.

19. Murphy, C. J.; Arkin, M. R.; Ghatlia, N. D.; Bossmann, S.; Turro, N. J.; Barton, J. K., Fast Photoinduced Electron-Transfer through DNA Intercalation. *Proceedings of the National Academy of Sciences of the United States of America* **1994,** 91, (12), 5315-5319.

20. Murphy, C. J.; Arkin, M. R.; Jenkins, Y.; Ghatlia, N. D.; Bossmann, S. H.; Turro, N. J.; Barton, J. K., Long-Range Photoinduced Electron-Transfer through a DNA Helix. *Science* **1993,** 262, (5136), 1025-1029.

21. Kelley, S. O.; Holmlin, R. E.; Stemp, E. D. A.; Barton, J. K., Photoinduced electron transfer in ethidium-modified DNA duplexes: Dependence on distance and base stacking. *Journal of the American Chemical Society* **1997,** 119, (41), 9861-9870.

22. Steenken, S.; Jovanovic, S. V., How easily oxidizable is DNA? One-electron reduction potentials of adenosine and guanosine radicals in aqueous solution. *Journal of the American Chemical Society* **1997,** 119, (3), 617-618.

23. Prat, F.; Houk, K. N.; Foote, C. S., Effect of guanine stacking on the oxidation of 8-oxoguanine in B-DNA. *Journal of the American Chemical Society* **1998,** 120, (4), 845-846.

24. Sugiyama, H.; Saito, I., Theoretical studies of GC-specific photocleavage of DNA via electron transfer: Significant lowering of ionization potential and 5'-localization of HOMO of stacked GG bases in B-form DNA. *Journal of the American Chemical Society* **1996,** 118, (30), 7063-7068.

25. Hall, D. B.; Barton, J. K., Sensitivity of DNA-mediated electron transfer to the intervening pi-stack: A probe for the integrity of the DNA base stack. *Journal of the American Chemical Society* **1997,** 119, (21), 5045-5046.

26. Hall, D. B.; Holmlin, R. E.; Barton, J. K., Oxidative DNA damage through long-range electron transfer. *Nature* **1996,** 382, (6593), 731-735.

27. Ly, D.; Sanii, L.; Schuster, G. B., Mechanism of charge transport in DNA: Internally-linked anthraquinone conjugates support phonon-assisted polaron hopping. *Journal of the American Chemical Society* **1999,** 121, (40), 9400-9410.

28. Nunez, M. E.; Hall, D. B.; Barton, J. K., Long-range oxidative damage to DNA: effects of distance and sequence. *Chemistry & Biology* **1999,** 6, (2), 85-97.

29. Rajski, S. R.; Jackson, B. A.; Barton, J. K., DNA repair: Models for damage and mismatch recognition. *Mutation Research-Fundamental and Molecular Mechanisms of Mutagenesis* **2000,** 447, (1), 49-72.

30. Kelley, S. O.; Barton, J. K., DNA-mediated electron transfer from a modified base to ethidium: Pi-stacking as a modulator of reactivity. *Chemistry & Biology* **1998,** 5, (8), 413-425.

31. Wan, C. Z.; Fiebig, T.; Kelley, S. O.; Treadway, C. R.; Barton, J. K.; Zewail, A. H., Femtosecond dynamics of DNA-mediated electron transfer. *Proceedings of the National Academy of Sciences of the United States of America* **1999,** 96, (11), 6014-6019.

32. Kelley, S. O.; Barton, J. K., Electron transfer between bases in double helical DNA. *Science* **1999,** 283, (5400), 375-381.

33. O'Neill, M. A.; Barton, J. K., Effects of strand and directional asymmetry on base-base coupling and charge transfer in double-helical DNA. *Proceedings of the National Academy of Sciences of the United States of America* **2002,** 99, (26), 16,543-16,550.

34. O'Neill, M. A.; Barton, J. K., 2-aminopurine: A probe of structural dynamics and charge transfer in DNA and DNA : RNA hybrids. *Journal of the American Chemical Society* **2002,** 124, (44), 13053-13066.

35. Gray, H. B.; Winkler, J. R., Electron transfer in proteins. *Annual Review of Biochemistry* **1996,** 65, 537-561.

36. Das, P.; Schuster, G. B., Effect of condensate formation on long-distance radical cation migration in DNA. *Proceedings of the National Academy of Sciences of the United States of America* **2005,** 102, (40), 14227-14231.

37. Meggers, E.; Michel-Beyerle, M. E.; Giese, B., Sequence dependent long range hole transport in DNA. *Journal of the American Chemical Society* **1998,** 120, (49), 12950-12955.

38. Williams, T. T.; Barton, J. K., The effect of varied ion distributions on long-range DNA charge transport. *Journal of the American Chemical Society* **2002,** 124, (9), 1840-1841.

39. Henderson, P. T.; Jones, D.; Hampikian, G.; Kan, Y. Z.; Schuster, G. B., Long-distance charge transport in duplex DNA: The phonon-assisted polaron-like hopping mechanism. *Proceedings of the National Academy of Sciences of the United States of America* **1999,** 96, (15), 8353-8358.

40. O'Neill, M. A.; Barton, J. K., DNA charge transport: Conformationally gated hopping through stacked domains. *Journal of the American Chemical Society* **2004,** 126, (37), 11471-11483.

41. Shao, F. W.; Augustyn, K.; Barton, J. K., Sequence dependence of charge transport through DNA domains. *Journal of the American Chemical Society* **2005,** 127, (49), 17445-17452.

42. Shao, F. W.; O'Neill, M. A.; Barton, J. K., Long-range oxidative damage to cytosines in duplex DNA. *Proceedings of the National Academy of Sciences of the United States of America* **2004,** 101, (52), 17914-17919.

43. Conwell, E. M.; Bloch, S. M., Base sequence effects on transport in DNA. *Journal of Physical Chemistry B* **2006,** 110, (11), 5801-5806.

44. Bradley, D. F.; Stellwag, N.C.; Paulson, C. M.; Okonski, C. T., Electric Birefringence and Dichroism of Acridine-Orange and Methylene-Blue Complexes with Polynucleotides. *Biopolymers* **1972,** 11, (3), 645-&.

45. Norden, B.; Tjerneld, F., Structure of Methylene-Blue DNA Complexes Studied by Linear and Circular-Dichroism Spectroscopy. *Biopolymers* **1982,** 21, (9), 1713-1734.

46. Tuite, E.; Kelly, J. M., The Interaction of Methylene-Blue, Azure-B, and Thionine with DNA: Formation of Complexes with Polynucleotides and Mononucleotides as Model Systems. *Biopolymers* **1995,** 35, (5), 419-433.

47. Tuite, E.; Norden, B., Sequence-Specific Interactions of Methylene-Blue with Polynucleotides and DNA: A Spectroscopic Study. *Journal of the American Chemical Society* **1994,** 116, (17), 7548-7556.

48. Arcamone, F., *Doxorubicin: Anticancer Antibiotics*. Academic Press: New York, 1981.

49. Leng, F. F.; Savkur, R.; Fokt, I.; Przewloka, T.; Priebe, W.; Chaires, J. B., Base specific and regioselective chemical cross-linking of daunorubicin to DNA. *Journal of the American Chemical Society* **1996,** 118, (20), 4731-4738.

50. Wang, A. H. J.; Gao, Y. G.; Liaw, Y. C.; Li, Y. K., Formaldehyde Cross-Links Daunorubicin and DNA Efficiently: HPLC and X-Ray-Diffraction Studies. *Biochemistry* **1991,** 30, (16), 3812-3815.

51. Taatjes, D. J.; Gaudiano, G.; Resing, K.; Koch, T. H., Redox pathway leading to the alkylation of DNA by the anthracycline, antitumor drugs adriamycin and daunomycin. *Journal of Medicinal Chemistry* **1997,** 40, (8), 1276-1286.

52. Houee-Levin, C.; Gardesalbert, M.; Ferradini, C.; Faraggi, M.; Klapper, M., Pulse-Radiolysis Study of Daunorubicin Redox Cycles: Reduction by E-Aq and Coo-Free-Radicals. *Febs Letters* **1985,** 179, (1), 46-50.

53. Houee-Levin, C.; Gardesalbert, M.; Rouscilles, A.; Ferradini, C.; Hickel, B., Intramolecular Semiquinone Disproportionation in DNA: Pulse-Radiolysis Study of the One-Electron Reduction of Daunorubicin Intercalated in DNA. *Biochemistry* **1991,** 30, (33), 8216-8222.

54. Rao, G. M.; Lown, J. W.; Plambeck, J. A., Electrochemical Studies of Anti-Tumor Antibiotics .3. Daunorubicin and Adriamycin. *Journal of the Electrochemical Society* **1978,** 125, (4), 534-539.

55. Kelley, S. O.; Barton, J. K.; Jackson, N. M.; Hill, M. G., Electrochemistry of methylene blue bound to a DNA-modified electrode. *Bioconjugate Chemistry* **1997,** 8, (1), 31-37.

56. Kelley, S. O.; Jackson, N. M.; Hill, M. G.; Barton, J. K., Long-range electron transfer through DNA films. *Angewandte Chemie-International Edition* **1999,** 38, (7), 941-945.

57. Napper, A. M.; Liu, H. Y.; Waldeck, D. H., The nature of electronic coupling between ferrocene and gold through alkanethiolate monolayers on electrodes: The importance of chain composition, interchain coupling, and quantum interference. *Journal of Physical Chemistry B* **2001,** 105, (32), 7699-7707.

58. Kelley, S. O.; Boon, E. M.; Barton, J. K.; Jackson, N. M.; Hill, M. G., Single-base mismatch detection based on charge transduction through DNA. *Nucleic Acids Research* **1999,** 27, (24), 4830-4837.

59. Hartwich, G.; Caruana, D. J.; de Lumley-Woodyear, T.; Wu, Y. B.; Campbell, C. N.; Heller, A., Electrochemical study of electron transport through thin DNA films. *Journal of the American Chemical Society* **1999,** 121, (46), 10803-10812.

60. Steenken, S.; Telo, J. P.; Novais, H. M.; Candeias, L. P., One-Electron-Reduction Potentials of Pyrimidine-Bases, Nucleosides, and Nucleotides in Aqueous-Solution: Consequences for DNA Redox Chemistry. *Journal of the American Chemical Society* **1992,** 114, (12), 4701-4709.

61. Liu, T.; Barton, J. K., DNA electrochemistry through the base pairs not the sugar-phosphate backbone. *Journal of the American Chemical Society* **2005,** 127, (29), 10160-10161.

62. Seo, D. K.; Hoffmann, R., Direct and indirect band gap types in one-dimensional conjugated or stacked organic materials. *Theoretical Chemistry Accounts* **1999,** 102, (1-6), 23-32.

63. Di Felice, R.; Calzolari, A.; Molinari, E.; Garbesi, A., *Ab initio* study of model guanine assemblies: The role of pi-pi coupling and band transport. *Physical Review B* **2002,** 65, (4).

Chapter 2 ELECTROCHEMICAL DETECTION OF SINGLE-BASE MISMATCHES ON A DNA-BASED CHIP

2.1 Introduction

DNA mutations are mainly caused by the misincorporation of bases during natural DNA replication or induced by exogenous agents, such as chemicals and high energy radiations. DNA repair machinery is composed of very sophisticated signaling pathways that are able to recognize, isolate, and fix most of these single base mismatches and lesions, keeping the cell healthy. However, naturally, when cells are constantly under stress and the repair machinery is inefficient, DNA mutations can accumulate[1-3] and, if not corrected, become permanent alterations of the hereditary material in the cell progeny. These genetic variations are called single nucleotide polymorphisms (SNPs). On average, SNPs occur in the human population more than 1% of the time. Because only about 3% to 5% of the genome codes for the production of proteins, most SNPs are found outside of "coding sequences," but those found within the coding sequences may alter the biological function of a protein. Although many SNPs do not produce any physical changes, other SNPs may be correlated to genetic predisposition to disease and even influence an individual's response to drug regimes.[4-7] From this point of view, it would be highly desirable to be able to know exactly if a person is allergic to a drug or even delay a disease before the manifestation of the symptoms.

A simple scheme for the detection of SNPs is based on the hybridization of a gene of known sequence with a target sequence; if a SNP is present within the gene, the heteroduplex can contain a mismatch. There has been tremendous development of technologies for the detection of single bases mismatches, of which the most known are high-throughput DNA chips, able to analyze thousands of gene in parallel by fluorescence techniques.[8-11] Electrochemical approaches have been always an attractive alternative to fluorescence-based mismatch detection owing to their inherent potential for miniaturization and easy readout. Many electrochemical techniques have been developed for the detection of mismatches and all heavily rely on stringent hybridization conditions for discrimination

between fully matched and mismatched DNA.[12-27] In fact, the thermodynamic instability obtained from a single base substitution is highly dependent on the sequence content and is generally very subtle, so that the discrimination and sensitivity are compromised, regardless of the technique employed. It would thus be desirable to develop a technique that is not limited in the discrimination of hybridization, where detection is obtained from fully paired duplexes, whether or not they have a mismatch.

Photoinduced charge transport in donor/DNA/acceptor systems has been observed over a wide range of conditions and photooxidants.[28-33] Consistently, charge transport along the DNA helix is found to be inhibited in the presence of an intervening stacking perturbation, such as bulges[34] and single base mismatches.[31] We have taken advantage of the sensitivity of the DNA π-stack to local perturbations for developing an alternative approach to the current diagnostic technologies. Electron transduction through double stranded DNA (dsDNA) at DNA-modified gold electrodes permitted the development of an electrochemical assay for the reliable detection of single point mutations.[35-38]

DNA films are formed by self-assembling 5'-thiol modified dsDNA on gold electrodes (see Materials and Methods). In the presence of high concentrations of Mg^{2+}, the negatively charged phosphate backbone of the DNA is screened and allows the formation of a well-packed monolayer, with a surface density estimated around 40-50 pmol/cm^2 (Figure 2-1).[38] In one first experiment performed on these DNA films, the redox intercalator daunomycin (DM) was site-specifically crosslinked to a guanine residue in the DNA duplex. By cyclic voltammetry (CV) a well-resolved peak, corresponding to the redox reaction of DM, was observed when the film was composed of Watson-Crick based-paired dsDNA. The signal was completely absent when the film was instead formed by dsDNA containing a single base mismatch. These experiments strongly suggest that the reduction of DM intercalated inside the DNA duplex occurs in a DNA mediated fashion, where the electrons travel through the π-stack (Figure 2-2). An electronic perturbation,

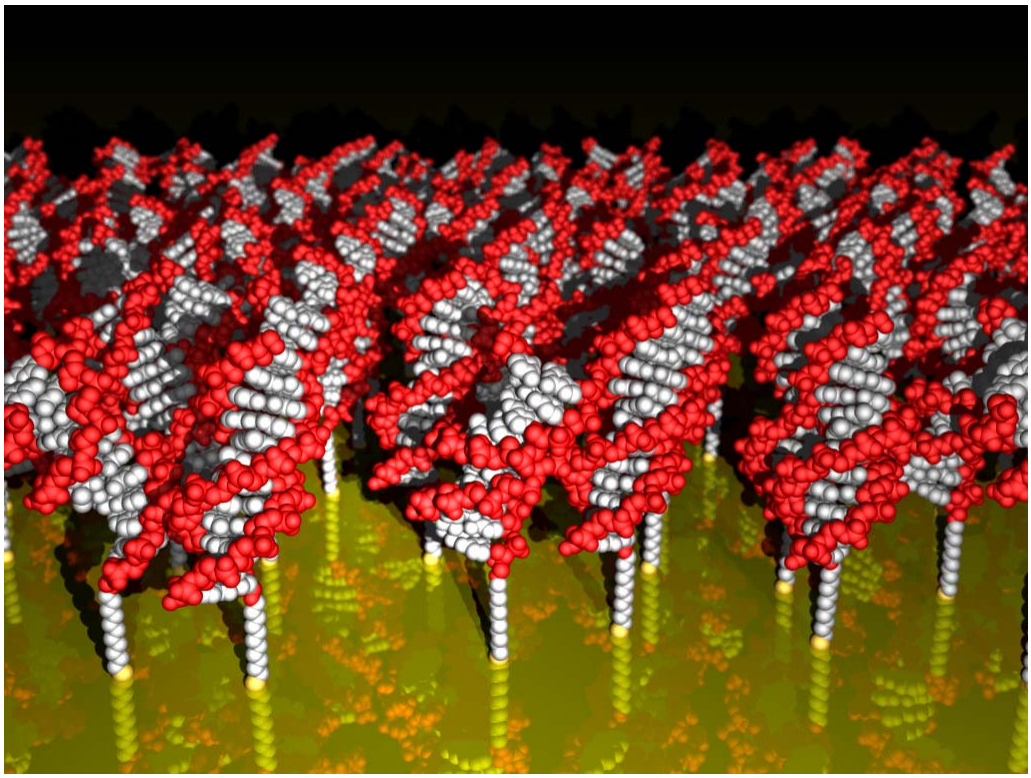

Figure 2-1: On-scale representation of a DNA film. The surface coverage of the film shown here is on the order of 15 pmol/cm^2 (2 nm average spacing between duplexes). For tighter packing, and in the presence of Mg^{2+}, we believe DNA self assemble on the surface adopting an hexagonal packing (see Chapter 4).

such as a mismatch, inhibits the electron transfer, probably by decoupling DM from the gold surface. While single-base mismatches induce subtle global structural perturbation in DNA duplexes (Figure 2-3), they can remarkably perturb the electronic structure.

We have subsequently established that when the DNA film is densely packed, freely diffusing DM could also intercalate in the DNA and the integration of the cyclic voltammetric peak revealed that the stoichiometric one-to-one ratio between DM and DNA was essentially maintained. Thus, in tightly packed DNA films, DM could not penetrate the film. Mismatch detection was then easily achieved under these conditions, indicating that indeed DM intercalates above the mismatch, at the top of the DNA film. This was an important result, because it indicated that the use of other freely diffusing redox intercalators, such as $Ir(bpy)(phen)(phi)^{3+}$ [39] and methylene blue (MB), would be possible.

Although the majority of mismatches have been detected by the electrochemical reduction of solution-borne intercalators, purine-purine mismatches, especially those containing guanine residues, are particularly difficult to discriminate electrochemically from normal Watson-Crick duplexes. This stability of particular mismatches can be seen visually in the X-ray crystal structures[40] (Figure 2-3) where a GT mismatch appears better stacked in the DNA duplex compared to the more destabilizing CA mismatch, which is clearly more distorted. Interestingly, we have found that electrocatalytic reduction of solution-borne ferricyanide ($Fe(CN)_6^{3-}$) by intercalated MB enhances the mismatch discrimination as well as improving the signal/noise ratio.[41, 42] In this chapter, we will take advantage of both the exquisite sensitivity of the DNA π-stack to mismatches and the signal enhancement obtained by electrocatalysis to develop a practical diagnostic tool for genetic analysis.

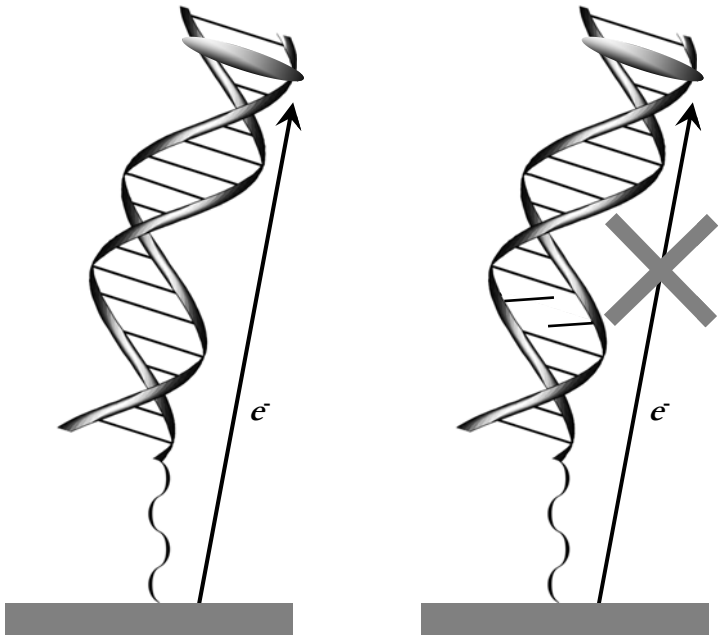

Figure 2-2: Electron transduction through DNA films. The electrochemical reduction of an intercalator placed at the end of the DNA duplex occurs via the bases π-stack. Electron transfer is efficiently inhibited by the presence of an intervening single base mismatch.

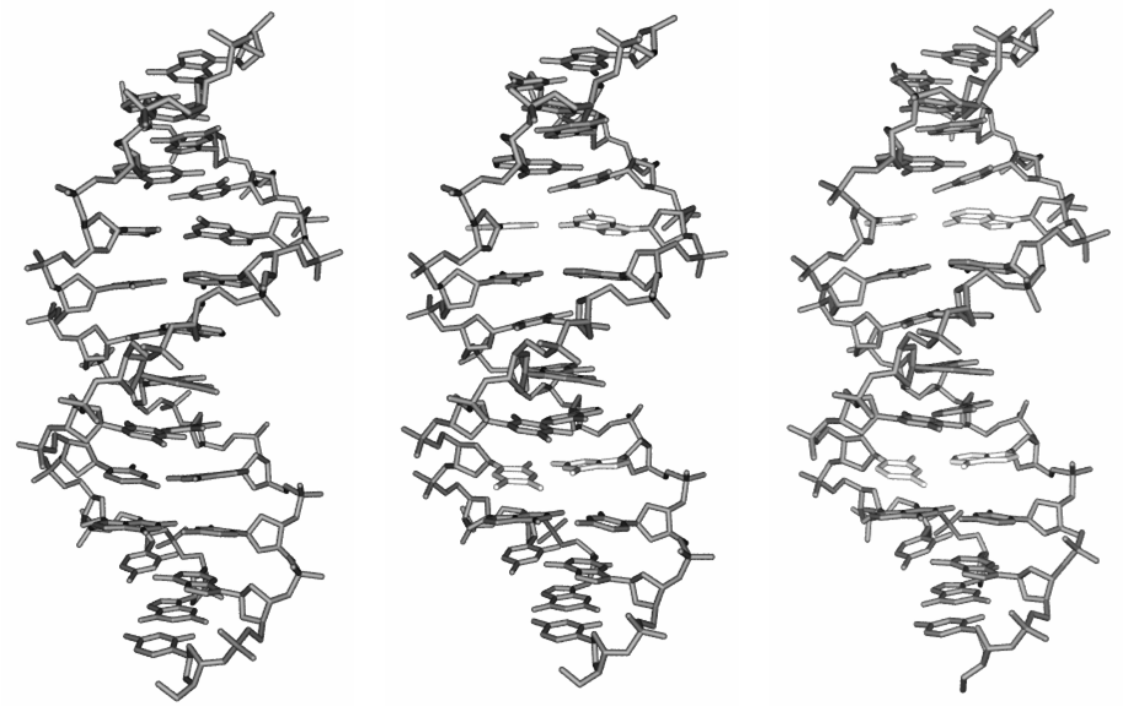

Figure 2-3: Crystal structures of DNA containing single base mismatches. The B-form DNA is the canonical Watson-Crick base-paired DNA. While the presence of a single base mismatch (in white) does not perturb the global structure of the DNA duplex, the ability of the base π-stack to transfer charges is highly affected. Locally a CA mismatch is thermodynamically more destabilizing than a GT mismatch. Crystal structures pdb: 1BNA (B-form DNA), 113D (GT), and 1D99 (CA).

2.2 Results and Discussions

2.2.1 Electrochemical Measurements on Macroelectrodes

Electrochemical reduction of MB in the presence of freely diffusing $Fe(CN)_6^{3-}$ (Figure 2-4) produces an electrocatalytic current at the electrode that greatly enhances the sensitivity for mismatches.[42] In the electrocatalytic process, MB is reduced in a DNA-mediated fashion, while $Fe(CN)_6^{3-}$ does not interact with the DNA because of electrostatic repulsion. Well-packed DNA films exhibit very low MB penetration, so that on average only about one MB per duplex is intercalated at the top of the film. This is a very important finding, as the reduction of MB intercalated below a mismatch would be insensitive to the electronic perturbation occurring above. We have thoroughly investigated the dynamics of MB and $Fe(CN)_6^{3-}$ at rotating disk electrodes[43] and have found that reduced MB, leuco-MB, dissociates slightly from the DNA where it can be reoxidized by its solution-borne counterpart $Fe(CN)_6^{3-}$. By shuttling the electron to $Fe(CN)_6^{3-}$ in the electrocatalytic cycle, MB allows continuous scanning of the DNA π-stack by electron transfer. In fact, we believe that the origin of the mismatch discrimination is related to the kinetics of the electrocatalytic cycle in combination with a dynamic, and not static, disruption of the DNA π-stack. Thus, the longer we probe the DNA electronic structure is probed by the electrocatalytic reduction of $Fe(CN)_6^{3-}$, the bigger we expect the difference in charge transduction between match and mismatched DNA to be.

The design of a practical device for mismatch detection requires the development of an *in situ* hybridization protocol that enables recycling of the surface for multiple testing. The simplest approach for dehybridizing DNA is by heat denaturing, i.e. dehybridizing the DNA in hot buffer. Because the DNA films employed in these studies have been constructed using high concentration of Mg^{2+}, they are particularly dense and the DNA

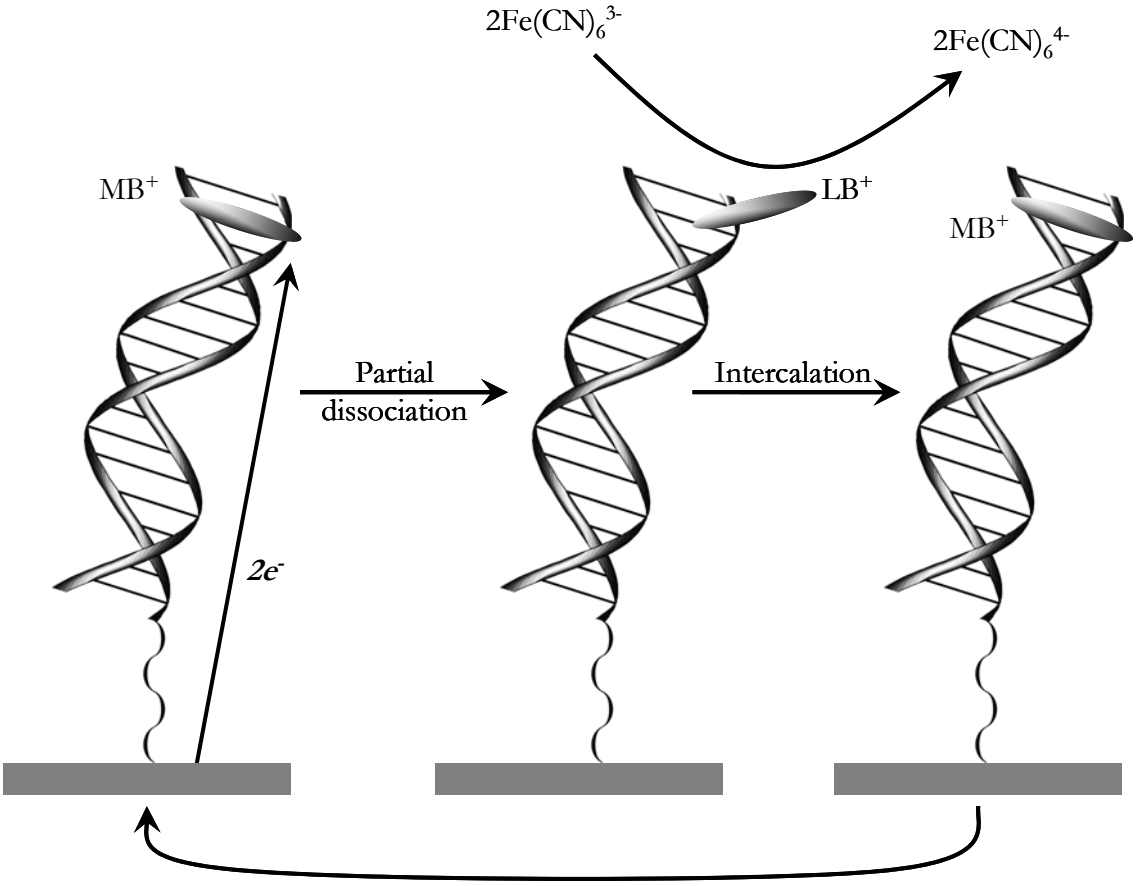

Figure 2-4: Electrocatalytic cycle of MB and $Fe(CN)_6^{3-}$ at DNA modified electrodes. MB is reduced by a two electron process (see Chapter 3) to leuco-MB (LB). LB has a lower binding affinity to the DNA and partly dissociates from the duplex. In the solution phase, LB reduces two equivalents of $Fe(CN)_6^{3-}$ regaining higher affinity to the DNA. After re-intercalation the catalytic cycle continues and each time the electron passes through the DNA p-stack, duplex is essentially probed for integrity. The current generated by electrocatalysis is several folds higher than with MB alone. In the presence of a mismatch, MB reduction is significantly inhibited and electrocatalysis cannot take place. In well-packed DNA films, MB intercalates almost exclusively at the very top of the film with a one-to-one stoichiometric ratio and $Fe(CN)_6^{3-}$ cannot be reduced directly at the gold surface.

melting temperature can be particularly high in this crowded environment. Moreover, high heat conditions can lead to permanent desorption of bound DNA, limiting the life time of the device. In order to test the possibility of dehybridization by this method and the subsequent stability of the films, we performed some tests on DNA films deposited on regular gold macroelectrodes (0.02 cm^2). We have chosen to study the sequence corresponding to a fragment of the p53 gene containing the codons 248 and 249, two well-known sites with high mutation frequency in several cancers.[†, 44] The specific sequence employed is HS-5'-ATG GGC CT**C** CGG TTC, where underlined C corresponds to the mutation side in codon 248 and bold **C** corresponds to the mutation site in codon 249. Three electrodes have been prepared by depositing three different sequences: the double stranded wild type (WT) p53 sequence, the sequence containing one mismatch at codon 248 (A paring with C), and another containing one mismatch at codon 249 (A paring with **C**), respectively. We identified these electrodes with the name of the deposited sequence: WT, 248, and 249. The electrodes fabricated in this way are such that the thiolated strand, and thus the one anchored to the surface, was always the same; only the complements contained the mutated bases. Figure 2-5 shows the chronocoulometric response of MB in the presence of $Fe(CN)_6^{3-}$ on the three samples. It is possible to see that good discrimination is achieved after only five seconds. It is also interesting to note the curvature of the chronocoulometric response: we shall see later how this curvature essentially disappears on microelectrode, revealing the dynamic character of the electrocatalytic process occurring at the modified surface.

In situ hybridization was achieved by the following steps: the electrodes were first incubated in hot buffer (90 °C) for about 10 minutes to dehybridize the duplex. At this point all three electrodes are identical as only the thiolated single stranded DNA is left on the surface. After thorough rinsing, the electrodes were then rehybridized by incubating

† The p53 tumor suppressor gene encodes a multifunctional transcription factor that plays a key role in the prevention of human cancer.

the electrode in a solution containing 500 pM of desired target sequence: ssWT, ss248, and ss249, where "ss" indicates single strand oligonucleotide. We chose to rehybridize electrode WT to a ss249, electrode 248 to ssWT, and electrode 249 to ss248. The result is shown in Figure 2-6. Electrocatalytic signals change as expected: recovery of the signal is observed for the electrode 248 rehybridized to the ssWT, while decrease of the signal is observed for the electrode WT rehybridized to ss249. No particular change is observed for the electrode with 249 rehybridized to 248, which is simply equivalent to a shift of the mutation site. However, the signals do not change to the full extent possible. For instance, the signal at electrode 248, after rehybridization to ssWT, does not reach the intensity measured before the dehybridization, probably because of partial dehybridization or even desorption of the thiol strand.

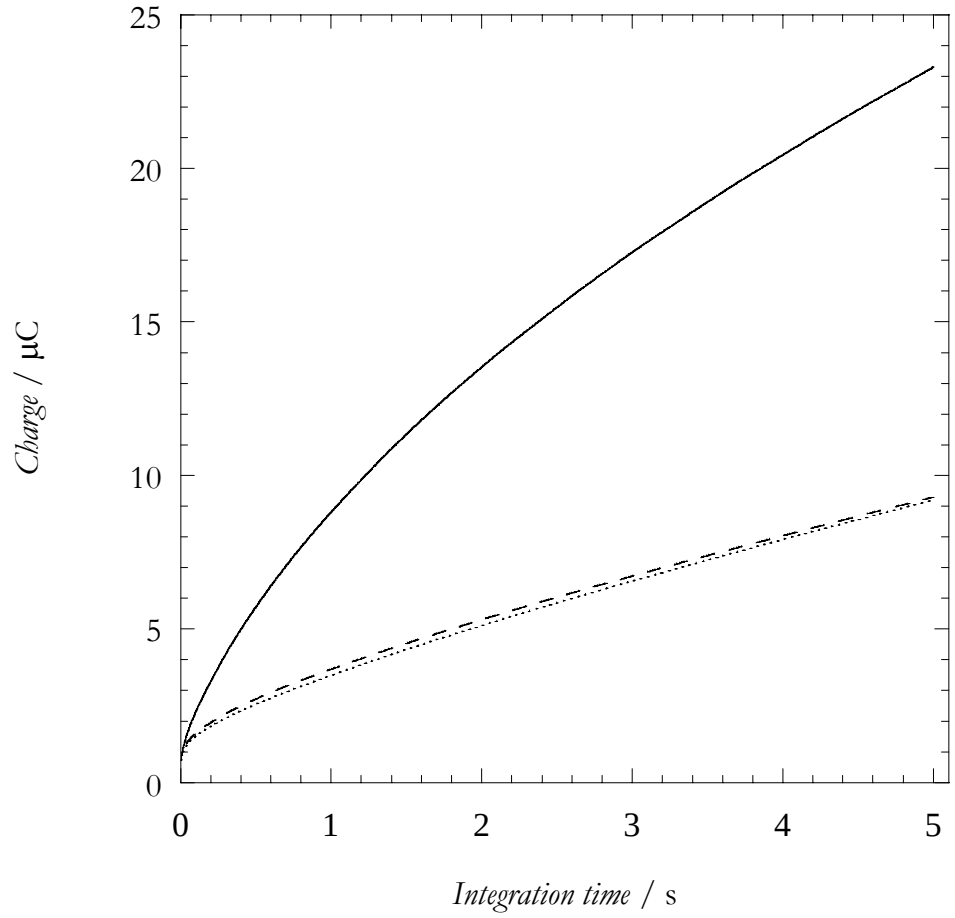

Figure 2-5: Chronocoulometry of 0.5 μM MB with 2 mM $Fe(CN)_6^{3-}$ at three gold electrodes modified with the p53 thiol-teminated sequence HS-5'-ATG GG<u>C</u> CT**C** CGG TTC-3' hybridized to a fully base-paired complement (WT, solid line), a complement that features an A opposite to <u>C</u> (248, dotted line), and a complement that features an A opposite to **C** (249, dashed line). The potential applied corresponds to the potential of the electrocatalytic peak. Good discrimination is obtained after only 5 seconds of charge integration.

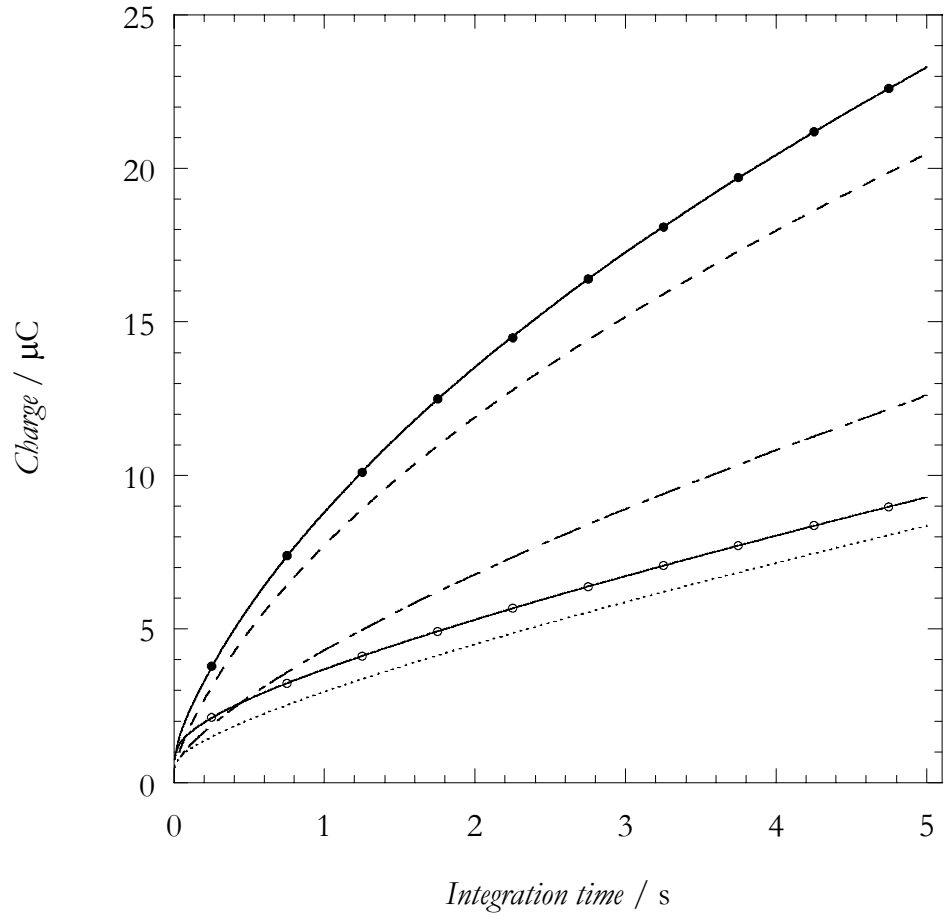

Figure 2-6: Chronocoulometry of 0.5 μM MB with 2 mM $Fe(CN)_6^{3-}$ at three gold electrodes, like in Figure 2-5. The solid lines with filled and empty circles correspond to the chronocoulometry prior dehybridization of the WT and 249 (or 248), respectively. Electrode WT exhibits low charge transduction when rehybridized to the ss249 sequence featuring a CA mismatch at codon 249 (dash-dot line). Electrode 248 instead regains electron transfer efficiency when rehybridized to the ssWT sequence, and thus removing the mismatch (dashed line). Electrode 249 is rehybridized to sequence 248 and no particular change is observed in the charge transduction, as the mismatch is simply shifted 3 bases from its original position (dotted line).

2.2.2 Fabrication of the DNA Chip

In order to develop a sensitive and practical diagnostic device, we wanted to accomplish two distinct goals on the same device. The first goal was to achieve *in situ* hybridization, as it is a necessary technique to develop a practical diagnostic device. One can imagine fabricating a device composed of several electrodes, each of them modified with distinct sequences that would function as capturing probes for solution-borne target oligonucleotides. As DNA-mediated electron transfer and, therefore, mismatch detection are essentially a duplex phenomenon, dehybridization and rehybridization have to be performed with 100% efficiency in order not to limit the detection sensitivity. The second goal we would like to achieve is miniaturization of the device, so that a relatively large number of sequences can be tested simultaneously. Because the detection is realized by an electrochemical technique, miniaturization seems quite straightforward by photolithography, but one has to be aware of two practical limitations. The first limitation is dictated by the sensitivity of the amplifier for the detection of the electrochemical current from ultramicroelectrodes; it would not be practical to perform the electrochemical readout when the signal is convoluted with noise coming from electromagnetic waves and ground fluctuations. Secondly, the device electrode density on the chip is limited by the size of the connection from the electrode to the external pads. Consequently, only low-throughput technologies can be achieved by miniaturization of devices based on electrochemical techniques. Nevertheless, there are many diseases associated with a limited number of SNPs (1-20), "hot spots," and detection of these can be extremely useful.

Lithography is the process of transferring patterns of geometric shapes on a mask to a thin layer of photoresist covering the surface of a semiconductor wafer.[45] The schematic representation of the process is shown in Figure 2-7. The pattern transfer is accomplished first by exposing a silicon wafer covered with a 0.5-1 μm spin-coated (1000 to 10,000 rpm) photoresist using a 200-400 nm light via the projection of a mask onto the

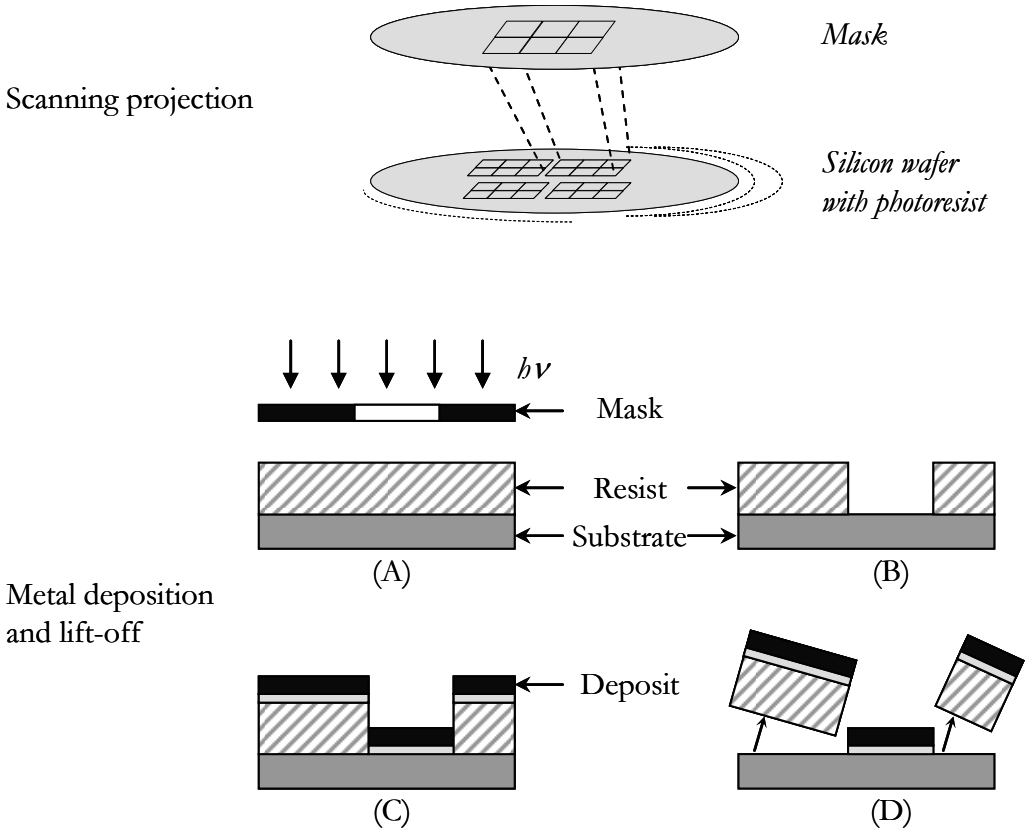

Figure 2-7: Schematic representation of the optical lithographic and lift-off transfer processes.

wafer. The technique is called scanning projection because the small image field is stepped over the wafer surface by the two-dimensional translation of the wafer, while the mask remains stationary. After exposure of one chip site, the wafer is moved to the next chip site and the process is repeated. Exposure of the photoresist to UV light produces a polymerization that allows it to become less soluble and thus more hardly removed in the development process in an organic solvent. After the removal of the unexposed photoresist, a thin film of a metal is vapor deposited over the wafer. The portion of the film on the resist is removed by selectively dissolving the resist layer in an appropriate liquid etchant so that the overlying film is lifted off and removed. In the fabrication of the DNA chip, the lithographic process was repeated two times: one for the transfer of the gold electrodes pattern, and the second for the deposition of a layer of Si_3N_4 (or SiO_2) that serves as insulator for the all the leads of the electrodes, leaving exposed only the actual electrodes and the wire-bonding pads. A scheme of the mask layout used for transferring the chip pattern is shown in Figure 2-8.[‡]

The fabricated chips are then individually assembled in a ceramic packages using silver paint to allow electric contact of the chip to the grounded chassis. Some pictures of the actual chip assembly are shown in Figures 2-9. The individual electrodes were wire-bonded with a 50 μm silver wire. Because the whole die is supposed to be immersed into the aqueous solution containing redox reporters, it is important to limit the background current by also insulating the silver wires. This was achieved by painting a thick layer of nail polish all around the die and on the leads of the package cavity, which resulted in a very efficient insulation The electrochemical cell was composed of a Teflon lid containing a silver wire quasi-reference electrode (QRE) and a platinum wire (auxiliary). The whole chip was then assembled on a 20-pin zero-insertion-force socket for the direct connection to a switch box that allowed the selection of the individual electrodes.

---

‡ The DNA-chip has been fabricated with this procedure in collaboration with Dr. M.J. Fitzsimmons at JPL (NASA) and subsequently with Dr. X. Yang in the Electronic Engineering laboratories at Caltech.

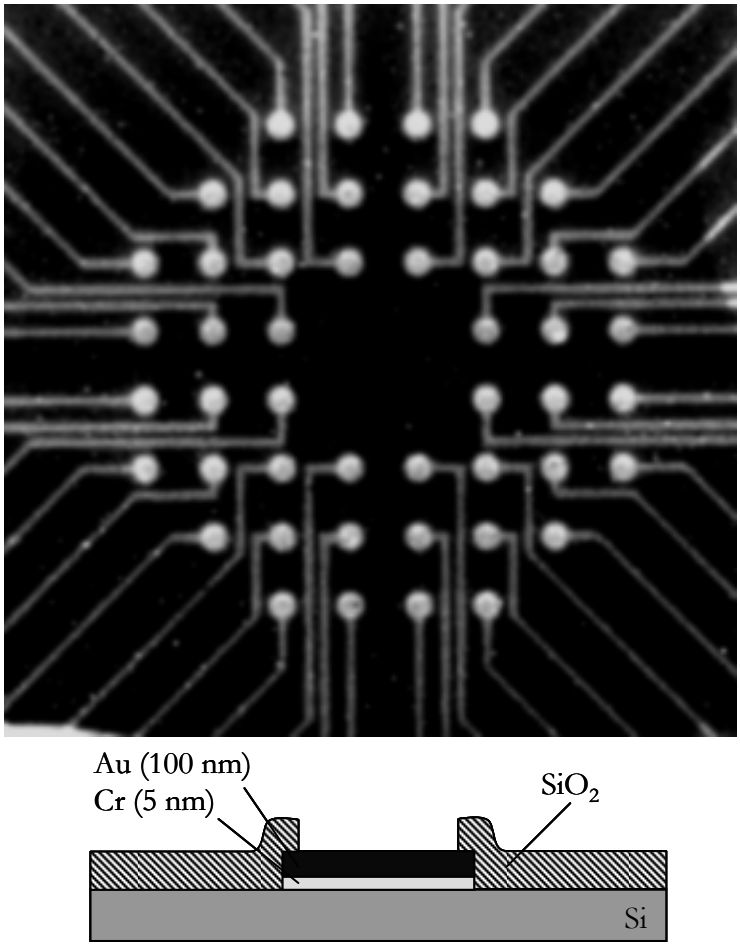

Figure 2-8: Picture of a DNA chip containing 48 gold electrodes. Bottom picture: schematic representation of the cross section of an electrode.

Figure 2-9 (on two pages): Pictures of the chip assembly. (A) The chip assembled in the package cavity. This chip has electrodes of different sizes, from 500 to 10 μm. (B) Detail of the electrochemical setup: a silver quasi-reference electrode and a platinum auxiliary wires are embedded in the Teflon lid. (C) DNA chip assembled and (D) inserted in the zero-insertion-force socket inside an aluminum Faraday cage. The blue switch box is visible in the background.

(A)

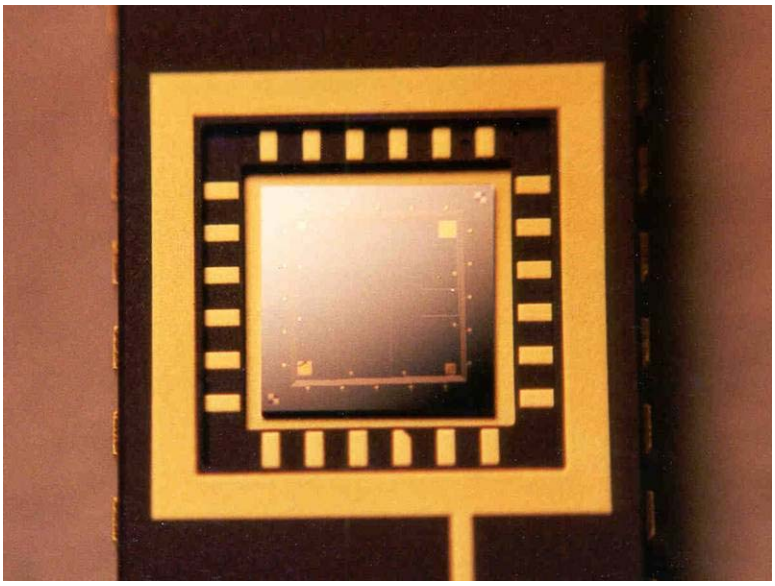

(B)

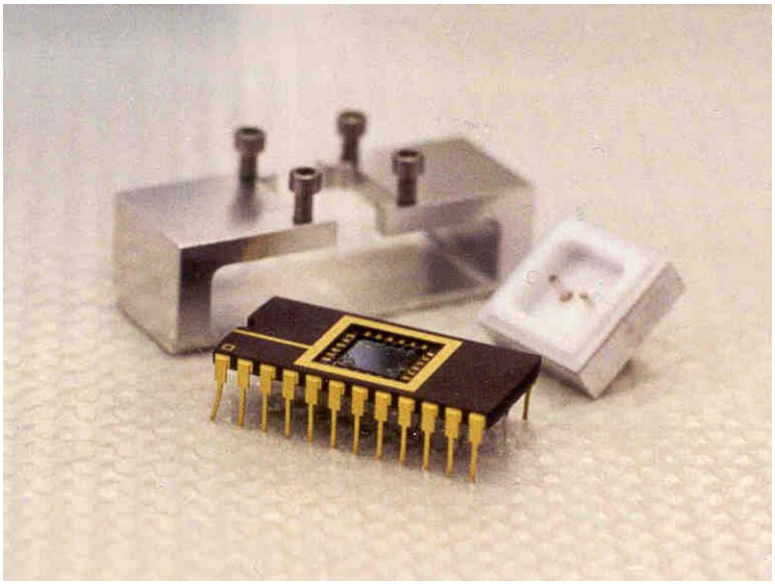

(C)

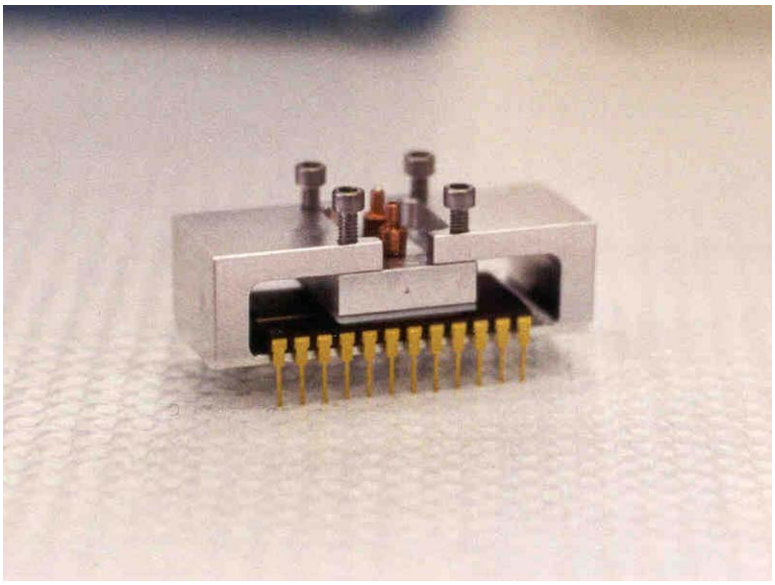

(D)

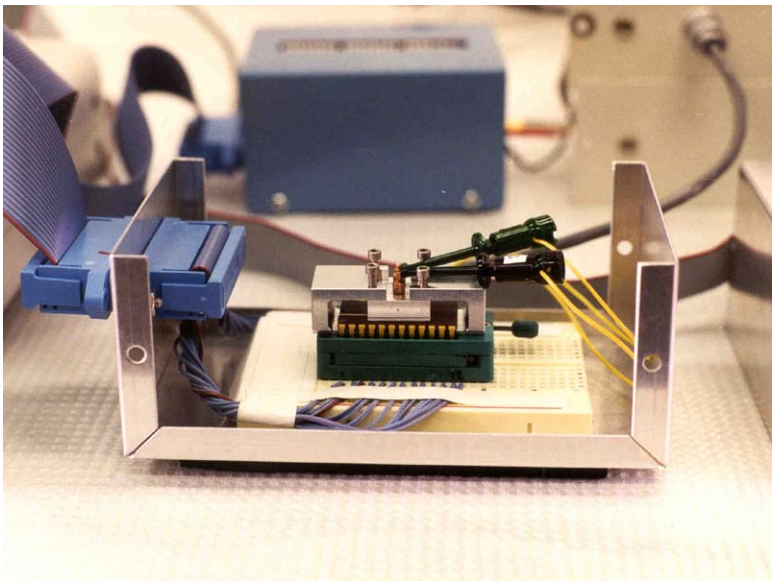

2.2.3 Electrochemical Characterization of the DNA Chip

Because the development of a practical diagnostic device requires miniaturization, we have investigated the electrochemical signal of MB at DNA modified microelectrodes as a function of the electrode size. Figure 2-10 shows the MB electrochemical signal at a 500 μm DNA-modified electrode in the presence and absence of $Fe(CN)_6^{3-}$. The signal amplification at the microelectrode is significantly enhanced compared to what one would observe at a macroelectrode. In fact, as the electrocatalytic reduction of $Fe(CN)_6^{3-}$ is diffusion limited,[43] $Fe(CN)_6^{3-}$ reduction is considerably faster due to the fast radial diffusion at microelectrodes.[46] The electrocatalytic signal at electrodes of different sizes modified with thiolated dsDNA exhibits a well-defined catalytic peak, very narrow background, and absence of direct reduction of $Fe(CN)_6^{3-}$ at the surface. The latter gives clear evidence that the electrodes are well passivated against $Fe(CN)_6^{3-}$ and that the electrochemical signal is only due to DNA-mediated reduction of MB coupled to the solution-borne $Fe(CN)_6^{3-}$. The narrow background and the sharp catalytic peak are a confirmation that the kinetics at microelectrodes are faster, both in terms of double layer capacitance (background) and fast diffusion of $Fe(CN)_6^{3-}$ to the electrode (sharp peak).

As the electrode size becomes smaller, the characteristic peak shape observed at macroelectrodes vanishes, becoming more of a S-like shape, indicating that the diffusion of $Fe(CN)_6^{3-}$ is converting from semi infinite to radial (Figures 2-11 and 2-12). The existence of a fast kinetic behavior can be understood by observing that the chronocoulometry profiles are more linear than in the case with macroelectrodes (Figure 2-13). Evidence that well-packed films are formed on electrodes whose diameter is as small as 40 μm is given by the lack of reduction of $Fe(CN)_6^{3-}$, as observed by CV: the voltammogram is featureless at positive potentials and the reverse step (from 0.5 to 1 sec) of the chronocoulometry experiment is flat. The plot of the catalytic peak current vs. the electrode area (Figure 2-14)

is essentially linear down to 40 μm where the electrochemical signal is generated from electron transfer through only $3 \cdot 10^8$ molecules (using 40 pmol/cm^2 as a surface density).

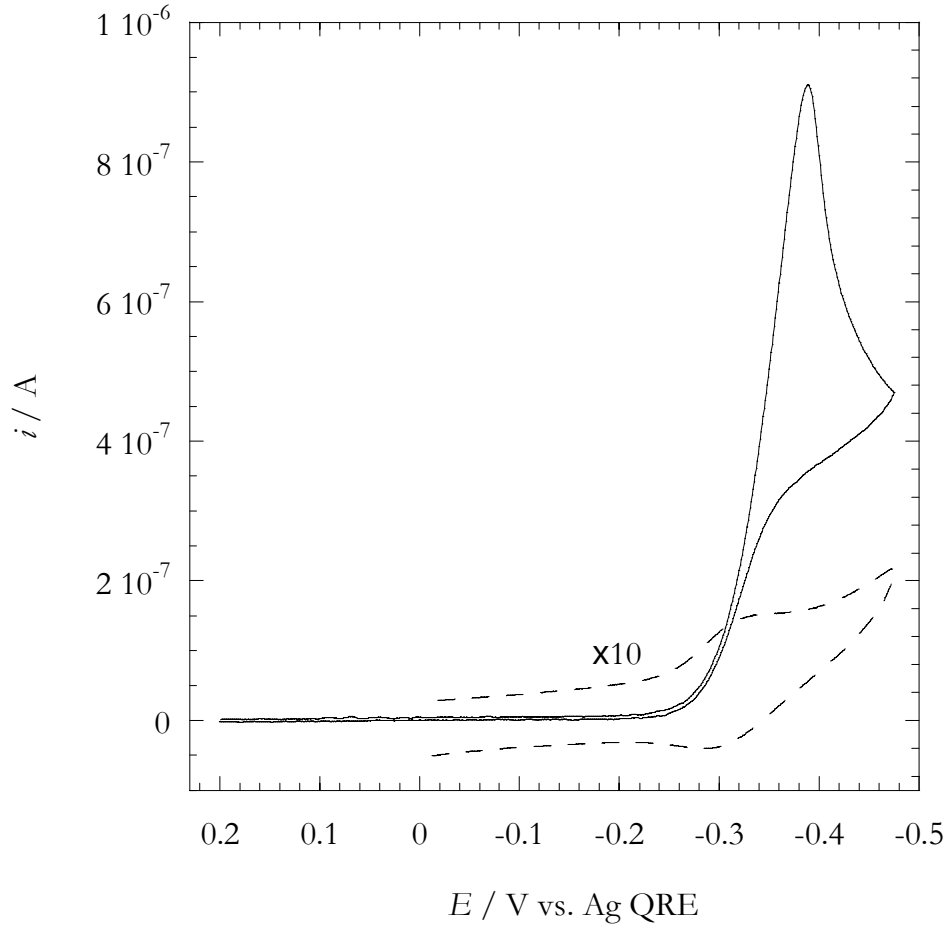

Figure 2-10: Cyclic voltammetry of 0.5 μM MB with (solid line) and without (dashed line) electrocatalytic amplification by 2mM $Fe(CN)_6^{3-}$ at a 500 mm DNA-modified electrode on the chip.

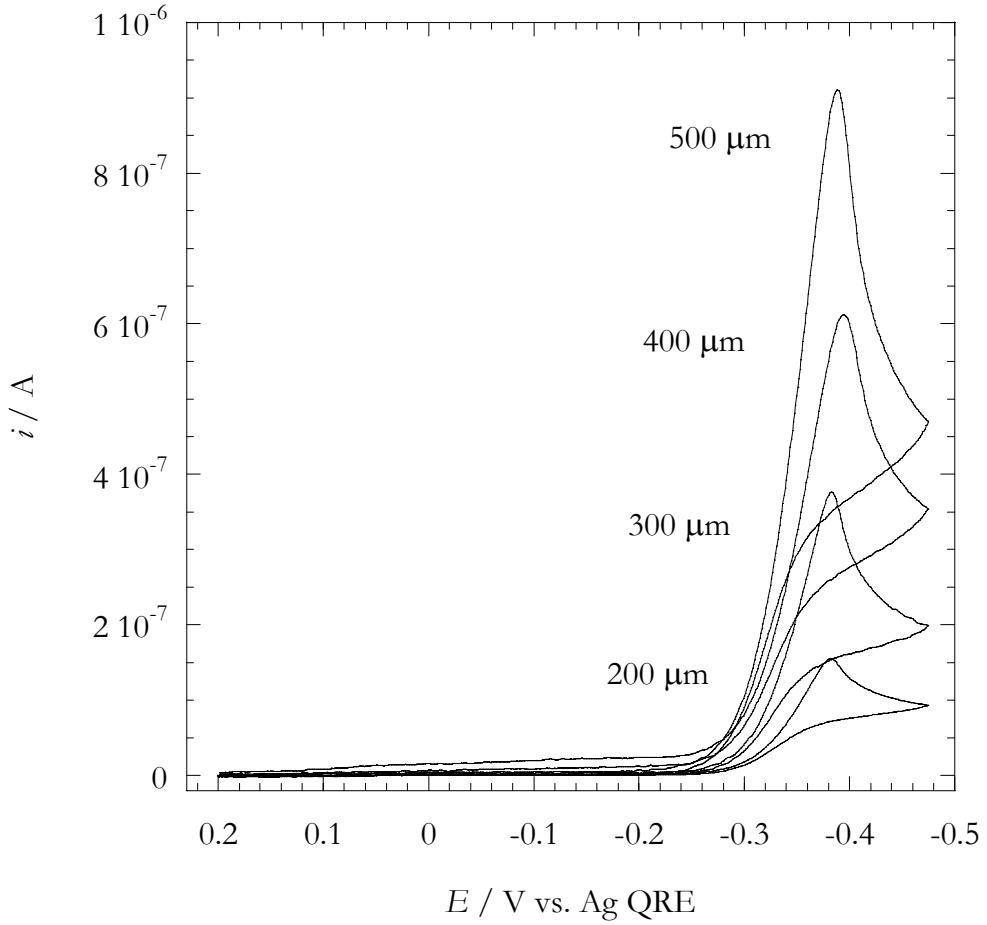

Figure 2-11: Electrocatalysis of 0.5 μM MB and 2 mM $Fe(CN)_6^{3-}$ at a DNA chip containing electrodes of size ranging from 500 μm to 40 μm modified with 5'-thiolated dsDNA of sequence HS-5'-ATG GGC CTC CGG TTC-3'. At these electrodes no direct reduction of $Fe(CN)_6^{3-}$ occurs as the DNA films are well packed.

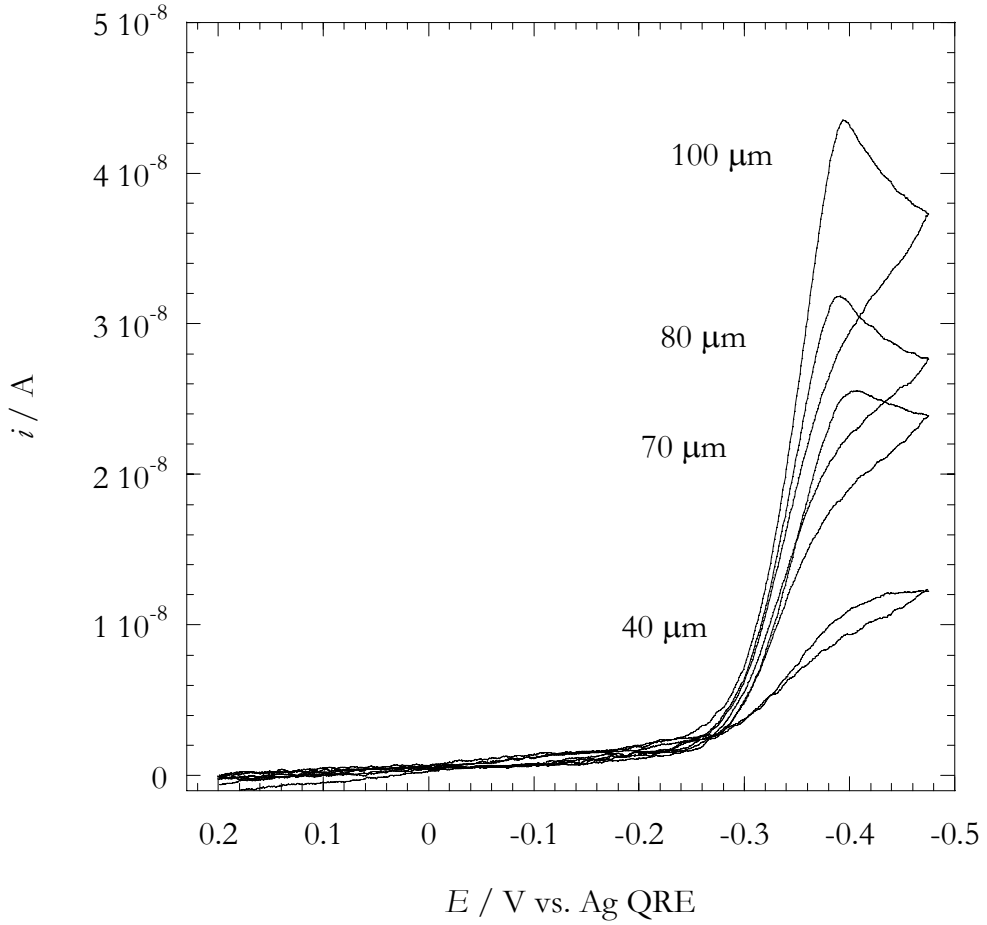

Figure 2-12: Same as Figure 2-11. Note the transition from semi-infinite to radial diffusion in the shape of the catalytic peak, as the electrode area is decreased.

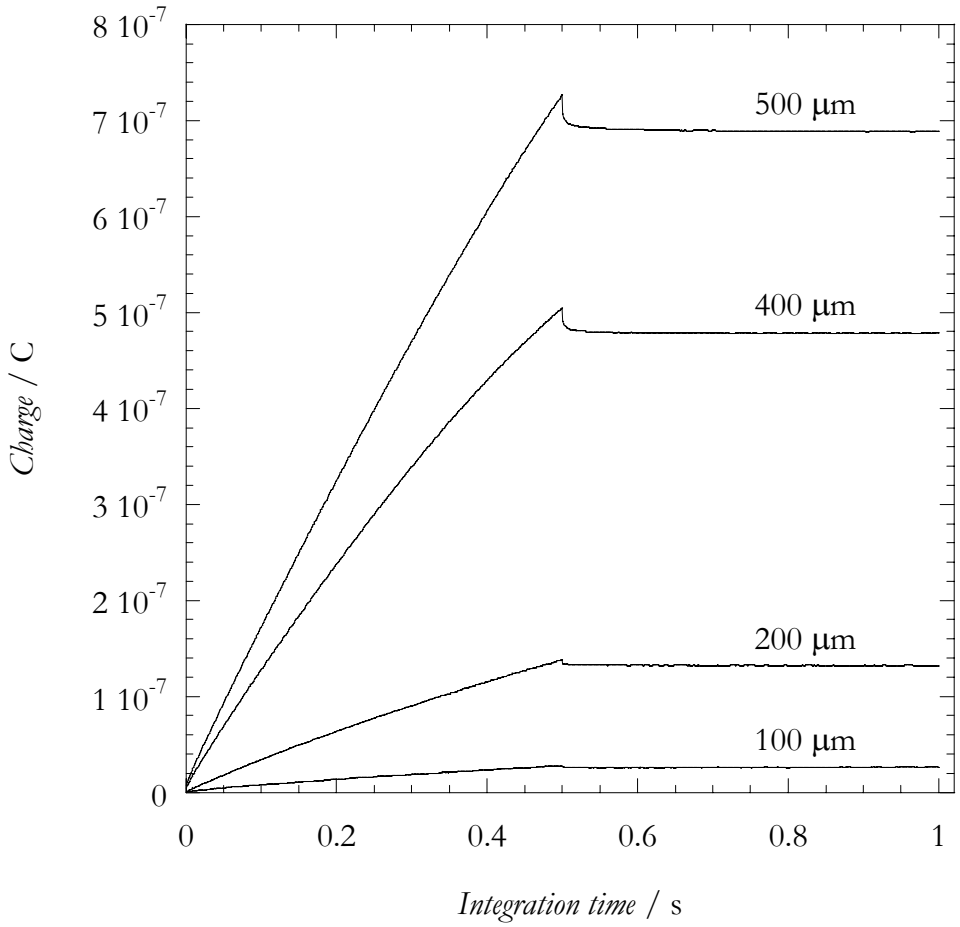

Figure 2-13: Chronocoulometry of 0.5 μM MB and 2 mM $Fe(CN)_6^{3-}$ at a DNA chip containing electrodes of size ranging from 500 μm to 100 μm modified with 5'-thiolated dsDNA (as in Figure 2-11).

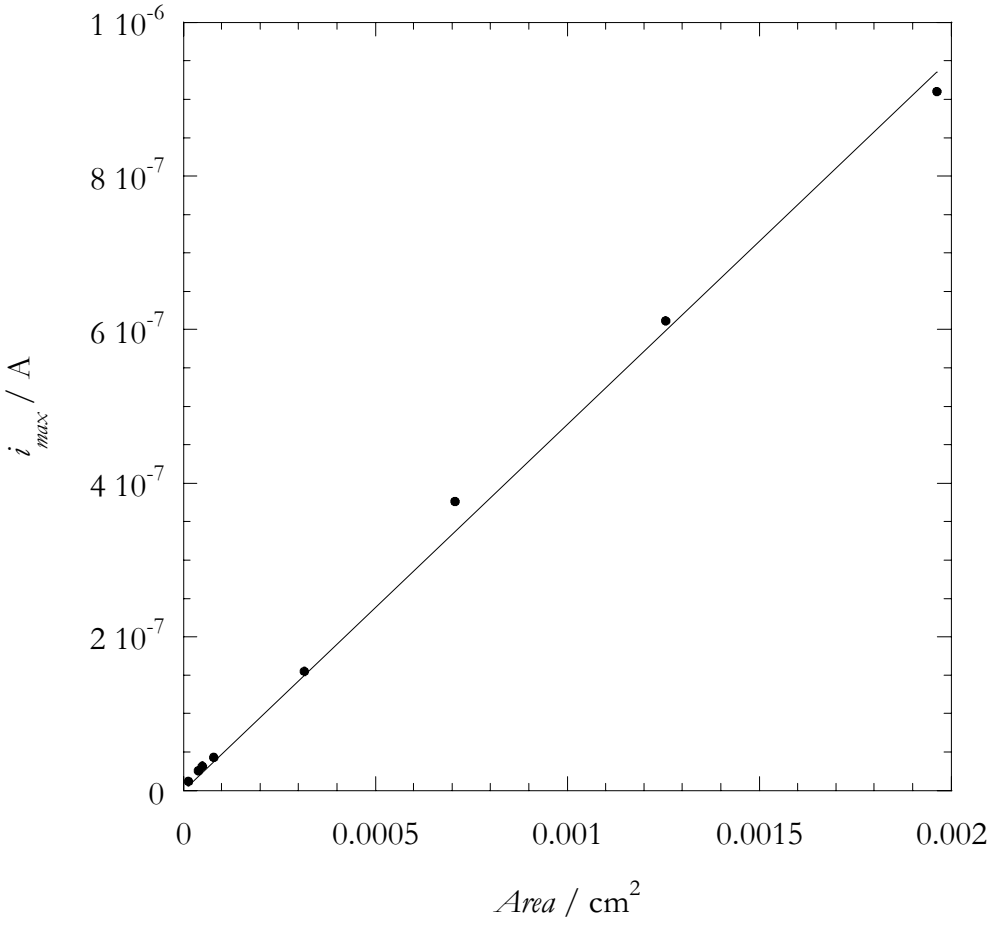

Figure 2-14: Plot of the electrocatalytic peak current as a function of the surface area of the microelectrodes on a DNA chip (same as Figure 2-11). Linear dependence is observed down to 40 μm electrodes. At this electrode, assuming a surface coverage of about 40 pmol/cm^2, the electrochemical signal is generated from charge transduction through a DNA monolayer made of about $3 \cdot 10^8$ molecules.

2.2.4 In Situ Hybridization on a DNA Chip

We have also investigated the possibility of detecting mismatches upon *in situ* hybridization with a target sequence on a DNA chip. Figure 2-15 shows the scheme of the apparatus used for performing *in situ* dehybridization and hybridization. A chip composed of four electrodes, each of 500 μm in diameter, was modified with a well-matched sequence (HS-5'-AGT ACA GTC ATC GCG, where the underlined C corresponds to the mismatch site while paring with an A) and interrogated in the presence of 0.5 μM MB and 2 mM $Fe(CN)_6^{3-}$ both by cyclic voltammetry and Chronocoulometry, in order to follow the dehybridization cycles. Hot buffer (90 °C) was first allowed to circulate over the chip for 5 minutes in order to remove the complementary strand and leave only single-stranded DNA bound to the surface. Subsequently, hot buffer (90 °C) containing 500 pM of the complementary strand with a single base mutation at the C site was circulated over the chip and the temperature was decreased slowly from 90 °C to room temperature, over about 1 hour.

Figure 2-16 shows the electrochemical response of MB with $Fe(CN)_6^{3-}$ before (as fully matched duplex), after dehybridization (as single stranded), and after rehybridization (as mismatched duplex). It is possible to see that the catalytic peak diminishes considerably upon hybridization with the mismatched strand. Interestingly, when the film is comprised of ssDNA, it does not passivate very well against $Fe(CN)_6^{3-}$ and in Figure 2-16 it is possible to see its direct reduction at the surface. Clearly the film is less packed than before dehybridization. Moreover, the catalytic peak is not very prominent, indicating that the majority of $Fe(CN)_6^{3-}$ is reduced at the surface before it can undergo electrocatalytic with leuco-MB. Upon rehybridization with a mismatched complement, the film now regains passivation against $Fe(CN)_6^{3-}$ as is evident by the featureless CV at positive potentials. However, the catalytic peak is still small due to the inefficient reduction of MB through a mismatched duplex. The chronocoulometric response of the same electrode during the *in*

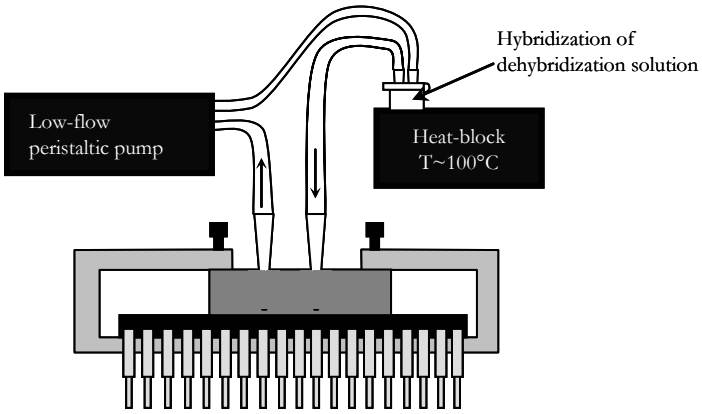

Figure 2-15: Apparatus for the automated *in situ* hybridization. A thermocouple placed at the inlet of the chip monitored the temperature inside the cell.

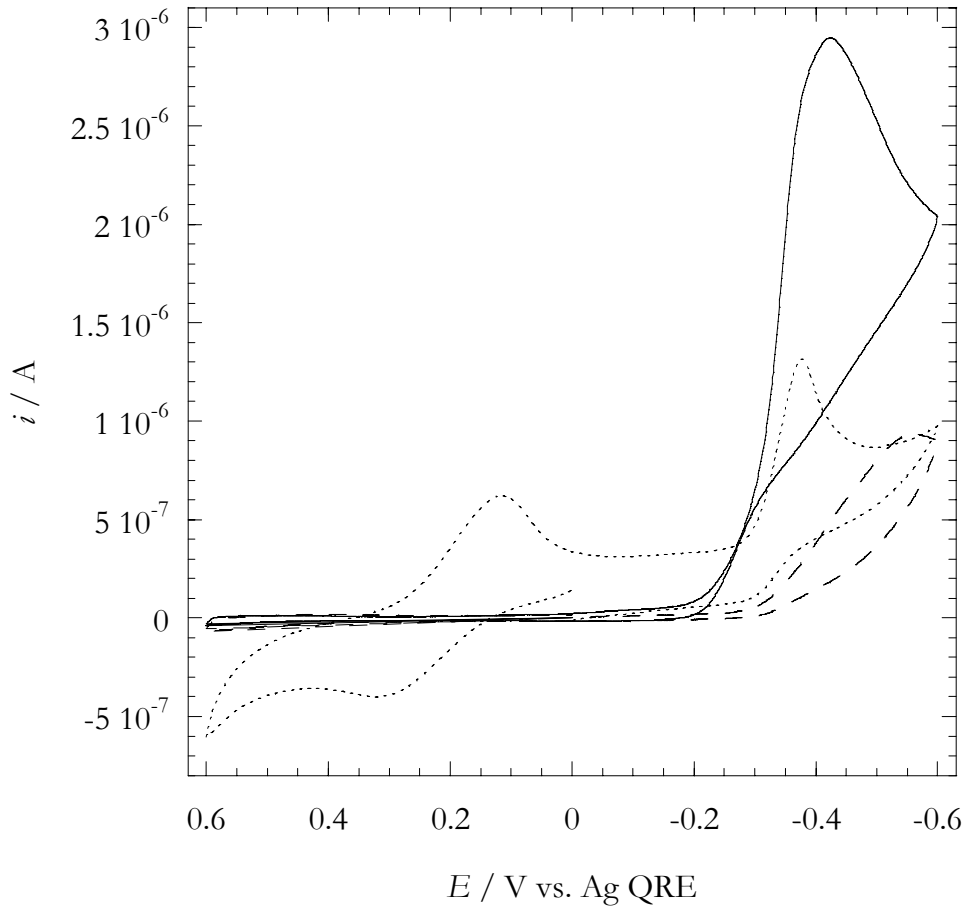

Figure 2-16: Cyclic voltammetry of 0.5 μM MB and 2 mM $Fe(CN)_6^{3-}$ at a 500 μm DNA-modified gold electrode on a DNA chip. Fully matched DNA duplex (solid line) exhibits large catalytic current at the reduction potential of MB, while after rehybridization with a mismatch complement the signal decreases substantially (dashed line). Interestingly the electrochemical response of ssDNA (dotted line) at the same electrode after dehybridization exhibits a current associated with the direct reduction of $Fe(CN)_6^{3-}$ and an intermediate catalytic response at MB reduction potential. This indicates that after dehybridization the DNA film is less packed and $Fe(CN)_6^{3-}$ can access the surface, but upon rehybridization the film regains packing and passivation against $Fe(CN)_6^{3-}$.

situ hybridization cycle is shown in Figure 2-17. Discrimination between matched and mismatched duplexes is also achieved consistently by the voltammetric response. Interestingly, the curvature of the electrocatalytic charge transduction at the single-stranded film indicates a poorly defined process which is most likely associated with the direct reduction of $Fe(CN)_6^{3-}$ at the gold surface.

In order to further corroborate the success of the *in situ* hybridization, we have analyzed *ex situ* the amount of DNA removed and added to the surface. Direct measurement by UV absorption of the DNA concentration is not possible owing to the low amount of DNA extracted from the chip. We therefore opted then for the more sensitive fluorescence spectroscopy of a single-strand specific dye (OliGreen), whose sensitivity is linear down to 100 pg/ml of oligonucleotides. Figure 2-18 shows the result of the *ex situ* quantitation based on three consecutive dehybridization/rehybridization cycles over two independent trials. As an internal standard, we have performed a dehybridization/rehybridization cycle using 1M NaOH at room temperature. Because we know the exact amount of single-stranded DNA we have added to the chip for rehybridization, there is no need to determine a calibration curve for OliGreen, but we rely only on the fact that the fluorescence intensity is proportional to the amount of single stranded DNA. The ratio between the fluorescence intensities of "hybridization" (i.e., corresponding to the amount *left* form the 0.5 pmoles (500 pM in 1 mL) solution used for the hybridization) and "dehybridization" (i.e., the amount extracted from the chip) is consistently equivalent to 0.62:

$$\frac{I_{hybridization}}{I_{dehybridization}} = \frac{0.5 - x}{x} = 0.62. \qquad 2\text{-}1$$

Based on this equation, we find that the amount of single stranded DNA that has been removed and added to the chip through the hybridization cycles is 0.31 pmoles. Because this DNA results from the dehybridization of duplexes self-assembled over four 500 μm electrodes, we were able to estimate that the surface coverage was about 41 pmol/cm^2, which is fully consistent with a well-packed DNA film. We can easily conclude that, under these conditions, complete dehybridization and rehybridization was achieved.

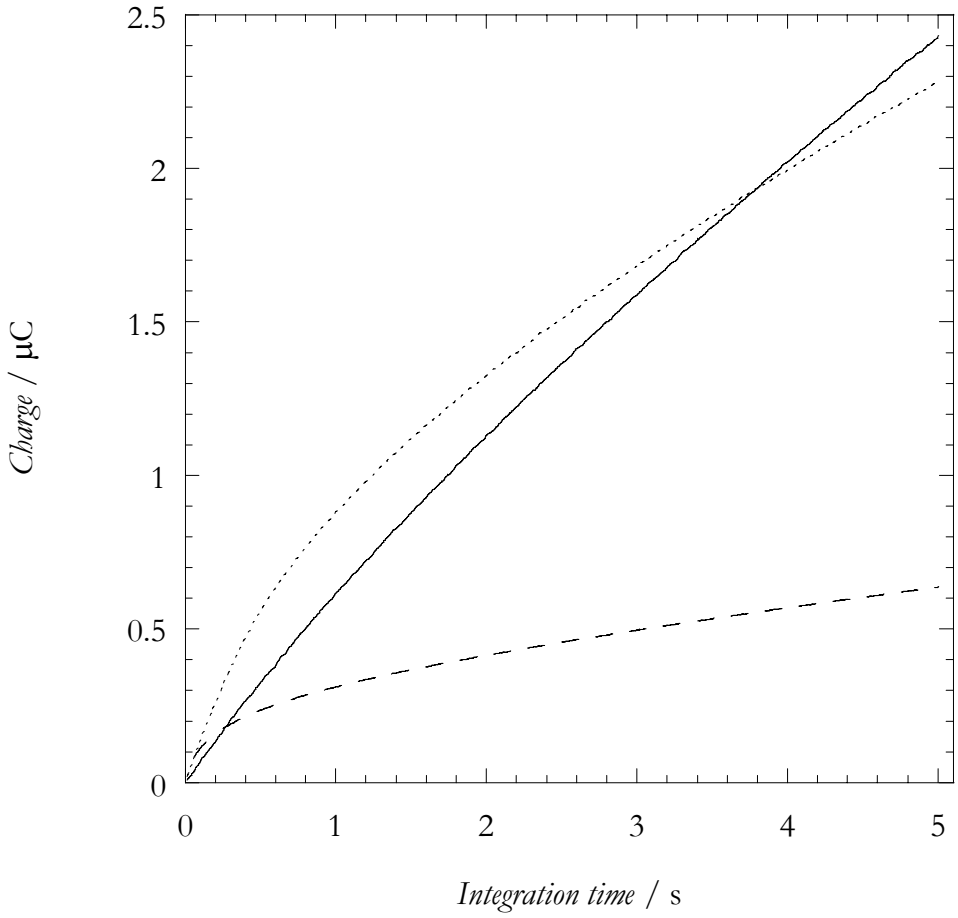

Figure 2-17: Chronocoulometry of 0.5 μM MB and 2 mM $Fe(CN)_6^{3-}$ at a 500 μm DNA-modified electrode on a DNA chip. Fully matched DNA duplex exhibits large transduced charge accumulated after 5 seconds at the reduction potential of MB (solid line), while after rehybridization with a mismatch complement it decreases substantially (dashed line). The electrochemical response of ssDNA at the same electrode after dehybridization (dotted line) exhibits a current associated with the direct reduction of $Fe(CN)_6^{3-}$.

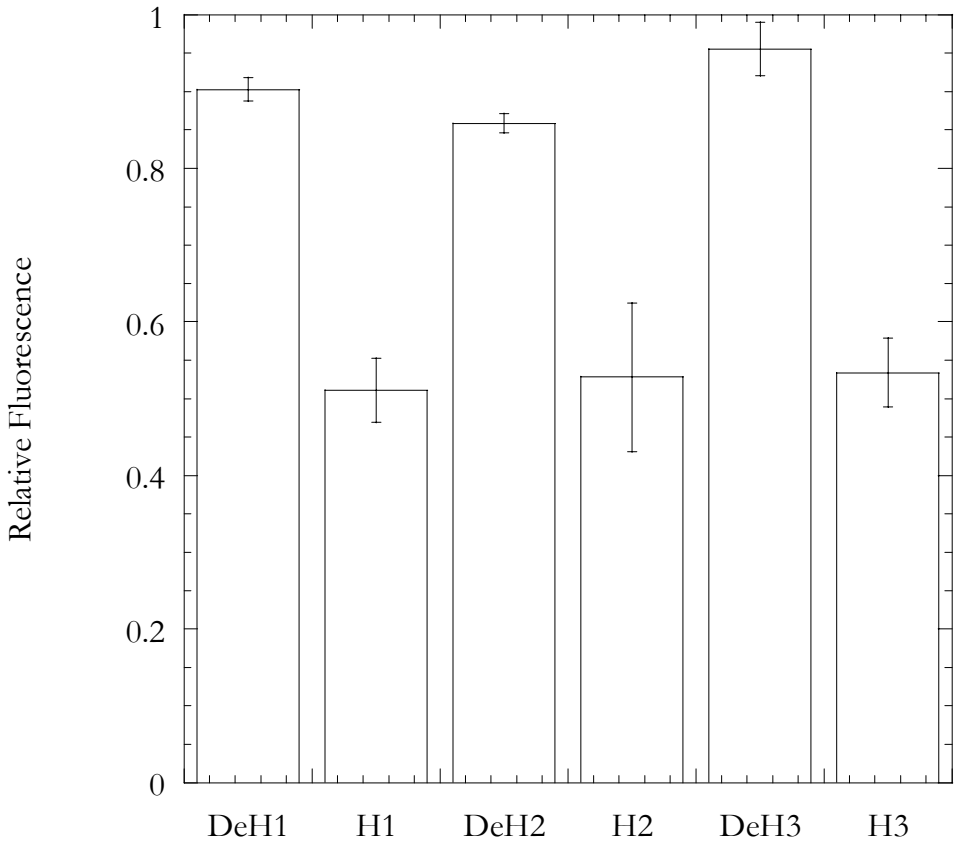

Figure 2-18: *Ex situ* quantitation by fluorescence of DNA single-strand specific dye OliGreen. DeH1 and DeH2 represent the dehybridization using hot buffer; H1, H2, and H3 represent the rehybridization of 500 pM complement by slow cooling. DeH3 is the dehybridization obtained using 1 M NaOH at room temperature. The average ratio between DeH and H is about 0.62. At each cycle 0.31 pmoles of DNA are removed from and added to four 500 μm electrodes. The estimated surface coverage is thus 41 pmol/cm^2.

2.3 Summary

We have shown here that electrocatalytic reduction of $Fe(CN)_6^{3-}$ by MB on DNA-modified electrodes can be used for the practical detection of single base mismatches. The strategy we have chosen to devise for a diagnostic tool is based on the simple heat denaturation of well-packed thiolated dsDNA on gold surfaces. Full dehybridization and rehybridization has been proven to be quantitative on macroelectrodes, leading to high discrimination between matched- and mismatched-DNA targets.

The application of this new technology has been established on a chip format, where lithographic techniques were employed to miniaturize the electrochemical cell. We observed a linear electrochemical response with respect to the electrode size and have been able to detect DNA-mediated electron transfer at microelectrodes of 40 μm in diameter. The relatively small amount of DNA required for a consistent electrochemical readout has been found to be on the order of 10^8 molecules, which suggests that this technology can eventually be employed for oligonucelatide detection without the need for PCR amplification.

The material used for the construction of the chip has been found to be compatible with oligonucleotides as well as the conditions for *in situ* hybridization. We have been able to discriminate between matched and mismatched DNA on a lithographically prepared 500 μm electrode with an exquisite reproducibility and stability. These findings strongly indicate that this DNA-chip based technology can be developed to a reliable, small, fast, and precise diagnostic tool able to detect genetic mutations, SNPs and lesions.

2.4 Materials and Methods

2.4.1 DNA Synthesis and Modification

5'-tethered oligonucleotides were prepared by first synthesizing the oligos via standard automated synthesis (trityl off) on high load (2.5 μmol) controlled pore glass (CPG) beads (Glen Research) under manual cleavage conditions. Post synthetic modification was first performed at the 5'-end of the oligos initially in the solid phase via activation of the 5'-hydroxyl termini with carbonyldiimidazole (Sigma, 80 mg in 1mL dioxane, 30-45 min) followed by 1,6-diamminohexane (Acros, 40 mg in 1 mL dioxane, 20-25 min). The amine-modified oligos were cleaved from the CPG beads and deprotected in concentrated ammonium hydroxide (J. T. Becker) for 8-12 hours at 60 °C and then treated with 2-pyridyldithiopropionic acid N-succinimide ester (Sigma, 45 min) to produce a disulfide linker. Subsequently, the sequences were purified by HPLC (semi-preparation reverse phase C18 columns), converted to free thiol with dithiothreitol (ICN, 0.5-1 M, 40-60 min), and HPLC repurified again.

The unmodified complements were synthesized by standard automated synthesis (trytil on) on a 1 μmol CPG glass under either manual or automatic cleavage. The oligos were HPLC purified, deprotected from the trytil in acetic acid (80%, 15-20 min) and repurified again in order to yield highly pure oligos. Prior to hybridization, both strands, thiol-modified and unmodified oliogs, were carefully desalted by precipitation in pure ethanol.

2.4.2 Sample Preparation

The thiol-terminated duplexes for a total amount of 100 μM duplex (5mM sodium phosphate buffer, pH 7.4, 100 mM $MgCl_2$), were deposited on either regular macroelectrodes (BAS) or on the chip and let to self assemble for 12-24 hours at room

temperature in a humid environment in order to avoid evaporation. Prior to each experiment, the DNA-modified surfaces were thoroughly rinsed with phosphate buffer (5mM sodium phosphate buffer, 50 mM NaCl, pH 7.4) in order to remove any excess of magnesium and non-specifically bound oligos.

2.4.3 Apparatus and Measurement

The electrochemical cell used for the analysis of the macroelectrodes was a standard three-compartment glass cell, using a platinum wire for auxiliary electrode and a SCE for reference. A modified Luggin capillary separated the working compartment of the electrochemical cell from the reference compartment. All measurements have been performed at room temperature and in solution thoroughly degassed with Ar. In the case of the electrochemical cell on the chip, we used a silver wire as a quasi-reference electrode, and a platinum wire as auxiliary electrode. Owing to the small size of the cell, all measurements were performed under aerobic conditions. All electrochemical measurements were performed using a BAS CV-50W electrochemical analyzer.

2.5 References

1. Kolodner, R., Biochemistry and genetics of eukaryotic mismatch repair. *Genes and Development* **1996,** 10, (12), 1433-1442.
2. Kolodner, R. D., Mismatch Repair: Mechanisms and Relationship to Cancer Susceptibility. *Trends in Biochemical Sciences* **1995,** 20, (10), 397-401.
3. Modrich, P., Mechanisms and Biological Effects of Mismatch Repair. *Annual Review of Genetics* **1991,** 25, 229-253.
4. Kwok, P. Y., Methods for genotyping single nucleotide polymorphisms. *Annual Review of Genomics and Human Genetics* **2001,** 2, 235-258.
5. Lazarus, R.; Vercelli, D.; Palmer, L. J.; Klimecki, W. J.; Silverman, E. K.; Richter, B.; Riva, A.; Ramoni, M.; Martinez, F. D.; Weiss, S. T.; Kwiatkowski, D. J., Single nucleotide polymorphisms in innate immunity genes: abundant variation and potential role in complex human disease. *Immunological Reviews* **2002,** 190, (1), 9-25.
6. Mango, R.; Vecchione, L.; Raso, B.; Borgiani, P.; Brunetti, E.; Mehta, J. L.; Lauro, R.; Romeo, F.; Novelli, G., Pharmacogenomics in cardiovascular disease: the role of single nucleotide polymorphisms in improving drug therapy. *Expert Opinion on Pharmacotherapy* **2005,** 6, (15), 2565-2576.
7. Syvanen, A. C., Accessing genetic variation: Genotyping single nucleotide polymorphisms. *Nature Reviews Genetics* **2001,** 2, (12), 930-942.
8. Fodor, S. P. A.; Rava, R. P.; Huang, X. H. C.; Pease, A. C.; Holmes, C. P.; Adams, C. L., Multiplexed Biochemical Assays with Biological Chips. *Nature* **1993,** 364, (6437), 555-556.
9. Fodor, S. P. A.; Read, J. L.; Pirrung, M. C.; Stryer, L.; Lu, A. T.; Solas, D., Light-Directed, Spatially Addressable Parallel Chemical Synthesis. *Science* **1991,** 251, (4995), 767-773.

10. Lemieux, B.; Aharoni, A.; Schena, M., Overview of DNA chip technology. *Molecular Breeding* **1998,** 4, (4), 277-289.

11. Schena, M.; Shalon, D.; Davis, R. W.; Brown, P. O., Quantitative Monitoring of Gene-Expression Patterns with a Complementary-DNA Microarray. *Science* **1995,** 270, (5235), 467-470.

12. Caruana, D. J.; Heller, A., Enzyme-amplified amperometric detection of hybridization and of a single base pair mutation in an 18-base oligonucleotide on a 7-mu m-diameter microelectrode. *Journal of the American Chemical Society* **1999,** 121, (4), 769-774.

13. Creager, S.; Yu, C. J.; Bamdad, C.; O'Connor, S.; MacLean, T.; Lam, E.; Chong, Y.; Olsen, G. T.; Luo, J. Y.; Gozin, M.; Kayyem, J. F., Electron transfer at electrodes through conjugated "molecular wire" bridges. *Journal of the American Chemical Society* **1999,** 121, (5), 1059-1064.

14. DeLumley-Woodyear, T.; Campbell, C. N.; Heller, A., Direct enzyme-amplified electrical recognition of a 30-base model oligonucleotide. *Journal of the American Chemical Society* **1996,** 118, (23), 5504-5505.

15. Drummond, T. G.; Hill, M. G.; Barton, J. K., Electrochemical DNA sensors. *Nature Biotechnology* **2003,** 21, (10), 1192-1199.

16. Hashimoto, K.; Ito, K.; Ishimori, Y., Novel DNA Sensor for Electrochemical Gene Detection. *Analytica Chimica Acta* **1994,** 286, (2), 219-224.

17. Johnston, D. H.; Thorp, H. H., Cyclic voltammetry studies of polynucleotide binding and oxidation by metal complexes: Homogeneous electron-transfer kinetics. *Journal of Physical Chemistry* **1996,** 100, (32), 13837-13843.

18. Millan, K. M.; Mikkelsen, S. R., Sequence-Selective Biosensor for DNA-Based on Electroactive Hybridization Indicators. *Analytical Chemistry* **1993,** 65, (17), 2317-2323.

19. Millan, K. M.; Saraullo, A.; Mikkelsen, S. R., Voltammetric DNA Biosensor for Cystic-Fibrosis Based on a Modified Carbon-Paste Electrode. *Analytical Chemistry* **1994,** 66, (18), 2943-2948.

20. Napier, M. E.; Loomis, C. R.; Sistare, M. F.; Kim, J.; Eckhardt, A. E.; Thorp, H. H., Probing biomolecule recognition with electron transfer: Electrochemical sensors for DNA hybridization. *Bioconjugate Chemistry* **1997,** 8, (6), 906-913.

21. Palanti, S.; Marrazza, G.; Mascini, M., Electrochemical DNA probes. *Analytical Letters* **1996,** 29, (13), 2309-2331.

22. Ropp, P. A.; Thorp, H. H., Site-selective electron transfer from purines to electrocatalysts: voltammetric detection of a biologically relevant deletion in hybridized DNA duplexes. *Chemistry and Biology* **1999,** 6, (9), 599-605.

23. Takenaka, S.; Yamashita, K.; Takagi, M.; Uto, Y.; Kondo, H., DNA sensing on a DNA probe-modified electrode using ferrocenylnaphthalene diimide as the electrochemically active ligand. *Analytical Chemistry* **2000,** 72, (6), 1334-1341.

24. Wang, J.; Cai, X. H.; Rivas, G.; Shiraishi, H.; Farias, P. A. M.; Dontha, N., DNA electrochemical biosensor for the detection of short DNA sequences related to the human immunodeficiency virus. *Analytical Chemistry* **1996,** 68, (15), 2629-2634.

25. Wang, J.; Palecek, E.; Nielsen, P. E.; Rivas, G.; Cai, X. H.; Shiraishi, H.; Dontha, N.; Luo, D. B.; Farias, P. A. M., Peptide nucleic acid probes for sequence-specific DNA biosensors. *Journal of the American Chemical Society* **1996,** 118, (33), 7667-7670.

26. Xu, X. H.; Bard, A. J., Immobilization and Hybridization of DNA on an Aluminum(III) Alkanebisphosphonate Thin-Film with Electrogenerated Chemiluminescent Detection. *Journal of the American Chemical Society* **1995,** 117, (9), 2627-2631.

27. Xu, X. H.; Yang, H. C.; Mallouk, T. E.; Bard, A. J., Immobilization of DNA on an Aluminum(III) Alkanebisphosphonate Thin-Film with Electrogenerated

Chemiluminescent Detection. *Journal of the American Chemical Society* **1994,** 116, (18), 8386-8387.

28. Holmlin, R. E.; Dandliker, P. J.; Barton, J. K., Charge transfer through the DNA base stack. *Angewandte Chemie-International Edition* **1997,** 36, (24), 2715-2730.

29. Kelley, S. O.; Barton, J. K., DNA-mediated electron transfer from a modified base to ethidium: pi-stacking as a modulator of reactivity. *Chemistry and Biology* **1998,** 5, (8), 413-425.

30. Kelley, S. O.; Barton, J. K., Electron transfer between bases in double helical DNA. *Science* **1999,** 283, (5400), 375-381.

31. Kelley, S. O.; Holmlin, R. E.; Stemp, E. D. A.; Barton, J. K., Photoinduced electron transfer in ethidium-modified DNA duplexes: Dependence on distance and base stacking. *Journal of the American Chemical Society* **1997,** 119, (41), 9861-9870.

32. O'Neill, M. A.; Barton, J. K., DNA-mediated charge transport chemistry and biology. In *Long-Range Charge Transfer in DNA I*, 2004; vol. 236, pp. 67-115.

33. Shao, F. W.; O'Neill, M. A.; Barton, J. K., Long-range oxidative damage to cytosines in duplex DNA. *Proceedings of the National Academy of Sciences of the United States of America* **2004,** 101, (52), 17914-17919.

34. Hall, D. B.; Barton, J. K., Sensitivity of DNA-mediated electron transfer to the intervening pi-stack: A probe for the integrity of the DNA base stack. *Journal of the American Chemical Society* **1997,** 119, (21), 5045-5046.

35. Kelley, S. O.; Boon, E. M.; Barton, J. K.; Jackson, N. M.; Hill, M. G., Single-base mismatch detection based on charge transduction through DNA. *Nucleic Acids Research* **1999,** 27, (24), 4830-4837.

36. Kelley, S. O.; Jackson, N. M.; Hill, M. G.; Barton, J. K., Long-range electron transfer through DNA films. *Angewandte Chemie-International Edition* **1999,** 38, (7), 941-945.

37. Kelley, S. O.; Barton, J. K.; Jackson, N. M.; McPherson, L. D.; Potter, A. B.; Spain, E. M.; Allen, M. J.; Hill, M. G., Orienting DNA helices on gold using applied electric fields. *Langmuir* **1998,** 14, (24), 6781-6784.

38. Kelley, S. O.; Barton, J. K.; Jackson, N. M.; Hill, M. G., Electrochemistry of methylene blue bound to a DNA-modified electrode. *Bioconjugate Chemistry* **1997,** 8, (1), 31-37.

39. Stinner, C.; Wightman, M. D.; Kelley, S. O.; Hill, M. G.; Barton, J. K., Synthesis and spectroelectrochemistry of Ir(bpy)(phen)(phi)(3+), a tris(heteroleptic) metallointercalator. *Inorganic Chemistry* **2001,** 40, (20), 5245-5250.

40. Hunter, W. N.; Brown, T.; Kneale, G.; Anand, N. N.; Rabinovich, D.; Kennard, O., The Structure of Guanosine-Thymidine Mismatches in B-DNA at 2.5 Å Resolution. *Journal of Biological Chemistry* **1987,** 262, (21), 9962-9970.

41. Boon, E.; Barton, J.; Hill, M., Electrochemical detection of single-base mismatches by electrocatalysis at DNA-modified electrodes. *Clinical Chemistry* **1998,** 44, (11), 2388-2388.

42. Boon, E. M.; Ceres, D. M.; Drummond, T. G.; Hill, M. G.; Barton, J. K., Mutation detection by electrocatalysis at DNA-modified electrodes. *Nature Biotechnology* **2000,** 18, (10), 1096-1100.

43. Boon, E. M.; Barton, J. K.; Bhagat, V.; Nersissian, M.; Wang, W.; Hill, M. G., Reduction of ferricyanide by methylene blue at a DNA-modified rotating-disk electrode. *Langmuir* **2003,** 19, (22), 9255-9259.

44. Hollstein, M.; Sidransky, D.; Vogelstein, B.; Harris, C. C., P53 Mutations in Human Cancers. *Science* **1991,** 253, (5015), 49-53.

45. Sze, S., *Semiconductor Devices, Physics and Technology*: John Wiley and Sons: 1985.

46. Bard, A. J.; Faulkner, L. R., *Electrochemical Methods, Fundamental and Applications*. 2nd ed.; John Wiley and Sons, 2001.

Chapter 3 ELECTROCHEMISTRY AT DNA-MODIFIED GOLD ELECTRODES

3.1 Introduction

Chemically modified electrodes have permitted the advance of the study of electron transfer kinetics through a great variety of molecules.[1-10] The lack of diffusion observed at such electrodes allowed fundamental studies to be conducted on the electron transfer properties of molecules without the complication of mass transfer. Moreover, the development of self-assembled monolayers (SAMs) further facilitated the fabrication of chemically modified electrodes and initiated the study of molecules potentially useful for many practical applications, such as molecular electronics. The exponential dependence of the standard rate constant on the redox molecule/surface distance made possible the modulation of the rates to experimentally more convenient ranges. Consequently, SAMs became a suitable benchmark for fundamental studies of heterogeneous kinetics, where theory can be verified and models are developed.

DNA SAMs (hereafter DNA films) have been increasingly employed for the development of diagnostic applications and the study of biological events such as DNA-protein interactions. Although probeless investigations of DNA films can be accomplished by AC methodologies, in general, electroactive probes are utilized to monitor electron transfer (ET) through the film. A category of electroactive reporters, which interact with DNA mainly via electrostatic interaction, enable the investigation of electron transfer in a DNA-*independent* fashion and direct contact with the underlying surface is a fundamental requisite. Because film structure can highly affect the electrochemical response, these electrostatic probes enabled the development of diagnostic devices that can analyze hybridization events. There are two types of electroactive probes suitable for the investigation of DNA films: electrostatic reporters and intercalators. Because of the highly charged character of DNA films, ionic probes such as ferricyanide ($Fe(CN)_6^{3-}$) and ruthenium hexamine ($Ru(NH_3)_6^{3+}$) are probably the most utilized redox indicators for DNA films. While $Fe(CN)_6^{3-}$ is repelled from the negatively charged DNA films and provides a

qualitative indication of the amount of negatively charged backbone on the surface, $Ru(NH_3)_6^{3+}$ has often been used for a quantitative measure of the actual number of molecules adsorbed on the surface. On the other hand, DNA-mediated ET can be studied using intercalators that avidly bind DNA; here, the DNA π-stack allows the electronic communication to and from the surface. The utilization of this class of redox reporters, namely intercalators, allowed the development of diagnostic devices aimed for genetic mutation detection (see Chapter 2). To date only a limited number of intercalators including methylene blue (MB) and daunomycin (DM) have been successfully employed for the investigation of the ground-state DNA-mediated ET.

3.2 Electrostatic Distribution in DNA Films

DNA is part of the family of the polyelectrolytes due to its charged sugar phosphate backbone. In DNA films, the ionic distribution associated with charge neutrality can dramatically affect thermodynamics as well as electron transfer kinetics of *all* redox probes, regardless of whether they are intercalators or electrostatic reporters. It is crucial to understand in detail how this ionic distribution is established and to what extent it can affect the interpretation of the data. This is of particular interest in the prediction of the electrochemical response of DNA films, as an accurate measure of kinetics and thermodynamics can provide useful insight about the structure of the film itself and therefore the ability of DNA to mediate electron transfer.

3.2.1 Structure of DNA films

The design of DNA-based devices for diagnostic analysis requires the manipulation of the surface coverage, which can be controlled at the moment of the fabrication by the adjustment of three parameters: DNA concentration, ionic strength, and deposition time. DNA self-assembly on gold surfaces has been extensively studied by both Tarlov and co-workers and Georgiadis and co-workers as a function of deposition time, concentration, and DNA length.[11-17] Because they were mainly interested in highly dispersed films in order to facilitate hybridization efficiency, they have never obtained the level of surface coverage we usually are aiming for. In fact, DNA films for mismatch detection using redox intercalators require a high degree of surface packing (see Chapter 2) in order to avoid intercalation below the mismatch. Surface coverages of 30-40 pmol/cm^2 has been measured using ^{32}P labeling on films obtained under our usual self-assembly conditions, which include high concentration of divalent cations such as Mg^{2+}.[18] At this concentration,

the interhelical spacing is about 6 Å.† It is known that the presence of divalent cations, in particular Mg^{2+}, helps the formation of highly packed structures and it is often used for inducing formation of DNA crystals.[19] We have also shown with *in situ* scanning tunneling microscopy (see Chapter 4) that DNA films are indeed very well packed and tend to assemble in a close hexagonal packing, reminiscent of that obtained in DNA crystals.[20] From this perspective, DNA films fabricated in the presence of high concentration of Mg^{2+} can probably be considered a two-dimensional liquid crystal.

How can DNA pack so well on the surface? The general phenomenon of DNA packing has been extensively investigated since the early 1970s, but still today it is not fully understood to its completeness.[21-24] The key issue is how the net electrostatic interaction between DNA molecules changes from repulsive to attractive. In the presence of multivalent cations, DNA can undergo a dramatic condensation to form three-dimensional macrostructures such as toroids, rods,[19, 25-29] and even two-dimensional films,[30-32] where the average inter-helical distance can be as small as 6 Å.[33] A likely explanation for the DNA condensation in the presence of multivalent counterions is charge inversion, a phenomenon in which a charged particle strongly binds to so many counterions in aqueous solution that its net charge changes sign.[34-37] In the case of the DNA, overscreening of the phosphate backbone by Mg^{2+} and Na^{+} can lead to charge inversion, followed by attraction of an adjacent DNA strand that is attracted and strongly binds. Two-dimensional condensation of DNA chains has been observed in[31] and on[30, 32] cationic membranes by the simple addition of divalent cations, such as Ca^{2+}, Mg^{2+}, and Mn^{2+}.[31] In the bulk, DNA condensation does not occur under the same conditions,[30-32] as it also requires the addition of alcohol in order to decrease the permittivity of the solvent.[26] It is likely, however, that the confinement of DNA in a two-dimensional space might help the phase transition in some way.

---

† Technically we have measured 50 pmol/cm² but because of a surface roughness factor greater than one the actual surface coverage must be corrected.

In the case of DNA films self-assembled on gold surfaces, the electrostatic situation might be similar to those observed for two-dimensional DNA condensation.[30-32] In order to obtain well-packed films, we usually deposit the DNA in the presence of high concentrations of Mg^{2+}. Under these conditions we do not observe DNA precipitation from the bulk suggesting that forcing the DNA into a two-dimensional space by the thiol-gold bond, induces phase transition (from "liquid" to "liquid crystal") and formation of a well-packed film. The high concentration of divalent cations presumably overscreens the negatively charged backbone so that adjacent DNA molecules can "feel" an attractive force when they are in close proximity. It is however reasonable to think that anions, namely HPO_4^{2-} and $H_2PO_4^-$, aslo participate as coions in the film.

The ionic distribution can be highly complex inside the film, where both divalent and monovalent cations and anions coexist. When we remove the film from the deposition solution containing a high concentration of Mg^{2+} and place it in a buffer containing no Mg^{2+}, the situation becomes even more uncertain as charge neutrality must be maintained at all times and the relative DNA position cannot change due to the thiol-gold bond. Thus, another ionic equilibrium that satisfies charge neutrality is established as a consequence of the structural packing of the film. This implies that the ionic distribution in the film is determined by the self-assembly conditions, such as supporting electrolyte identity and concentration, DNA concentration, and deposition time.

3.2.2 Donnan Potentials

Charge neutrality is important not only because it affects the simple fabrication of the film but also the formal potential of redox probes incorporated therein. The potential difference at zero current (i.e., at equilibrium) between the solution phase and a polyelectrolyte film is called Donnan potential, E_D (Figure 3-1B). This potential is the result of an unequal distribution of diffusible ions between the two ionic phases (film and

solution) because the junction is *impermeable* to at least one of the ionic species present. Variation of the E_D is directly related to the concentration of the supporting electrolyte in the bulk and clearly ions of different sizes might have a relative permeability to the film. It is natural to assume this permselectivity will be highly selective so that electroneutrality, after a redox reaction, is ensured only by penetration or ejection of counterions (C_S^+) from and to the supporting electrolyte. Hence, pH, concentration, as well as electrolyte type, can greatly contribute to the modulation of the formal potential of redox species incorporated in polyelectrolyte films. The half-reaction describing an *n* electrons/*m* protons (ne^- / mH^+) reduction of a cationic redox species incorporated in an anionic polyelectrolyte film can be expressed by[38]

$$Ox^{b+} + (n-m)C_S^+ + ne^- + mH^+ \rightleftharpoons \left[Red \cdot H_m\right]^{(b-n+m)+} + (n-m)C_f^+ \qquad 3\text{-}1$$

and the apparent formal potential for the redox couple is then given by

$$E_{1/2}^{app} = E^{0'} + \frac{RT}{F}\frac{(n-m)}{n}\ln\left[\frac{C_S^+}{C_f^+}\right] + \frac{RT}{F}\frac{m}{n}\ln\left[H^+\right] \qquad 3\text{-}2$$

As a result, $E_{1/2}^{app}$ is expected to change by $(n\text{-}m)/n \cdot 59$ mV (at 25 °C) for every 10-fold change in C_S^+ or by $m/n \cdot 59$ mV for every pH unit. From (3-2), it can be seen that only by performing titration of both the salt and pH is it possible to determine the exact number of electrons *and* protons involved in the surface reaction. In simple cases, pH dependence can exhibit a 30 mV/pH unit slope that is a clear consequence of a $2e^- / 1H^+$ reaction. Although in this case salt concentration dependence might not be strictly necessary, it is possible to see that a slope of 30 mV/decade is also observed only if one can assume that

the total amount of cations in the film (C_f^+) does not change and the penetration of those in solution, C_S^+, is solely responsible for maintaining charge neutrality.

Being negatively charged, DNA films are expected to exhibit a high degree of permselectivity. The value of the Donnan potential is in fact a direct consequence of charge neutrality across DNA films, and the degree of permselectivity according to the electrolyte composition, concentration, and also identity. Charge equilibration at DNA films can highly modulate the formal potentials of all redox couples incorporated therein. From a general perspective, there are two possible scenarios of interfacial charge dependences. Partial penetration of counterions in the film can produce an interfacial permanent potential drop that extends over a distance comparable to the height of the film. This situation is illustrated in Figure (3-1) where the potential gradually changes across the film to reach the solution potential. Because the potential drop at charged interface is usually large (10^6-10^9 V/cm), one might expect to observe a substantial change in the formal potential of a redox couple bound to the film depending on the relative penetration. However, in our experiments we have never observed redox reactions at potentials particularly removed from those recorded at bare electrodes or with a particular distribution of formal potentials. A second scenario is where a Donnan potential is experienced at both sides of the film. The majority of the potential drop occurs primarily in close proximity of the electrode, within the linker portion of the film. Then the potential is constant for the whole depth of the film, but shifted by E_D with respect to the solution potential, as seen in Figure 3-1. This seems a more plausible situation as the highly charged character, as well as the high solubility of the DNA film might facilitate charge neutrality in its totality. But because of differential permselectivity, however, the potential in the film is different from that in solution. This situation is what we usually observe at DNA-modified electrodes, where the redox reactions of electroactive reporters do not exhibit any particular distribution of formal potentials and the redox wave is seemingly centered at a potential that is also observed in the absence of DNA.

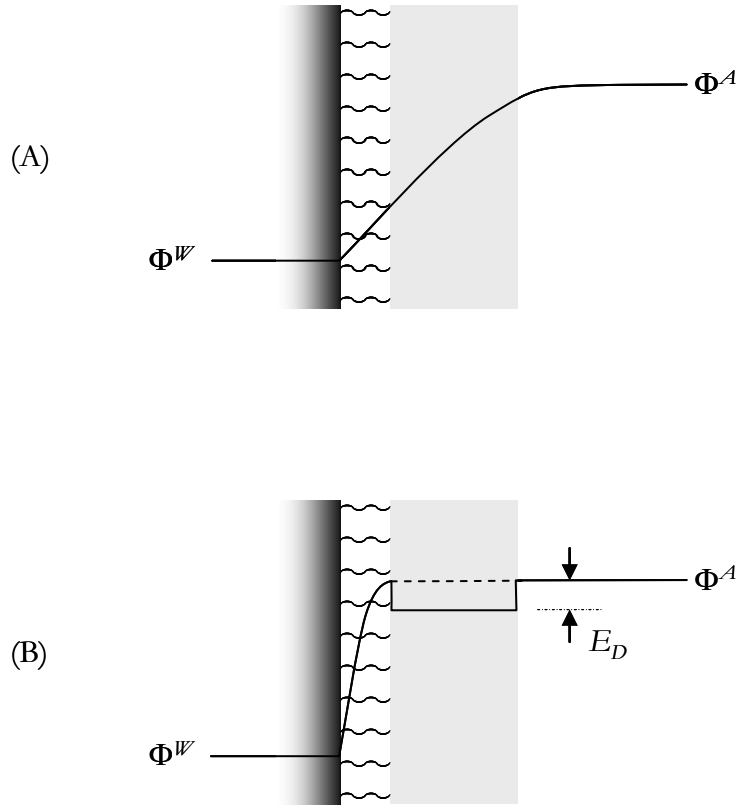

Figure 3-1: Possible electrostatic potential profiles for a DNA film in the case of (A) partial and (B) complete permeation of the film. In case (A) penetration of a redox species in the film can cause a variation in the apparent redox potential. In (B) instead the potential is constant along the whole film depth, but shifted by the value of the Donnan potential E_D. This potential is the result of an unequal distribution of diffusible ions between the solution and the DNA film because the junction is impermeable to at least one of the ionic species present.

3.3 Results and Discussion

3.3.1 Electrochemistry of MB at DNA-Modified Electrodes

We have prepared DNA films by depositing thiolated dsDNA in the presence of 100 mM Mg^{2+}, in order to produce a well-packed film. Titration of MB on these films exhibits a typical Lamgmuir binding isotherm indicating that the film reaches a saturation point, where all available sites are occupied.[18] The cyclic voltammetric response of MB at DNA modified electrodes is typical of a surface bound species. We have previously reported that the dissociation rate of MB is very low (0.043 s^{-1})[39] so that, over the time scale of the cyclic voltammogram, we can consider the concentration of bound MB to be constant. The ratio of the peak area between cathodic and anodic scans has never been equal to one because of a difference in the binding constants of MB and the reduced MB, leuco-MB. Because the DNA film is well packed and only about one MB can bind per duplex it is possible to determine the DNA surface coverage by integration of the cathodic cyclic voltammetric peak, assuming a two electron process.

3.3.1.1 pH and ionic strength dependence of MB formal potential in p-nitrophenol buffer

The dependence of the Donnan potential on pH and electrolyte is predictable and has been extensively utilized for describing the correlation between polyelectrolyte films and the formal potential shift of redox couples with respect to bare electrodes. By taking a closer look, one can realize that the generic equation describing the apparent formal potential exhibited by a redox couple incorporated into a polyelectrolyte film, equation (3-2), is strictly dependent on three important parameters: pH, cation concentration in solution (C_S^+) and in the film (C_f^+). If C_S^+ and C_f^+ do not vary, the Pourbaix diagram for MB at DNA-modified surfaces should exhibit a slope of 30 mV per pH unit, which is expected for a $2e^- / 1H^+$ reaction. This is indeed observed for the pH dependent shift of

MB formal potential determined in p-nitrophenol (p-NP), whose pK_a of about 6.5 is suitable for the pH ranging between 5 and 8. Figures 3-2 and 3-3 show the cyclic voltammograms at different pHs and the Pourbaix diagram for MB, respectively, in p-NP.

For a $2e^- / 1H^+$ redox reaction at a DNA film, according to equation (3-2), the ionic strength dependence should also exhibit a 30 mV shift per decade change in C_S^+ concentration. In Figure 3-4 the formal potential for MB determined by square wave voltammetry is plotted against the bulk concentration of Na^+. As expected, the potential change is approximately 30 mV per decade, which confirms that MB reduction occurs by a $2e^- / 1H^+$. This result shows that DNA films are indeed polyelectrolyte films and equation (3-2) is valid for describing the dependence of the formal potential on pH and ionic strength.

3.3.1.2 pH dependence of MB formal potential in phosphate buffer

We have also investigated the pH dependence of MB reduction in a 5 mM phosphate buffer (100 mM Na^+). To our surprise, the Pourbaix diagram showing the pH dependence of MB formal potential (Figure 3-5) in phosphate buffer is not linear but, instead, uniformly curved over the entire pH range. Usually slope changes in Pourbaix diagrams are associated with pK_as of either the film or the actual redox couple. However, here, we are not expecting any pK_a of either MB or DNA and the uniformity of the slope change as a function of the pH suggests that another mechanism might be involved.

Figure 3-6 shows the shift of the normalized cathodic peak as a function of the pH. The voltammogram shape is always constant suggesting that the film is invariant over the entire pH range and time. The average amount of MB bound to the film is about 0.53(1) pmoles as measured by integration of the cathodic peak (over all pHs), which corresponds to a surface coverage of approximately 20 pmoles/cm^2. This value is consistent with a well-packed film that is not fully saturated.

In Figure 3-7, one can see a comparison between cyclic voltammograms obtained in phosphate and p-NP buffers under similar ionic strength. The change in background capacitance is a clear indication that the two electrolytes interact with the film in different ways. The remarkable difference in the redox behavior between p-NP and phosphate buffer is strongly suggesting that the identity of the anions, in particular the divalent anion HPO_4^{2-}, in solution affects the delicate ionic balance of the DNA film. As described earlier, the conditions in which the film is self-assembled on the electrode determine the relative amount of anions and cations in the film. As the pH in phosphate buffer changes, the monovalent/divalent anions ratio, namely $H_2PO_4^-$/ HPO_4^{2-}, changes as well according to the Henderson-Hasselbalch equation, inducing a variation in the ionic balance that ensures charge neutrality of the film.

One can easily be convinced of the dependence of the formal potential on the relative amount of divalent and monovalent anions in the film by reversing equation (3-2) and plotting C_f^+ as a function of the pH (using $E^{0'}$=-0.058 V obtained from the intercept of the linear fit for the Pourbax diagram in p-NP). Figure 3-8 shows the variation of C_f^+ in the film as a function of the pH. It is interesting to note that the maximum is reached at the pK_a of phosphate buffer (pK_a = 6.8), suggesting the existence of a direct relationship between C_f^+ and the ratio $H_2PO_4^-$/ HPO_4^{2-}. Moreover, an additional demonstration of the validity of equation (3-2) for describing the formal potential shift in DNA films can be obtained by determining the slope of the Pourbaix diagram at the phosphate pK_a, pH 6.8. At this pH, the influence of the variation of C_f^+ is minimal and, according to equation (3-2), the formal potential depends essentially only on the pH. Indeed, at pH 6.8 we find a slope of 30 mV per pH unit. This is undeniably a demonstration that we are actually observing a real change in C_f^+ in the film.

3.3.1.3 pH dependence of MB reduction standard rate constant in phosphate buffer

We have previously reported that the standard rate constant for the reduction of DM and MB is on the order of 100 s^{-1} on DNA-modified electrodeds.[18] We have attributed this rate to electron tunneling through the σ bonds on the linker portion of the film and systematic variation of the length of the linker showed that the tunneling decay parameter is about one per CH_2.[40] Here, we have investigated the pH dependence of the standard rate constant and observed that it also varies with pH. We have analyzed the data as a function of the scan rate according to the heterogeneous Marcus kinetic theory.[41] Figure 3-9 shows the peak splitting of MB redox wave as a function of the scan rate. We can see that the k^0 is inversely proportional to the pH and varies from about 70 s^{-1} at pH 5.5 to 20 s^{-1} at pH 8.5.

This result is fully consistent with the previous observation as here we attribute this change to variation of the linker length due to a compression of the film. We have already seen that thermodynamics of MB reduction is highly dependent on charge neutrality conditions established in the film. We believe that in this case the actual film structure is also affected by this delicate balance. As the pH is increased, more divalent anions penetrate the film, probably changing the potential profile and causing the compression. According to data previously published,[40] a variation of the standard rate constant from 20 to 70 s^{-1} is equivalent to a slight compression of the linker comparable to about one methylene group.

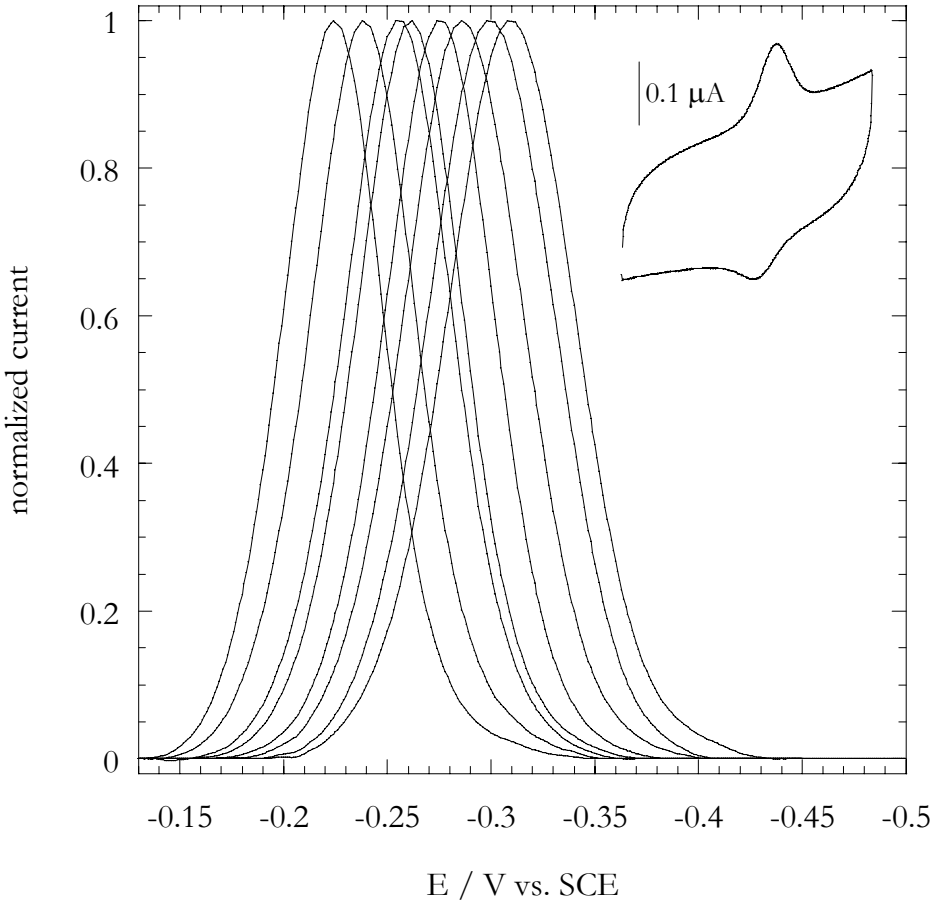

Figure 3-2: Normalized, background-subtracted cathodic peak of MB in p-NP buffer at pHs (form left to right) 5.5, 6.0, 6.5, 6.7, 7.2, 7.5, 8.0, and 8.5. The inset shows a typical cyclic voltammogram of 2 μM MB at a DNA-modified electrode obtained in p-NP pH 7.2, at 100 mV/s from 0 to -0.45 V vs. SCE.

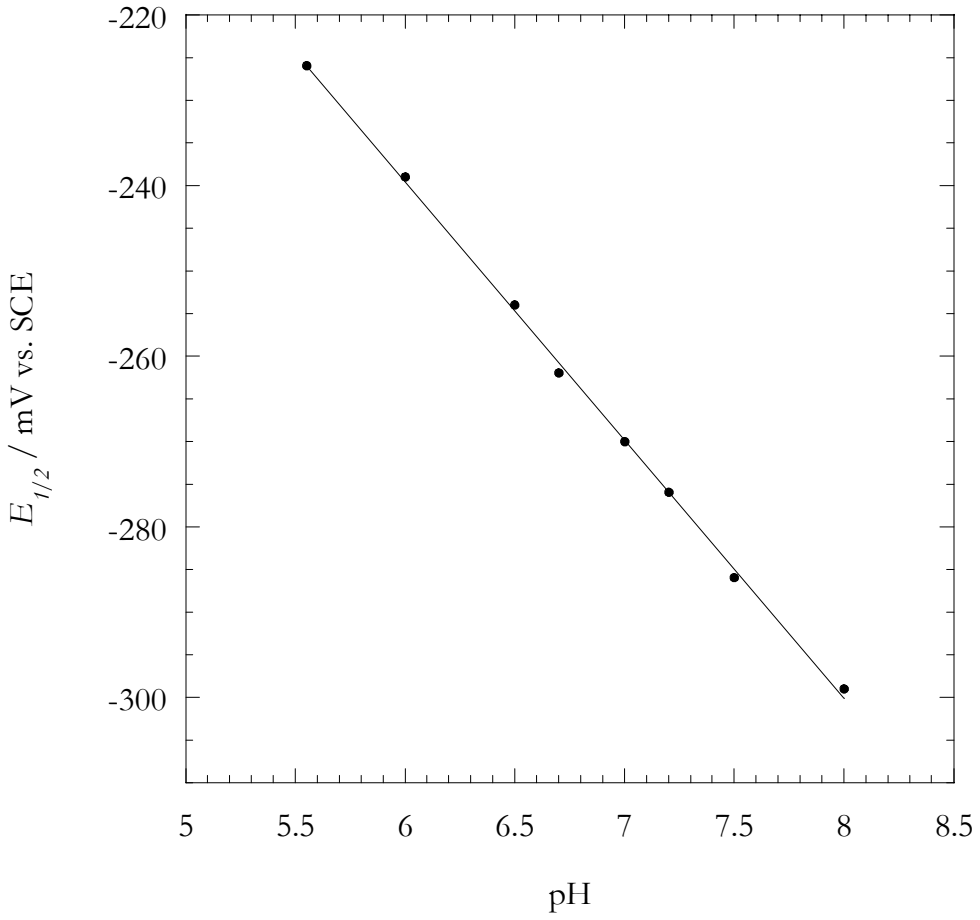

Figure 3-3: Pourbaix diagram for MB on a DNA-modified gold electrode in p-NP buffer. The solid line is the linear fit with slope of 30.3 mV per pH unit (R=0.999).

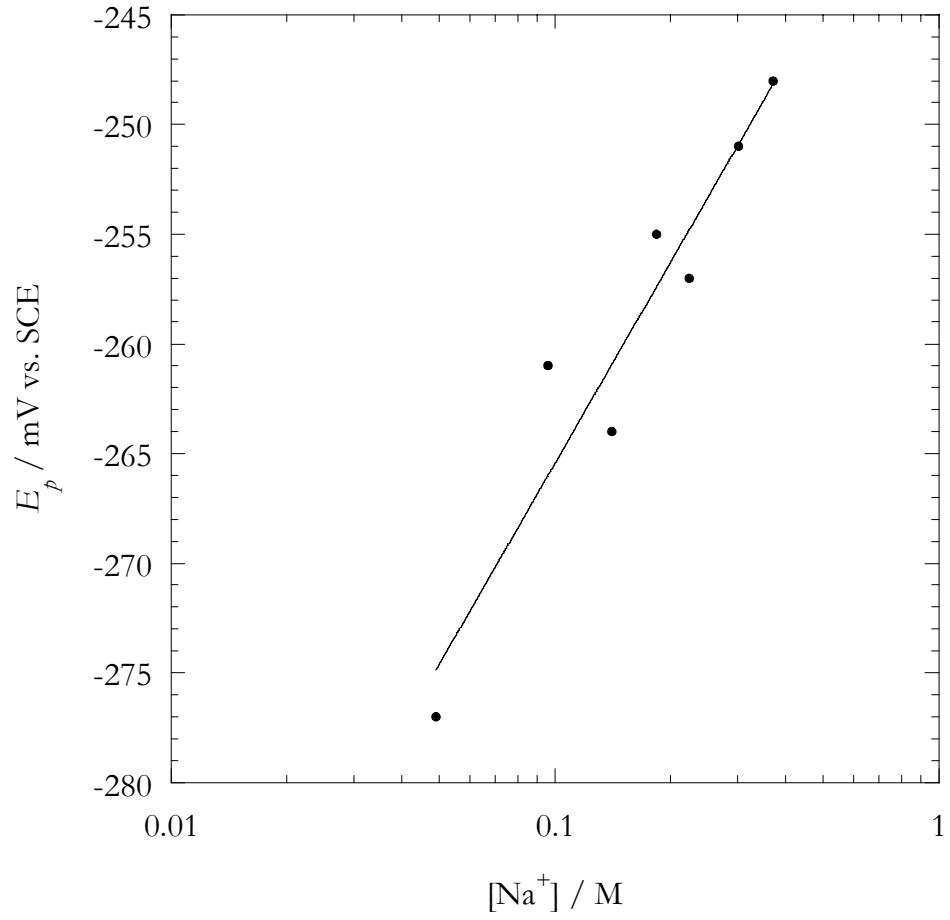

Figure 3-4: Ionic strength dependence of MB reduction in p-NP buffer at a DNA-modified gold electrode obtained at pH 7.2. The solid line is the logarithmic fit αlog[Na+] with α =30.4 mV per decade (R=0.954).

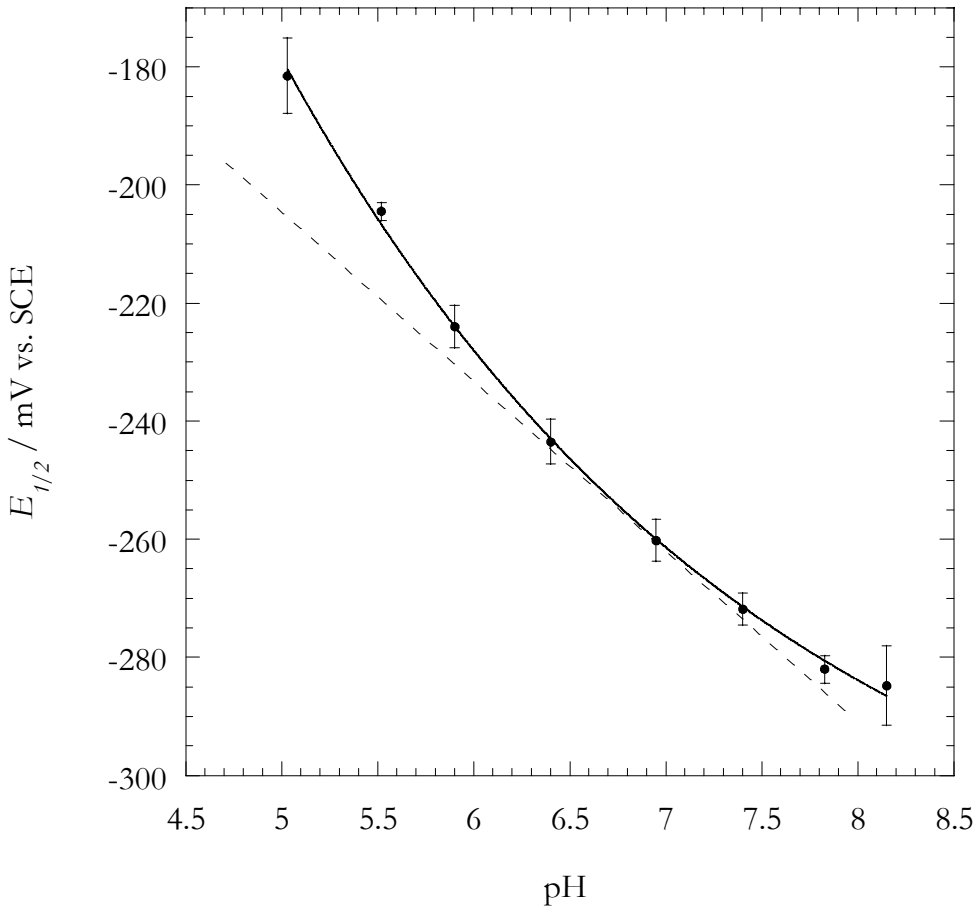

Figure 3-5: Pourbaix diagram for MB on a DNA-modified gold electrode in the presence of phosphate buffer. Error bars represent the standard deviation over three independent trials. The solid line serves as a visual guide for showing better the non-linear character of the plot. The dotted line represents the tangent of the curve at pH 6.8, with a 30 mV/decade slope.

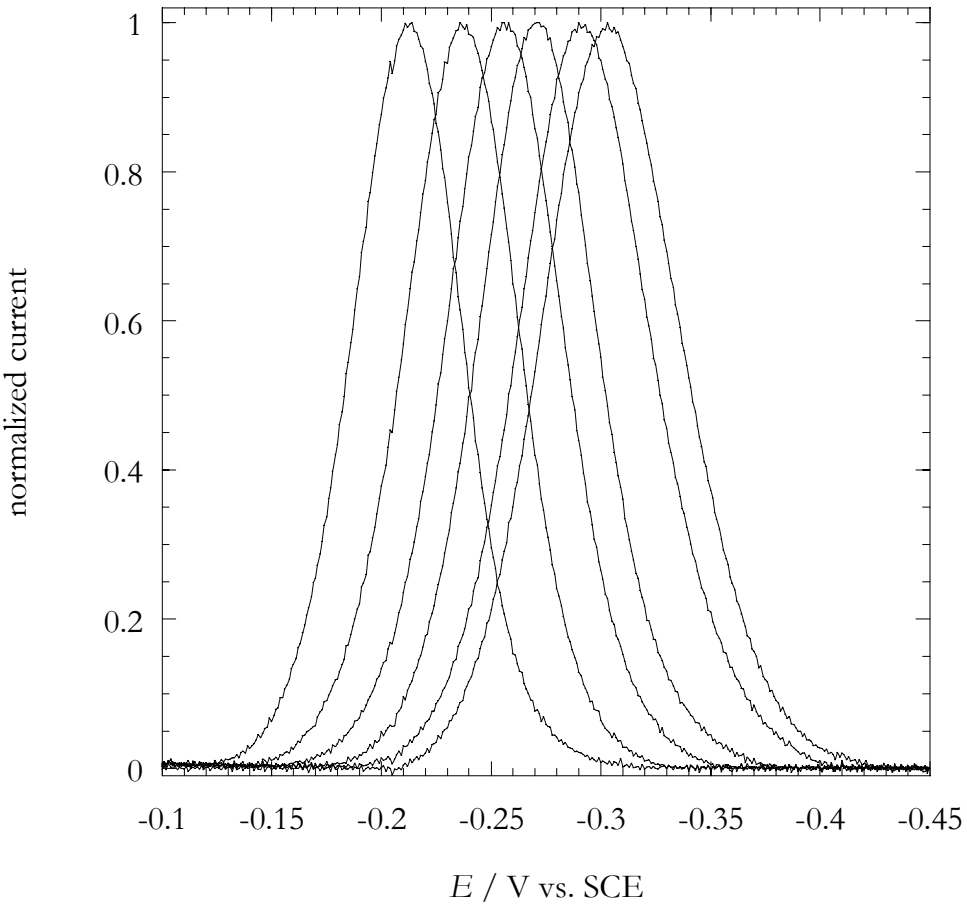

Figure 3-6: Normalized, background-subtracted cathodic peak of MB in phosphate buffer at pHs (form left to right) 5.5, 5.9, 6.4, 7.0, 7.4, 7.8, and 8.2.

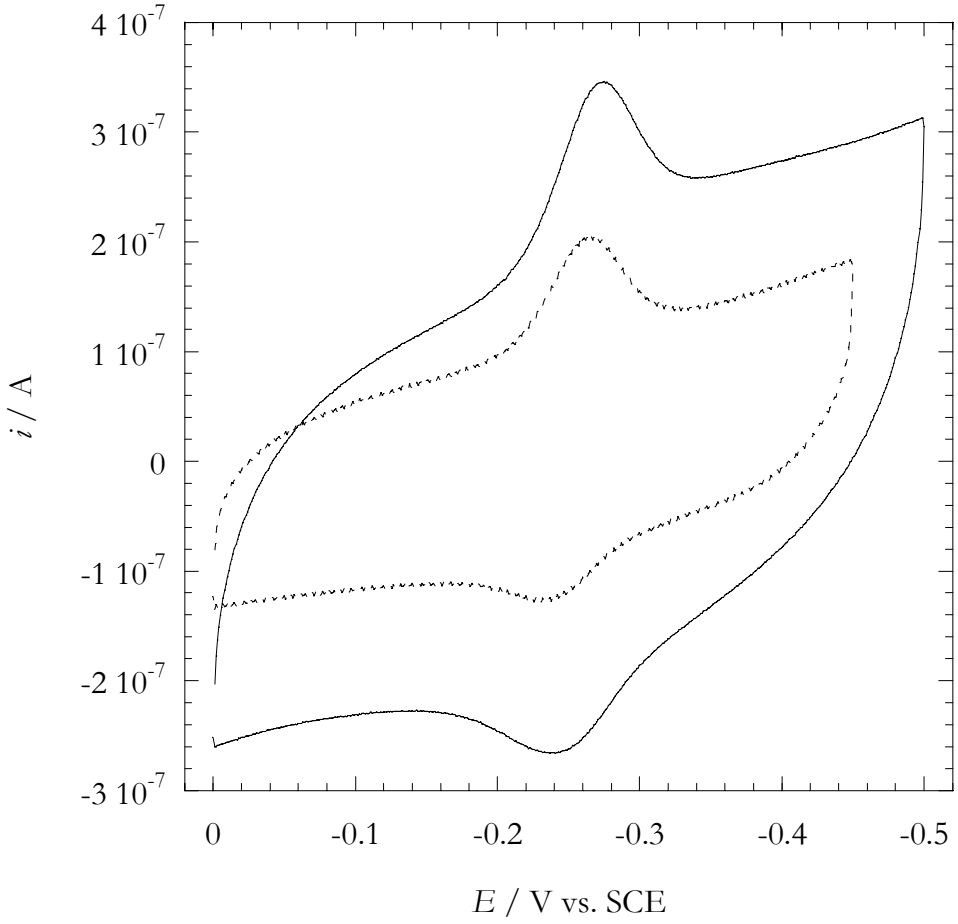

Figure 3-7: Typical cyclic voltammogram of 2 μM MB at a DNA-modified gold electrode in 5 mM phosphate buffer, 100 mM NaCl (solid line) and 5 mM p-NP buffer, 200 mM NaCl (dashed line) both at pH 7.0 and at 100 mV/s.

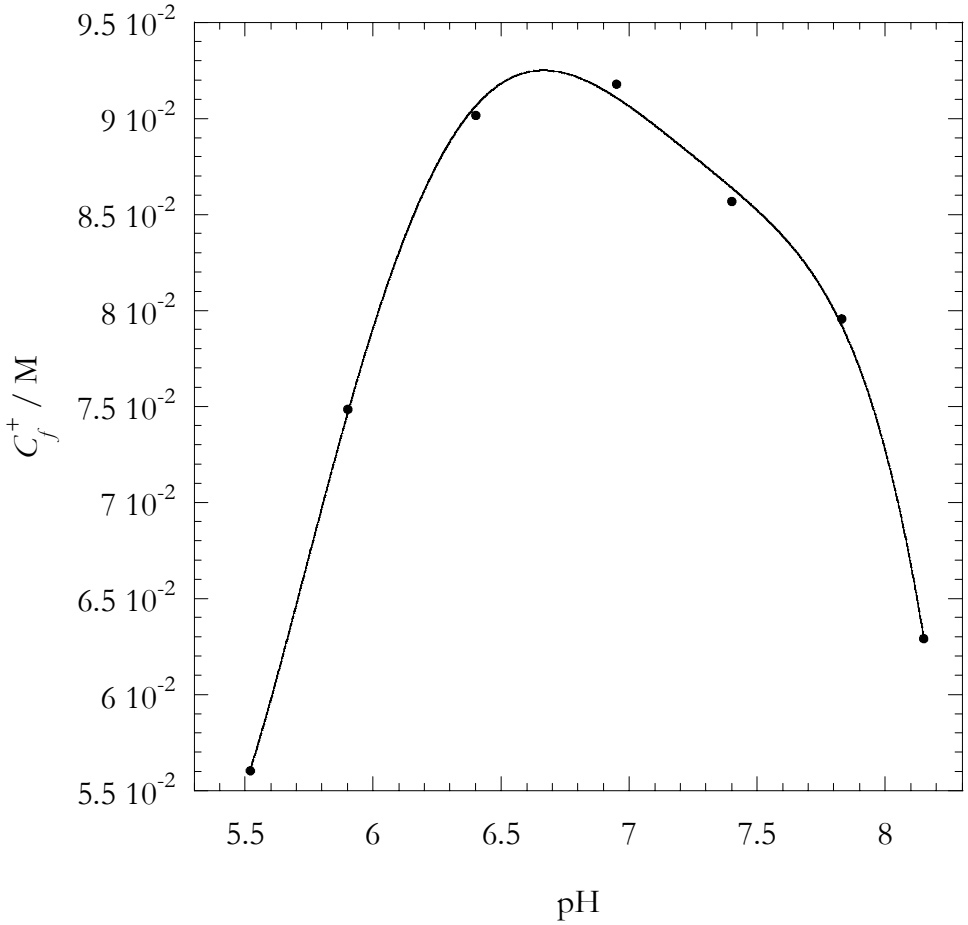

Figure 3-8: Variation of the counterion concentration inside the DNA film as function of the pH obtained from equation (3-2). The solid line serves as a visual guide.

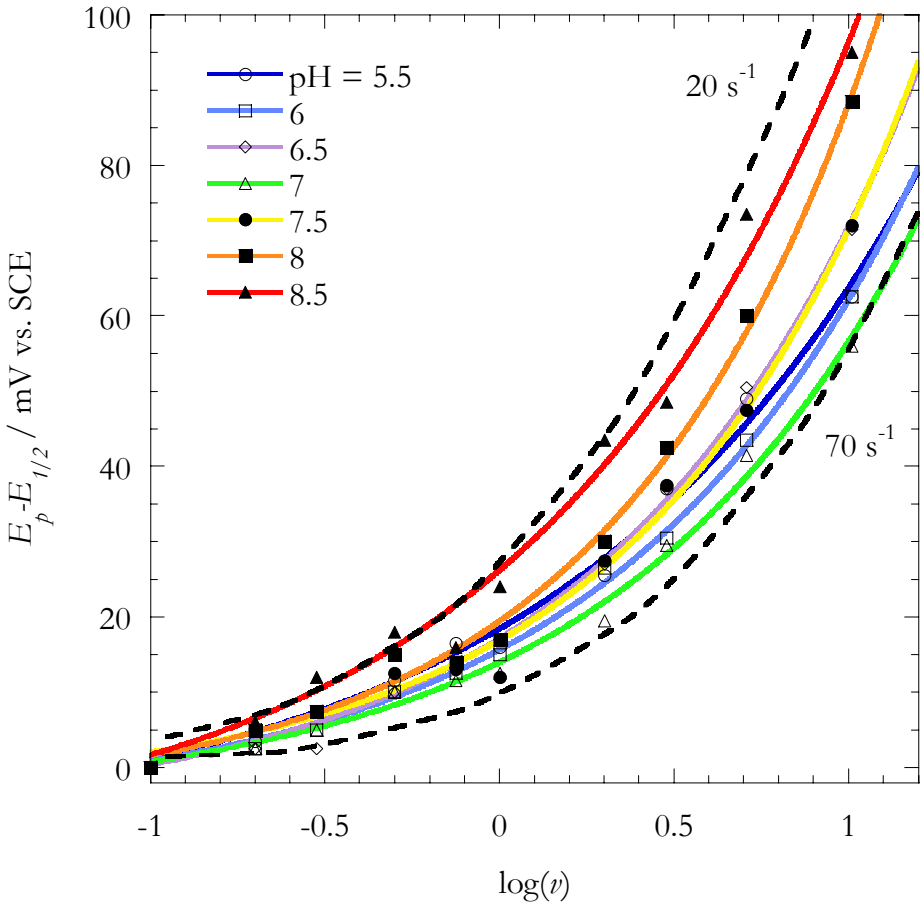

Figure 3-9: Peak splitting vs. the log of the scan rate. The two dotted lines represent the working curves for 20 and 70 s-1 standard rate constant. The colored lines serves as guides; they have been determined by the fit of the data points with a triple exponential function. It is possible to see that as a general trend, for lower pHs the electron transfer rates are faster than those at higher pH. This difference is consistent with the compression of the film whithin the linker portion of about a methylene group.

3.3.2 Electrochemical Behavior of Ionic Redox Metals at DNA Films

Tarlov and coworkers have introduced the concept that the number of incorporated $Ru(NH_3)_6^{3+}$ is directly proportional to the amount of negative charges in the DNA film, which are the phosphates of the DNA backbone.[15] Since then, $Ru(NH_3)_6^{3+}$ has been frequently utilized for electrochemical quantitation of oligonucleotides on surfaces. Penetration into and strong interaction with the DNA film by $Ru(NH_3)_6^{3+}$ is evident in the cyclic voltammetric response that resembles that of a surface-bound species, where the peak shape is symmetric and lacks a diffusive tail (Figure 3-10). However, $Ru(NH_3)_6^{3+}$ is localized in, rather than bound to, the film in close proximity to the electrode and unable to escape in the bulk. Based on the experimental evidences discussed in this Chapter, in the absence of competitive counterions, such as Na^+, $Ru(NH_3)_6^{3+}$ serves to maintain the requirements of charge neutrality and the electrochemical response and kinetics are expected to be highly dependent on the degree of packing and structure of the film. Because we have observed variation of the concentration of C_f^+ due to non-linear factors, the amount of $Ru(NH_3)_6^{3+}$ incorporated in the film is most likely *not* to be strictly proportional to the amount of DNA backbone phosphates.

It has been reported that when DNA surface coverage is relatively high, $Ru(NH_3)_6^{3+}$is also unable to migrate freely inside the film and the kinetics is highly dependent on the surface coverage.[42, 43] Moreover, in our experiments with highly packed films, we have never been able to find consistent agreement between the surface coverage measured by $Ru(NH_3)_6^{3+}$ and that measured by integration of the adsorbed MB or DM cyclic voltammetric peak. It is natural to assume that only a small amount of $Ru(NH_3)_6^{3+}$ is effectively reduced at the electrode. Thus, underestimation of the surface coverage is an inevitable consequence of this technique. It is clear that, because $Ru(NH_3)_6^{3+}$ is so sensitive to the structural nature of the film, quantitation of hybridization efficiencies can be highly misinterpreted, except with very low surface coverages.

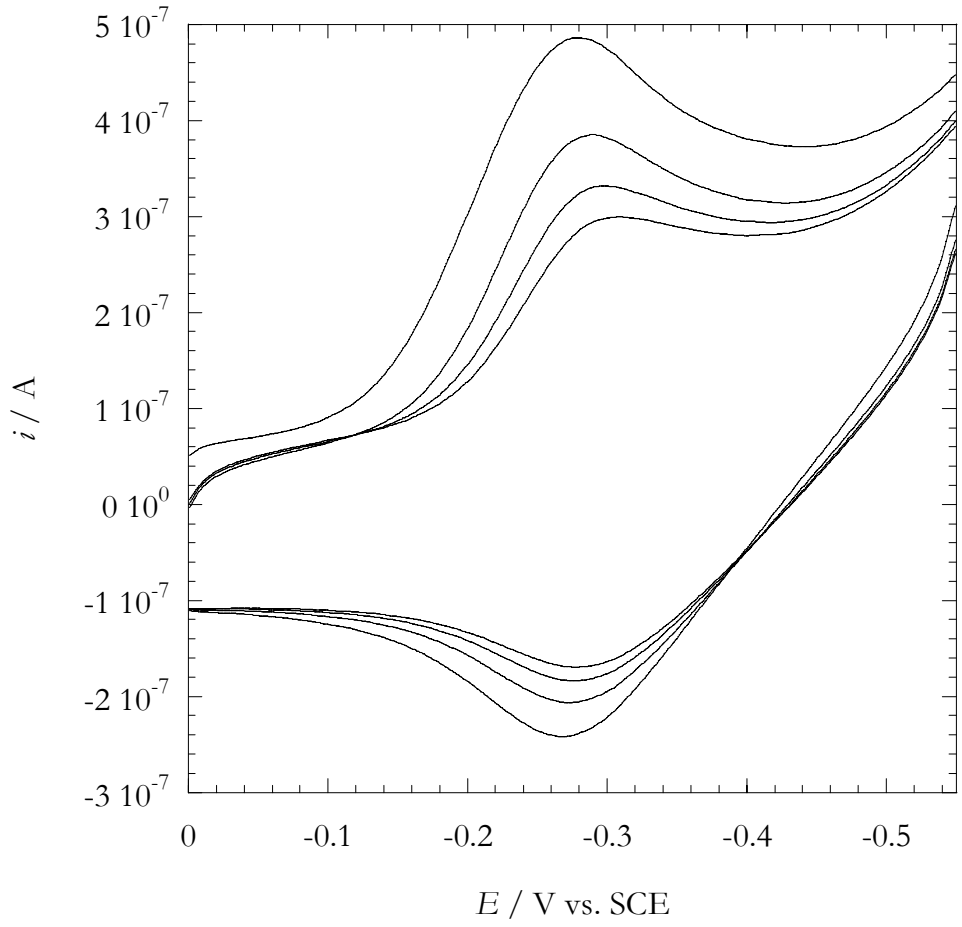

Figure 3-10: Cyclic voltammogram of 5 μM $Ru(NH3)_6^{3+}$ in 10 mM Tris-HCl, pH 8.0, on a loosely packed DNA film. The integrated peak charges at each cycle are: 220, 150, 100, 80 nC, a variation of about 65%.

The cyclic voltammetric response of 5 μM $Ru(NH_3)_6^{3+}$ at a loosely packed DNA film in the absence of competing Na^+ is shown in Figure 3-10, where the cyclic voltammogram is clearly not stable with subsequent scans. Because of the dynamic character of RuHex binding to the DNA film, equilibrium is eventually reached. However, this equilibrium is strictly dependent on the differential electrostatic affinity of the oxidized ($Ru(NH_3)_6^{3+}$) and charged-lowered reduced ($Ru(NH_3)_6^{2+}$) forms. The voltammetric integrated charge can vary considerably depending on the number of scans; hence the determination of the surface coverage is already impaired by this instability.

Long-range electrostatic interaction of anions with DNA is much less sensitive to the actual film structure. A macroscopic characterization of DNA films can be easily obtained by the electrochemical response of redox anionic reporters, such as $Fe(CN)_6^{3-}$. We have previously reported that $Fe(CN)_6^{3-}$ can be used to provide information regarding the formation of DNA films based on electrostatic repulsion. Cyclic voltammograms of $Fe(CN)_6^{3-}$ at well-packed DNA films are usually featureless, indicating that $Fe(CN)_6^{3-}$ cannot easily access the surface. On the other hand, more loosely packed films exhibit features that typically suggest either sluggish kinetics or access of $Fe(CN)_6^{3-}$ through pinholes. While in the former case, peak splitting is considerably large and often shifts the anodic peak potential well beyond the solvent limit, penetration of $Fe(CN)_6^{3-}$ through pinholes is characterized by an "S" shape voltammogram, typical of active surfaces approximately a few micrometers in diameter. In either case, by CV, it is not possible to obtain analytical information about the nature of the film.

An easy protocol for monitoring slight changes in DNA coverage can then rely on the fact that $Fe(CN)_6^{3-}$ interacts minimally with DNA. Because of a relatively long-range electrostatic interaction, repulsion of $Fe(CN)_6^{3-}$ by DNA is insensitive to film morphology, but is expected to be highly sensitive to the amount of negative charges present of the surfaces and thus on the amount of DNA. This is a great advantage, compared to $Ru(NH_3)_6^{3+}$, considering the variability DNA films can have, depending on the self-

assembly conditions (buffer's ionic strength, deposition time, single stranded vs. double stranded DNA structures). Thus, here, we have applied this concept for monitoring hybridization events on the surface, where the amount of negatively charge phosphate backbone provides the modulation for the anionic repulsion to $Fe(CN)_6^{3-}$.

3.3.2.1 Brief introduction to electrochemical impedance spectroscopy

Electrochemical impedance spectroscopy (EIS) is a sensitive technique that enables the measurement of kinetic processes at equilibrium and allows for a detailed description of physical properties that is far more accurate than large-amplitude potential techniques, such as CV. EIS is widely applied for the systematic study of polyelectrolyte multilayers as it can provide information regarding the dielectric properties,[44] stability,[45] and permeability of ionic species.[46] A small oscillating potential perturbation (5 mV) is applied at the formal potential of a redox reporter and the impedance is measured over a frequency spectrum that ranges from 0.1 to 10^5 Hz.[47, 48] The plot of the impedance in the complex plane (Nyquist plot) is essentially composed of a semi-arc at high frequency, representative of capacitative processes, and a 45° straight line at low frequencies, which represents slow processes, such as mass transport to the electrode (Figure 3-11). The degree of electrode passivation is manifested in the lack of mass transport, whereas the degree of permeability is manifested in the high frequency impedance arc. In the context of a simplified Randles equivalent circuit (Figure 3-11), the diameter of the impedance arc (on the real axis of the impedance) is equivalent to the electron transfer resistance, R_{ET}. The latter can be used as a direct measure of the degree of passivation. In the case of DNA films, $Fe(CN)_6^{3-}$ partial penetration can be determined by EIS where R_{ET} provides a direct measure of the extent of interaction of $Fe(CN)_6^{3-}$ with DNA films and thus a quantitative determination of the relative surface coverage.

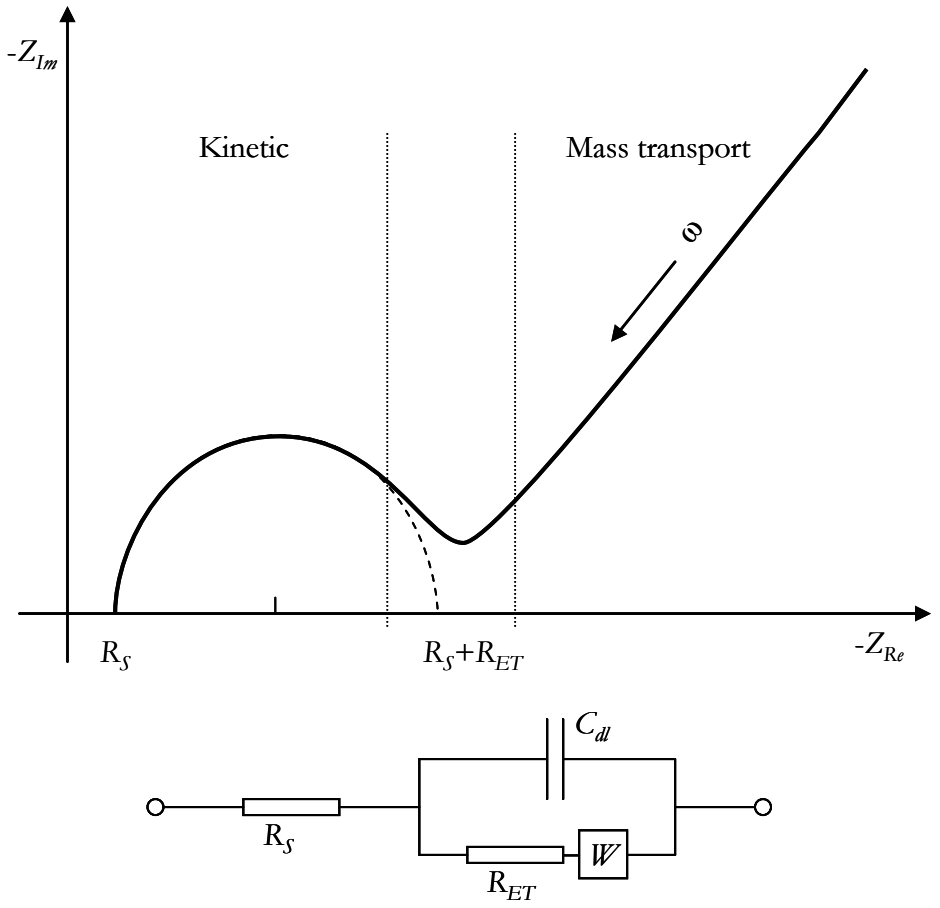

Figure 3-11: A typical Nyquist plot showing the frequency response of the impedance response in the complex plane. The arrow indicated the direction for increasing frequencies. The diameter of the arc is equivalent to the electron transfer resistance across the film, R_{ET}. The equivalent Randles circuit is also shown where W represents the Warburg elements, which accounts for mass transport. C_{dl} and R_S are the double layer capacitance and the solution resistance, respectively.

3.3.2.2 Voltammetric and impedance responses of $Fe(CN)_6^{3-}$ on MCH films

It is known that alkane-thiol films undergo reorganization upon heating.[49, 50] Because we have decided to perform dehybridization of DNA using heat, we have investigated to what extent temperature affects the electrochemical response of $Fe(CN)_6^{3-}$ on a mercaptohexanol (MCH) film. In Figure 3-12 the cyclic voltammograms of $Fe(CN)_6^{3-}$ on a fresh MCH film is shown. It is known from the literature that ferri/ferrocyanide redox reaction at a metallic surface is not always reversible and is accompanied by a gradual passivation, probably by the formation of a prussian blue-like layer that decreases the rate of interfacial electron transfer.[51] This process can be easily observed by the progressive decrease of the peak current and the concomitant increase of peak splitting of the cyclic voltammogram. On a MCH film, however, this secondary process does not occur and the $Fe(CN)_6^{3-}$ redox reaction behaves nearly ideally (dashed curve in Figure 3-12).

Upon heating the film in 64 °C buffer, the morphology of the MCH changes and seems to facilitate electron transfer (solid line in Figure 3-12). The cyclic voltammogram is clearly more reversible (and as stable as before heating). Based on these observations, however, it is not possible to comment on the exact morphology of the MCH film after heating. Nevertheless, the film is now behaving seemingly ideally, where heterogeneous electron transfer occurs much faster and in the absence of non-specific adsorption of $Fe(CN)_6^{3-}$. Digital simulation of the cyclic voltammogram has been used to determine the kinetic parameters of the heterogeneous reaction and we obtain a rate constant of $1.3 \cdot 10^{-2}$ cm/s (Figure 3-13). One might think that the decrease of R_{ET} could be associated with the formation of pinholes in the film upon reorganization, where $Fe(CN)_6^{3-}$ can now directly access the surface. The stability (i.e., the lack of formation of the prussian blue-like passivation layer), however, of the volammetric and impedance responses suggest that electron transfer instead occurs through the film, but at a faster rate than before heating.

From the perspective of the EIS, the change in the impedance response before and after heating is dramatic. On a MCH film electrode, passivation by prussian blue does not occur and the redox process still exhibits an ideal behavior. However, after heating the electrode in a 64 °C buffer, it is apparent from the impedance plot in the complex plane that the R_{ET} is almost vanished (or apparently less than the solution resistance) and only mass transfer dominates the redox process (Figure 3-14).

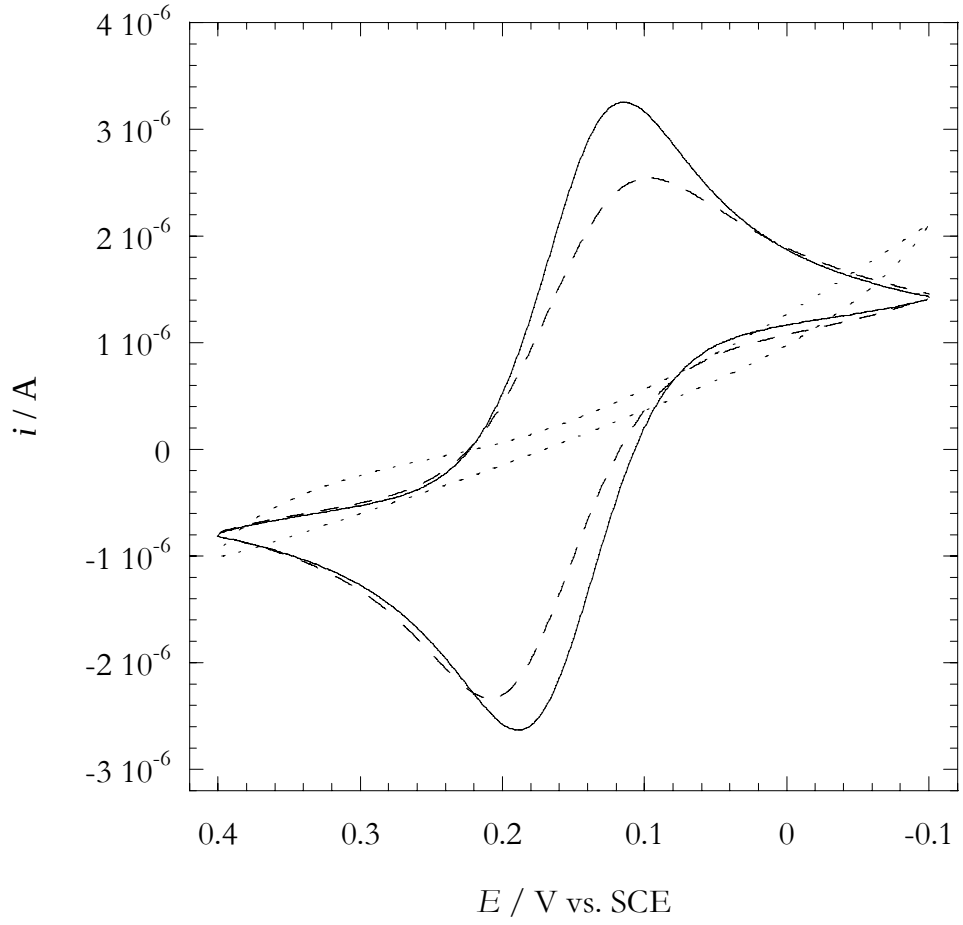

Figure 3-12: Cyclic voltammogram of $Fe(CN)_6^{3-}$ on a MCH-modified electrode before (dashed line) and after heat treatment in Tris buffer at 64 °C (solid line). The dotted line is the electrochemical response of $Fe(CN)_6^{3-}$ on a DNA-MCH mixed monolayer. Conditions: 50 mM phosphate buffer, pH 7.0, 1 mM $Fe(CN)_6^{3-}$, 50 mV/s.

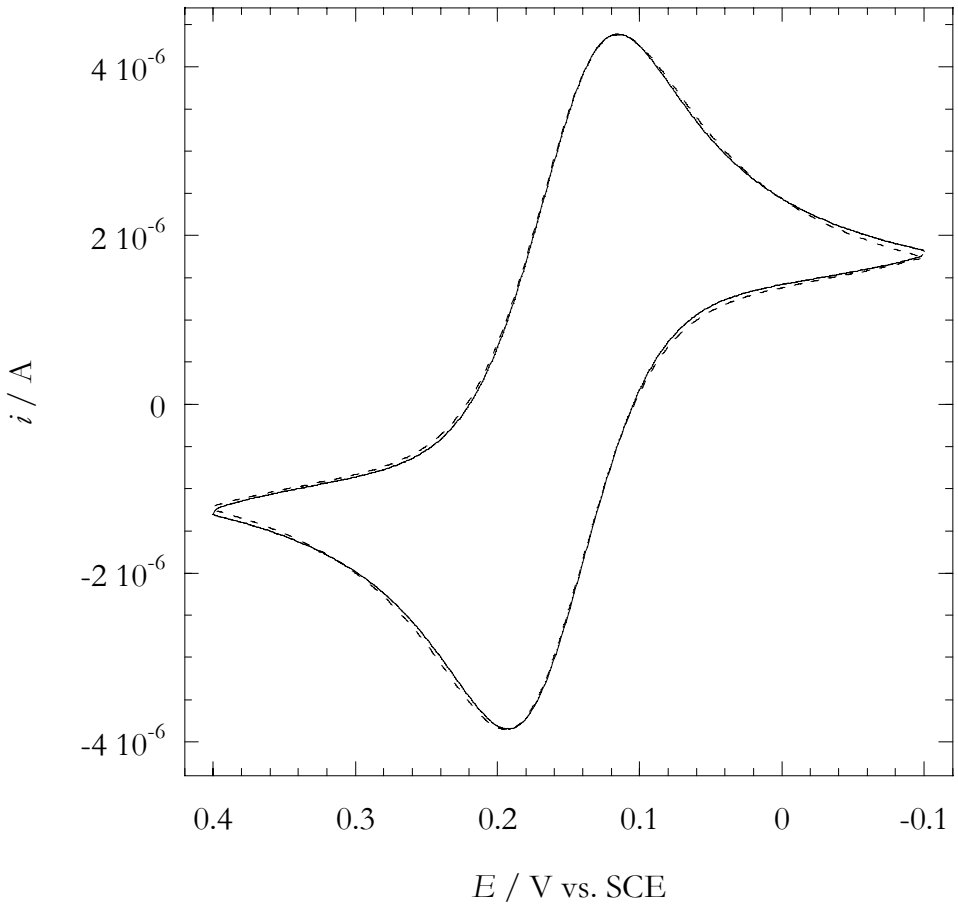

Figure 3-13: Cyclic voltammogram of $Fe(CN)_6^{3-}$ on a MCH-modified electrode after heat treatment (solid line) and digital simulation (dashed line). The parameters for the simulation are: k^0=0.013, α=0.5, D_O=D_R=0.95·10^{-5} cm^2/s, v =100 mV/s.

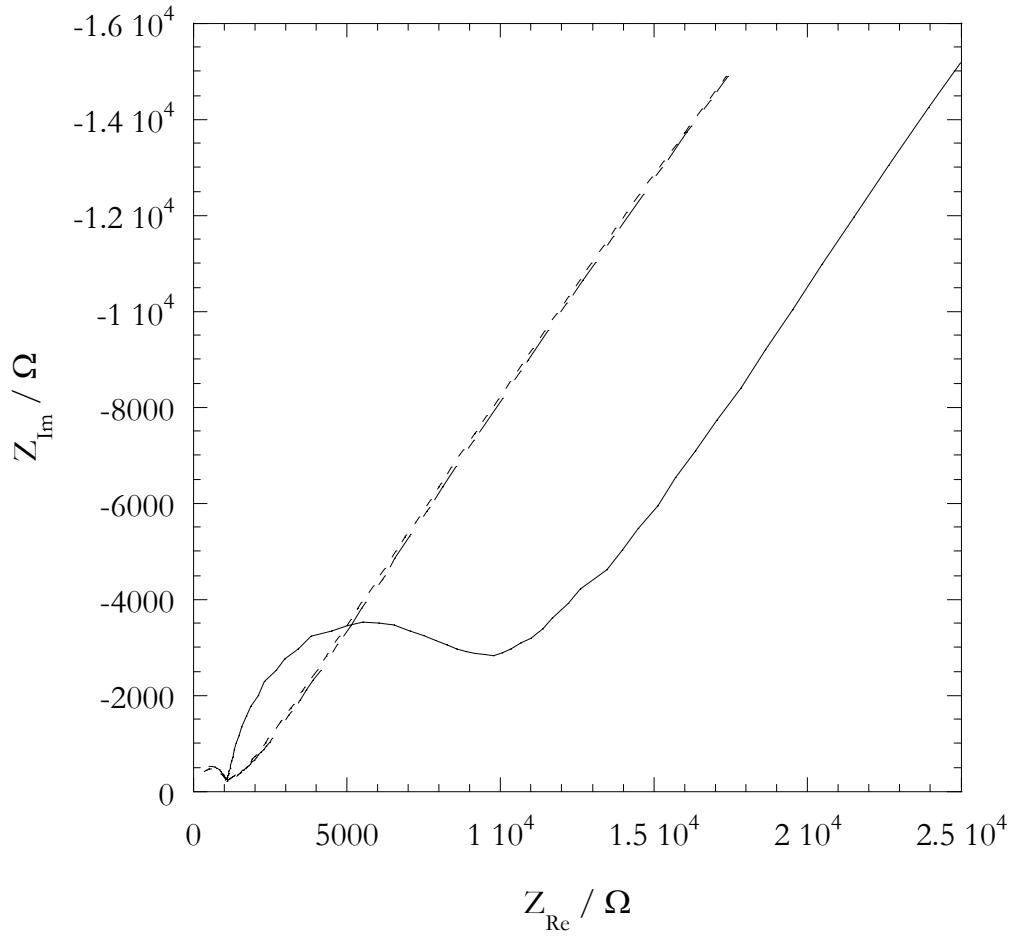

Figure 3-14: Nyquist plot for $Fe(CN)_6^{3-}$ on a fresh MCH-modified electrode (solid line), after heat treatment (dot-dashed line), and after incubation with 1 μM ssDNA for 20 min at room temperature (dotted line).

3.3.2.3 Monitoring hybridization events by electrochemical impedance spectroscopy

MCH films provide a biocompatible surface where non-specific adsorption does not occur. We have already reported that MCH backfilling does not specifically interact with proteins or DNA, as demonstrated by studies on DNA/protein interaction on DNA-modified surfaces. Incubation of a MCH film in a solution containing single stranded DNA (ssDNA) does not affect the impedance response of $Fe(CN)_6^{3-}$, suggesting that ssDNA does not adsorb on the film to any appreciable degree (dashed line vs. dotted line in Figure 3-14). One has to remember that the electrochemical impedance of $Fe(CN)_6^{3-}$ is expected to change dramatically with changes in DNA surface concentration, because of the electrostatic repulsion on a one-to-five basis; one DNA molecule containing 15 negative phosphates will repel three $Fe(CN)_6^{3-}$ molecules. This biocompatibility is a very important feature for any DNA microarray.

The voltammetric response of $Fe(CN)_6^{3-}$ on the mixed monolayer of DNA and MCH is typical of a blocked surface (dotted curve in Figure 3-12). The absence of a linear slope at low frequencies in the impedance response provides additional evidence for the lack of mass transport to the surface. Figure 3-15 shows the impedance responses for several cycles of hybridization and dehybridization. The solid line curve with filled dots represents the impedance response of a freshly prepared electrode, after thorough rinsing in a dehybridization buffer (DHB, see Experimental Details) at room temperature. A slight increase of R_{ET} is observed after incubation of the electrode in the same buffer at 37 °C (a temperature that is below the melting temperature of the DNA) for about 20 min. This indicates that rinsing in DHB, which lacks Na^+, might have slightly decreased the ionic strength in the film, decreasing the Debye screening and resulting in a greater repulsion for $Fe(CN)_6^{3-}$. Only after incubation of the electrode in hot (64 °C) DHB, DNA starts to dehybridize and leave the surface, as is evident by the decrease of R_{ET}. Dehybridization was performed in three subsequent steps of 7, 5, and 23 minutes each. At each step, more

DNA was dehybridized until a limit, where no further dehybridization can occur and only ssDNA exists on the surface. We have been able to perform a long series of dehybridization and rehybridization cycles, demonstrating the remarkable stability and reproducibility of the DNA film. Incubation of the electrode in a rehybridization buffer (RHB, see Experimental Details) for 15 min at room temperature brings the R_{ET} back almost to its original value. After incubation for an additional 15 minutes, we can see that the film is now exactly how it was at the beginning of the experiment. We can conclude that complete hybridization and dehybridization, under these conditions, can be accomplished within about 20 minutes of incubation. Intermediate incubation times result in respective intermediate levels of hybridization. A plot of the module of the impedance for some incubation times is shown in Figure 3-16. Most importantly, rehybridization utilizing non-complementary sequence exhibits substantially no effect, supporting our assertion that observed changes are due to actual hybridization and not non-specific adsorption (Figure 3-17).

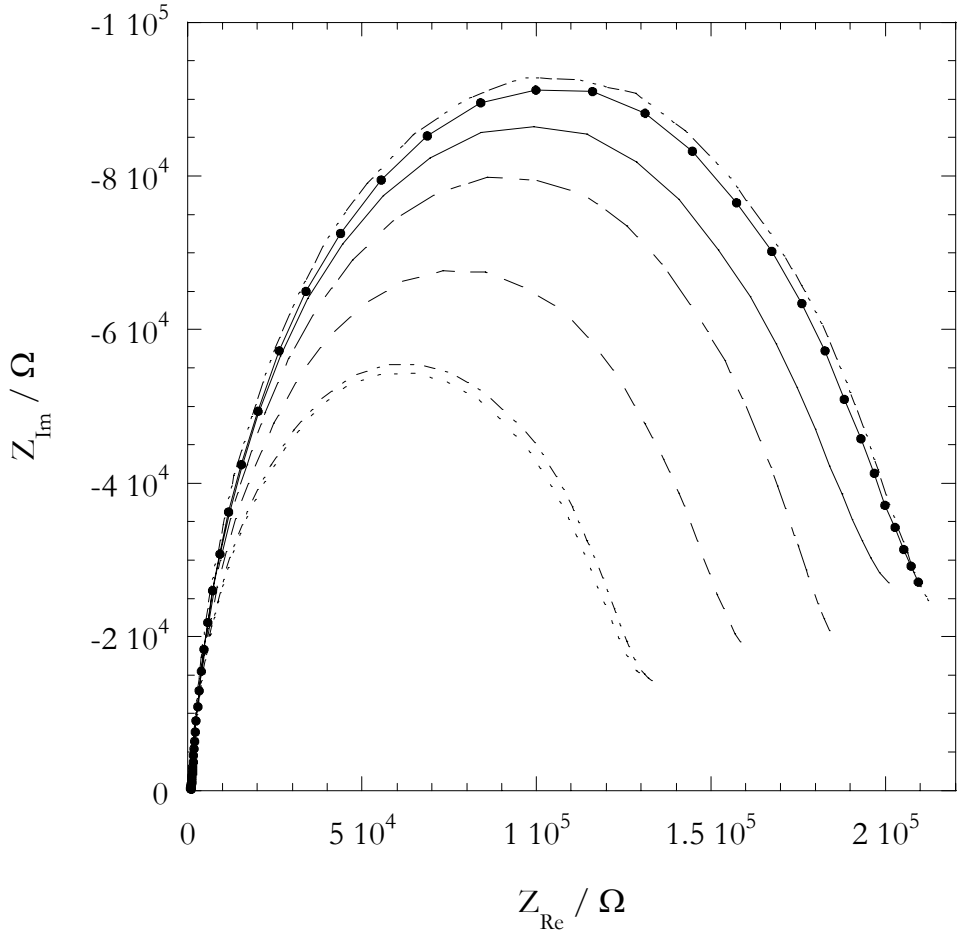

Figure 3-15: Nyquist plots for $Fe(CN)_6^{3-}$ on a DNA-modified electrode backfilled with MCH for a series of dehybridization and rehybridization times: fresh electrode (solid), after heating at 37 °C for 45 min in DHB (solid-filled cicles), after dehybridization for 7 min (dash-line), additional 5 min dehybridization (line-line), and for 33 min (dot-line) and 10 min more (dotted), rehybridization for 15 min with complementary strand (dot-dot-line). Dehybridization was performed by incubation of the electrode in the DHB at 64 °C, while rehybridization was done by incubating the electrode in RHB containing 1 μM complementary DNA at room temperature.

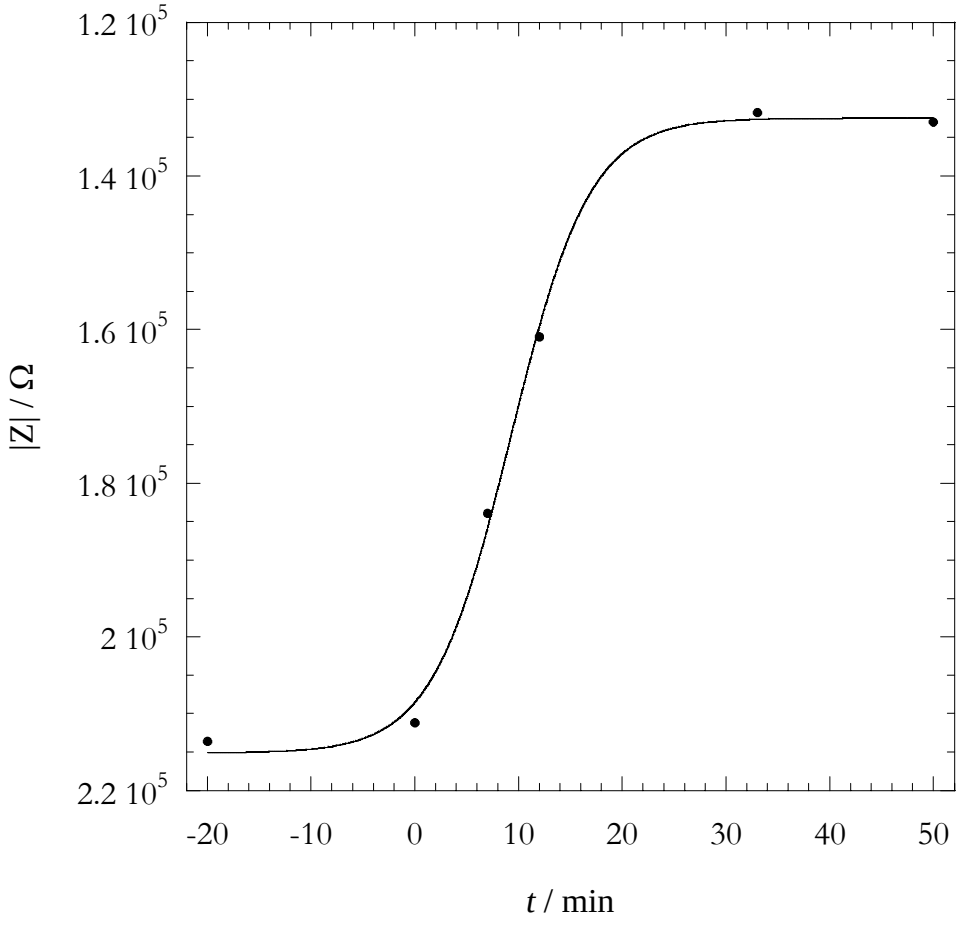

Figure 3-16: Plot of the module of the impedance at low frequency as function of the incubation time for the hybridization of a complementary DNA strand on a DNA film.

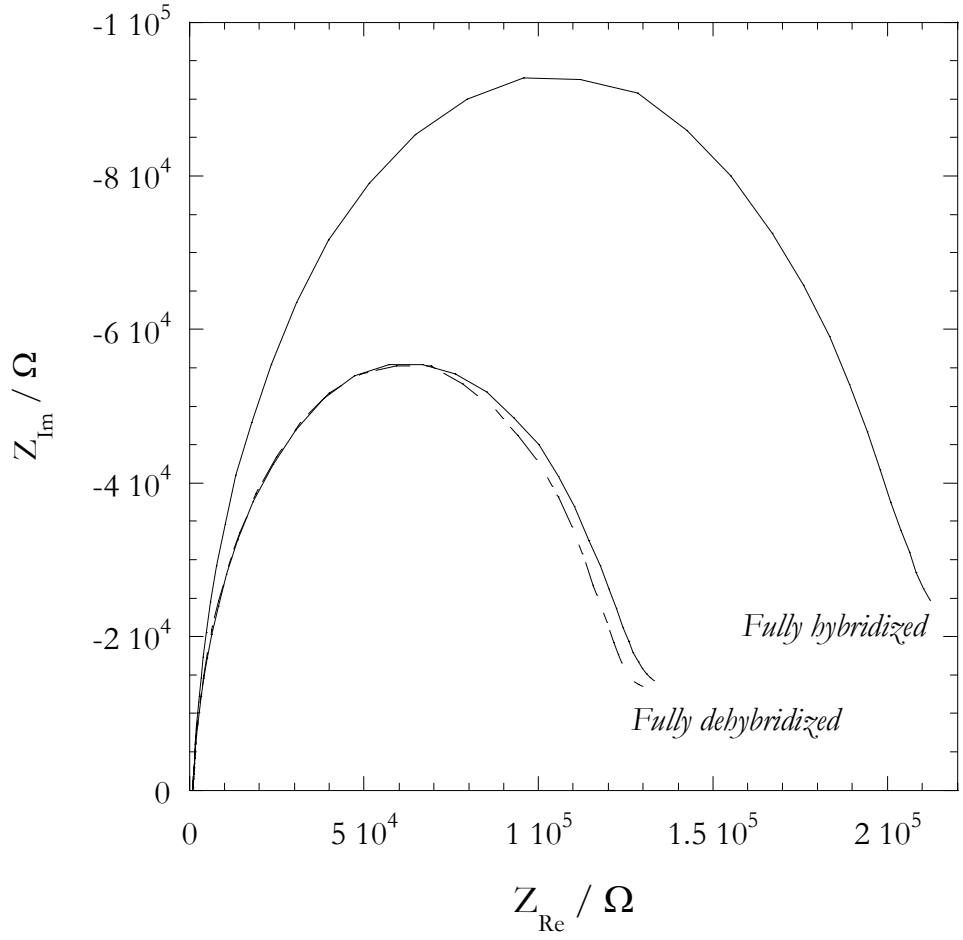

Figure 3-17: Nyquist plots for $Fe(CN)_6^{3-}$ on a DNA-modified electrode backfilled with MCH. The two solid line curves represent the cases where the film is fully dehybridized (small impedance) or fully hybridized (high impedance). Rehybridization for 20 min in the conditions of Figure 3-9 with noncomplementary DNA does not change appreciably the impedance of the surface (dash-line curve).

3.4 Summary

DNA films are polyelectrolytes and cannot be treated as simple monolayers mediating the transfer of electrons without taking into account their ionic character. Because the electrostatic interaction between DNA molecules determines the extent of permselectivity for both cations and anions, Donnan potentials across the films are highly sensitive to packing, solution ionic strength, and identity of the electrolyte. We have shown that non-linear dependence of the Donnan potential on pH for the reduction of MB is a consequence of permselectivity of the film to the different ions in solution. The extent of the permselectivity seems to be related to the initial deposition conditions, where the inter-duplex distances are dictated by the overscreening of the negative phosphate backbone. This subtle interplay between ionic strength and film structure is an important factor that has to be taken into account when DNA films are investigated using redox mediators, whether they are intercalators or simply groove binders, such as MB or $Ru(NH_3)_6^{3+}$, respectively. Quantitation of DNA surface coverage by $Ru(NH_3)_6^{3+}$ is fundamentally deficient and tends to provide underestimates. This is a direct consequence of the fact that permselectivity of the film is not exclusively limited to cations, but to all ionic species in solution. Because of the non-linear behavior of cation permeation, it is natural to assume that there is no direct relationship between the $Ru(NH_3)_6^{3+}$ film content and the number of DNA molecules, especially between dehybridization and rehybridization cycles, where the structure of the film changes dramatically. We have then provided an alternative and easy qualitative method for monitoring the extent of surface coverage based on electrostatic repulsion between DNA and $Fe(CN)_6^{3-}$. The long-range interaction between the anionic redox probe and the film is insensitive to subtle morphological changes on the surface. The impedance response of $Fe(CN)_6^{3-}$ on DNA films provides then a reliable, although indirect, readout of the surface coverage, without the disadvantages encountered with $Ru(NH_3)_6^{3+}$ due to DNA packing.

3.5 Experimental Details

3.5.1 Film preparation

Well-packed DNA films were prepared by depositing 50 μM double-stranded thiolated DNA on a freshly polished and etched gold surface[‡] for about 12 hours in the presence of 100 mM $MgCl_2$. The electrodes are thoroughly rinsed in buffer and immediately used in the experiments. Mixed monolayers are formed by depositing 100 μM double-stranded thiolated DNA on a freshly etched gold surface for one to two hours in absence of diavalent cations in order to avoid tight packing. Subsequently, after thorough rinsing in buffer, the electrode was incubated in a solution of 1 mM MCH (50 mM phosphate buffer, pH 7.0, 1% ethanol) for approximately 1 hour, for backfilling.

3.5.2 Buffers for pH dependence

For pH dependence: 5 mM phosphate buffer, 100 mM Cl^- of different pHs has been prepared such that the ionic strength and total cation concentration would vary minimally, using Henderson-Hasselbalch equation, and a pK_a = 6.8. The pH of 5 mM p-nitrophenol (Sigma), 200 mM NaCl ware adjusted accordingly with NaOH and HCl.

3.5.3 Dehybridization and rehybridization

Dehybridization is performed by incubating the electrode at 64 °C for the specified time in a dehybridization buffer (DHB, 10 mM Tris-HCl, pH 8.0 measured at RT)[#] lacking Na^+ in order to decrease the DNA melting temperature. Rehybridization is achieved by

---

[‡] It is very important to etch the electrode in H_2SO_4 before performing any type of experiments. Heating of a modified electrode may result in loss of DNA because of surface instability. It has been found that during etching loosely bound gold atoms are removed, leaving a more stable and reliable surface.

[#] The pH of Tris solutions is temperature dependent and decreases approximately 0.03 pH units for each 1 °C in temperature.

incubating the electrode in the rehybridization buffer (RHB, 50mM phosphate buffer, pH 7.0) containing 1 μM ssDNA at room temperature for the specified time.

3.5.4 Equipments

Electrochemical measurements were performed with a 760B biopotentiostat (CH Instruments) in a typical three electron configuration electrochemical cell: gold (BAS) working electrode, Pt (Alfa) auxiliary electrode, and SCE reference. The reference electrode is connected to the main cell via a Luggin capillary. All potentials are reported vs. SCE. We have used 2 μM MB (Fluka, 99% puris) and 1 mM FeCN.

3.6 References

1. Carter, M. T.; Rowe, G. K.; Richardson, J. N.; Tender, L. M.; Terrill, R. H.; Murray, R. W., Distance Dependence of the Low-Temperature Electron-Transfer Kinetics of (Ferrocenylcarboxy)-Terminated Alkanethiol Monolayers. *Journal of the American Chemical Society* **1995,** 117, (10), 2896-2899.
2. Chidsey, C. E. D., Free-Energy and Temperature-Dependence of Electron-Transfer at the Metal-Electrolyte Interface. *Science* **1991,** 251, (4996), 919-922.
3. Chidsey, C. E. D.; Bertozzi, C. R.; Putvinski, T. M.; Mujsce, A. M., Coadsorption of Ferrocene-Terminated and Unsubstituted Alkanethiols on Gold: Electroactive Self-Assembled Monolayers. *Journal of the American Chemical Society* **1990,** 112, (11), 4301-4306.
4. Finklea, H. O., Electrochemistry of organized monolayers of thiols and related molecules on electrodes. In *Electroanalytical Chemistry: a Series of Advances, Vol 19*, 1996; pp. 109-335.
5. Liu, B.; Bard, A. J.; Mirkin, M. V.; Creager, S. E., Electron transfer at self-assembled monolayers measured by scanning electrochemical microscopy. *Journal of the American Chemical Society* **2004,** 126, (5), 1485-1492.
6. Miller, C. J., In *Heterogeneous Electron-Transfer Kinetics at Metallic Electrodes*, Rubinstein, I., ed. Marcel Dekker: New York, 1995; pp 27-79.
7. Murray, R. W., In *Electroanalytical Chemistry*, Bard, A. J., ed. Marcel Dekker: New York, 1984; p. 192.
8. Sikes, H. D.; Smalley, J. F.; Dudek, S. P.; Cook, A. R.; Newton, M. D.; Chidsey, C. E. D.; Feldberg, S. W., Rapid electron tunneling through oligophenylenevinylene bridges. *Science* **2001,** 291, (5508), 1519-1523.

9. Smalley, J. F.; Finklea, H. O.; Chidsey, C. E. D.; Linford, M. R.; Creager, S. E.; Ferraris, J. P.; Chalfant, K.; Zawodzinsk, T.; Feldberg, S. W.; Newton, M. D., Heterogeneous electron-transfer kinetics for ruthenium and ferrocene redox moieties through alkanethiol monolayers on gold. *Journal of the American Chemical Society* **2003,** 125, (7), 2004-2013.

10. Walsh, D. A.; Keyes, T. E.; Forster, R. J., Modulation of heterogeneous electron-transfer dynamics across the electrode/monolayer interface. *Journal of Physical Chemistry B* **2004,** 108, (8), 2631-2636.

11. Georgiadis, R.; Peterlinz, K. P.; Peterson, A. W., Quantitative measurements and modeling of kinetics in nucleic acid monolayer films using SPR spectroscopy. *Journal of the American Chemical Society* **2000,** 122, (13), 3166-3173.

12. Peterson, A. W.; Heaton, R. J.; Georgiadis, R., Kinetic control of hybridization in surface immobilized DNA monolayer films. *Journal of the American Chemical Society* **2000,** 122, (32), 7837-7838.

13. Peterson, A. W.; Heaton, R. J.; Georgiadis, R. M., The effect of surface probe density on DNA hybridization. *Nucleic Acids Research* **2001,** 29, (24), 5163-5168.

14. Peterson, A. W.; Wolf, L. K.; Georgiadis, R. M., Hybridization of mismatched or partially matched DNA at surfaces. *Journal of the American Chemical Society* **2002,** 124, (49), 14601-14607.

15. Steel, A. B.; Herne, T. M.; Tarlov, M. J., Electrochemical quantitation of DNA immobilized on gold. *Analytical Chemistry* **1998,** 70, (22), 4670-4677.

16. Steel, A. B.; Herne, T. M.; Tarlov, M. J., Electrostatic interactions of redox cations with surface-immobilized and solution DNA. *Bioconjugate Chemistry* **1999,** 10, (3), 419-423.

17. Steel, A. B.; Levicky, R. L.; Herne, T. M.; Tarlov, M. J., Immobilization of nucleic acids at solid surfaces: Effect of oligonucleotide length on layer assembly. *Biophysical Journal* **2000,** 79, (2), 975-981.

18. Kelley, S. O.; Barton, J. K.; Jackson, N. M.; Hill, M. G., Electrochemistry of methylene blue bound to a DNA-modified electrode. *Bioconjugate Chemistry* **1997,** 8, (1), 31-37.

19. Bloomfield, V. A., DNA condensation by multivalent cations. *Biopolymers* **1997,** 44, (3), 269-282.

20. Ceres, D. M.; Barton, J. K., In situ scanning tunneling microscopy of DNA-modified gold surfaces: Bias and mismatch dependence. *Journal of the American Chemical Society* **2003,** 125, (49), 14964-14965.

21. Maniatis, T.; Venable, J. H.; Lerman, L. S., Structure of Psi DNA. *Journal of Molecular Biology* **1974,** 84, (1), 37.

22. Manning, G. S., Limiting Laws and Counterion Condensation in Polyelectrolyte Solutions .5. Further Development of Chemical-Model. *Biophysical Chemistry* **1978,** 9, (1), 65-70.

23. Rill, R. L., Liquid-Crystalline Phases in Concentrated Aqueous-Solutions of Na+ DNA. *Proceedings of the National Academy of Sciences of the United States of America* **1986,** 83, (2), 342-346.

24. Schellman, J. A.; Parthasarathy, N., X-Ray-Diffraction Studies on Cation-Collapsed DNA. *Journal of Molecular Biology* **1984,** 175, (3), 313-329.

25. Aubouy, M.; Trizac, E.; Bocquet, L., Effective charge versus bare charge: an analytical estimate for colloids in the infinite dilution limit. *Journal of Physics A: Mathematical and General* **2003,** 36, (22), 5835-5840.

26. Bloomfield, V. A., DNA condensation. *Current Opinion in Structural Biology* **1996,** 6, (3), 334-341.

27. Minasov, G.; Tereshko, V.; Egli, M., Atomic-resolution crystal structures of B-DNA reveal specific influences of divalent metal ions on conformation and packing. *Journal of Molecular Biology* **1999,** 291, (1), 83-99.

28. Stevens, M. J., Simple simulations of DNA condensation. *Biophysical Journal* **2001,** 80, (1), 130-139.

29. Tellez, G.; Trizac, E., Nonlinear screening of spherical and cylindrical colloids: The case of 1 : 2 and 2 : 1 electrolytes. *Physical Review E* **2004,** 70, (1).

30. Fang, Y.; Yang, J., Effect of cationic strength and species on 2-D condensation of DNA. *Journal of Physical Chemistry B* **1997,** 101, (18), 3453-3456.

31. Koltover, I.; Wagner, K.; Safinya, C. R., DNA condensation in two dimensions. *Proceedings of the National Academy of Sciences of the United States of America* **2000,** 97, (26), 14046-14051.

32. Sun, X. G.; Cao, E. H.; Zhang, X. Y.; Liu, D. G.; Bai, C. L., The divalent cation-induced DNA condensation studied by atomic force microscopy and spectra analysis. *Inorganic Chemistry Communications* **2002,** 5, (3), 181-186.

33. Rau, D. C.; Parsegian, V. A., Direct Measurement of the Intermolecular Forces between Counterion-Condensed DNA Double Helices: Evidence for Long-Range Attractive Hydration Forces. *Biophysical Journal* **1992,** 61, (1), 246-259.

34. Allahyarov, E.; Gompper, G.; Lowen, H., Attraction between DNA molecules mediated by multivalent ions. *Physical Review E* **2004,** 69, (4).

35. Nguyen, T. T.; Grosberg, A. Y.; Shklovskii, B. I., Macroions in salty water with multivalent ions: Giant inversion of charge. *Physical Review Letters* **2000,** 85, (7), 1568-1571.

36. Nguyen, T. T.; Grosberg, A. Y.; Shklovskii, B. I., Screening of a charged particle by multivalent counterions in salty water: Strong charge inversion. *Journal of Chemical Physics* **2000,** 113, (3), 1110-1125.

37. Tanaka, M.; Grosberg, A. Y., Giant charge inversion of a macroion due to multivalent counterions and monovalent coions: Molecular dynamics study. *Journal of Chemical Physics* **2001,** 115, (1), 567-574.

38. Naegeli, R.; Redepenning, J.; Anson, F. C., Influence of Supporting Electrolyte Concentration and Composition on Formal Potentials and Entropies of Redox Couples Incorporated in Nation Coatings on Electrodes. *Journal of Physical Chemistry* **1986,** 90, (23), 6227-6232.

39. Boon, E. M.; Barton, J. K.; Bhagat, V.; Nersissian, M.; Wang, W.; Hill, M. G., Reduction of ferricyanide by methylene blue at a DNA-modified rotating-disk electrode. *Langmuir* **2003,** 19, (22), 9255-9259.

40. Drummond, T. G.; Hill, M. G.; Barton, J. K., Electron transfer rates in DNA films as a function of tether length. *Journal of the American Chemical Society* **2004,** 126, (46), 15010-15011.

41. Tender, L.; Carter, M. T.; Murray, R. W., Cyclic Voltammetric Analysis of Ferrocene Alkanethiol Monolayer Electrode-Kinetics Based on Marcus Theory. *Analytical Chemistry* **1994,** 66, (19), 3173-3181.

42. Su, L.; Sankar, C. G.; Sen, D.; Yu, H. Z., Kinetics of ion-exchange binding of redox metal cations to thiolate-DNA monolayers on gold. *Analytical Chemistry* **2004,** 76, (19), 5953-5959.

43. Yu, H. Z.; Luo, C. Y.; Sankar, C. G.; Sen, D., Voltammetric procedure for examining DNA-modified surfaces: Quantitation, cationic binding activity, and electron-transfer kinetics. *Analytical Chemistry* **2003,** 75, (15), 3902-3907.

44. Durstock, M. F.; Rubner, M. F., Dielectric properties of polyelectrolyte multilayers. *Langmuir* **2001,** 17, (25), 7865-7872.

45. Boubour, E.; Lennox, R. B., Stability of omega-functionalized self-assembled monolayers as a function of applied potential. *Langmuir* **2000,** 16, (19), 7464-7470.

46. Harris, J. J.; Bruening, M. L., Electrochemical and *in situ* ellipsometric investigation of the permeability and stability of layered polyelectrolyte films. *Langmuir* **2000,** 16, (4), 2006-2013.

47. Bard, A. J.; Faulkner, L. R., *Electrochemical Methods, Fundamental and Applications*. 2nd ed.; John Wiley and Sons, 2001.

48. MacDonald, J. R., Fundamentals of Impedance Spectroscopy. In *Impedance Spectroscopy, Emphazising Solid Materials and Systems*, MacDonald, J. R., ed. John Wiley and Sons: New York, 1987; pp. 1-20.

49. Qian, Y.; Yang, G.; Yu, J.; Jung, T. A.; Liu, G., Structures of Annealed Decanethiol Self-Assembled Monolayers on Au(111): an Ultrahigh Vacuum Scanning Tunneling Microscopy Study. *Langmuir* **2003,** 19, (15), 6056-6065.

50. Xiao, X.; Wang, B.; Zhang, C.; Yang, Z.; Loy, M. M. T., Thermal annealing effect of alkanethiol monolayers on Au(1 1 1) in air. *Surface Science* **2001,** 472, (1-2), 41-50.

51. Petrovic, S. C., Cyclic Voltammetry of Hexachloroiridate (IV): An Alternative to the Electrochemical Study of the Ferricyanide Ion. *Chemical Educator* **2000,** 5, (5), 231.

Chapter 4 Investigation of DNA Films by In Situ Scanning Tunneling Microscopy

4.1 Introduction

Solution phase experiments probing the yields and rates of charge transport (CT) have provided doubtless evidence that DNA can serve as a charge mediator between redox partners.[1-6] In the first experiments with photoexcited metal intercalators, we have consistently observed oxidation of bases with lower oxidation potentials, such as Gs, while no oxidation has been found for bases with higher oxidation potentials, such as As.[7] A widely accepted model that attempted to account for these experimental observations described DNA mediated CT as a mixed mechanism, comprised of tunneling through high potential bases and bridge occupancy on low potential bases.[8, 9] An electron hole residing on a low energy site, such as a GG doublet, can be trapped by water or oxygen generating a permanent damage at the base. Since the oxidation yields in DNA seemed to follow the trend of the oxidation potentials of isolated bases, we have concluded that the energies of the bases are not substantially affected by whether they are isolated or inside DNA. However, inconsistent results from different laboratories suggested that perhaps this energetic model was not entirely correct as it did not seem possible to reconcile them under a unified theory.

In 1961 Eley and Spivey wrote: "*The bases […] are thus arranged like a pile of coins along the helix axis, and their interplane spacing of approximately 3.4 Å is closely similar to that of graphite. It seemed, therefore, reasonable to suppose that a DNA molecule might behave as a one-dimensional aromatic crystal and show a π-electron conductivity down the axis.*"[10] They were partly wrong: DNA is not a simple stack of isolated bases. Systematic spectroscopic studies on DNA-mediated CT, using fluorescence quenching of 2-aminopurine (Ap), revealed interesting features of DNA CT.[5] The appearance of an oscillatory behavior of the fractional quenching as a function of the distance, strongly suggested not only that DNA CT is a complex non-linear process but mainly that the energetics of the DNA bridge are affected by a complex combination of factors associated with DNA structural dynamics. A

new model had to be introduced in order to account for this new experimental evidence. Additional evidences came with recent experiments exploiting kinetic hole traps, such as N^4-cyclopropylcytosine (cpC) and N^2-cyclopropylguanine (cpG). Consistent observation of comparable oxidations of high-energy pyrimidines (cpC) and low energy purines (cpG) suggests that the DNA bases are strongly interacting with each other causing the energetic of single bases to be modulated by interactions with near neighbors.[11, 12] The extent of this mutual interaction seems to be dependent on the structural dynamics of the local DNA sequence. These experiments demonstrated that the concept of a DNA bridge constituted by isolated bases is not fully correct and a new understanding of the energetic structure of the DNA has now emerged.

As a demonstration of the complexity of the DNA electronic structure, it is sufficient to consider that the hypochromic effect measured in duplex DNA occurs with no significant spectral shift, such as is typically observed for interacting dipoles. Strong exciton coupling along the DNA, combined with efficient excimer decay, may be responsible for the optical properties of the DNA, and is probably implicated in the protection of the DNA from damage caused by UV irradiation.[13] This hypothesis may provide direct evidence that indeed the electronic structure of duplex DNA might have a specific reason for being so complex. Perhaps, because DNA is the depository of all hereditary information, it may have evolved in such a way as to acquire these features that are so important for any living organism.

4.2 The Electrochemical Paradox

Experimental observation of ground state electron transfer (ET) provides an additional evidence that the electronic structure of DNA is significantly altered from that of isolated bases. Electrochemical reduction of redox intercalators well coupled into the DNA π-stack at energies well below the lowest LUMO of the individual DNA bases, and at distances beyond a reasonable tunneling decay, implies that the deviation of the electronic structures (from the isolated bases) extends not only over the entire DNA length, but also over a wide range of energies.[2, 14-18] In fact, if we suppose that simple thermal accessibility of the DNA bridge from a redox intercalator is the mechanism for DNA mediated ET, from the classical transition state theory we can estimate the first-order rate constant for ET, k_{ET}, by

$$k_{ET} = \kappa_{el} \nu_{el} \exp(\frac{-\Delta G^*}{k_B T}), \qquad 4\text{-}1$$

where κ_{el} is the electronic transmission coefficient (or averaged transition probability), ν_{el} is an effective frequency for nuclear motion along the reaction coordinate, ΔG^* is the free energy of activation for the ET process, and k_B is the Boltzmann constant. For instance, thermally induced reduction of methylene blue (MB), whose redox potential is about 0 V vs. NHE is a process with an energy barrier of at least 1 eV.† Assuming an adiabatic process ($k_{el} = 1$, $k_{el}\nu_{el} = 10^{13}$ s^{-1}), the rate for thermal accessibility of DNA bases from MB is about $40 \cdot 10^{-6}$ s^{-1}, i.e. more than six orders of magnitude smaller than the rate

† Thymine is the DNA base with the lowest reduction potential, with a redox potential of about -2.1 V in acetonitrile or -1.7 V in water (19. Steenken, S.; Jovanovic, S. V., How easily oxidizable is DNA? One-electron reduction potentials of adenosine and guanosine radicals in aqueous solution. *Journal of the American Chemical Society* **1997,** 119, (3), 617-618.).

experimentally measured (100 s^{-1}). The standard rate constant on the order of 100 s^{-1} has been observed consistently with MB and daunomycin (DM) and seemingly corresponds to the rate of electron transfer through the alkane-thiol linker employed to immobilize the DNA on a gold surface. Indication that the electron transfer in DNA must be faster also comes from the systematic variation of the position of DM in the DNA, which has resulted in similar rates regardless of the distance the electron has to travel inside the DNA. From these considerations, one can understand that the DNA-mediated ET process at the ground state would be paradoxical if explained in simple terms of tunneling or superexchange. Based on experiments, it seems reasonable to suggest that the existence of energetically low electronic states in DNA may provide a viable pathway for ground state ET. In this chapter we will use scanning tunneling microscopy to probe the electronic structure of DNA and directly investigate the existence of energetically localized states in DNA.

4.3 Introduction to Scanning Tunneling Microscopy and Molecular Electronics

Scanning tunneling microscopy (STM), invented by G. Binnig and H. Rohrer at the IBM laboratory in Zürich in the early 1980s, initiated the new era of microscopic investigations of surfaces.[20] Nowadays, STM is used almost routinely in many physical laboratories for surface characterization as well as the study of new types of substrates. The advantage of STM is twofold. Firstly, STM allows atomic-scale resolution images of the crystal packing of metallic or semiconductive surfaces to be obtained. Secondly, it can provide extremely important insight regarding the electronic properties of the surface itself, or even of molecular layers. Most recently, electrochemical STM (EC-STM) has permitted the study of biological molecules under physiological conditions, thus extending the application of this technique to fields outside of physical chemistry.[21-24]

Despite its extraordinary analytical power, the principles underlying STM are remarkably simple. Figure 4-1 shows the schematic diagram of an EC-STM. The tip, usually made of a sharpened tungsten (W) or iridium-platinum (Ir-Pt) alloy wire, is attached to a piezoelectric element that allows fine adjustment of the tip position above the sample. When the tip and sample are biased, i.e., when a potential difference is applied, and if the tip is close enough (but not touching) the surface, a current flowing from the surface to the tip can be measured and amplified. One of the most common used modes of an STM is the "constant current mode." In this mode, under a given bias, the tip-sample distance is controlled by the piezoelectric element via a feedback loop in order to maintain a pre-defined current, the current setpoint. The tip is scanned in the x-y plane and the z displacement is then plotted color coded on the computer screen.[25]

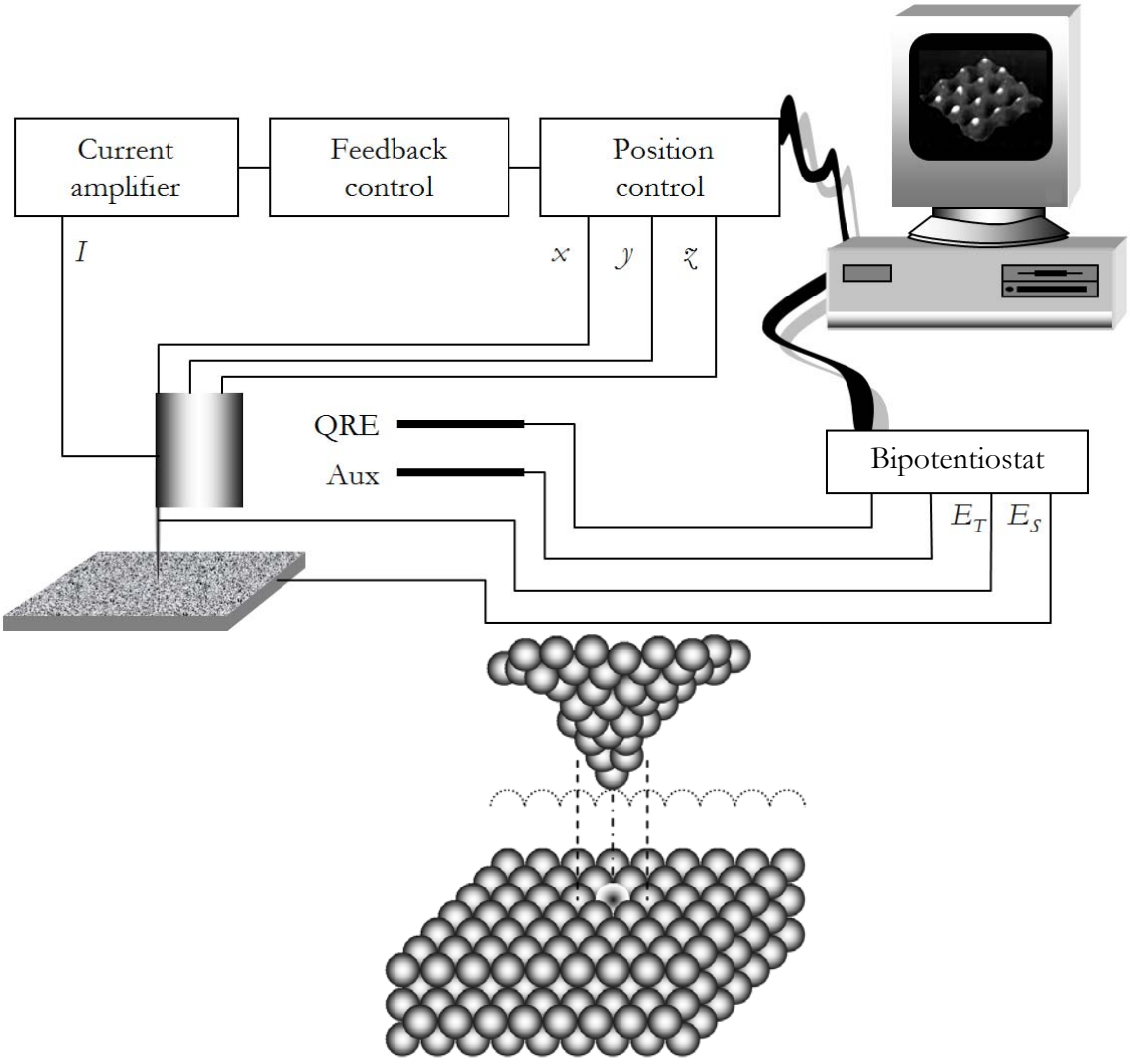

Figure 4-1: Schematic diagram of an EC-STM. In the constant current mode, the current *I* is kept constant by adjusting the position of the tip via a feedback control. As the tip is scanned over the sample in the *x*-*y* plane the *z* position is recorded and displayed on the monitor screen as a grayscale map. The tip and substrate potentials, E_T and E_S, respectively provide the bias, whereas the auxiliary (Aux, platinum wire) and quasi-reference electrode (QRE, silver wire) control the solution potential. In the bottom image, a schematic representation of the tip above the sample is shown. The tip is kept at a constant current (dotted line). The tunneling current is limited to the outer most atoms of the tip (dashed lines) providing a high lateral resolution.

4.3.1 Electron Tunneling

Imaging of atomic arrangements of atoms on surfaces is easily achieved by STM. This impressive sensitivity is due to the exponential character of the tunneling current between the sample and the tip. In order to illustrate this feature, let us discuss the concept of tunneling in a one-dimensional model. As the STM tip and sample are not in contact, there is no direct current flowing between them. This situation is illustrated in Figure 4-2. In classical mechanics, an electron with energy E moving in a potential $U(z)$ is described by

$$\frac{p_z^2}{2m} + U(z) = E, \tag{4-2}$$

where m is the electron mass ($9.1 \cdot 10^{-28}$ g), and p_z is the momentum in the z direction. In the region with $E<U(z)$ between tip and sample, where the electron cannot penetrate, its momentum is null, and thus $U(z)$ plays the role of a potential barrier. However, if now we treat the same problem from a quantum mechanical perspective, the state of an electron is described by the wavefunction $\Psi(z)$ that satisfies the Schrödinger equation

$$-\frac{\hbar}{2m}\frac{d^2}{dz^2}\Psi(z) + U(z)\Psi(z) = E\Psi(z). \tag{4-3}$$

In the classically allowed region, where E>U(z), the solution of 4-3 is

$$\Psi(z) = \Psi(0)e^{\pm ikz}, \tag{4-4}$$

where $\Psi(0)$ satisfies the boundary conditions inside the well, and

$$k = \frac{\sqrt{2m(E-U)}}{\hbar} \tag{4-5}$$

is the wave vector.

The electron, in the allowed region, moves with a constant momentum $p_z = \hbar k$ and a constant velocity $v_z = p_z / m$, exactly as in the classical case. However, in the forbidden region, where $E<U(z)$, the wave vector becomes an imaginary number and the wavefuntion (4-4) describes a real exponential decay

$$\Psi(z) = \Psi(0)e^{-\kappa z}, \tag{4-6}$$

where the decay constant is defined by

$$\kappa = \frac{\sqrt{2m(U-E)}}{\hbar}. \tag{4-7}$$

Thus the probability density to find an electron inside the energy barrier is

$$\left|\Psi(z)\right|^2 = \left|\Psi(0)\right|^2 e^{-2\kappa z}, \tag{4-8}$$

which is non-zero inside the barrier.

From these simple considerations, we can already understand some fundamental properties of the metal-vacuum-metal tunneling. For instance, in the vacuum, the height of the tunneling barrier is equal to the work function of the metal, which is the same as the Fermi energy of the metal, defined as the upper limit of the occupied states in the metal, $E_F = -\Phi$. We can see (Figure 4-2) that current can flow only if a bias eV is applied and

there is an overlap between filled and empty states of the two metals. If the bias is small compared to the work function ($eV << \Phi$) we observe that only electrons in electronic states in the proximity of the Fermi energy are able to tunnel, i.e., $U - E \approx \Phi$. Thus, the decay constant (4-7) is proportional to the square root of the work function: $\kappa = 0.51\sqrt{\Phi}$ Å^{-1}.

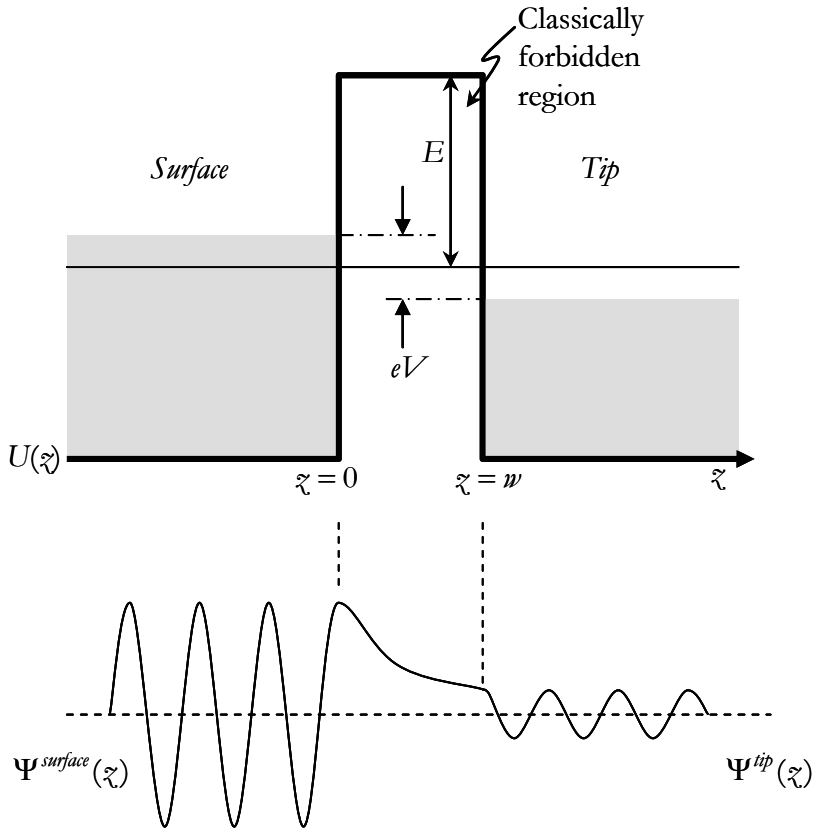

Figure 4-2: A one-dimensional metal-vacuum-metal tunneling junction. The electron wavefunction in the surface penetrates and decays exponentially in the energy barrier. In the tip the electron wavefunction has a diminished amplitude (reduced probability), but conserved energy.

4.3.2 Tunneling Current

The tunneling current in a metal-vacuum-metal interface can be generally expressed in terms of the transmission probability of an electron, as described below:

$$I = e\sum_{\mu\omega} P_{\mu\omega} f(\varepsilon_\omega)[1 - f(\varepsilon_\mu)], \qquad 4\text{-}9$$

where e is the charge of the electron, $P_{\mu\omega}$ is the transfer probability from the surface (μ) to the tip (ω), $f(\varepsilon)$ is the Fermi-Dirac distribution, and the sum is over all overlapping electronic states of the surface and tip. Thus, current occurs between the surface and the tip if there is an overlap between occupied surface states ($f(\varepsilon_\omega)$) and unoccupied tip states ($1\text{-}f(\varepsilon_\mu)$), via a probability function $P_{\mu\omega}$ that depends on the actual orbital shape and density of states of the surface and the tip involved in the tunneling. In other words, the study of the tunneling current is "reduced" to the study of the probability of transmission. In 1961, Bardeen[26] (when trying to explain the tunneling current between two metal plates separated by an oxide layer)[27, 28] proposed the formalism for describing the tunneling current. He realized that the current could be quantitatively accounted for only under the assumption that the relevant factor is the local density of state (LDOS). Thus, the transition probability can be given by $(2\pi/\hbar)|M|^2\delta(\varepsilon_\mu - \varepsilon_\omega)$, where M is the matrix element and the δ function indicates that only the states with same energy can tunnel into each other. Thus, the generalized expression for the tunneling current, in Bardeen's formalism, is given by

$$I = \frac{2\pi e}{\hbar}\int_{-\infty}^{+\infty} f(\varepsilon)[1 - f(\varepsilon + eV)]\left|M_{\mu\omega}\right|^2 \mu(\varepsilon)\omega(\varepsilon)d\varepsilon, \qquad 4\text{-}10$$

where

$$M_{\mu\omega} = \frac{\hbar^2}{2m}\int d\vec{S}\cdot(\Psi_\mu^*\vec{\nabla}\Psi_\omega - \Psi_\mu\vec{\nabla}\Psi_\omega^*), \qquad 4\text{-}11$$

and the integral is over any surface lying entirely within the vacuum barrier separating the two sides. The quantity in parenthesis of (4-11) is called the current operator and contains the wavefunctions of the surface and tip. In (4-10), one can easily identify the bias term eV, the matrix element $M_{\mu\omega}$ describing the transition probability between surface and tip, and $\mu(\varepsilon)$ and $\omega(\varepsilon)$ are the tip and surface LDOS', respectively. It can be shown that for a finite temperature, the integral of $f(\varepsilon)[1-f(\varepsilon+eV)]$ is equivalent to one in the energy range [0,eV] and zero everywhere else. The essential problem here is to calculate an appropriate tunneling matrix element that describes the system. In the first order approximation, Bardeen assumed that $M_{\omega\mu} = M$ is constant over small energy differences. Thus equation (4-10) simplifies to

$$I = \frac{2\pi e}{\hbar}|M|^2\int_0^{eV}\mu(E_F+\varepsilon)\omega(E_F-eV+\varepsilon)d\varepsilon. \qquad 4\text{-}12$$

This is called the Bardeen formula, which indicates that the tunneling current is determined by the convolution of the LDOS of the two leads. Thus, the electronic structures are interchangeable and both contribute equally to the tunneling current. Tersoff and Hamann have calculated an explicit expression for the tunneling current assuming that the tip has a spherical structure of radius R.[29, 30] Thus, (4-12) can be evaluated and the tunneling current results as

$$I = 32\pi^3\hbar^{-1}e^2\Phi^2\mu(E_F)R^2\kappa^{-4}e^{2\kappa R}V\int_0^{eV}\left|\Psi_\omega(z)\right|^2 d\varepsilon, \qquad 4\text{-}13$$

where $\mu(E_F)$ is the LDOS of the tip at E_F, κ is given by (4-7) with $U - E = \Phi$, Φ is the work function, V is the applied voltage, and all other parameters have their usual meaning. We can see that the current is directly proportional to the density of states of the tip (which is constant) and the applied voltage. The term in the integral represents the density of state of the surface evaluated at the center of the tip, at a distance z. In constant current mode, equation (4-13) states that an STM image represents a contour map of the constant surface LDOS. One can substitute this density of states with equation (4-8) in order to obtain explicitly the distance dependence of the current. Thus, we can write a simple expression for the tunneling current:

$$I \propto eVe^{-2\kappa z}\int_0^{eV}\omega(E_F - eV + \varepsilon)d\varepsilon. \qquad 4\text{-}14$$

We can see that on gold ($\Phi_{Au} = 5.4$ eV), the decay constant κ is about 1.2 Å^{-1}. This means that the magnitude of the tunneling current decreases by more than an order of magnitude per each Å inside the tunneling barrier. Because of this steep distance dependence, STM can be extremely sensitive not only to morphological but also to electronic fluctuations.

Equations (4-12) and (4-14) are very important for the interpretation of scanning tunneling spectroscopy (STS), which is an extension of STM.[25] In general there are two types of spectroscopies (we shall introduce later a third type): the first is where the tip is kept still over the *x*-*y* plane and the current is measured while the tip is made to oscillate

fast in the z direction. Because the tunneling current is exponentially decaying with surface/tip distance (4-14), it is possible to measure the work function of the sample from the slope of ln(I) vs. z. The second type of STS technique is performed by keeping the tip still in a given position above the surface while the potential is scanned. From a generic perspective and by considering equation (4-12), we can see that the I/V characteristics can depend on both the surface and tip LDOS. Figure 4-3 provides an illustration of some such situations. However, if in a first approximation the tip orbitals can be considered spherical, the I/V curves are associated only with variation in energy of the surface's LDOS. Nevertheless, because STM tips are usually W or Pt Ir- alloys, tip orbitals are never s-type but rather d-type and thus equation (4-14) cannot be applied. We shall see later how this is an important factor to take into account when interpreting the data in detail.

When STM experiments are performed on biological samples adsorbed on a metallic surface, equation (4-14) is still valid. This has great significance because now STM provides an ideal tool for investigating the molecule's LDOS and its conductivity properties. In fact, when molecules are placed between the surface and tip, their LDOS can contribute to the overall tunneling current and STS experiments can generate useful information regarding their electronic structures. We can rewrite equation (4-12) in the case of an intervening molecular LDOS, $\varphi(\varepsilon)$,

$$I = \frac{2\pi e}{\hbar}\sigma e^{-\beta z}\int_0^{eV}\mu(E_F+\varepsilon)\varphi(\varepsilon)\omega(E_F-eV+\varepsilon)d\varepsilon. \qquad 4\text{-}15$$

Here, the tunneling matrix element M has been replaced by $\sigma e^{-\beta z}$, where σ is proportional to the electronic coupling between resonant states and $e^{-\beta z}$ represents the exponential decay of the current within the tunneling barrier, between the adlayer and the tip. β is not equivalent to the previously introduced κ, but is rather a combination of the

surface and molecular layer's work functions. In particular, it might account for abnormalities of the tunneling decay that has been reported in aqueous solutions, probably due to polarization of water molecules within the gap.[31, 32] This substitution does not affect the generality of the expression of the tunneling current, as we are typically interested in the dependence of the current with respect to the voltage. The exponential dependence is also generic and valid, as we know this reflects electron tunneling.

Before discussing the experimental results, it is useful to introduce the concept of molecular orbital. Electronic transitions between molecular orbitals occur only by resonant tunneling, i.e., between two levels with the same energy. A molecular orbital, however, is never localized at a single energy, and the function describing its energy distribution is a Lorentzian function[33] (Figure 4-4),

$$\varphi(\varepsilon) = \frac{2}{\pi\theta k_B T}\frac{1}{\left(\frac{4(\varepsilon-\varepsilon_0)^2}{(\theta k_B T)^2}+1\right)}, \qquad 4\text{-}16$$

where ε_0 is the resonance energy, and θ is a factor describing the width of the function in thermal energy (k_BT) units. An electron with energy ε in a metal will tunnel into a molecular orbital when there is a finite probability of transition. There are two main factors determining the magnitude (i.e., the probability) of a tunneling current mediated by a molecule. The molecular orbital with energy closer to the electronic level would contribute more than those with further energy. However, because of the particular shape of the state, the current would decay by the energy difference $1/\Delta E^2$ ($\Delta E=\varepsilon-E_{MO}$, where E_{MO} is the energy at the peak). The second important factor is the strength of the electronic coupling with the surface and the STM tip, σ^S and σ^T, respectively. The width of the molecular state is proportional to the product $\sigma^S\sigma^T$ and the current is proportional to the square of this product.

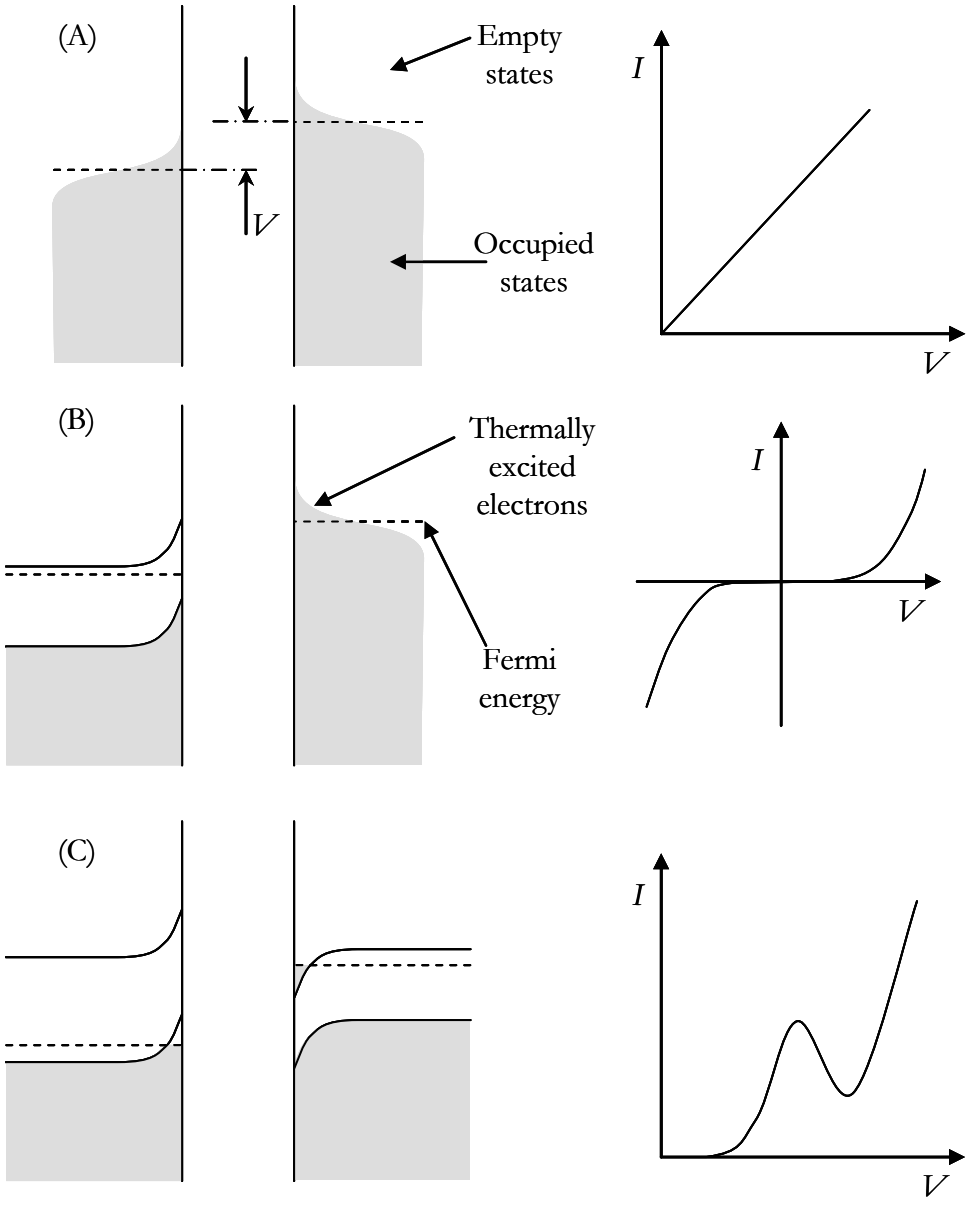

Figure 4-3: Tunneling spectroscopy in classic tunneling junctions. (A) If both electrodes are metallic, the I/V curve is linear. (B) If one electrode has an energy gap, an edge occurs in the I/V curve. (C) If both electrodes have energy gaps, two edges occur and negative differential conductance (NDR) can exist (typical in tunneling diodes).

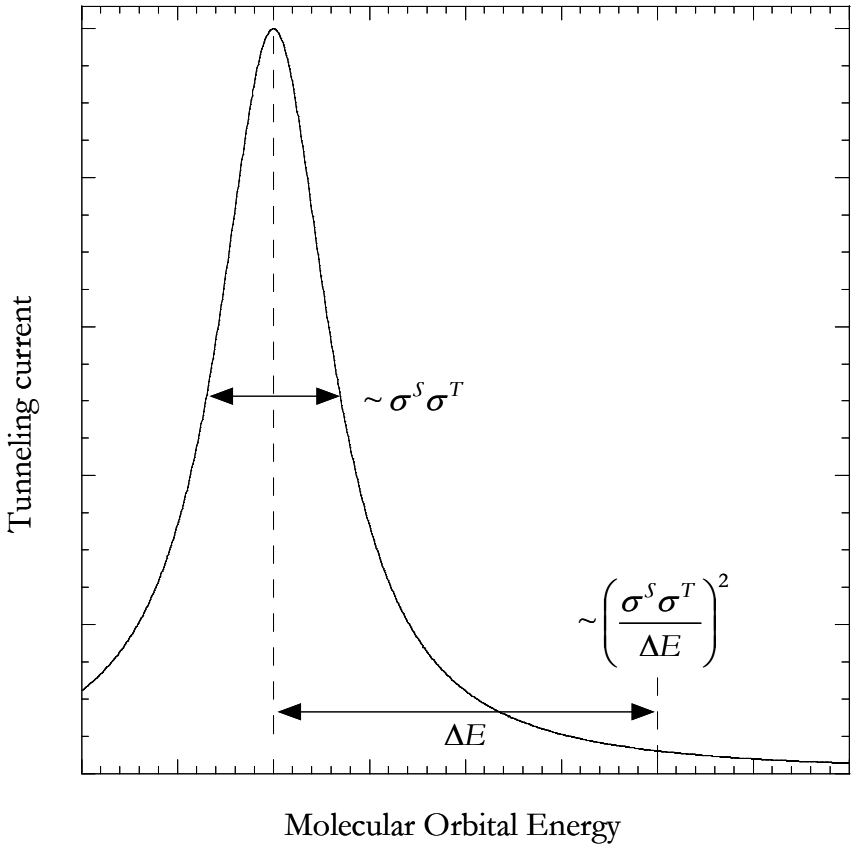

Figure 4-4: Schematic representation of the Lorentzian current resonance associated with a given molecular orbital and its tail crossing the energy of the electron inside the metal. The molecular orbital electronic interactions with the surface and tip are σ^S and σ^T, respectively.

4.4 Results and Discussion

Conductivity experiments, where DNA molecules are positioned between two electrodes, have shown contradictory results: superconductor,[34] ohmic conductor,[35] and semiconductor.[36] Those experiments, however, lack rigorous control of DNA structure and flexibility, which vary significantly with counterion and solvent composition. Disruption of the duplex structure or metal-molecule contacts may induce HOMO/LUMO distortions, orbital localization, and molecular polarons, which lead to loss of conductivity.[37, 38] STM, however, is arguably a less invasive approach for studying electron transfer in biological molecules under physiological conditions. We present here results about DNA conductivity that have been obtained for the first time under physiological conditions.

4.4.1 Bias and Mismatch Dependence

To probe the electronic properties of DNA in a metal-molecule-metal assembly under physiological conditions, we have examined thiol-modified DNA films on gold surfaces using *in situ* STM. We have shown[39] that self-assembly of duplex DNA anchored to the surface through an alkane thiol linker at the 5'-end yields well-organized films, where the DNA, at open circuit potential, forms a ~45° angle with respect to the surface. Furthermore, these atomic force microscopy (AFM) studies show that an applied potential restrains the polyanionic DNA either in the upright position, for repelling negative values, or flat on the surface, for attractive positive values. Using STM at different applied potentials, one can then directly interrogate the electronic properties of the DNA film as a function of duplex orientation. Thus, one can obtain information about the electronic states of DNA "looking" down the helical axis. Because the tunneling current, to a first approximation, is proportional to the LDOS of the sample (see Section 3.2.2),[29, 30] images obtained at a constant current do not necessarily provide the topographical morphology of

the surface, but rather important insight into the LDOS of the DNA. Since these STM studies are carried out in aqueous solution using structurally well-characterized 14-mer oligonucleotides bound to the gold surface,[17, 39] these studies may provide a first description of the electronic properties of well-defined, oriented B-form DNA in a metal-molecule-metal assembly. Moreover, since the projection of the tunneling current from the STM tip on the sample is ~1 nm in diameter,[25] only a few DNA molecules are effectively "illuminated." Because the electronic properties arise primarily from these few molecules, we consider the *in situ* STM as a quasi-single molecule investigation.

DNA-modified gold surfaces were examined as a function of the applied potential and the percentage of perfectly matched (PM) duplex content in the films. Figure 4-5 shows samples of 100% and 85% PM content, under different applied potentials. The differences between positive and negative bias potential is striking. At positive potentials with respect to the silver wire quasi-reference electrode (QRE), the images show only gold features, i.e., 60° angles lines and large flat plateaus indicating the presence of planes (111), and the DNA is completely transparent to the current from the gold. Conversely, when the surface potential is negative, the gold surface is covered by stable features that we attribute to agglomerates of DNA. Figure 4-6 shows another sample of 100% PM where the potential is scanned concomitantly to the image scan. It is possible to see that the DNA only appears on the surface in the negative region. The cluster diameter of 7-13 nm is reminiscent of hexagonal packing of DNA in crystals,[40, 41] and indeed ^{32}P-labeling experiments[17] give evidence that is consistent with close duplex packing on the gold surface. These extra features are stable during the scanning and the whole duration of the experiment. This is a clear indication that the tip is located above the sample and does not interact (or at least not appreciably) with the DNA film. Though higher resolution is not achieved under these conditions, the STM images are consistent with AFM studies, in which films were found to be morphologically uniform and densely packed,[17] the high Mg^{2+} concentrations used to fabricate the DNA.

Figure 4-5: STM images of DNA films, 100% PM (left column) and 85% PM (right column), on gold. (A) Under negative bias (-400 mV vs. ground, substrate negative) the features are stable during the scan and are 7-12 nm in diameter, reminiscent of the DNA hexagonal packing. (B) The bias is changed during scanning and extra features appear on the surface. (C) Under positive bias (+400 mV vs. ground, substrate positive) it is possible to observe the underlying gold with atomic planes at 60° angles, characteristic of gold (111). Conditions: current setpoint 50 pA, tip potential kept at 0 V vs. ground, interfacial potential kept at 0 V vs. Ag wire QRE using a Pt auxiliary electrode; tip insulated with Apiezon wax, background faradic current less then instrument sensitivity (30 pA); images taken under aqueous conditions: 10 mM Tris-HCl, pH 7.0; scan size 300 nm for 100% PM, and 260 nm for 85% PM.

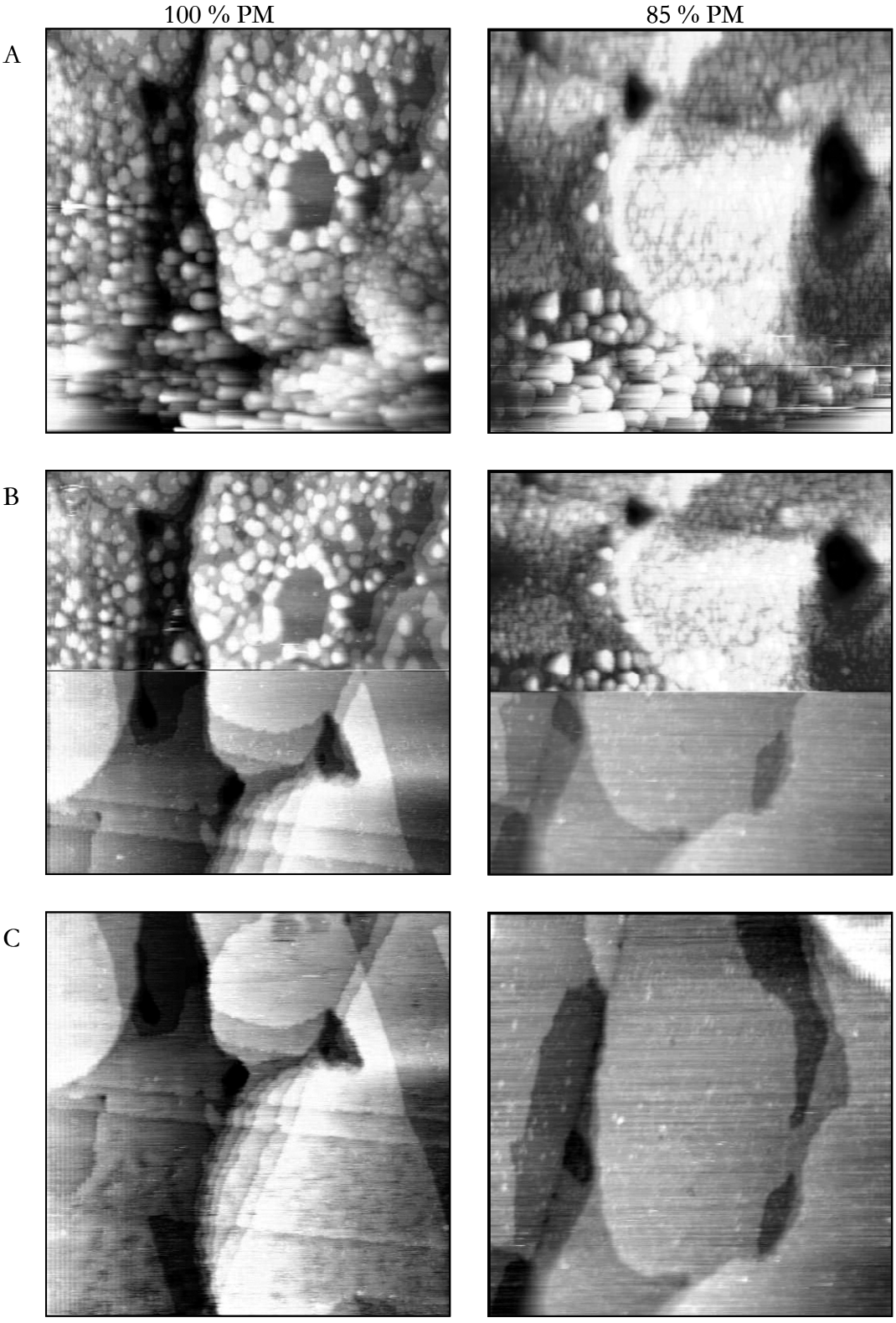
100 % PM
85 % PM
A
B
C

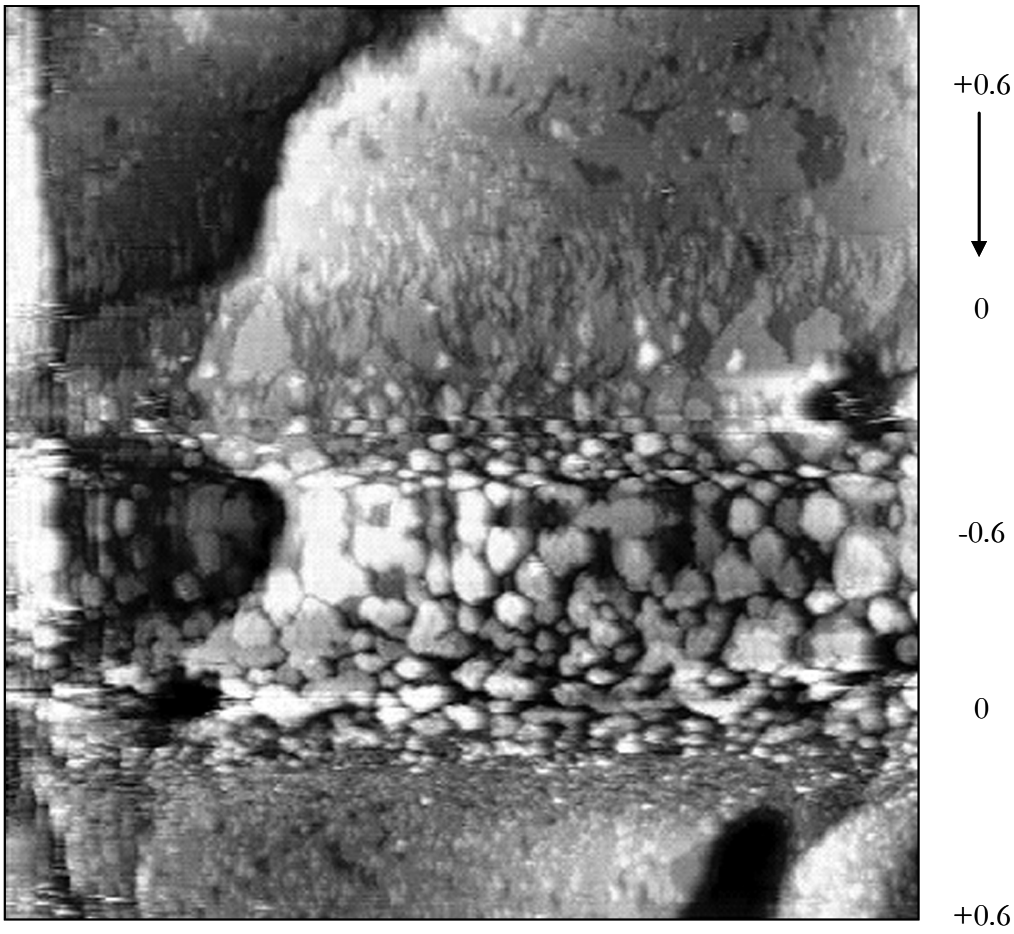

Figure 4-6: STM images of a DNA film, 100% PM, on gold. The image was recorded as the potential was changed from +0.6 to 0 V and back to +0.6 V vs. ground. The tip movement is indicated by the arrow. Only in the negative region it is possible to observe the DNA film, whereas everywhere else the DNA film is transparent. Conditions: same as in Figure 3-5; scan size 300 nm.

films serve to neutralize phosphate repulsions among DNA duplexes. Our STM images are also similar to recently reported STM images of DNA films in vacuum after synthesis on silicon surfaces.[42, 43]

Potential-dependent behavior has been reproducibly observed for different samples with PM contents higher than 75% (Figure 4-7). For samples with lower PM content, however, the STM images do not exhibit bias potential dependence. Instead, they appear blurry and noisy (Figure 4-8). This blurriness is an indication that the STM tip is penetrating the soft film in order to maintain the constant setpoint current. With high PM content, in contrast, clear images are observed using a range of setpoint currents, 50 pA-1 nA. Thus, the presence of an internal mismatch in the film causes attenuation of the film conductance even with the DNA duplexes in the upright orientation. Note that the mismatch sensitivity also suggests ionic conductivity is not a critical factor here.

It would be difficult to interpret these data without consideration of the contribution of the LDOS of the DNA to the electronic communication from the gold surface to the STM tip (Figure 4-9). If one considers the orientation of the DNA with respect to the STM tip, effective orbital overlap between DNA base pairs and the metal electronic states is likely when the DNA is in the upright position. In this orientation, an efficient tunneling process through the energy gap (between tip and DNA) can occur. Conversely, when the potential is more positive, the DNA tilts with respect to the surface normal, and the coupling between DNA and tip decreases. In this orientation, the tip can no longer probe the LDOS of the DNA. As a result, the DNA becomes *transparent*, and in the STM images, only the features of the gold surface are visible. Interestingly, as in the AFM studies, in recording the images as a function of the applied surface potential (Figure 4-10), a hysteresis was observed, which we attribute to mechanical motion of the DNA in the film and not to an on-off resonance mechanism. Thus, only well-matched DNA films oriented in an upright position possess a non-negligible LDOS nearby the Fermi level of the gold surface.

Intervening mismatches in the DNA duplex, even if properly oriented, alter the STM images. Despite causing little change to the duplex DNA structure and no detectable change to the DNA film structure,[18] intervening mismatches lead to significant electronic perturbations. Theoretical calculations have shown that the states of sulfur atoms can mix with those of the alkane tethers introducing additional electronic states in the HOMO-LUMO gap,[44] yet the states of the sulfur atoms should not be affected by a mismatch inside the DNA duplex (20 Å from the sulfur atoms). In fact, for a PM content less than 70%, the LDOS of the DNA is not sufficient to keep the tip outside the film. The results with lower PM content are also inconsistent with a tunneling mechanism over the 6.8 nm length of DNA plus linker, since the intervening mismatch should not affect this long range tunneling. Instead, the results observed with less than 70% PM may be a consequence of the local electronic perturbation induced by the mismatch on the integrity of the π-orbital interactions that provide an electronic pathway inside the DNA. With the intervening mismatch, DNA orbitals are no longer efficiently coupled and conductivity through DNA is turned off.

Figure 4-7 (on two pages): STM images of DNA films containing different PM contents. Left column is for negative bias, the right column is for positive bias. In particular the biases and scan sizes for the individual PM contents are 95%: -0.4/+0.2 V, 500 nm; 90%: -0.4/+0.4 V, 125 nm; 85% -0.4/+0.4 V, 260 nm; 80%: -0.4/+0.4 V, 400 nm; 75%: -0.4/+0.4 V, 400 nm. Conditions: same as in Figure 3-5.

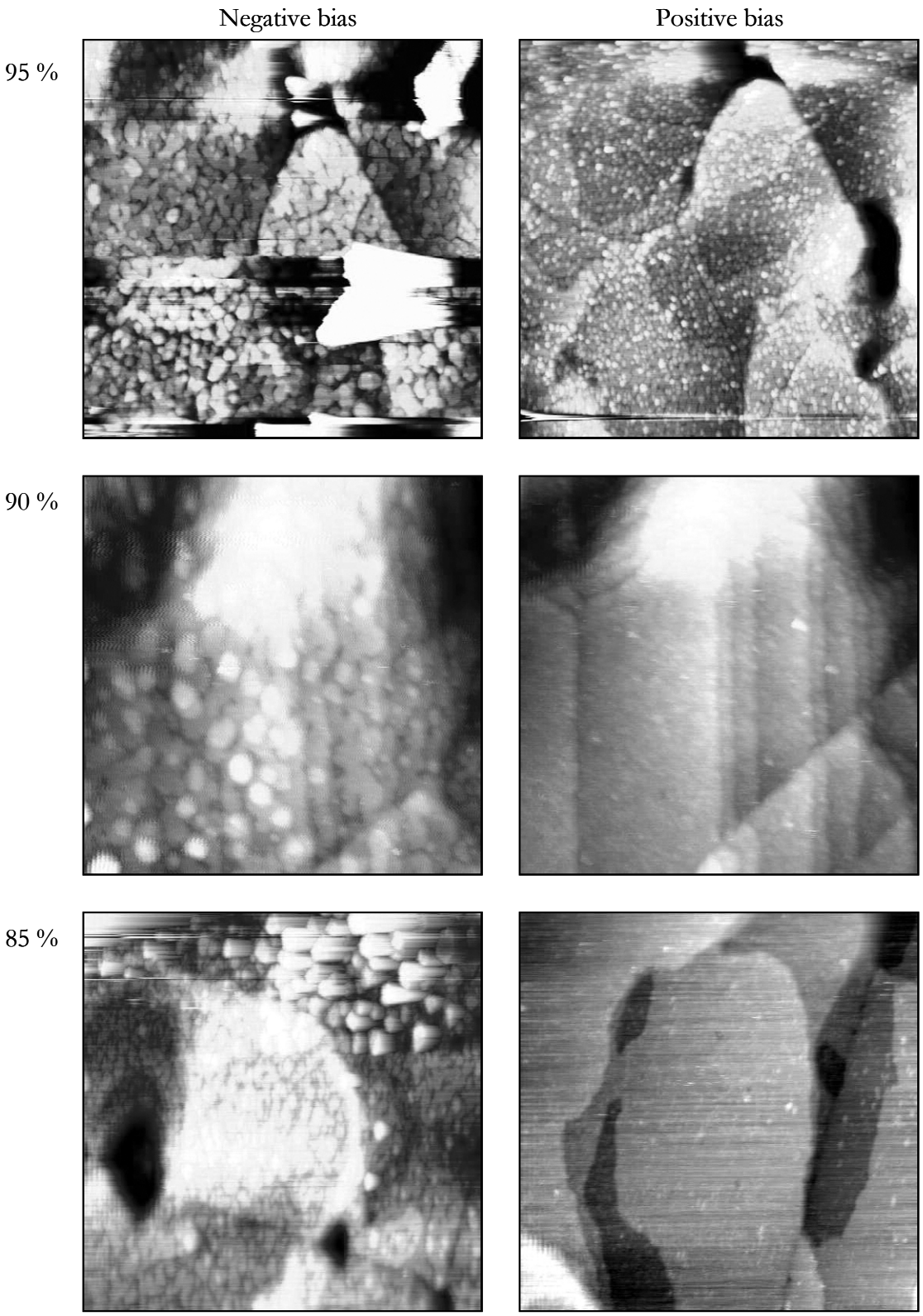
Negative bias
Positive bias
95 %
90 %
85 %

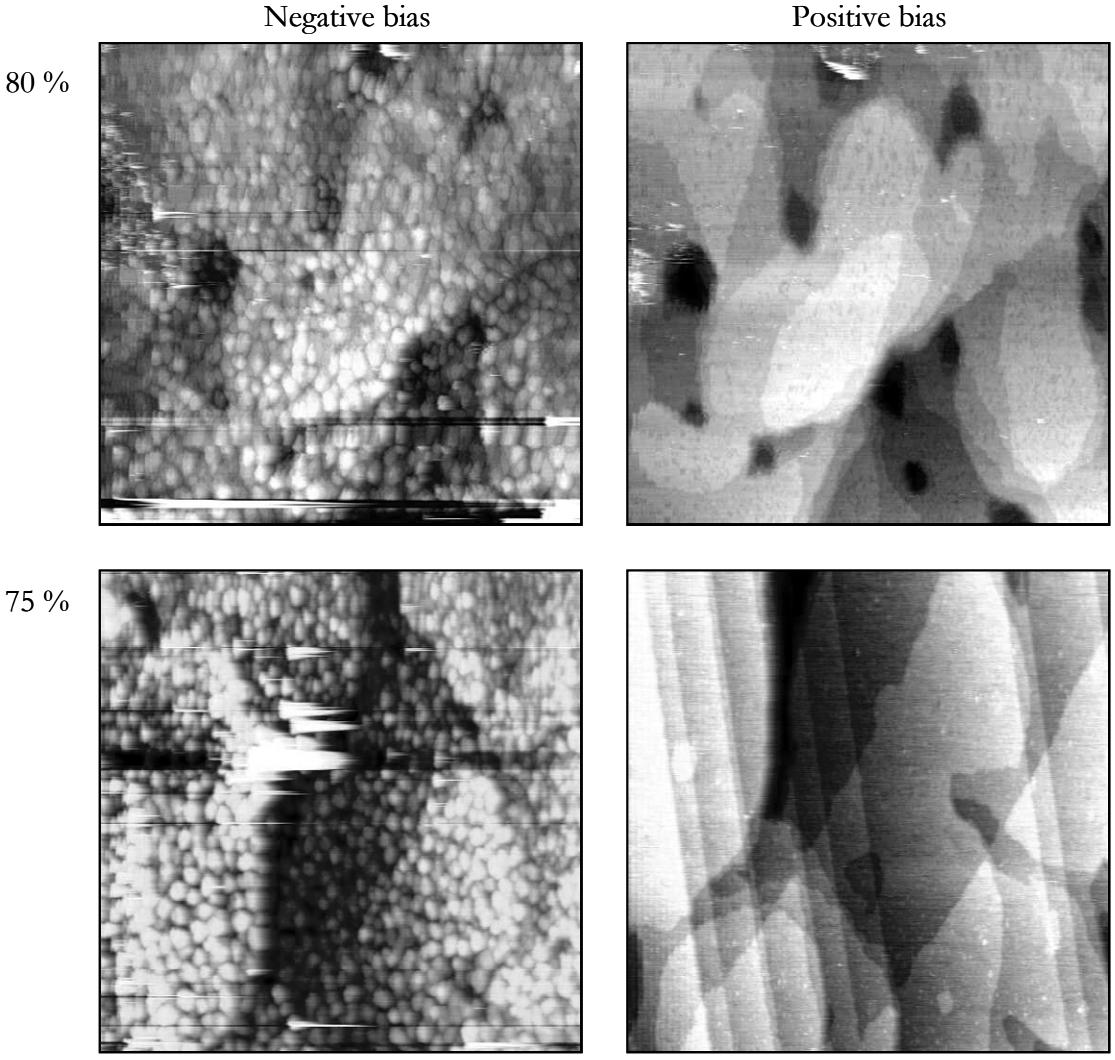
Negative bias
Positive bias
80 %
75 %

Figure 4-8: STM images of DNA films containing PM contents less than 75%. The images become blurry as the STM is penetrating the film: DNA is less conductive because of the mismatch. Left column is for negative bias, the right column is for positive bias. In particular the biases and scan sizes for the individual PM contents are: 70%: -0.4/+0.4 V, 200 nm; 60%: -0.4/+0.4 V, 300 nm; 50% -0.4/+0.2 V, 100 nm. Conditions: same as in Figure 3-5.

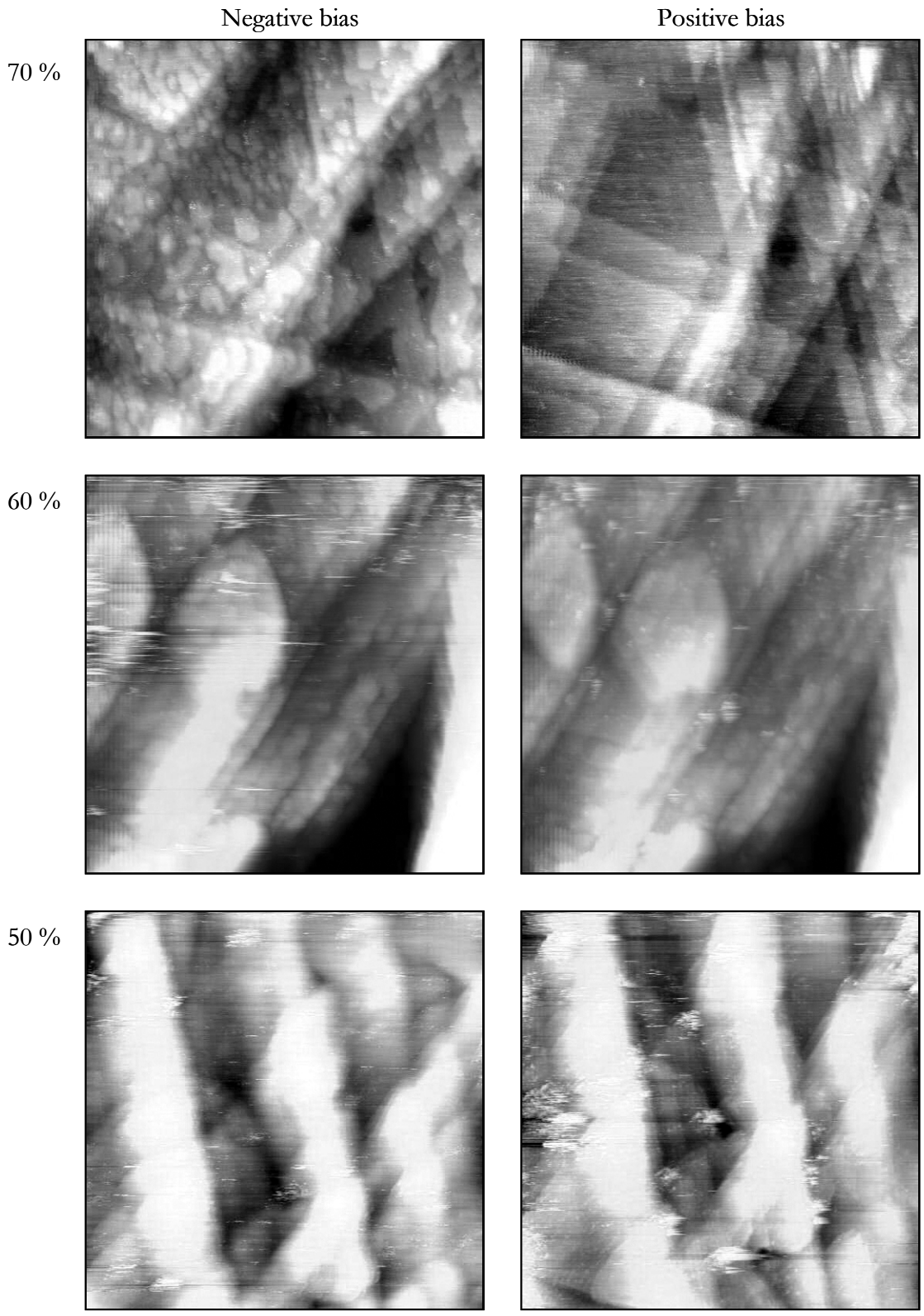
Negative bias
Positive bias
70 %
60 %
50 %

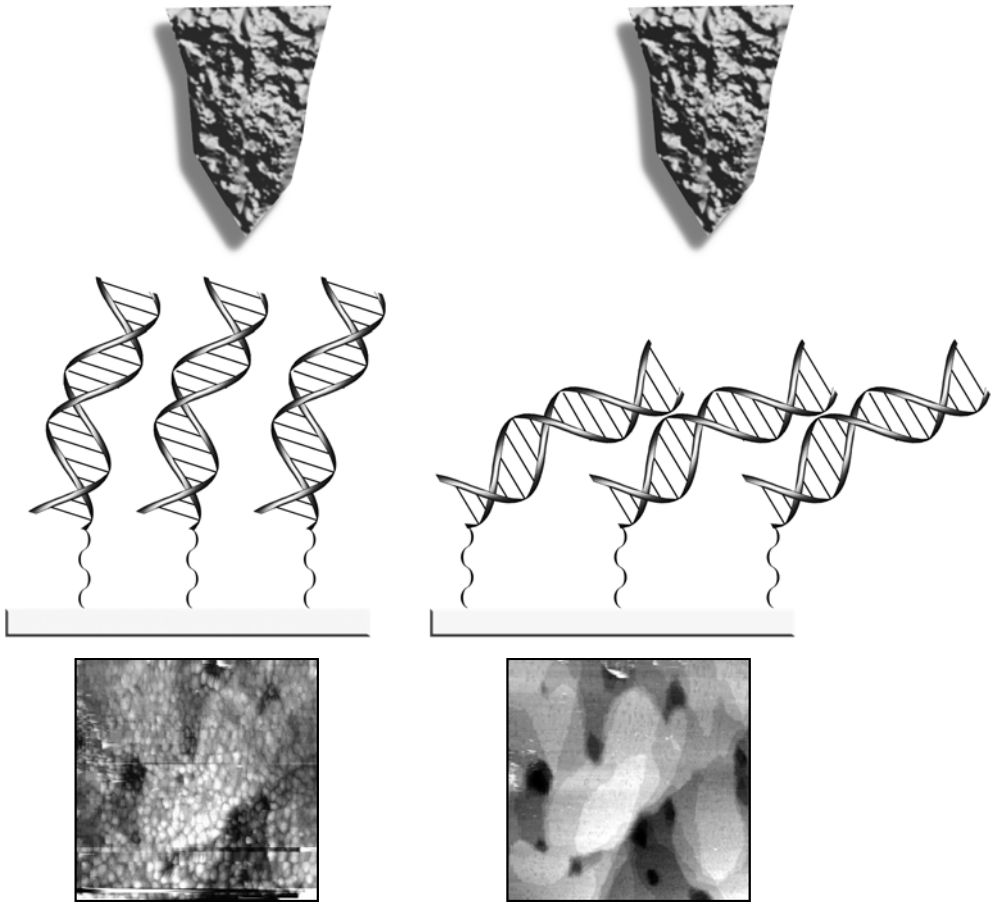

Figure 4-9: Schematic representation of the gold-DNA-tip tunneling junction. When the surface potential is negative and DNA is the upright position, the tip states are decoupled from the gold surface and allow imaging the DNA film. Conversely, when the surface potential is positive and the DNA is tiled, the tip states are now decoupled from the DNAs and only the underlying gold surface can be visualized.

Figure 4-10 (on two pages): Series of STM images of a DNA film containing 75% PM under different bias potentials. The images have been acquired few minutes after the potential change in order to achieve equilibrium. When the bias is changed from a negative (-0.4 V) to a positive (+0.4 V) potential, there is a transition around +0.1 V. Instead, when changing the bias from a positive (+0.4 V) to a negative (-0.4 V) potential (second page), the transition occurs at -0.01 V. This hysterisis has been attributed to the mechanical motion of the DNA molecules in response to surface polarization.

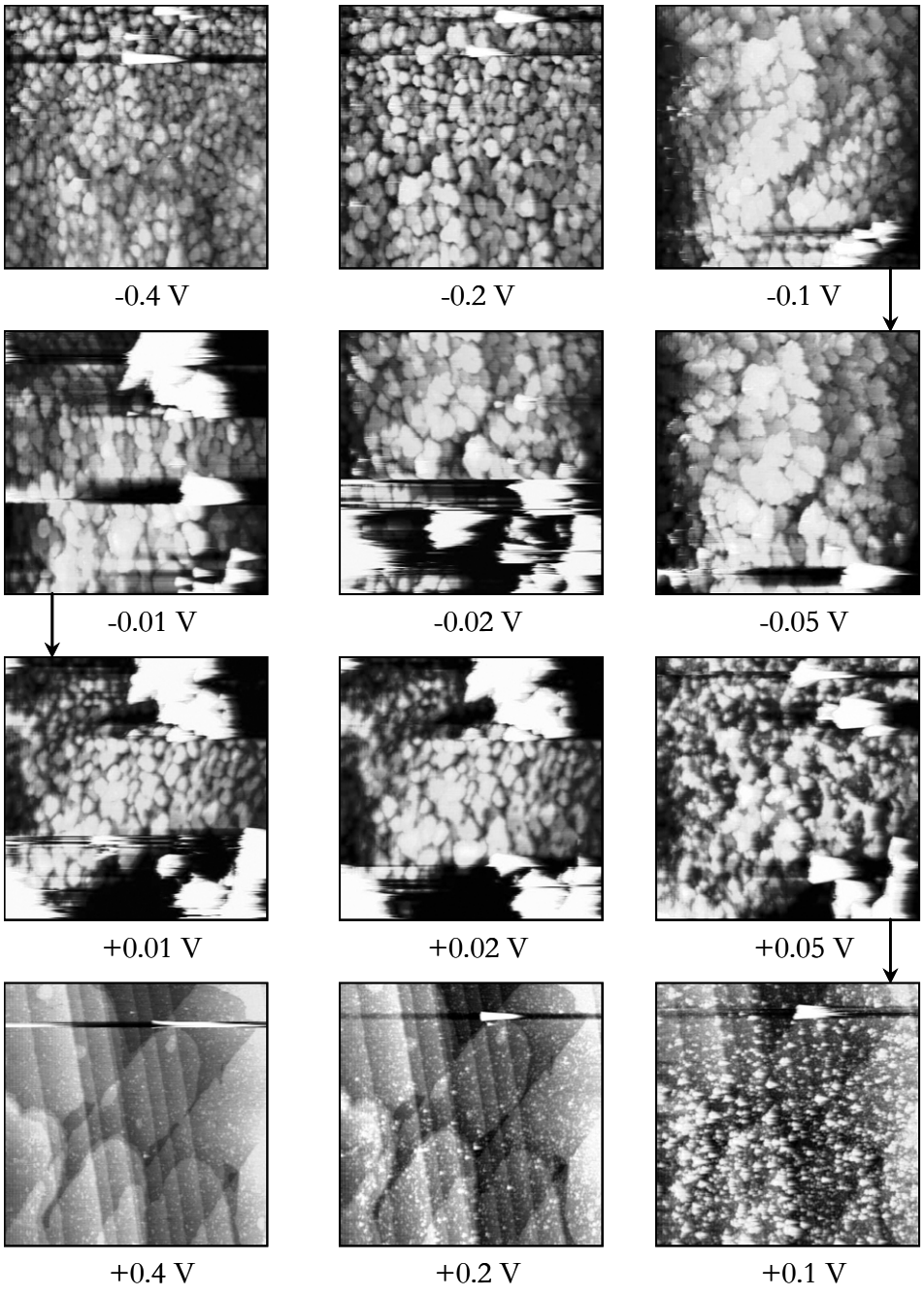
-0.4 V
-0.2 V
-0.1 V
-0.01 V
-0.02 V
-0.05 V
+0.01 V
+0.02 V
+0.05 V
+0.4 V
+0.2 V
+0.1 V

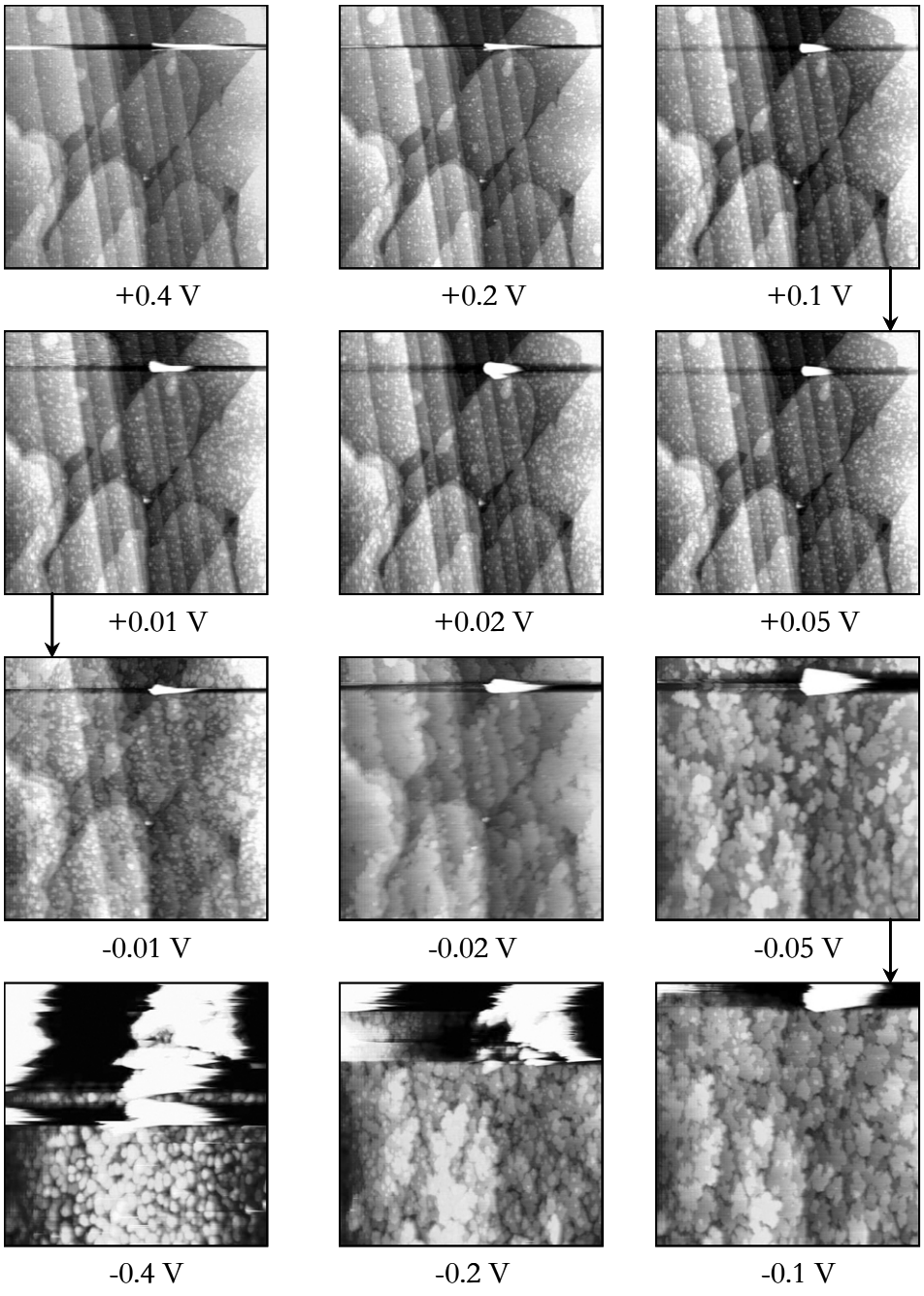
+0.4 V
+0.2 V
+0.1 V
+0.01 V
+0.02 V
+0.05 V
-0.01 V
-0.02 V
-0.05 V
-0.4 V
-0.2 V
-0.1 V

4.4.2 Determination of the DNA Local Density of States

Investigation of DNA films by *in situ* STM has proven that DNA does possess an appreciable LDOS in the region nearby the Fermi level of gold. The measure of the DNA conductivity is now simply reduced to the determination of the characteristic curve of tunneling current vs. applied potential, I/V curve. Scanning tunneling spectroscopy (STS) techniques would allow the determination of the DNA LDOS as function of the applied potential.[25] In general, I/V curves are determined by STS by keeping the tip fixed at a particular distance from the surface, achieved by turning the feedback off, while the potential is scanned over the energy region of interest. However, this approach requires careful experimental attention, as thermal expansion of the piezoelectric element usually causes the tip to drift towards the surface, thus affecting the measurements.

In order to overcome this problem, it is important to recognize that the generic expression describing the tunneling current, equation (4-15), contains two independent factors: the exponential distance dependence and the voltage-dependent density of states. Considering these two factors independently is equivalent to saying that the current decay constant β is not voltage dependent and that the molecular layer's LDOS is not affected by the tip position. These two conditions are often easily satisfied and it is possible perform an experiment where the tip is held at a constant current (feedback loop on) while the potential is scanned and the tip displacement recorded as a function of the applied potential. Reversing equation (4-15) in order to obtain the local density of states as a function of z, we have, for a given constant tunneling current

$$e^{\beta z(V)} \propto \int_0^{eV} \mu(E_F + \varepsilon)\varphi(\varepsilon)\omega(E_F - eV + \varepsilon)d\varepsilon. \qquad 4\text{-}17$$

We can easily see, comparing (4-15) with (4-17), that the plot of $e^{\beta_{\pi}(V)}$ vs. V is directly equivalent to plotting I vs. V by holding the tip at a constant height. We may describe hereafter these data in terms of I/V curves, as we assume that (4-15) and (4-17) are interchangeable.

The I/V curves for bare gold and the DNA film (100% PM) are shown in Figure 4-11 and 4-12. The curves represent the average of 5-12 consecutive curves (see Experimental Details). The linear relationship between current and voltage for bare gold is an indication that the experimental approach is correct and that (4-17) is truly proportional to the current (see Figure 4-3 with ideal curves). The lack of data points around 0 V is due to the fact that the tip was not allowed to approach the surface too close in order to avoid damages due to contact. When the same technique is applied on a DNA film, interestingly, the plot exhibits negative differential resistance (NDR) between 0.11 and 0.22 V, suggesting the presence of energetically localized density of states in the DNA films. Figure 4-13 shows the details of the DNA film exhibiting NDR.

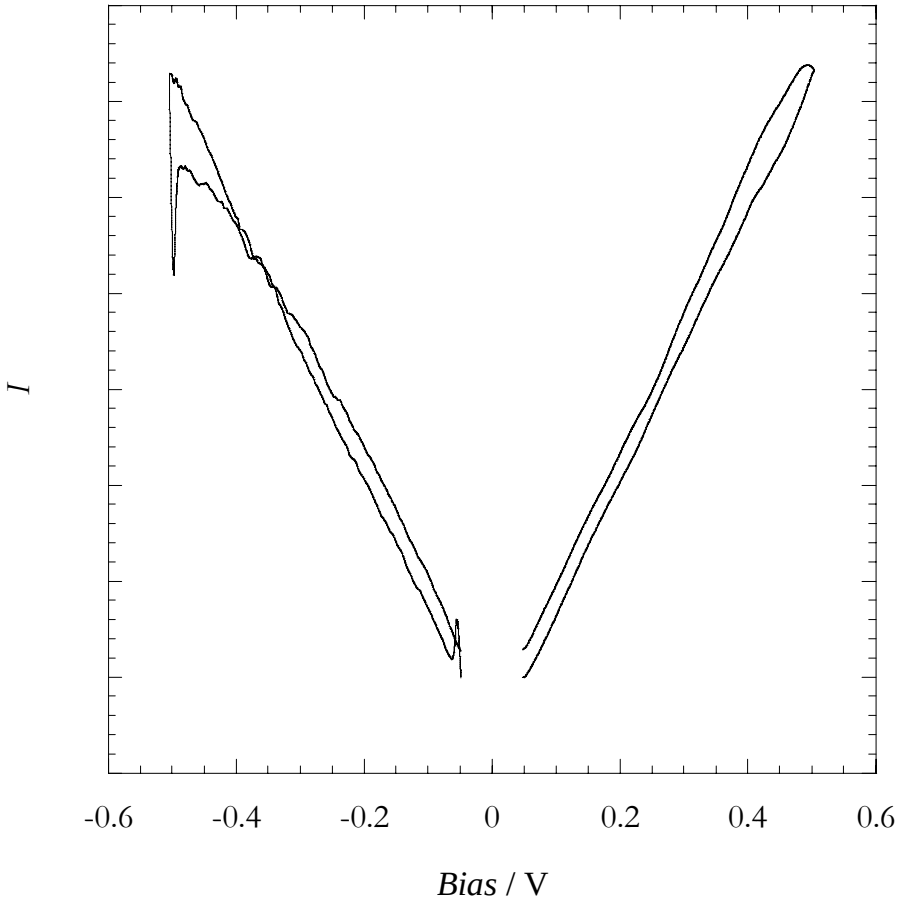

Figure 4-11: I/V curve for gold in aqueous solution obtained by recording the z displacement of the tip as a function of the applied bias potential while the feedback control keeps the tip at a constant current of 50 pA (equation 4-17). The linearity of the curves proves the validity of the method for determining the density of states of the surface.

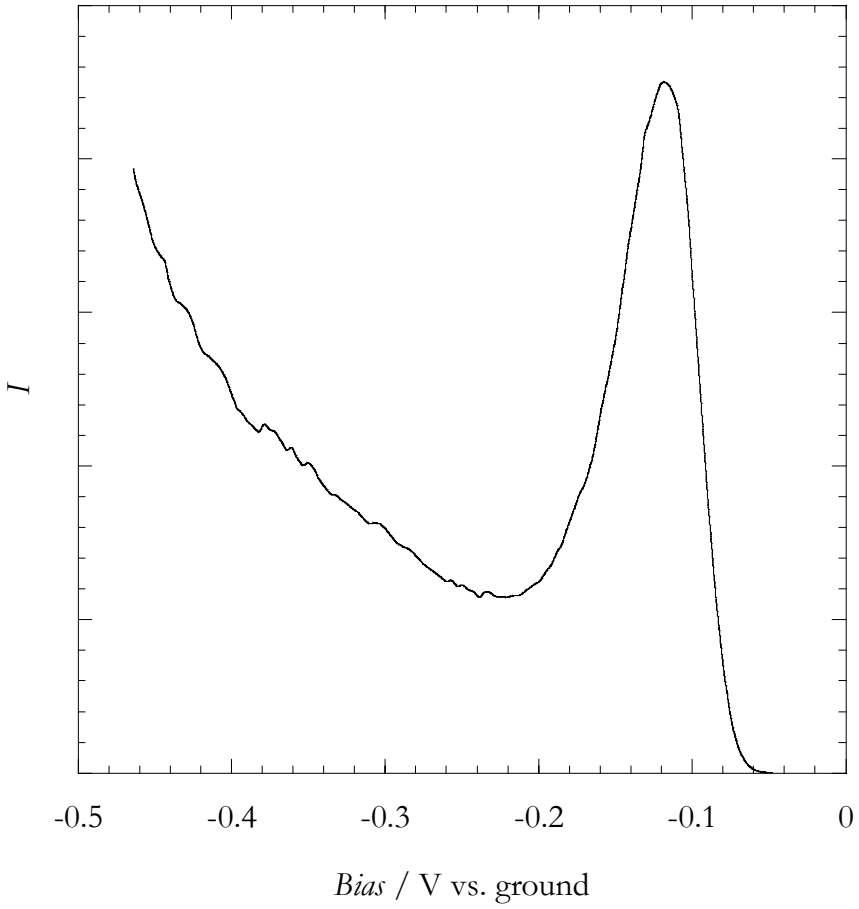

Figure 4-12: I/V curve for a DNA film containing 100% PM on gold in buffer obtained by recording the z displacement of the tip as a function of the applied bias potential while the feedback control keeps the tip at a constant current of 50 pA (equation 4-17). The NDR (positive slope between 0.11 and 0.22 V) suggests the presence in the DNA of an energetically localized energy band in proximity of the Fermi energy of the gold surface.

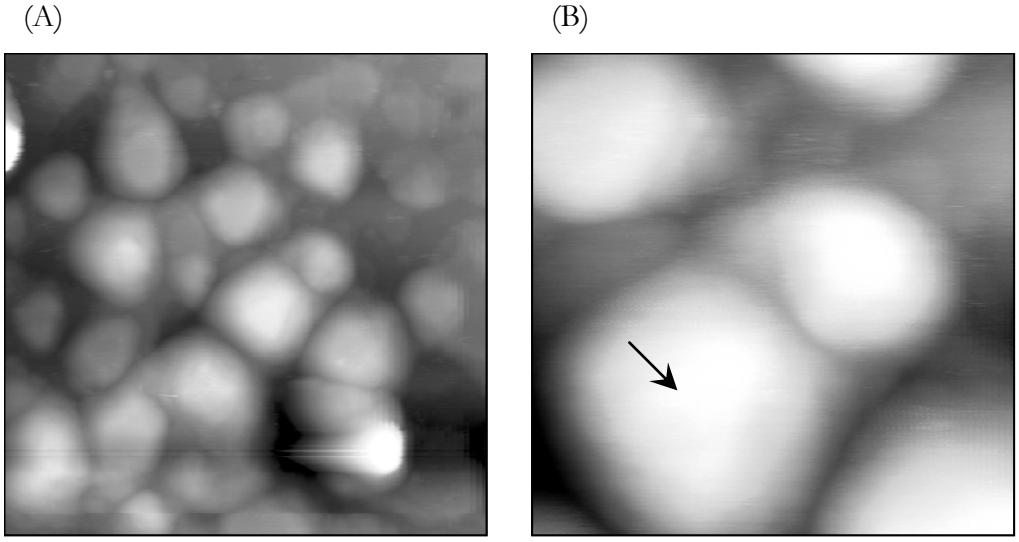

Figure 4-13: STM images a DNA film containing 100% PM at a bias voltage of -0.4 V: scan size of 100 nm (A) and 20 nm (B). The arrow shows the detail of the site exhibiting NDR. The features on the surface are 6-12 nm in diameter reminiscent of the DNA hexagonal packing.

4.4.3 Origin of Negative Differential Resistance in DNA Films

To date, NDR has been observed frequently, for instance, for break-junction devices,[45] single molecules adsorbed on silicon substrates,[46] and C_{60}-mediated electron transfer.[47, 48] In general, this phenomenon is commonly attributed to the convolution of energetically localized tip or substrate states with the molecular density of state.[47, 49, 50] We have seen that the tunneling current is a convolution of the LDOS of the two electrodes and the molecular intervening layer (Equation 4-15). In most of the cases, however, the situations are relatively similar to one another and can be understood by observing how a tunneling diode works (see Figure 4-3C for a simplified model). When two semiconductors (p and n) are in proximity, electron tunneling may occur when there is overlap between occupied and unoccupied states. When a bias is applied between the two electrodes, the Fermi levels move accordingly and a current can flow. However, because of the existence of an energy gap in both electrodes, there will be a current only within a particular energy range (Figure 4-3C). As the Fermi levels move apart, the current can decrease because there is no longer overlap between states. From this example, it is possible to make a generalization of the requirements for NDR: when two densities of states exhibit features, in particular sharp features, that move (by the applied potential) with respect to each other, NDR can be observed.

Most of the NDR observed, are associated with the convolution of the LDOS of a semiconducting substrate and molecular states. However, NDR has rarely been observed on metallic surfaces. Xue et al. have been able to observe NDR in the I/V characteristics of a self-assembled monolayer of 4-p-terphenylthiol molecules on gold surfaces measured using platinum tips. They argue that NDR arises from the convolution of sharp features in the tip apex states with the molecular states that depends on the electrostatic potential profile across the junction. A tip exhibiting featureless LDOS, in virtue of equation (4-15), would not be able to produce NDR. However, the electronic structure of the sharp $Pt_{0.8}$-

$Ir_{0.2}$ tip might exhibit sharp features in the LDOS at its apex in the proximity of the equilibrium Fermi level.[49-51] The presence of tip localized states does not appear in the I/V for the bare gold although one would expect at least a non-linear potential dependence. In fact, the coupling of the tip apex to gold is relatively strong and enlarges the resonance considerably, such that, over the potential range, it can be considered constant. Thus the integral of (4-12) is essentially equivalent to eV and the current is directly proportional to the applied voltage. On the other hand, in the presence of the DNA film and at a negative bias, the tip state is completely decoupled from the surface. The decoupling from the gold and the weak coupling with the DNA localized molecular orbital substantially increase the sharpness of the localized tip state and allows for the discrimination of the DNA LDOS.[33, 50]

This phenomenon of electronic states broadening and sharpening can also explain the bias dependence of the image contrast described in the previous section. In fact, when the potential is switched to a positive bias, the gold surface reappears as a consequence of the fact that the DNA is tilted. The DNA film is essentially transparent as now the tip has a large coupling with the gold surface and the localized tip state is broader, losing "resolution" for the DNA molecular orbitals. Evidence of this phenomenon is provided by the fact that the tip comes closer to the DNA film when the surface is biased negative and is farther away when the bias is positive (data not shown), i.e., the tip is closer when the DNA is standing up because the coupling is weaker, while the tip is farther up when the DNA is laying down because the tip has a strong coupling with the underlying surface (Figure 4-14).

As predicted by Xue et al.,[50] while the bias potential is scanned, the relative energies of tip and molecular states have to move according to the electrostatic potential within the junction in order to observer NDR.[50, 52] To what extent are the energy of DNA and tip states affected by the electrostatic potential in the junction? The situation we are modeling is illustrated in Figure 4-15. Although, the interfacial potential between the tip and the

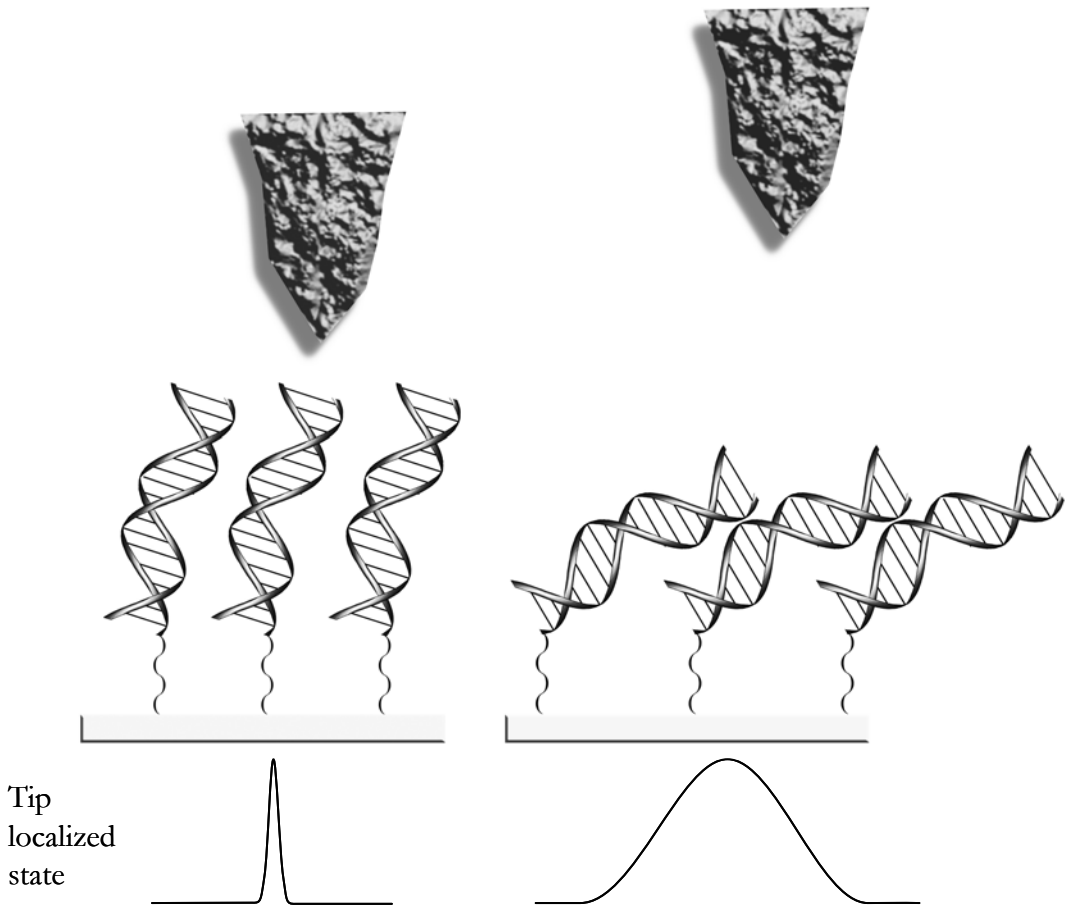

Figure 4-14: Schematic representation of the gold-DNA-tip tunneling junction. When the surface potential is negative and DNA is the upright position, the tip states are decoupled from the gold surface and sharp. The tip is then closer to the surface because of the weaker coupling with the DNA film. Conversely, when the surface potential is positive and the DNA is tilted, the tip states are now decoupled from the DNAs and only the underlying gold surface can be visualized. Also, the tip is farther away because of the stronger coupling with the surface. Moreover, the tip's localize state is now broader and loses "resolution" of the DNA states.

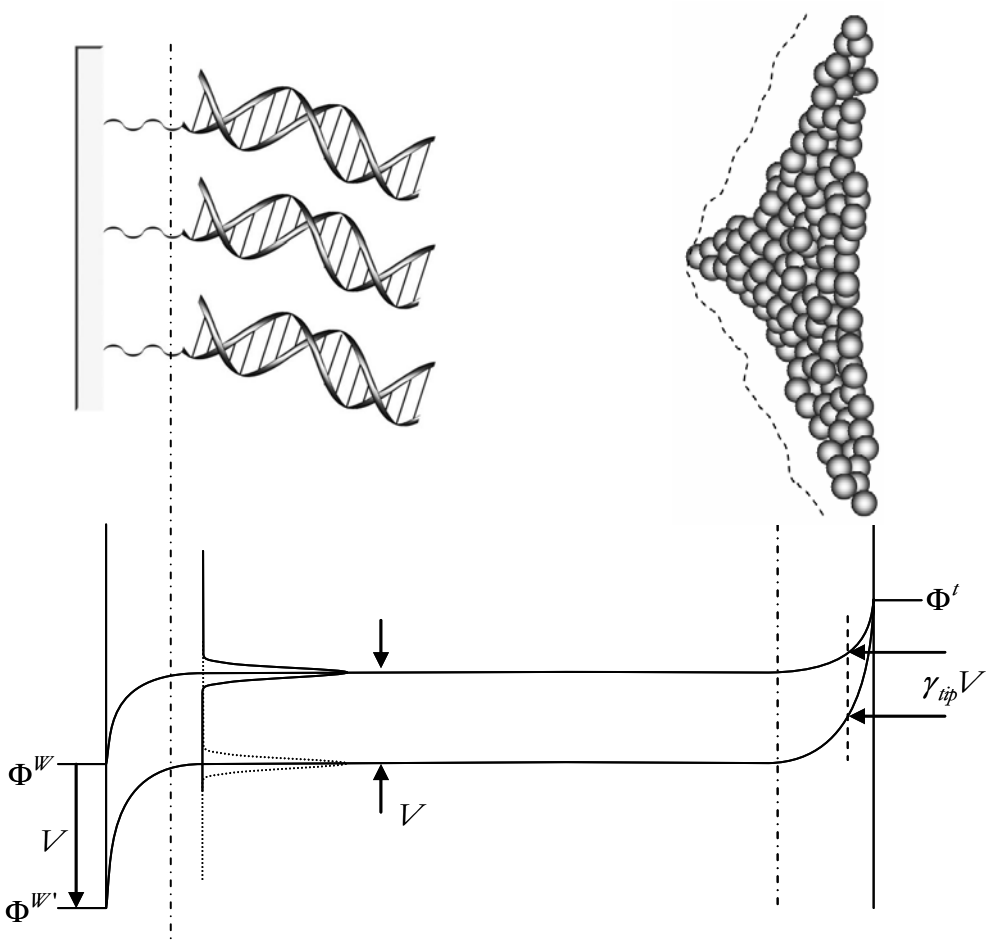

Figure 4-15: Schematic illustration of the potential distribution in the tunneling junction (not to scale). The DNA localized states is fully located beyond the double layer potential drop and its energy changes by the quantity eV. The tip state is partly extruding into the double layer and its energy, compared to the tip main body, changes by a fraction of eV. The long-dash-dot lines represent the end of the double layer, the dashed line on the tip side indicates the isopotential surface around the tip.

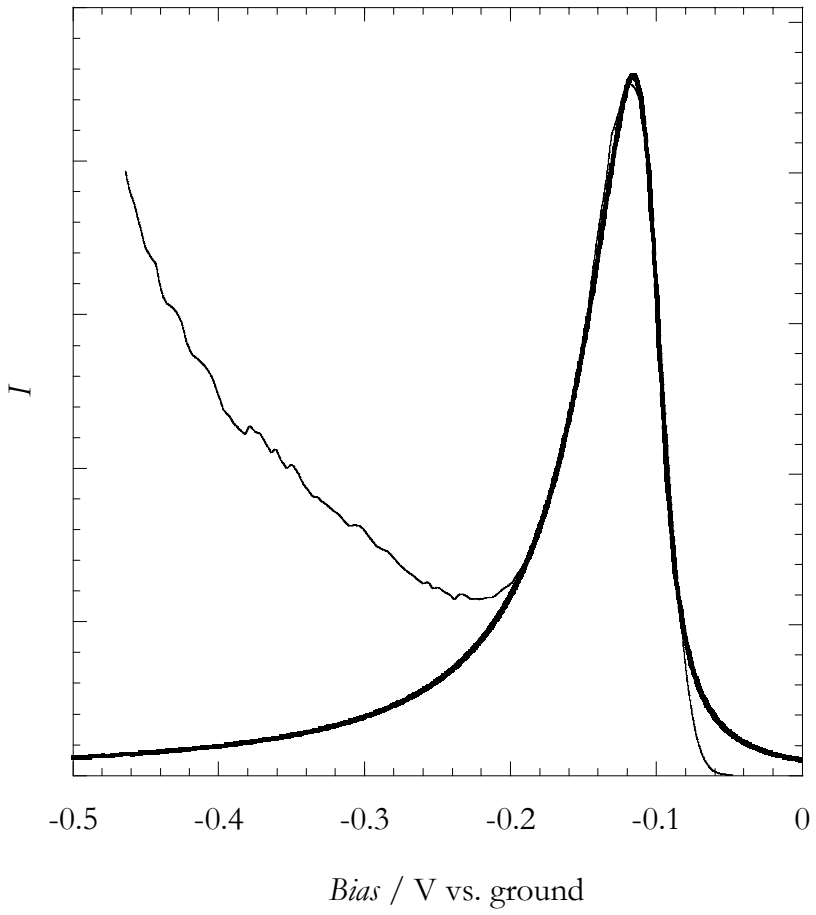

Figure 4-16: Simulated I/V curve (dark solid line) overlapped to the experimental I/V for a DNA film containing 100% PM on gold in buffer (see Figure 4-12). The simulation has been obtained (using equations (4-17), (4-18), and (4-19)) considering two localized states in the DNA film and on the tip apex. The DNA states are fully located within the junction potential with γ_{DNA}=1, while the tip is partly solvated with γ_{tip}=0.85. In the simulation we have used ε_r^0 = 0 V, ε_t^0 = -0.015 V, ω_{DNA}=0.41, ω_{tip}=0.14. The peak-like curve suggests the presence of an energetically localized energy band in the DNA in the proximity of the Fermi energy of the gold surface.

DNA film is controlled by the auxiliary and reference electrodes, locally the electrostatic potential between the film and the tip is not. In fact, while the solution potential in the bulk is kept constant by the auxiliary electrode, change of the gold electrode Fermi level affects the potential between tip and film. The situation is equivalent to having a microscopic electrochemical cell at the junction, where the gold electrode serves as an auxiliary and the tip potential is constant. Thus, the solution potential within the junction moves according to the applied bias. In the DNA film, the energetically localized state is fully located beyond the double layer potential drop. As the potential is scanned more negative, NDR occurs because DNA's LDOS is localized at an energy more positive than the tip's. As the potential is changed at the gold electrode, the DNA state moves from energies below to higher than the tip's state energy. The scanning of the DNA states across the tip states causes the differential effect. NDR would not be observable if the two states did not move with respect to each other.[50] Also the tip's state can be partly located in the junction potential; in fact, as the atoms that form the tip apex are protruding into the double layer generated by the main tip body, the localized state might be located somewhere in the potential drop of the double layer.

We have simulated this situation by modeling the localized states using the Lorentizian shapes expressed by equation (4-16), and solving equation (4-17),

$$\varphi(\varepsilon) = \frac{2}{\pi\theta_{DNA}k_BT}\frac{1}{4\left(\dfrac{\varepsilon-\varepsilon^r}{\theta_{DNA}k_BT}\right)^2+1} \qquad 4\text{-}18$$

and

$$\mu(\varepsilon) = \frac{2}{\pi\theta_{tip}k_BT}\frac{1}{4\left(\dfrac{\varepsilon-\varepsilon^t}{\theta_{tip}k_BT}\right)^2+1}, \qquad 4\text{-}19$$

where $\varepsilon^r = \varepsilon_0^r + eV\gamma_{DNA}$ and $\varepsilon^t = \varepsilon_F^t + eV\gamma_{tip}$ represents the energy of the localized states within the junction potential, γ_i are the potential fractions in the double layer, and θ_i are the widths of the respective localized states. For DNA γ_{DNA} we assumed that is equal to one. The simulated current using equations (4-17) , (4-18), and (4-19) is shown in Figure 4-16. It can be seen that the simulation overlaps well with the shape of the NDR of the tunneling current. Interestingly, the slight asymmetry of the peak is associated with the fact that the tip state is indeed partly located inside the double layer. If the state did not move as a function of the applied potential, the peak would be perfectly symmetric.

4.5 Conclusions

In summary, we have observed effective charge transport behavior of DNA films on gold surfaces under physiological conditions that depends sensitively on DNA orientation, probed by varying the bias potential, and the integrity of base pair stacking, probed by varying PM content. Importantly, intervening mismatches exert dramatic effects on the conductive properties of DNA, in agreement with electrochemical,[16] biochemical,[53] and photophysical[3] studies. These experiments render duplex DNA a promising candidate in molecular electronics, but only in arrangements where the orbitals can efficiently overlap with the electronic states of the electrodes and the environment does not constraint the DNA in non-native, poorly stacked conformations.

The determination of the DNA LDOS demonstrated the existence of an energetically localized state in proximity of the Fermi level of the gold surface. The I/V curves reconstructed from the potential-dependent tip displacement exhibit NDR, attributed to resonant tunneling between the DNA and tip's localized states. The DNA states appear to be fully located in the potential established within the junction, consistent with the idea that the double layer in DNA films occurs within the linker portion of the film. The tip's state is partly located inside the double layer potential drop and its potential varies with a fraction of the applied bias. The relative movement of the two energy states with respect to each other produces the differential effect observed in the tunneling current.

The demonstration of the existence of energetically localized states at low energy has several practical consequences. With these experimental results, we are now able to formulate a model that not only can describe electron transfer at DNA-modified surfaces but also ground state DNA-mediated electron transfer. The DNA bridge is indeed occupied at energies that are in close proximity to the Fermi energy of the gold electrode. This is consistent with the idea that the DNA bases may form energetically localized states

in the HOMO-LUMO gap upon stacking. The electronic structure is probably typical of an indirect band gap, where the optical gap is presumably unchanged. This can explain the peculiar optical features of the DNA molecule, such as hypochromism and exciton coupling. Moreover, when organized in highly dense films, the relatively rigid environment imposed by the tightness might facilitate the formation of extended well-coupled π-stacked domains, inducing an anisotropic (longitudinal, along the axis) conductivity. Most likely, in DNA films, this orbital is extended along the entire length of the short DNA duplexes, thus providing an efficient coupling over short (10 nm) distances. DNA molecules are able to conduct electrons, but they have to be well stacked and under physiological salt and pH conditions. Finally, the contact resistance plays an important role. Thiol-gold bonds possess fairly good orbital overlap and allow for direct access to the DNA π-stack. Moreover, the electronic coupling between DNA and tip orbitals shows how critical their relative orientations are, which is analogous to the observation that a well-stacked intercalator can only access the DNA π-stack if appropriately oriented.

4.6 Experimental Details

4.6.1 DNA Synthesis and Modification

5'-tethered oligonucleotides were prepared by first synthesizing the oligonucleotides via standard automated synthesis (trityl off) on high load (2.5 μmol) controlled pore glass (CPG) beads (Glen Research) under manual cleavage conditions. Post-synthetic modification was first performed at the 5'-end of the oligonucleotides initially in the solid phase via activation of the 5'-hydroxyl termini with carbonyldiimidazole (Sigma, 80 mg in 1 mL dioxane, 30-45 min) followed by 1,6-diamminohexane (Acros, 40 mg in 1 mL dioxane, 20-25 min). The amine-modified oligonucleotides were cleaved from the CPG beads and deprotected in concentrated ammonium hydroxide (J. T. Becker) for 8-12 hours at 60 °C and then treated with 2-pyridyldithiopropionic acid N-succinimide ester (Sigma, 45 min) to produce a disulfide linker. Subsequently, the sequences were purified by HPLC (semi-preparation reverse phase C18 columns), converted to free thiol with dithiothreitol (ICN, 0.4-1 M, 40-60 min), and HPLC repurified again.

The unmodified complements were synthesized by standard automated synthesis (trytil on) on a 1 μmol CPG glass under either manual or automatic cleavage. The oligonucleotides were HPLC purified, deprotected from the trytil in acetic acid (80%, 14-20 min) and repurified again in order to yield highly pure oligonucleotides. Prior to hybridization, both strands, thiol-modified and unmodified oligonucleotides, were carefully desalted by precipitation in pure ethanol. The sequence used in this work was HS - 5'-AGT ACT GCA GTA GCG- 3' hybridized to the respective perfect matching complement or a mismatched strand containing a T paired to the G in the seventh position (underlined) to form a perfect match (PM) duplex or a mismatch (MM) duplex, respectively.

4.6.2 Sample Preparation

The thiol-terminated duplexes containing different percentages of PM and MM duplexes (vide infra), for a total amount of 100 μM duplex (5 mM sodium phosphate buffer, pH 7.4, 100 mM $MgCl_2$), were deposited on substrates of gold on mica (Molecular Imaging) and let to self assemble for 12-24 hours at room temperature in a humid environment in order to avoid evaporation. Prior to each experiment, the DNA-modified surfaces were thoroughly rinsed with 10 mM Tris buffer (in Milli-Q water and filtered with 0.22 μm cellulose acetate filter, pH 7), in order to remove any excess of magnesium ion and non-specifically bound oligonucleotides. The electrochemical cell utilized for the *in situ* STM experiments contained a platinum wire (auxiliary electrode) and a silver wire (quasi-reference electrode, QRE). The electrical contact from the gold surface to the STM base was made with a silver paste outside the fluid cell. The potential of the tip and the substrate were controlled with a bipotentiostat (Nanoscope III, Digital Instrument, Veeco, Santa Barbara, CA) with respect to the QRE. The bias potential is referred as the potential of the substrate vs. ground, as the tip is grounded and interfacial potentials of the surface and tip are constantly kept at 0 V vs. QRE.

4.6.3 Apparatus and Measurements

In order to reduce faradic currents, $Pt_{0.8}Ir_{0.2}$ tips (Molecular Imaging) were insulated with melted Apiezon wax following the procedure described by Linsay and co-workers,[54] with the only exception that the stage temperature was kept constant (about 132°C) using a temperature controller. Prior to imaging, each tip was tested in solution (10mM Tris buffer, pH 7) by measuring the background current using the STM controller (Nanoscope III, Digital Instrument, with bipotentiostat base EC-STM) in the electrochemical mode. Each tip presented a background current lower than the actual instrument sensitivity (about 30 pA, from Johnson noise). The entire *in situ* STM investigation presented here has been

carried in the constant current mode, in solution (10 mM Tris, pH 7), at room temperature, and with a setpoint current of 50 pA, unless otherwise specified. The bias potential was always kept in the window ±600 mV in order to prevent damage to the DNA film by thiol desorption or water electrolysis.

Recording of the tip displacement as a function of the applied bias was obtained by positioning the tip in a fixed *x-y* position over a DNA cluster with a current setpoint of 30 pA. The potential bias was applied using an external wave generator (Agilent) via the NanoScope Signal Access Module (Veeco). The triangular potential wave and the apparent scan frequencies were adjusted in order to have a full potential cycle per each sampling line. The bias frequency (1 Hz) did not exceed the time response of the piezoelectric element. The image respresenting the sampling line vs. the applied potential was recorded with the maximum resolution of 512 lines. Subsequently, the image was treated using the scanning probe microscopy software WSxM (Nanotec Electronica S. L.) by taking the average of all 512 lines. The theoretical model of the tunneling current via localized states was done by numerical calculation using a personal computer running Maple 9.5 (Waterloo Maple) and then plotted with KaleidaGraph 3.5 (Synergy Software).

4.7 Appendix

4.7.1 In Situ STM Characterization of Gold Surfaces

The gold substrates used in these experiments have been characterized *in situ* in order to determine the morphology of the gold surfaces prior to self-assembly. The purchased gold is lightly flame annealed and individually stored under nitrogen by the manufacturer. We found that the gold surfaces were essentially flat and generally exhibited the characteristic 60° angle features of the plane (111) (Figure 4-16) and we opted not to further flame anneal them.

Investigation of the gold etching process (Figure 4-17) was carried out in 0.02 M sulfuric acid in order to determine the state of the surface. We found that the gold surface undergoes severe reconstruction resulting in clear loss of smoothness as well as structural order (loss of the (111) edge planes) probably leading to a more homogeneous distribution of low index planes, (110) and (100). It is clear from the images that the major consequence of the etching is desorption of atomic layers. This result reinforces what is already known about electrochemical etching of gold electrode.

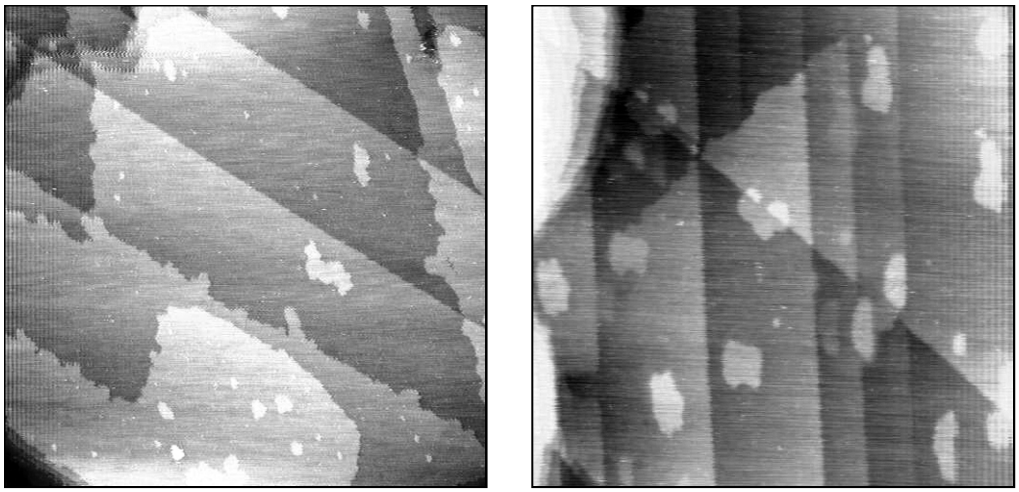

Figure 4-17: *In situ* STM images of a gold surface used for self-assembling the DNA films. It is possible to distinguish the atomic planes; the 60º angle of the gold planes is indicative of highly oriented gold surface, mainly (111). Conditions: 10 mM Tris-HCl, pH 7.0, current setpoint 100 pA, tip potential 0 V vs. QRE, scan size 500 nm.

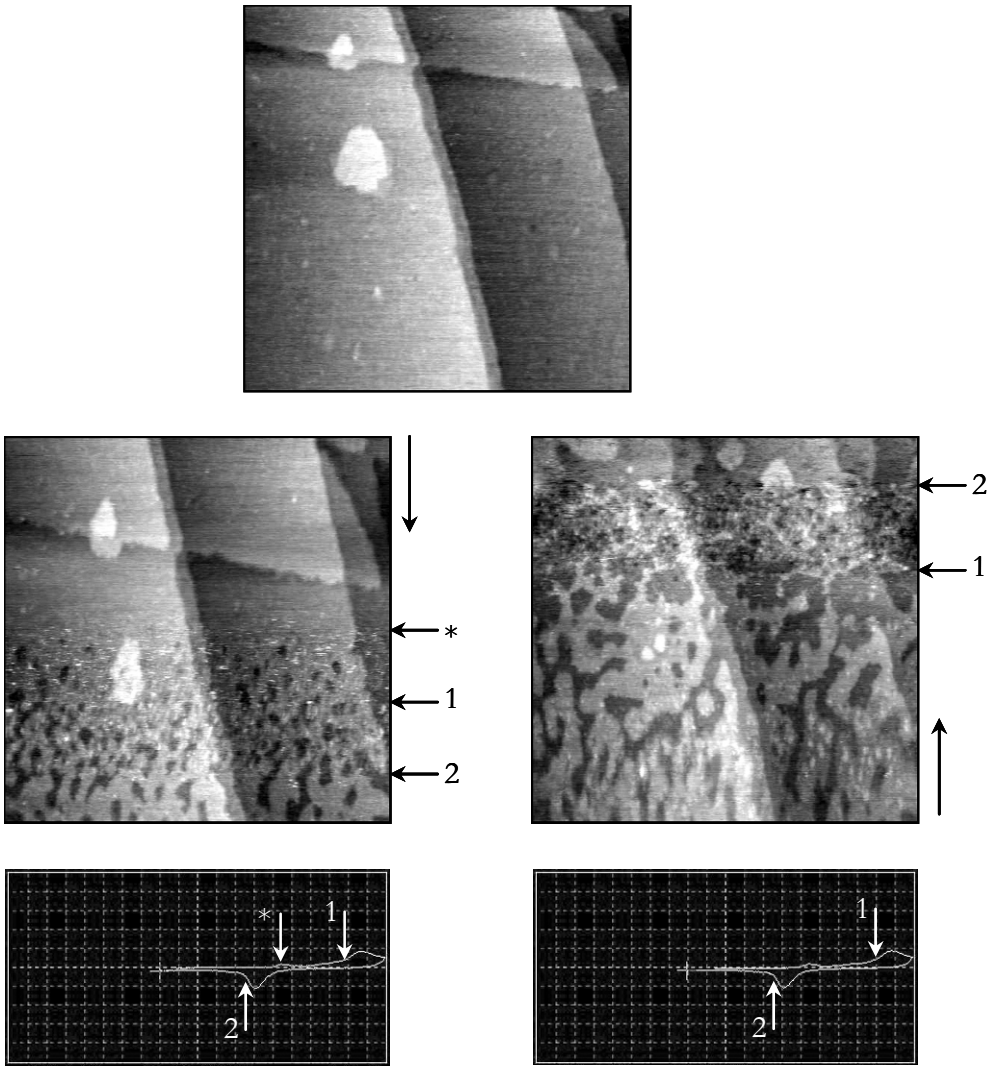

Figure 4-18: *In situ* STM images of three subsequent electrochemical etching of gold in 0.02 M H_2SO_4. The arrows indicate the corresponding region in the CV and images. During electrochemical etching the surface becomes rougher by losing atomic layers. Conditions: same as in Figure 3-16, scan rate 5.09 Hz, ramp rate 34 mV/s, scan size 200 nm.

4.8 References

1. Kelley, S. O.; Barton, J. K., Electron transfer between bases in double helical DNA. *Science* **1999,** 283, (5400), 375-381.
2. Kelley, S. O.; Boon, E. M.; Barton, J. K.; Jackson, N. M.; Hill, M. G., Single-base mismatch detection based on charge transduction through DNA. *Nucleic Acids Research* **1999,** 27, (24), 4830-4837.
3. Kelley, S. O.; Holmlin, R. E.; Stemp, E. D. A.; Barton, J. K., Photoinduced electron transfer in ethidium-modified DNA duplexes: Dependence on distance and base stacking. *Journal of the American Chemical Society* **1997,** 119, (41), 9861-9870.
4. O'Neill, M. A.; Barton, J. K., DNA-mediated charge transport chemistry and biology. In *Long-Range Charge Transfer in DNA I*, 2004; vol. 236, pp 67-115.
5. O'Neill, M. A.; Barton, J. K., DNA charge transport: Conformationally gated hopping through stacked domains. *Journal of the American Chemical Society* **2004,** 126, (37), 11471-11483.
6. Stinner, C.; Wightman, M. D.; Kelley, S. O.; Hill, M. G.; Barton, J. K., Synthesis and spectroelectrochemistry of Ir(bpy)(phen)(phi)(3+), a tris(heteroleptic) metallointercalator. *Inorganic Chemistry* **2001,** 40, (20), 5245-5250.
7. Holmlin, R. E.; Dandliker, P. J.; Barton, J. K., Charge transfer through the DNA base stack. *Angewandte Chemie-International Edition* **1997,** 36, (24), 2715-2730.
8. Das, P.; Schuster, G. B., Effect of condensate formation on long-distance radical cation migration in DNA. *Proceedings of the National Academy of Sciences of the United States of America* **2005,** 102, (40), 14227-14231.
9. Meggers, E.; Michel-Beyerle, M. E.; Giese, B., Sequence dependent long range hole transport in DNA. *Journal of the American Chemical Society* **1998,** 120, (49), 12950-12955.

10. Eley, D. D.; Spivey, D. I., Semiconductivity of Organic Substances .9. Nucleic Acid in Dry State. *Transactions of the Faraday Society* **1962,** 58, (470), 411-&.

11. Shao, F. W.; O'Neill, M. A.; Barton, J. K., Long-range oxidative damage to cytosines in duplex DNA. *Proceedings of the National Academy of Sciences of the United States of America* **2004,** 101, (52), 17914-17919.

12. Shao, F. W.; Augustyn, K.; Barton, J. K., Sequence dependence of charge transport through DNA domains. *Journal of the American Chemical Society* **2005,** 127, (49), 17445-17452.

13. Crespo-Hernandez, C. E.; Cohen, B.; Kohler, B., Base stacking controls excited-state dynamics in A-T DNA. *Nature* **2005,** 436, (7054), 1141-1144.

14. Boon, E.; Barton, J.; Hill, M., Electrochemical detection of single-base mismatches by electrocatalysis at DNA-modified electrodes. *Clinical Chemistry* **1998,** 44, (11), 2388-2388.

15. Boon, E. M.; Barton, J. K.; Bhagat, V.; Nersissian, M.; Wang, W.; Hill, M. G., Reduction of ferricyanide by methylene blue at a DNA-modified rotating-disk electrode. *Langmuir* **2003,** 19, (22), 9255-9259.

16. Boon, E. M.; Ceres, D. M.; Drummond, T. G.; Hill, M. G.; Barton, J. K., Mutation detection by electrocatalysis at DNA-modified electrodes. *Nature Biotechnology* **2000,** 18, (10), 1096-1100.

17. Kelley, S. O.; Barton, J. K.; Jackson, N. M.; Hill, M. G., Electrochemistry of methylene blue bound to a DNA-modified electrode. *Bioconjugate Chemistry* **1997,** 8, (1), 31-37.

18. Kelley, S. O.; Jackson, N. M.; Hill, M. G.; Barton, J. K., Long-range electron transfer through DNA films. *Angewandte Chemie-International Edition* **1999,** 38, (7), 941-945.

19. Steenken, S.; Jovanovic, S. V., How easily oxidizable is DNA? One-electron reduction potentials of adenosine and guanosine radicals in aqueous solution. *Journal of the American Chemical Society* **1997,** 119, (3), 617-618.

20. Binning, G.; Rohrer, H.; Gerber, C.; Weibel, E., Surface Studies by Scanning Tunneling Microscopy. *Physical Review Letters* **1982,** 49, (1), 57-61.

21. Ikai, A., STM and AFM of bio/organic molecules and structures. *Surface Science Reports* **1996,** 26, (8), 263-332.

22. Losic, D.; Shapter, J. G.; Gooding, J. J., Scanning tunneling microscopy studies of glucose oxidase on gold surfaces. *Langmuir* **2002,** 18, (14), 5422-5428.

23. Patel, N.; Davies, M. C.; Heaton, R. J.; Roberts, C. J.; Tendler, S. J. B.; Williams, P. M., A scanning probe microscopy study of the physisorption and chemisorption of protein molecules onto carboxylate terminated self-assembled monolayers. *Applied Physics a-Materials Science & Processing* **1998,** 66, S569-S574.

24. Roberts, C. J.; Williams, P. M.; Davies, M. C.; Jackson, D. E.; Tendler, S. J. B., Atomic-Force Microscopy and Scanning-Tunneling-Microscopy: Refining Techniques for Studying Biomolecules. *Trends in Biotechnology* **1994,** 12, (4), 127-132.

25. Chen, C. J., *Introduction to Scanning Tunneling Microscopy*: Oxford University Press, 1993.

26. Bardeen, J., Tunnelling from a Many-Particle Point of View. *Physical Review Letters* **1961,** 6, (2), 57.

27. Giaever, I., Electron Tunneling between 2 Superconductors. *Physical Review Letters* **1960,** 5, (10), 464-466.

28. Nicol, J.; Shapiro, S.; Smith, P. H., Direct Measurement of the Superconducting Energy Gap. *Physical Review Letters* **1960,** 5, (10), 461-464.

29. Tersoff, J.; Hamann, D. R., Theory and Application for the Scanning Tunneling Microscope. *Physical Review Letters* **1983,** 50, (25), 1998-2001.

30. Tersoff, J.; Hamann, D. R., Theory of the Scanning Tunneling Microscope. *Physical Review B* **1985,** 31, (2), 805-813.

31. Hahn, J. R.; Hong, Y. A.; Kang, H., Electron tunneling across an interfacial water layer inside an STM junction: tunneling distance, barrier height and water polarization effect. *Applied Physics A: Materials Science and Processing* **1998,** 66, S467-S472.

32. Pan, J.; Jing, T. W.; Lindsay, S. M., Tunneling Barriers in Electrochemical Scanning-Tunneling-Microscopy. *Journal of Physical Chemistry* **1994,** 98, (16), 4205-4208.

33. Sautet, P., Images of adsorbates with the scanning tunneling microscope: Theoretical approaches to the contrast mechanism. *Chemical Reviews* **1997,** 97, (4), 1097-1116.

34. Kasumov, A. Y.; Kociak, M.; Gueron, S.; Reulet, B.; Volkov, V. T.; Klinov, D. V.; Bouchiat, H., Proximity-induced superconductivity in DNA. *Science* **2001,** 291, (5502), 280-282.

35. Fink, H. W.; Schonenberger, C., Electrical conduction through DNA molecules. *Nature* **1999,** 398, (6726), 407-410.

36. Porath, D.; Bezryadin, A.; de Vries, S.; Dekker, C., Direct measurement of electrical transport through DNA molecules. *Nature* **2000,** 403, (6770), 635-638.

37. Lang, N. D.; Avouris, P., Effects of coadsorption on the conductance of molecular wires. *Nano Letters* **2002,** 2, (10), 1047-1050.

38. Seminario, J. M.; Zacarias, A. G.; Tour, J. M., Theoretical study of a molecular resonant tunneling diode. *Journal of the American Chemical Society* **2000,** 122, (13), 3015-3020.

39. Kelley, S. O.; Barton, J. K.; Jackson, N. M.; McPherson, L. D.; Potter, A. B.; Spain, E. M.; Allen, M. J.; Hill, M. G., Orienting DNA helices on gold using applied electric fields. *Langmuir* **1998,** 14, (24), 6781-6784.

40. Koltover, I.; Wagner, K.; Safinya, C. R., DNA condensation in two dimensions. *Proceedings of the National Academy of Sciences of the United States of America* **2000,** 97, (26), 14046-14051.

41. Rau, D. C.; Parsegian, V. A., Direct Measurement of the Intermolecular Forces between Counterion-Condensed DNA Double Helices: Evidence for Long-Range Attractive Hydration Forces. *Biophysical Journal* **1992,** 61, (1), 246-259.

42. Patole, S. N.; Pike, A. R.; Connolly, B. A.; Horrocks, B. R.; Houlton, A., STM study of DNA films synthesized on Si(111) surfaces. *Langmuir* **2003,** 19, (13), 5457-5463.

43. Zhang, Z. L.; Pang, D. W.; Zhang, R. Y.; Yan, J. W.; Mao, B. W.; Qi, Y. P., Investigation of DNA orientation on gold by EC-STM. *Bioconjugate Chemistry* **2002,** 13, (1), 104-109.

44. Li, B.; Zeng, C. G.; Li, Q. X.; Wang, B.; Yuan, L. F.; Wang, H. Q.; Yang, J. L.; Hou, J. G.; Zhu, Q. S., First-principles simulation of scanning tunneling microscopy images of individual molecules in alkanethiol self-assembled monolayers on Au(111). *Journal of Physical Chemistry B* **2003,** 107, (4), 972-984.

45. Chen, J., Large on-off ratios and negative differential resistance in a molecular electronic device. *Science* **1999,** 286, (5444), 1550-1552.

46. Guisinger, N. P., Room temperature negative differential resistance through individual organic molecules on silicon surfaces. *Nano letters* **2004,** 4, (1), 55-59.

47. Grobis, M.; Wachowiak, A.; Yamachika, R.; Crommie, M. F., Tuning negative differential resistance in a molecular film. *Applied Physics Letters* **2005,** 86, (20).

48. Zeng, C. G., Negative differential-resistance device involving two C-60 molecules. *Applied physics letters* **2000,** 77, (22), 3595-3597.

49. Lyo, I. W.; Avouris, P., Negative Differential Resistance on the Atomic Scale: Implications for Atomic Scale Devices. *Science* **1989,** 245, (4924), 1369-1371.

50. Xue, Y. Q.; Datta, S.; Hong, S.; Reifenberger, R.; Henderson, J. I.; Kubiak, C. P., Negative differential resistance in the scanning-tunneling spectroscopy of organic molecules. *Physical Review B* **1999,** 59, (12), R7852-R7855.

51. Yeyati, A. L., Conductance quantization and electron resonances in sharp tips and atomic-size contacts. *Physical review. B, Condensed matter* **1997,** 56, (16), 10369-10372.

52. Fan, F. R. F.; Lai, R. Y.; Cornil, J.; Karzazi, Y.; Bredas, J. L.; Cai, L. T.; Cheng, L.; Yao, Y. X.; Price, D. W.; Dirk, S. M.; Tour, J. M.; Bard, A. J., Electrons are transported through phenylene-ethynylene oligomer monolayers via localized molecular orbitals. *Journal of the American Chemical Society* **2004,** 126, (8), 2568-2573.

53. Bhattacharya, P. K.; Barton, J. K., Influence of intervening mismatches on long-range guanine oxidation in DNA duplexes. *Journal of the American Chemical Society* **2001,** 123, (36), 8649-8656.

54. Nagahara, L. A.; Thundat, T.; Lindsay, S. M., Preparation and Characterization of Stm Tips for Electrochemical Studies. *Review of Scientific Instruments* **1989,** 60, (10), 3128-3130.

Appendix ELECTROCHEMICAL TECHNIQUES FOR KINETICS ANALYSIS AT MODIFIED SURFACES

A.1 Introduction

In this chapter, we will review and implement the electrochemical techniques that are useful for analyzing kinetic processes at modified surfaces. A comprehensive understanding of the underlying physics of the electrode/electrolyte interface is very important in order to explain, predict, and apply electrochemistry at chemically modified electrodes. In particular, DNA films are extremely useful for diagnostic applications as well as a platform for shedding light on fundamental biophysical processes involving electron transfer. Owing to their high charge, DNA-films are very complex with interfacial properties dramatically different from simple films like alkane-thiols. Moreover, because the biologically relevant electron transfer occurs inside the DNA, in the π-stack, only a limited number of probes (intercalators) can be used to investigate this property. Because of this complexity, before entering the details of DNA-mediated electron transfer on surfaces, we need to develop tools that can help us decipher experimental data.

We will start by introducing the principles of the charged interface and the thermodynamic concepts that govern the interaction between redox species in an electrolyte and a metallic surface. Subsequently, we will introduce three fundamental electrochemical techniques that are indispensable for an accurate analysis of any surface process. In particular, we will emphasize how to obtain kinetics and thermodynamics information from each technique.

A.2 Physics of the Charged Interface

An understanding of metal/electrolyte junctions requires the consideration of some fundamental principles from physics. When two charged metallic parallel plates are placed in the vacuum, the electrostatic potential profile between them is linear (Figure A-1A). The electric field, defined as the space derivative of the potential, is therefore simply $\Delta\Phi/d$ where $\Delta\Phi$ is the potential difference and d the distance between the plates. In general, when a neutral molecule is placed between the two plates the electric field tends to polarize the orbitals by reorienting them, and, in extremely strong electric fields (10^6-10^9 V/cm), the molecule can even be ionized, losing an electron.

When the metallic electrodes are now placed in an electrolyte solution (Figure A-1B), ions redistribute in proximity of the surfaces because the electrostatic potentials of the solution and electrodes are different. As in the extended Debye-Huckel model for hydrated radii of ions,[1, 2] the solvation shell is limited to the immediate surroundings where solvent and ions are polarized and reorganized to produce an electric field of opposite direction and equal intensity, to an extent that depends on the dielectric of the solvent. For a metal/ electrolyte interface, ions and solvent polarize in the same fashion as the electrode can be considered like an ion of infinite radius. The potential profile now is completely different from that in vacuum, as the polarization of the solvent and ionic drift shield completely the electric field. Thus, in the bulk of the solution, the electric field is null, i.e., the potential is constant and ions do not "feel" the presence of the electrodes. Because the potential of the electrodes does not appreciably change and in virtue of the potential continuity, at the electrode/solution interface the potential experiences a very strong gradient, which depends greatly on the ionic strength and dielectric of the electrolyte as well as its composition. Consequently, as predicted by the extended Debye-Hückel theory, the potential fall-off at the interface is faster at higher ionic strengths.

The interface between electrode and electrolyte is also called the electrical double layer because Helmholtz[3, 4] first had recognized that it behaves like a capacitor, where charges of opposite sign are accumulated on two close parallel planes. The so-called Helmholtz layer is composed of two layers. The inner plane contains molecules said to be specifically adsorbed or contact adsorbed, whereas the outer plane contains solvated molecules or ions. Away from the surface, the ionic distribution decays following a Boltzmann distribution. Because the majority of the potential drop $\Delta\Phi$ occurs essentially within the outer Helmholtz layer (less than 1 nm), the entire potential difference between the two electrodes occurs at the charged interface. It is in this region of high electric field ($\sim 10^6$ V/cm) that *all* electrochemical reactions take place. In an electrochemical setup, the two electrodes are called working (*W*) and auxiliary (*A*). The working electrode is the one at which electrochemical reactions are occurring and monitored.

Although we are only interested in the interfacial potential at the working electrode, it is not possible to measure it directly. However, a relative measurement can be achieved using a second electrode, a reference electrode (*R*), whose interfacial potential, $\Delta\Phi^R$, is known to be always constant. Thus, $\Delta\Phi^W$ can only be expressed relative to $\Delta\Phi^R$ by measuring the reference potential, Φ^R, with respect to the potential of the working electrode, Φ^W,

$$\Delta\Phi^W = \Delta^W\Phi^R + \Delta\Phi^R = \Phi^R + \Delta\Phi^R, \qquad \text{A-1}$$

where the potential difference between the working and reference electrodes, $\Delta^W\Phi^R$, is equivalent to the Φ^R, as the working electrode is usually connected to the same ground. When the potential at the auxiliary electrode, Φ^A, is moved, the interfacial potential $\Delta\Phi^W$ varies in order to satisfy the charge balance described earlier. Because the interfacial

potential drop at the auxiliary electrode, $\Delta\Phi^{A}$, is *not* always constant (although it should be constant over time for a given potential), the change of $\Delta\Phi^{W}$ is not linear with Φ^{A}. This is especially true when a reaction (reduction or oxidation) occurs at the working electrode and the charge balance at the interface is transiently altered. Thus, in order to vary the interfacial potential at the working electrode in a controlled manner, the bulk potential must be constantly measured using the reference electrode and adjusted accordingly with a feedback loop by varying Φ^{A}. It is clear that a fast feedback control is then very important in all electrochemical experiments. Due to the finite resistivity of the electrolyte solution, the passage of a current might generate a potential gradient in the cell and the potential measured at the reference electrode is not exactly the potential at the working electrode. In fact, because the physical separation between the reference and working electrodes the actual control potential (ACP) at the reference electrode differs from that of the desired control potential (DCP) at the interface of the working electrode by the quantity iR_S, where R_S is the (uncompensated) solution resistance (Figure A-1C).

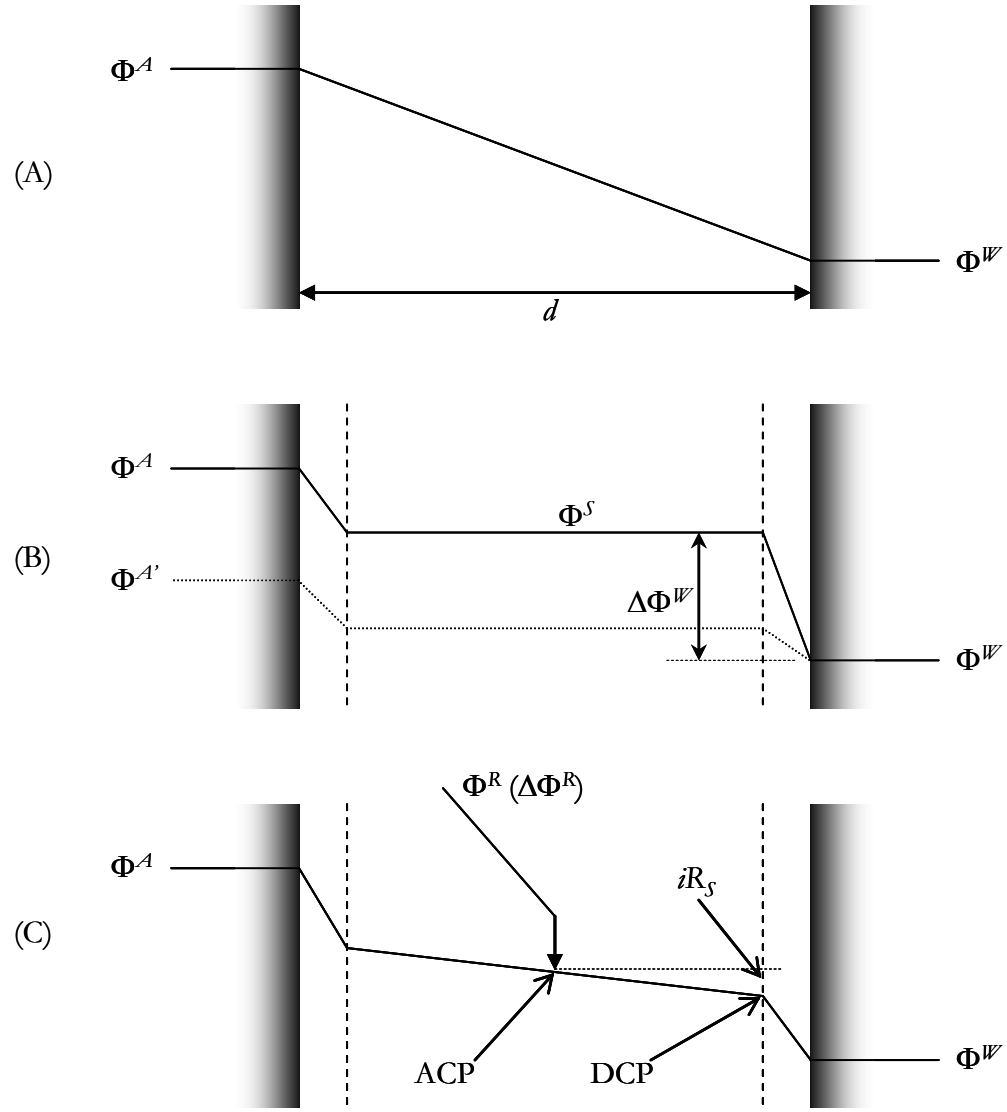

Figure A-1: Schematic representation of the potential gradients (A) in vacuum, (B) in an electrolyte, and (C) in a three-electrode cell for $i \neq 0$. Φ^A, Φ^R, and Φ^W are the auxiliary, reference, and working electrodes potentials, respectively. ACP and DCP are the actual and desired control potentials, respectively. In (B), when the potential at the auxiliary electrode is moved to $\Phi^{A'}$, the solution potential shifts accordingly, changing the interfacial potential at the working electrode. In (C), an electrochemical reaction at the working electrode induces a current to cross the cell. Owing to a finite solution resistance R_S, a potential gradient is built in the cell and as the reference and working electrodes are separated, the solution potentials at ACP and DCP are different by a quantity iR_S.

A.3 Nernst Equation and Electrochemical Reversibility

Let us consider a reversible reaction at the working electrode:

$$O + ne \underset{k_-}{\overset{k_+}{\rightleftharpoons}} R \qquad \text{A-2}$$

When the solution phase containing a redox species is brought in contact with the metallic electrode, equilibrium is established. In order to understand how this occurs we have to remember that molecules in the proximity of the electrode surface are experiencing a strong electric field due to the initial interfacial potential difference $\Delta\Phi^{W}$. As reaction (A-2) is reversible, it will reach equilibrium when the Fermi level of the electrode matches the one of the solution, as for many physical equilibria.

The Fermi level of a solution phase is determined by its electron affinity, which, in terms of electrochemical potentials, is the electrochemical potential of the electron in that phase.[5, 6] Let us first introduce some fundamental definitions of thermodynamics. The electrochemical potential of a phase is defined as the chemical potential plus a term that describes the electrostatic potential if the redox species is charged:

$$\overline{\mu}_i = \mu_i + z_i F\Phi^{S}, \qquad \text{A-3}$$

where z_i is the total charge of molecule i, and Φ^{S} is the electrostatic potential of the solution. The chemical potential is defined as

$$\mu_i = \mu_i^0 + RT\ln(a_i), \tag{A-4}$$

where μ_i^0 is the standard chemical potential and a_i is the activity of the species *i*.

The Fermi energy of a solution containing a redox species, ε_F^S, is simply the electrochemical potential of the electron and can be expressed as

$$\varepsilon_F^S = \overline{\mu}_e^S = \overline{\mu}_R - \overline{\mu}_O, \tag{A-5}$$

In a similar way, we can express the Fermi level of a metallic surface as the electrochemical potential of the electrons,

$$\varepsilon_F^{Au} = \overline{\mu}_e^{Au} = \mu_e^0 - nF\Phi^{Au}, \tag{A-6}$$

where we have assumed the affinity of an electron to be one. By subtracting (A-5) from (A-6), we obtain the following important non-equilibrium relation for a reversible reaction,

$$\begin{aligned} \varepsilon_F^S - \varepsilon_F^W &= \mu_R^0 - \mu_O^0 - \mu_e^0 + nF(\Phi^{Au} - \Phi^S) + RT\ln(R/O) \\ \varepsilon_F^S - \varepsilon_F^W &= \Delta G^0 + nF\Delta\Phi^W + RT\ln(R/O), \end{aligned} \tag{A-7}$$

where, here, we have identified the activity of the species with their concentrations in the bulk and set $\Delta G^0 = G^0_{products} - G^0_{reactants}$, where $G^0_i = \sum \mu^0_i$. By substituting $E^0 = -\Delta G^0 / nF$ and $E = \Delta\Phi^W$ into (A-7) we obtain

$$\frac{1}{nF}\left(\varepsilon_F^S - \varepsilon_F^W\right) = E - E^0 - \frac{RT}{nF}\ln(O/R), \qquad \text{A-8}$$

which is only valid before the system evolves towards equilibrium.

Let us consider the equilibrium case of (A-8). When the system is set at equilibrium, $E=E_{eq}$, and both Fermi energies are equal the interfacial potential will be determined by the standard free energy change of the redox system and the relative concentrations:

$$E_{eq} = E^0 + \frac{RT}{nF}\ln(O/R), \qquad \text{A-9}$$

This is the well-known Nernst equation, which describes any system that is thermodynamically or electrochemically reversible (or Nernstian). Equation (A-9) states that the interfacial potential is determined by the relative concentrations of *O* and *R*, and, inversely, the concentrations can be changed by applying a controlled potential, as described earlier. However, the Nernst equation is valid only when the system is at equilibrium and no current is observed at the working electrode surface. Consequently, because most electrochemical techniques (chronoamperometry, chronocoulometry, cyclic voltammetry, etc.) bring the system away from equilibrium, the Nernst equation cannot

describe the change in relative concentrations, unless the rate of electron transfer is extremely fast and equilibrium is reestablished quickly at the surface.

If now we establish equilibrium at the formal potential of the redox couple, by setting $E_{eq}=E^0$, the ratio O/R will be equal to one. In this case, when we step the potential E away from the equilibrium by a quantity η, we can rewrite A-8 as

$$\varepsilon_F^S - \varepsilon_F^W = nF\left(E - E^0\right) = e\eta, \qquad \text{A-10}$$

where η is called the overpotential ($e\eta$ has unit of eV).

Equation (A-10) is an important relationship that correlates the Fermi level difference with the electrochemical potentials just before the system moves towards equilibrium. The evolution of the system afterwards is only dependent on the rate, which is, as we shall see later, a function of the overpotential. We shall see later how experimentally we can deal with this case. It is possible to realize, comparing the situations leading to (A-8) and (A-10), that the two solution Fermi energies are different by the quantity $\ln[O/R]$, which has been determined by the initial equilibrium conditions.

A.4 Electrochemical Techniques for Kinetics Analysis

Now that we have established the conditions of equilibrium just after a perturbation is applied, let us describe the current that one can observe at the working electrode as a function of time when a reaction described in (A-2) takes place. It is clear, from (A-9) and (A-10) that the equilibrium after the perturbation is reestablished by the change of the relative concentrations. The current is then governed by Faraday's law,[7, 8] which states that the amount of chemical reaction is proportional to the amount of charge passed. The differential equation describing the time evolution towards equilibrium is

$$\frac{d\theta_O}{dt} = -\frac{d\theta_R}{dt} = -k_+\theta_O + k_-\theta_R, \qquad \text{A-11}$$

where $\theta_i = \Gamma_i/(\Gamma_O + \Gamma_R)$ represent the fractional coverages and Γ_i is the actual surface coverage of species *i*, and k_+ and k_- are the forward and the back heterogeneous formal rate constants, respectively. It is important now to realize that the steady state condition $d\theta_i/dt = 0$ is equivalent to the equilibrium condition $\varepsilon_F^S = \varepsilon_F^W$.

The net current measured at the electrode is simply the sum of the forward current and the back current

$$i = -FA\Gamma_T \frac{d\theta_O(t)}{dt} = FA\Gamma_T\left(k_+\theta_O(t) - k_-\theta_R(t)\right), \qquad \text{A-12}$$

where Γ_T is the total surface coverage. In (A-12) we have made the assumption that n=1. For n>1, the analytical expression of the faradaic current becomes more complicated and

depends on the nature of the surface reaction and whether or not it is coupled to subsequent chemical reactions in solution. For the rest of the chapter, we will consider a simple one-electron reaction.

The analytical expression of the current is obtained by solving (A-12), with $\theta_R = 1 - \theta_O$. For each applied overpotential, the transient currents are of the form

$$i(t) = FA\Gamma_T e^{-(k_+ + k_-)t}\left(\theta_O^0(k_+ + k_-) - k_-\right), \qquad \text{A-13}$$

where θ_O^0 is the initial condition for *O*. A plot of the ln[*i*(*t*)] vs. *t* will provide a direct measurement of the rate constant $(k_+ + k_-)$ of the reaction at that overpotential.

The electron-transfer rate constant is clearly potential dependent. In fact, like for homogeneous reactions, an energy barrier has to be overcome. For an electrode reaction, it is possible to modulate this activation energy by modulating the interfacial potential. Arrhenius[9] found an empirical form of the rate as a function of the energy barrier $\Delta G^{\ddagger}$, and it is described by

$$k \propto e^{-\Delta G^{\ddagger}/RT}. \qquad \text{A-14}$$

From the Nernst equation (A-8), we have found that if the applied potential E_{eq} is equal to the standard potential E^0 equilibrium is reached when the quotient is equal to one. The reason for this equilibrium is that the rate of forward and back electron transfer are equal, which can be readily seen in (A-14) in the case of equal energy barriers for forward and back electron transfer. If from this equilibrium condition we change the applied

potential by η, both the driving force and the energy barriers will also change by the same quantity. We can now define the following quantities

$$\begin{aligned} \eta &= F\left(E - E^{0'}\right) \\ \Delta G_{+}^{\ddagger} &= \Delta G_{0}^{\ddagger} + \alpha\eta \\ \Delta G_{-}^{\ddagger} &= \Delta G_{0}^{\ddagger} - (1-\alpha)\eta, \end{aligned} \qquad \text{A-15}$$

where α is the transfer coefficient that depends on the shape of the intersection region of the reaction surfaces and can range from zero to one, and η is the overpotential. By combining these new relationships with (A-12) and (A-14) we obtain the Butler-Volmer current-overpotential equation:

$$i = FA\Gamma_T k^0 \left(\theta_O(t)e^{-\alpha f\eta} - \theta_R(t)e^{(1-\alpha)f\eta}\right), \qquad \text{A-16}$$

where $f = F/RT$. This equation, though, is only an approximate model as it makes several important assumptions: (1) it considers the reaction surface to be linear rather than parabolic; and (2) it ignores the contribution of all electronic states in the electrode that can undergo electron transfer with the solution.

For the case of non-adiabatic electron transfer, i.e., electron transfer with weak electronic coupling, the rate is governed by the distribution overlap of electronic states of the solution and metal. In Section A.5, we introduce the description of the states and construct in detail the expression for the rates as a function of overpotential. The key point to realize is that resonant electron transfer (i.e., between levels of the same energy) can take

place from any energy level in the metallic electrode to the solution states. Electrochemical reduction of electroactive species occurs from occupied surface states to an unoccupied orbital of the oxidized species (*O*). Inversely, an electrochemical oxidation occurs from the occupied electronic orbital of a reduced species (*R*) to an unoccupied surface state. Because of the continuum of available states in the electrode, the total rate is the sum (integral) of the rates at each energy. The Fermi-Dirac distribution, describing the electronic occupation in the metal is

$$f_{\pm}(\varepsilon) = \left[1 + \exp\left(\pm \frac{\varepsilon - \varepsilon_F^W}{k_B T}\right)\right]^{-1}, \qquad \text{A-17}$$

where $f_+(\varepsilon)$ and $f_-(\varepsilon)$ are the distribution of the occupied and unoccupied states in the metal, respectively. The signs + and - have the same meaning as earlier. The solution states (see A.5) are now localized and can be expressed as

$$\omega_{\pm}(\lambda, \varepsilon) = \frac{1}{\sqrt{4\pi\lambda k_B T}} \exp\left[-\frac{[\lambda \mp (\varepsilon - \varepsilon_F^W - e\eta)]^2}{4\lambda k_B T}\right], \qquad \text{A-18}$$

where $\omega_+(\lambda, \varepsilon) = \omega_O(\lambda, \varepsilon)$ and $\omega_-(\lambda, \varepsilon) = \omega_R(\lambda, \varepsilon)$ are the distribution of the oxidized *O* and reduced *R* states, respectively, and are centered about the Fermi energy of the solution (Figure A-2). Note the inverse sign in the exponential factor. Thus, the generalized expression of the rates becomes

$$k_{\pm} = \nu \int_{-\infty}^{+\infty} \kappa_{\pm}(\varepsilon) \omega_{\pm}(\lambda, \varepsilon) f_{\pm}(\varepsilon) \mu(\varepsilon) d\varepsilon, \qquad \text{A-19}$$

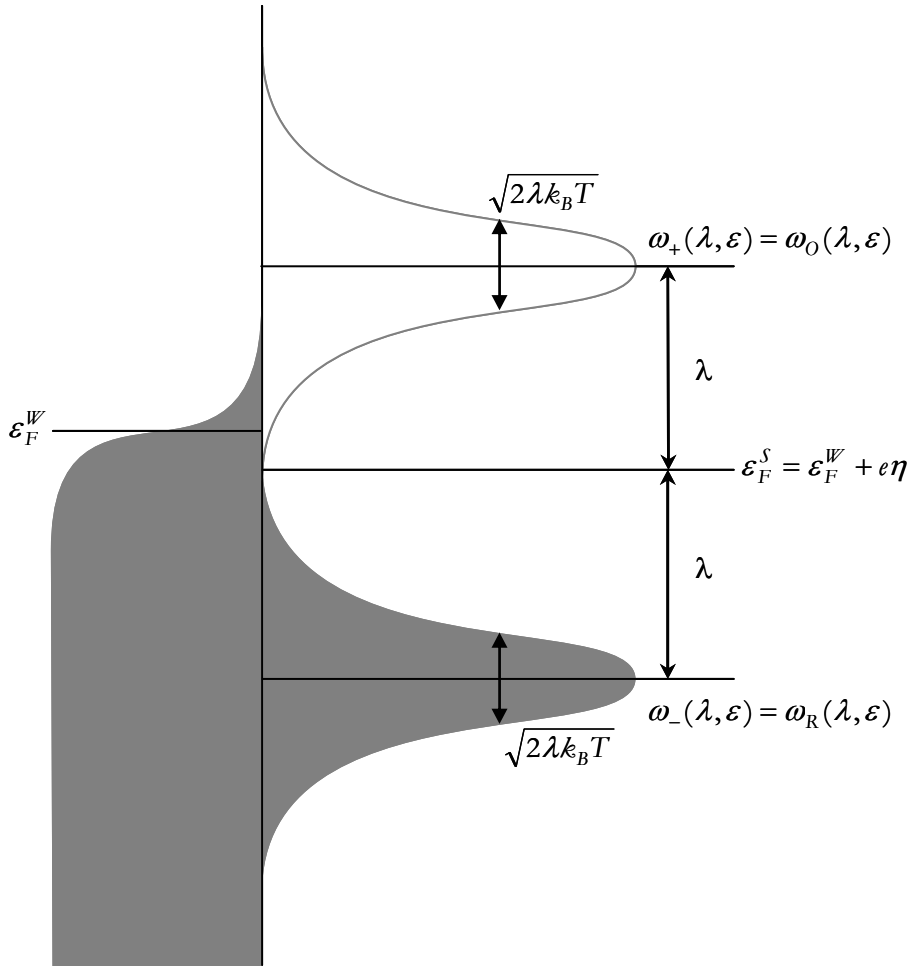

Figure A-2: Relationship among electronic states at the interface between a metal electrode and a solution containing species *O* and *R*. The concentration density functions, D_i, are proportional to the probability density functions ω_i. The solution states are centered about the Fermi energy of the solution, and separated by λ. Filled states are denoted on both sides of the interface by dark shading. Since filled states overlap with (empty) *O* states, reduction can proceed, and since the (filled) *R* states overlap with filled electrode states, oxidation is blocked. The case represented here is where the equilibrium conditions have been established at the formal potential of the redox couple. However, if equilibrium is established at a different potential, one has to be aware that the solution Fermi level will shifted from the center of the distributions, by a quantity equal to ln[*O*/*R*]. Clearly, the concentration density functions will be no longer symmetric either.

where $\kappa_+(\varepsilon) = \kappa_{red}$ and $\kappa_-(\varepsilon) = \kappa_{ox}$ are proportionality factors and $\mu(\varepsilon)$ is the density of states of the metal. Usually, ν is identified as the nuclear vibrational frequency ν_n. It is important to note that because of the generality of this equation, it might be possible to account for variations of the rate constant caused by non-ideal density of states. The proportionality factors κ are usually considered constant over the energy range of an experiment and are associated with the tunneling probability κ_{el}. Moreover, $\mu(\varepsilon)$ is also considered constant over a small energy range. All these factors compose the integral prefactor that often is used to account for kinetics effects. Ultimately, by combining equations (A-17), (A-18), and (A-19) the rates can be expressed by the well-known expression

$$k_{\pm} = \nu_{el}\kappa_{el}\sigma\mu\sqrt{\frac{k_BT}{4\pi\lambda}}\int_{-\infty}^{+\infty}\exp\left\{-\left[\theta - \frac{(\lambda \mp e\eta)}{k_BT}\right]^2 \frac{k_BT}{4\lambda}\right\}\left[1+\exp(\theta)\right]^{-1} d\theta, \qquad \text{A-20}$$

where here we have changed the variables $(\pm(\varepsilon - \varepsilon_F)/k_BT = \theta)$. The factor $\kappa(\varepsilon)$ has been decomposed to $\kappa_{el}\sigma$, where σ is proportional to the electronic coupling (usually identified with the coupling matrix element) between resonant states and κ_{el} describes the distance dependence of the coupling, which is $\exp(-\beta r)$ if the transition accounts for a tunneling process. Chidsey proved the validity of this model,[10] and a typical plot of $\log[k_+ + k_-]$ vs. η is shown in Figure A-3. This is the electrochemical equivalent of the plot of log[k] vs. $-\Delta G^0$ for homogeneous reactions in solution, but it is important to notice here the absence of the inverted region as a direct consequence of the electronic states continuum available below the Fermi level of the metal electrode. The standard rate constant k^0, by definition, is given by (A-20) for η=0.

We have developed this treatment for the case where the system is first equilibrated at a potential E_{eq}=E^0 and then the stepped to an overpotential η. Thus, the initial O/R

ratio is equal to one. However, the exact same treatment can be done using a generic ΔE, where the equilibrium conditions have been established at a potential different from the formal potential E^0. However, because the concentrations now are not equal to one another, the Fermi energy of the solution is shifted by the quantity ln[O/R]. Thus, in this case the solution electronic density of states is shifted according to equation (A-8). In determining the actual driving force (see A.5) one has to include the fact that the solution distributions are not symmetric by setting $\varepsilon_F^S = \varepsilon_F^W + e\eta - RT\ln(O/R)$ and the solution Fermi level in Figure (A-2) is then no longer centered in the middle of the distributions.

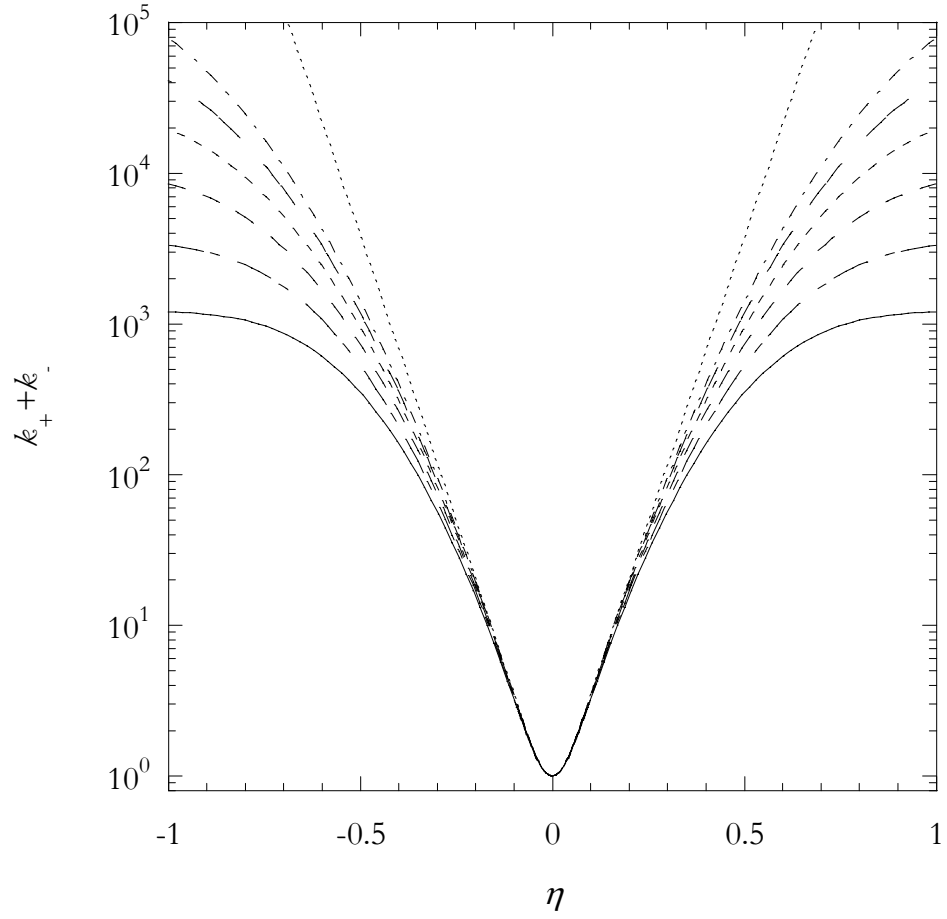

Figure A-3: Plot of the calculated rate constants using equation (A-20) with k^0=1 s^{-1} for different values of reorganization energies, (in the order of increasing rates λ is 0.6, 0.7, 0.8, 0.9, 1.0, and 1.1). The straight dotted line represent the Butler-Volmer's limiting case ($\lambda >> e\eta$). Experimentally, variation of the pre-exponential factor in equation (A-20) is usually accounted in terms of standard rate constant. It is usually appropriate measuring many data point in proximity of the standard rate constant and the working curves are usually shifted along the *y*-axis in order to match the standard rate constant.

A.4.1 Chronoamperometry

The direct determination of the electron transfer rates as a function of the overpotential can be obtained directly by chronoamperometry. The current transient for a *one*-electron transfer reaction associated with the reequilibration of the reduced and oxidized species is monitored as function of time and the profile is given by (A-13). If the system is let to equilibrate at E^0 and the potential is stepped by η for instance towards the reduction, we can make the approximation $k_+ >> k_-$ and (A-13) can be simplified to

$$i(t) = FA\Gamma_O k_+ e^{-k_+ t} = Q(t)k_+, \qquad \text{A-21}$$

where $Q(t)$ is the charge associated with O that has remained and Γ_O is the initial surface coverage of O. The approximation $k_+ >> k_-$ is acceptable as the difference between forward and back electron-transfer rate is about 1% within the first 10 mV around η=0.

The recording of the current transients is a very powerful technique because it permits the direct measurement of electron transfer processes at the surface although, experimentally, a correct measurement can be significantly challenging. In fact, during a transient experiment, the measured current also contains the so-called charging current, which is due to change of the electrostatic potential at the interface. Ionic redistribution and reorientations of the dipoles is not instantaneous and can produce a change in the electrostatic potential inside the working electrode that is recorded as a current, although no charge has actually passed across the interface. This current can be significant compared to the actual faradaic current. In fact, especially at large overpotential, the electron-transfer rate can be very fast and the faradaic current can be hidden by the charging current. In a general sense, the decay of the charging current cannot be determined a priori because of

the complexity of kinetic effects of ions and water at the metal/solution interface. In particular cases, where the charging current is reduced by utilizing ultramicroelectrodes in very fast electrolytes, there is the tendency to validate the measurement when the plot of ln[$i(t)$] vs. t is linear over a significant length of time. However, because of the finite resistance of the solution, the applied potential is *always* affected by the iR drop. Because of this physical limitation the actual applied overpotential experienced at the interface of the working electrode is

$$\eta_{app}(t) = \eta_0 - i(t)R_S, \qquad \text{A-22}$$

where η_0 is the set overpotential, $i(t) = i_f(t) + i_c(t)$ the total current, $i_c(t)$ the charging current, $i_f(t)$ the faradaic current, and R_S is the (uncompensated) solution resistance.

It is understandable from (A-22) that the actual applied overpotential at the interface will change until the total current is zero and the system reaches its new equilibrium. No matter how fast the charging current is, the physical limitation of the solution resistance implies that the overpotential will never be constant. As the rates are highly dependent on the overpotential, we can conclude that the electron transfer rate constant will also be varying as a function of time. Thus the faradaic current is

$$i_f(t) = FA\Gamma_T\theta_O(t)k_+(t) = Q(t)k_+(t). \qquad \text{A-23}$$

Experimentally, in order to separate the faradaic current from the total current, we have to remember that the charging current is a consequence of the fact that the interface behaves like a capacitor. Thus

$$i_c(t) = C_{dl}\frac{d\eta_{applied}(t)}{dt} = -R_S C_{dl}\frac{di(t)}{dt}. \qquad \text{A-24}$$

The proportionality constant $R_S C_{dl}$ is the time constant of the electrochemical cell. Because of this limitation, it is not possible to measure any electron transfer rate faster than $(R_S C_{dl})^{-1}$. In order to determine the cell time constant, it suffices measuring a charging transient by applying a small (1-5 mV) potential step in a region where no faradaic processes occur and fitting the curve to an single exponential decay with characteristic time $\tau_c = R_S C_{dl}$. The faradaic current is then simply obtained by the subtraction $i_f(t) = i(t) - i_c(t)$. The amount of charge left, $Q(t)$, can be easily determined by integration of the faradaic current over time

$$\begin{aligned} Q(t) &= q_0 - q(t) \\ q_0 &= \int_0^\infty i_f(\tau)d\tau \\ q(t) &= \int_0^t i_f(\tau)d\tau. \end{aligned} \qquad \text{A-25}$$

It is easy to see now that $Q(t)$ and $i_f(t)$ can be determined purely from the experimental transient, so that the time-dependent rate constant is expressed by the ratio

$$k(t) = \frac{i_f(t)}{Q(t)}, \qquad \text{A-26}$$

The theory developed in the previous section on the density of states can also be applied to the case of a time-dependent rate constant with the natural assumption that the densities of states remain stable over the time range of the experiment while the potential is changing. A key point to keep in mind is that the $\eta(t)$ varies with time and will be equivalent to the desired one, η_0, only when the current is zero. If, for a set of η_0, we now suppose to measure the rate given by (A-26) at a particular time τ ($k(\tau)$) and plot it against the desired overpotentials η_0 (i.e., $\log[k(\tau)]$ vs. η_0) we obtain the curves shown in Figure A-4, where $\eta(t)$ has been simulated with a simple exponential function. We can see that the curves converge towards the limiting case $\eta(t\rightarrow\infty)=\eta_0$. A good approximation is reached for τ greater than about three times the averaged current decay constant (τ_j). Alternatively, one can plot $k(t)$ against the instantaneous applied overpotential $\eta(t)$ ($\log[k(t)]$ vs. $\eta(t)$). This is equivalent to "march" a curve shown in Figure A-3 for a given λ, from t=0 ($\eta(0)=0$) to $t\rightarrow\infty$ ($\eta(\infty)=\eta_0$).

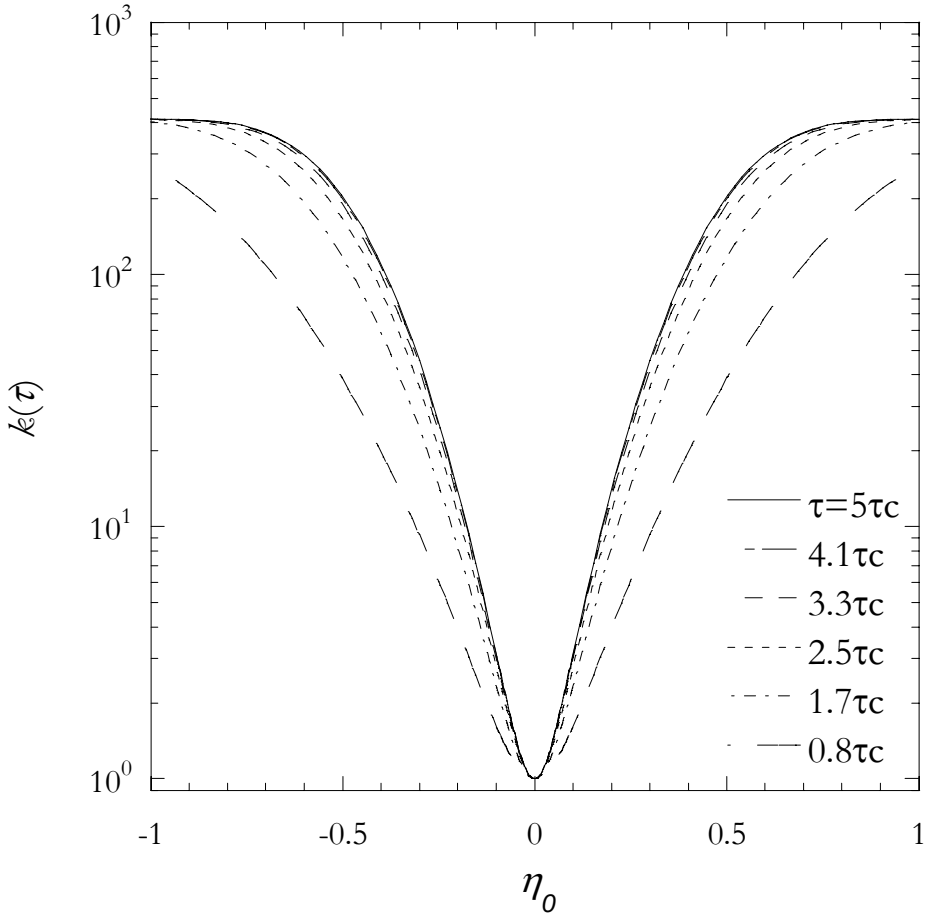

Figure A-4: Plot of the calculated rate constant ($k = k_+ + k_-$) using equation (A-20) with k^0=1 s^{-1}, λ=0.5 eV and assuming an exponential decay for the overpotential ($\eta_{app}(t)=\eta_0(1-\exp[-t/\tau c])$) for different values of t, as indicated in the legend. One can easily see that for times greater than about $3\tau_c$ the curves are essentially overlapping. This indicates that the electron transfer rate can be estimated from the current transients for times greater than $3\tau_c$ and considering $\eta_{app}=\eta_0$. For earlier times, however, the rates diverge substantially from the real one, and η_{app} cannot be considered constant anymore. In this case, one has to account for its variation with time (equation A-22).

A.4.2 Cyclic Voltammetry

Cyclic voltammetry (CV) is one of the most utilized electrochemical techniques for the mechanistic study of redox systems. It is a large-amplitude controlled-potential technique because the potential is scanned over a large range in which a redox process occurs. This is in contrast to the small-amplitude controlled-potential techniques, such as AC impedance, where the voltage is varied over a small range, usually in the order of a few mV. CV is often the first experiment performed in order to find the potential of the peaks and characterize the system. In general, the most useful characterization by CV is performing scan rate dependence, where the system is interrogated for reversibility and stability. The latter will not be discussed in detail in this chapter, but if a system is not stable over time, subsequent scans will show a voltammogram that evolves as a function of the scan cycles. The rates of decomposition or secondary chemical reactions can be extrapolated in some limiting cases. In this section, we will only discuss the response of a reversible and a quasi-reversible system as a function of the scan rate; in particular, the cyclic voltammetric analysis of redox species-electrode kinetics based on Marcus theory.

Theory, which allows for the investigation of heterogeneous electron transfer rate from CV of surface-bound redox species, has been proposed some time ago and is based on the Butler-Volmer's free energy/rate relation (equations A-15 and A-16).[5] We have already discovered that this type of analysis, however, is not accurate as it assumes idealized reaction surfaces and, most importantly, neglects the contribution of the continuum of states in the electrode. From the perspective of Marcus theory, the Butler-Volmer's formalism is an extreme case where the reorganizational energy barrier (λ) is much bigger than the applied overpotential (η).[11]

The determination of the standard rate constant (k^0) can be achieved by measuring the peak splitting of the redox wave as a function of the scan rate.[11] In order to obtain the rate, the resulting curve is compared to working curves that have been constructed from

the analysis of Marcus theory combined with a treatment of potential sweep voltammetry. Usually, the construction of these working curves is the result of finite element analysis of heterogeneous electron transfer rate applied to the potential scan, which is solvable as a numerical solution only. In this section, we will determine an analytical form for linear sweep voltammetric currents, which provides a direct way for comparing simulated curves to experimental cyclic voltammograms.

We first start by decomposing the potential sweep in discrete steps of $\Delta\eta$ and Δt, such that

$$\Delta\eta = \Delta t \cdot v, \tag{A-27}$$

where v is the scan rate in units of V/s. We can see that each potential step is equivalent to a chronoamperometric problem that has been introduced in the previous section. At each potential step we have a current transient whose magnitude is expressed by (A-21), which now we rewrite as

$$i_n(t) = FA\Gamma_O^n k_+^n e^{-k_+ t} = Q_O^{n-1} k_+^n e^{-k_+ t}, \tag{A-28}$$

where n represents the nth potential step ($\eta_n = \eta_0 \pm n\Delta\eta$, depending on the direction scan, + for positive and – for negative scans) and Q_O^{n-1} is the initial amount of O remained on the surface at the nth potential step. We have to remember here that we have made the assumption that, for instance during reduction for overpotential greater than 10 mV, the reverse rate constant is negligible and only k_+ is the determining factor. It is important also to recognize that the rates are dependent on the overpotential as shown in (A-20).

As far as the first step is concerned, the amount of charge Q_O^0 remaining on the surface is determined by the Nernst equation (A-8) at the initial equilibrium potential η_0, whereas the subsequent one depends on the length of the potential step. Thus, we can write, using (A-27) and (A-28),

$$\begin{aligned} Q_O^1 &= Q_O^0 - \int_0^{\Delta t} i_1(\tau)d\tau = Q_O^0 e^{-k_+(\eta_1)\Delta t} \\ Q_O^2 &= Q_O^0 e^{-(k_+(\eta_1)+k_+(\eta_2))\Delta t} \\ Q_O^{n-1} &= Q_O^0 \exp\left[-\frac{1}{v}\sum_{i=1}^{n-1}\left(k_+(\eta_i)\Delta\eta\right)\right]. \end{aligned} \qquad \text{A-29}$$

By inserting (A-29) into (A-28), we can write the current transients at each potential step, as well as the total current as a function of the overpotential and scan rate in the limiting case where $\Delta\eta \to 0$:

$$i(\eta_n, t) = k_+^n e^{-k_+ t} Q_O^0 \exp\left[-\frac{1}{v}\sum_{i=1}^{n-1}\left(k_+(\eta_i)\Delta\eta\right)\right] \xrightarrow{\Delta t\to 0, \Delta n\to 0, t\to 0}$$

$$i(\eta) = Q_O^0 k_+(\eta)\exp\left[-\frac{1}{v}\int_{\eta_0}^{\eta} k_+(x)dx\right], \qquad \text{A-30}$$

where η_0 is the initial overpotential where the system is at equilibrium and Q_O^0 is determined by the Nernst equation, and v is the scan rate. It is important to realize that (A-30) is based on the simple assumption that the back electron transfer is negligible compared to the forward. It would not be possible to obtain an analytical function of the current without this assumption as the integration in (A-29) using (A-13) is not solvable and numerical calculation is therefore required.

A plot of the calculated normalized voltammetric waves based on this heterogeneous Marcus kinetics analysis is shown in Figure A-5 for different values of $\log[v/k^0]$ (increasing scan rates v is equivalent to decreasing k^0 in these calculations). At very slow scan rates (or very fast standard rate constant), the voltammogram has almost a reversible shape. For a surface bound species, the voltammogram for a reversible species results centered at the formal potential, completely symmetric with respect to the η=0 axis. In that case, the rate of electron transfer is much faster than the scan rate and the system is virtually always at equilibrium. For slower standard rate constants, where the system now is not able to regain the equilibrium conditions, the peak is shifted from the η=0 axis; the faster the scan rate the more shifted the peak is. An important feature that distinguishes heterogeneous Marcus kinetics from Butler-Volmer's kinetics is the presence of a substantial distortion of the peak shape for large $\log[v/k^0]$: the peak becomes broader and the peak current smaller, developing a more "diffusion-like" tail. This phenomenon is the direct consequence of the reorganization energy of the system (Figure A-6) that provides an extra energy barrier for electron transfer. However, regardless of the peak shape, the plot of the peak splitting (E_{peak}-$E^{0'}$) vs. the log of the scan rate provides an indirect measure of the standard rate constant. The error inherent in this calculation is nevertheless less then 1% around η=0 (±10 mV) where k_+ and k_- are almost equivalent. Nevertheless, for most of quasi-reversible redox processes k^0 is only accessible at relatively high scan rate and thus for large peak splitting away form η=0.

There are a few limitations of this technique for measuring standard rate constants and reorganization energies. For systems with relatively low standard rate constant and low reorganization energy, the determination of the peak potential can become problematic from an experimental point of view. In fact, while peak broadening can be an impediment for peak potential measurement, the peak potential at high scan rate can be very close to the solvent edge, limiting the range of the scan rate; this is particularly true for aqueous solutions. The second limitation is associated with the kinetic dispersions in the film. In

some cases, an apparent distribution of rate constants can be the consequence of changes of the effective formal potential as a function of the O/R ratio. Additionally, since the measure of the peak splitting is referred to with respect to the standard potential E^0, a distribution of the actual E^0 values among the surface redox species would introduce an uncertainty of the measurement. Moreover, a particular disadvantage is associated with surface inhomogeneities due to surface imperfections, such as roughness and grain boundaries of self-assembled monolayers. This inhomogeneity produces species located on fast sites and other on slower sites resulting in kinetic dispersion.

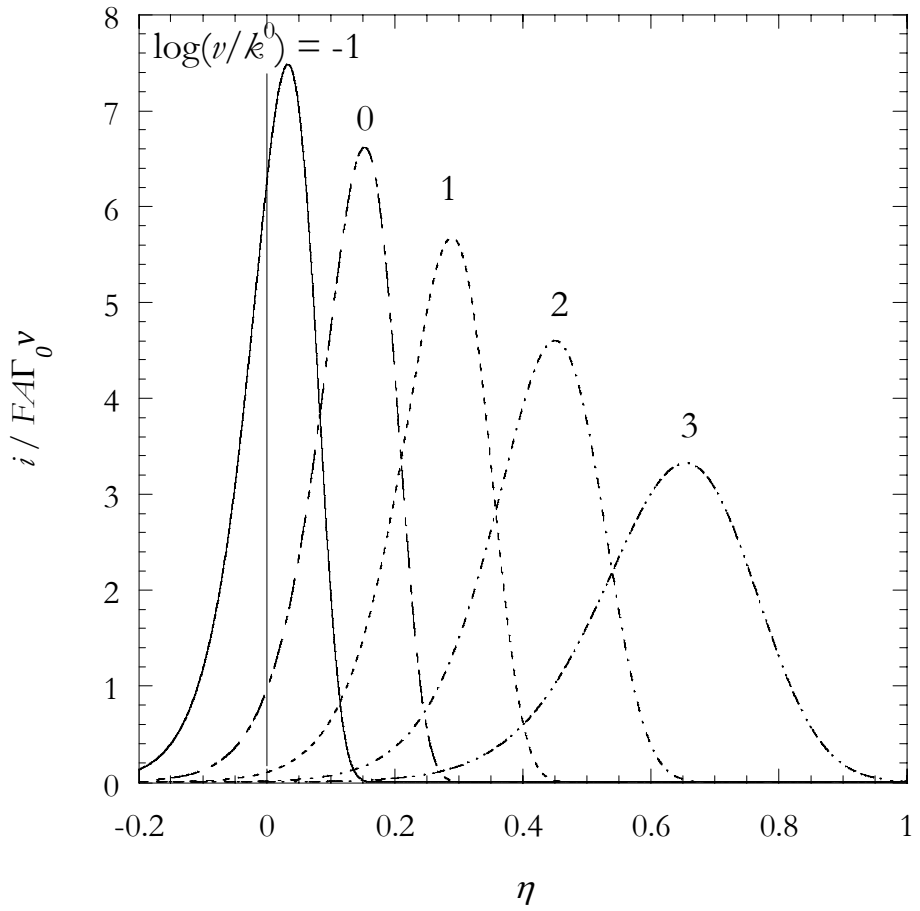

Figure A-5: Calculated, normalized voltammetric waves based on heterogeneous Marcus kinetics using equation (A-30), for λ = 0.85 eV, and different values of log[v/k^0].

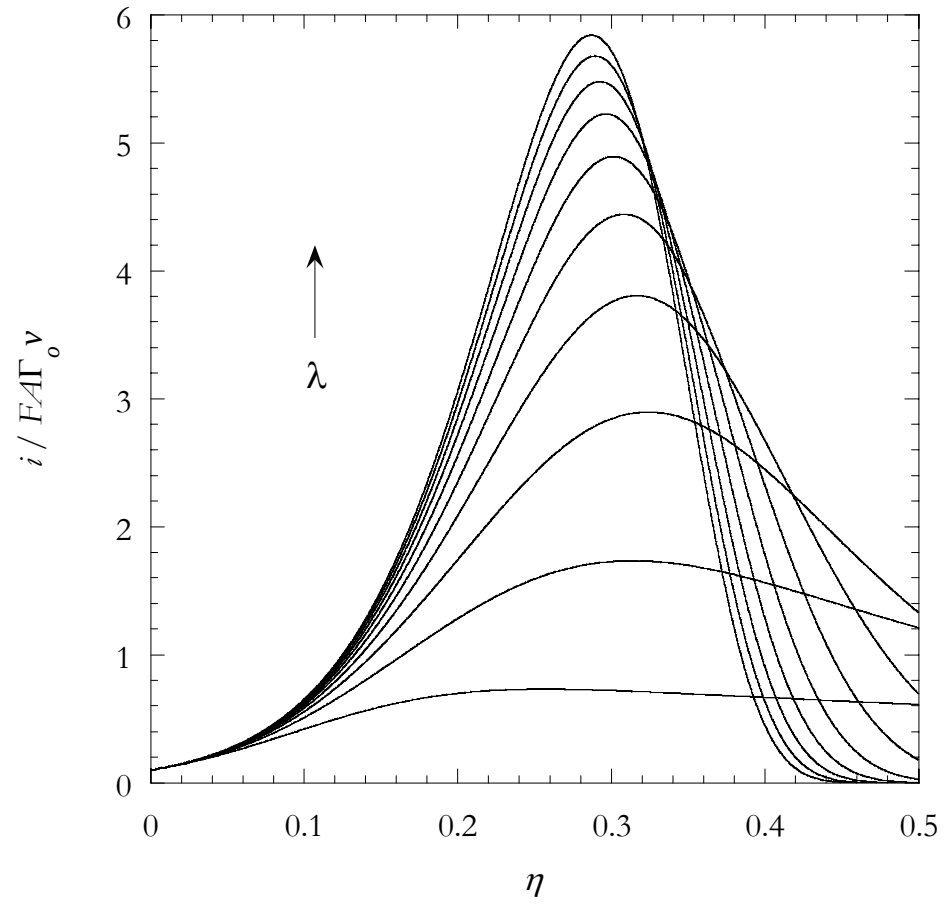

Figure A-6: Dependence of calculated, normalized voltammetric wave shape on the reorganization energy λ, based on heterogeneous Marcus kinetics using equation (A-30), for (top to bottom) λ=1.0, 0.9, 0.8, 0.7, 0.6, 0.5, 0.4, 0.3, 0.2, and 0.1 eV, at $\log[\nu/k^0]$=1.0.

A.4.3 Impedance and AC Voltammetry

A method for avoiding interference of kinetic dispersion and reorganization energy-related peak broadening is to take advantage of small amplitude potential perturbations. By sweeping the interfacial potential, as is the case of CV, we drive the system far from equilibrium and observe how it behaves in these non-ideal extreme conditions. However, by perturbing the system with only small oscillating potentials we might be able to observe how it behaves at equilibrium and obtain a description of the physical properties that is far more accurate than in the case of a large-amplitude potential scan. These measurements can be performed in the presence and even absence of electroactive species and we can gain information regarding the electron transfer, species behavior at the interface, and physical properties of the interface itself.

The typical AC measurements are the electrochemical impedance spectroscopy (EIS) and AC voltammetry (ACV) and they essentially rely on the fact that the relationship between current and potential is linear at low overpotentials.[†] The main advantage of observing a multicomponent system in the *frequency domain* rather than in the time or potential domains is that all kinetic processes can be decomposed in the sum of signals of different frequencies in virtue of the superposition principle (Fourier synthesis) and can be considered independent in the absence of intermolecular interactions. Because of this double linearity of the signal with the overpotential and kinetic processes, the electrochemical cell, and in particular the solution/electrode interface, can be described simply by an equivalent circuit of parallel components, each representing a particular physical process (Figure A-7).

The classical equivalent circuit is the Randles equivalent circuit that comprises two elements in series: the bulk of the solution and the interfacial impedances, Z_S and Z_I,

---

[†] This can be readily seen by the limited development to the first order of the Butler-Volmer's current-overpotential expression (A-16), knowing that $e^x \approx 1+x$ when x is sufficiently small and $\theta_R = \theta_O$.

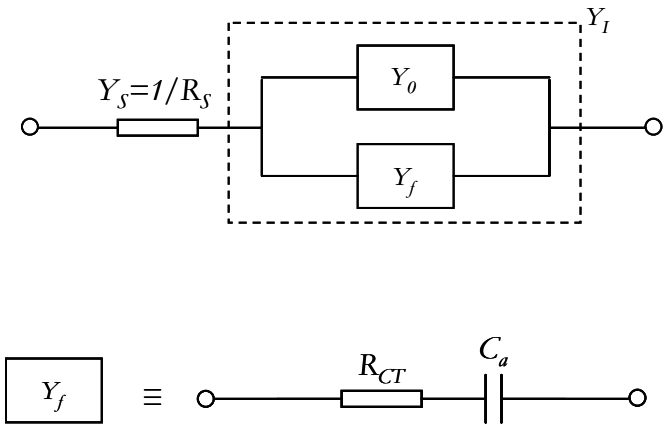

Figure A-7: Generalized equivalent circuit of an electrochemical cell. The Randles circuit is obtained by placing a capacitor representing the double layer instead of Y_0. Y_S, Y_I, and Y_f are the solution, interfacial, and faradaic admittances. Y_0 represents here the "background" admittance, and in general contains all processes that are not faradaic. R_{CT} is the electron transfer resistance and C_a is the adsorption pseudocapacitance.

respectively.[12-15] Because of the linearity of surface processes, the interfacial impedance is decomposed into parallel processes. In particular, for the Randles equivalent circuit, the double layer is modeled as a capacitor and the faradaic impedance as a charge transfer resistor in series with a capacitor (Figure A-7). The theory for the analysis of the faradaic impedance was first developed by Laviron for covalently bound or strongly adsorbed electroactive species, in the limit of a small AC perturbation and in absence of intermolecular interactions.[16] The faradaic impedance is represented as a series combination of frequency-*independent* R_{CT} and C_a, where R_{CT} is the charge transfer resistance and C_a is the adsorption pseudocapacitance. For an easy justification for the use of this configuration for the faradaic impedance, one has to simply consider that a capacitor and a resistor in series represent a high-pass filter. As the frequency increases the impedance decreases linearly because the electron transfer can follow the perturbation, i.e., the rate is faster than the applied perturbation frequency. This continues until a point where the rate cannot keep up with the perturbation frequency, the signal is rate limited by the electron transfer rate, and the impedance reaches a steady value.

In general, frequency analysis of interfacial process is approached by the fit of the impedance in the complex plane (Nyquist plot) using complex plane nonlinear least-squares method.[17] This rather difficult and ambiguous method leads to modeling in detail processes that are non-linear. For instance, the ideal impedance Nysquit plot, for a surface bound species, is represented by a perfect semicircle at high frequency and a straight vertical line at low frequencies. However, because the presence of non linear phenomena due to *frequency dispersion* of elements such as the double layer capacitance and solution resistance (i.e., variation of R_S and C_{dl} with frequency), this phenomenon, especially at low frequencies, is not ideal and commonly accounted for by introducing a constant phase element (CPE) in place of capacitive elements.[18, 19] However, there is no agreed physical meaning for this element.

Let us analyze in detail the Randles equivalent circuit in order to determine the faradaic component. For practicality, we shall discuss from here on in terms of admittance, rather then impedance. From the total circuit admittance, Y_T, one can write the interfacial admittance as

$$Y_I = \left[Y_T^{-1} - Y_S^{-1}\right]^{-1}, \qquad \text{A-31}$$

where, here, the reciprocal of the solution admittance, Y_S^{-1}, is simply equivalent to the (uncompensated) solution resistance R_S (Figure A-7).

The interfacial admittance now, contains elements that are not necessarily linear with respect to the frequency but we assume that are independent, i.e., decoupled. In this case, a generic expression of the faradaic admittance is

$$Y_f = Y_I - \sum Y_i = Y_I - Y_0, \qquad \text{A-32}$$

where Y_0 represents all other processes except the faradaic one. In ACV, for a given sampling frequency, (A-32) is equivalent to subtracting the background from the interfacial AC voltammogram, in the same way one would do it for a regular DC cyclic voltammogram. The "background" subtraction of the interfacial AC voltammogram, although rather arbitrary as it depends on the experimentalist's judgment, is an excellent way to exclude phenomena that are otherwise impossible to model. On the other hand, in AC voltammograms, when obtained over a relatively wide range of DC potentials on both sides of the redox formal potential, it is relatively easy to identify fluctuations of the background admittance.

Typically, kinetic analysis by ACV is a tedious process that involves the acquisition of many AC voltammograms over a wide range of frequencies.[20, 21] As a result, this technique is very time consuming and does not seem to be very accessible. Because of the superposition principle, this technique can provide a very detailed description of parallel processes occurring on the surface, but depending on the number of points collected (i.e., the number of AC voltammograms) the analysis can be highly affected by a poor spectral resolution. An easy method to increase the spectral resolution is based on the assumption that the frequency-dispersed background is essentially constant at the base of the AC peak. Thus, it suffices to determine the frequency response of the admittances at the formal potential and at both edges of the AC peak (usually $\pm$150 mV from the formal potential). The frequency-dependent faradaic admittance (at the formal potential) is obtained using (A-31) and then background subtracted using equation (A-32), where the background is simply the average of the two frequency-dependent admittances obtained at potentials where no faradaic processes occur.

There are multiple advantages of extrapolating the faradaic admittance. There can be many faradaic-related processes on the surface and they can all be decomposed in the frequency domain due to the high resolution of the spectrum. From a qualitative perspective, this is very important because it provides a viable tool for assessing the quality, homogeneity, and stability of the surface in addition to provide information of the specific type of processes. For instance, diffusion-limited processes are generally observed as a tailing of the phase at low frequency. On the other hand, well-defined processes that exhibit low kinetic dispersion will be evident, as multiple resonances in the phase plot, as well as plateaus in the total admittance plot (like for a high-pass filters).

Although there might still many equivalent circuits that can describe the faradaic admittance, determination of the standard rate constant does not require a detailed knowledge of the individual components. It is however impossible to account for all processes that can occur on the surface. For complicated systems, binding, molecular

motions, and proton-coupled reactions are part of the faradaic admittance, but not possible to deconvolute, unless strong assumptions are made on the structure and dynamics of the film. However, if background subtraction is done properly, the faradaic admittance directly reflects the frequency dependence of the electron transfer and associated processes. This can be seen by writing (A-16) for a small perturbation:

$$i_f(\eta) = -\frac{F^2 A\Gamma_T k^0}{2RT}\eta, \qquad \text{A-33}$$

Ohm's law can be easily identified where the faradaic admittance is now (at 293 K)

$$\left|Y_f\right| = \frac{F^2 A\Gamma_T}{2RT}k^0 = 1.91\cdot 10^6 A\Gamma_T k^0. \qquad \text{A-34}$$

(A-34) represents a direct relationship between the module of the faradaic admittance and the standard rate constant. In the case of a pure electron transfer process, the standard rate constant is determined by the maximum value of Y_f. In Figure A-8, the frequency response of the faradaic admittance and phase has been modeled using two simplified faradaic admittances similar to that in Figure A-7. It is assumed that all non-linear, frequency-dependent admittances have been subtracted.

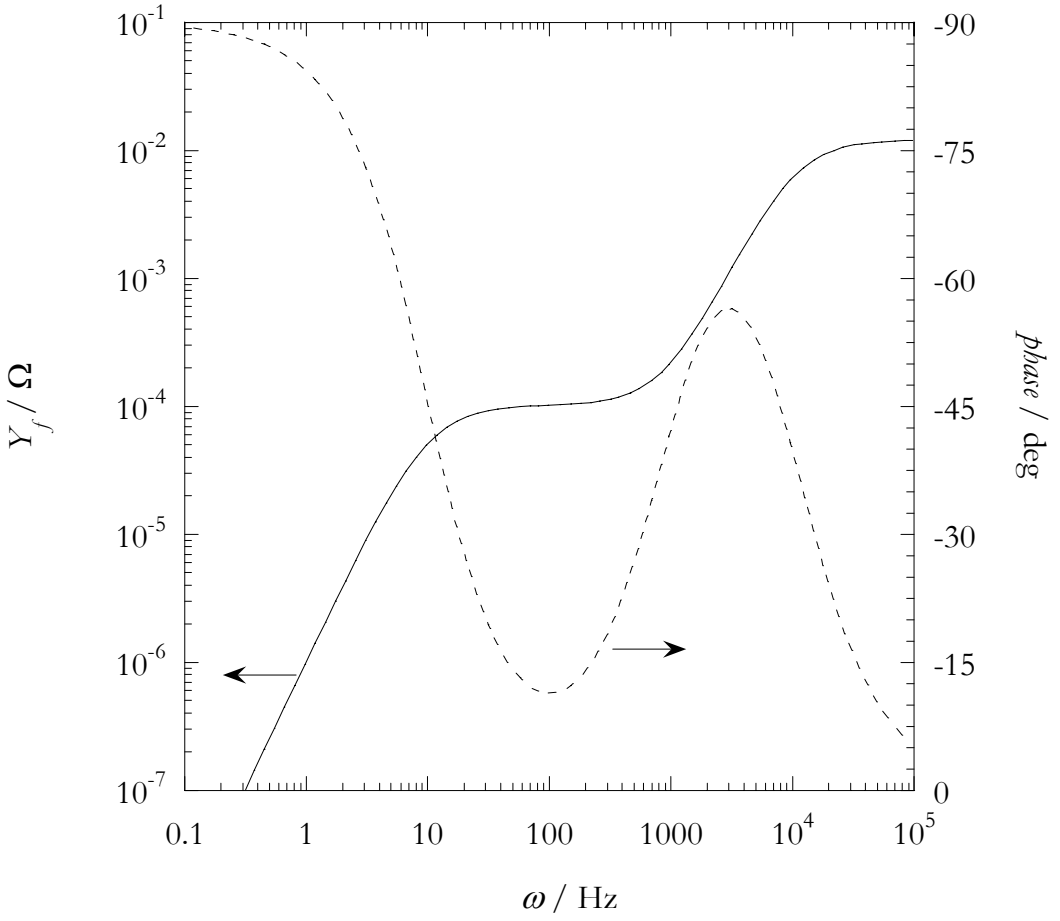

Figure A-8: Plot of calculated faradaic admittance comprised of two electron transfer admittances, with values $R_{ct\text{-}1}$=*10* Ω, $C_{a\text{-}1}$=1·10^{-5} F, $R_{ct\text{-}2}$=*100* Ω, $C_{a\text{-}2}$=1·10^{-3} F. The two plateaus at correspond to the maximum of the faradaic admittances and are correlated to the standard rate constant of the two electron transfer processes.

A.5 Electrode and Solution States

A.5.1 Description of the Electrode States

Let us start by describing the electronic states in the metal electrode. At thermal equilibrium, the probability that an electronic state of energy ε is occupied by an electron is given by the probability distribution described by the Fermi-Dirac distribution $f(\varepsilon)$

$$f(\varepsilon) = \left[1 + \exp\left(\frac{\varepsilon - \varepsilon_F}{k_B T}\right)\right]^{-1}, \qquad \text{A-35}$$

where ε_F is the energy of the Fermi level, which defines the energy of the topmost filled orbital (at 0 K).

It is intuitively understandable that for any given electronic transition that occurs at the metal-liquid interface, only the surface states are involved. Thus, the number of occupied states available for the transition, i.e., from the electrode surface to the solution in the energy range between ε and $\varepsilon+d\varepsilon$ is given by

$$N_{occ}(\varepsilon) = A f(\varepsilon)\mu(\varepsilon)d\varepsilon, \qquad \text{A-36}$$

where A is the electrode area [cm^{-2}], $f(\varepsilon)$ the Fermi-Dirac distribution (dimensionless), and $\mu(\varepsilon)$ the surface density of states [$cm^{-2}eV^{-1}$]. In a similar manner, one can define the number of surface states that are unoccupied by

$$N_{unocc}(\varepsilon) = A\big(1 - f(\varepsilon)\big)\mu(\varepsilon)d\varepsilon. \qquad \text{A-37}$$

Electron transfer processes can only take place from an occupied to an unoccupied orbital when their energies are matching within the thermal fluctuations ($\varepsilon \pm k_B T$). Electrochemical reduction of electroactive species occurs from occupied surface states to an unoccupied orbital of the oxidized species (O). Inversely, an electrochemical oxidation occurs from the occupied electronic orbital of a reduced species (R) to an unoccupied surface state. Because of the continuum of available states in the electrode, the total rate is the sum (integral) of the rates at each energy.

A.5.2 Description of the Solution States

In the solution side, the density of occupied and unoccupied states are provided by the local concentration of different chemical species, namely reduced (*R*) and oxidized (*O*) species. These states differ from those of the electrode in being localized.

Let us consider the case of a reduction; the oxidation can be obtained by a similar method. For purely diffusing species, only the O species close to the surface, within the diffusion layer, can undergo ET with the surface. The solution states can be described by a concentration density function $D_O(\lambda,\varepsilon)$ with dimensions of [$cm^{-3}eV^{-1}$]

$$D_O(\lambda,\varepsilon) = N_A C_O(0,t)\omega(\lambda,\varepsilon), \qquad \text{A-38}$$

where N_A is the Avogadro's number, $C_O(0,t)$ is the concentration near the electrode in [mol cm^{-3}], and $\omega(\lambda,\varepsilon)$ is the probability density function with units of [eV^{-1}] of the O species. In the case of surface bound species, we can reformulate equation (A-38) without losing the generality of the treatment by replacing the "local concentration" by the time-dependent surface density $\Gamma_O(t)$ with units of [mol cm^{-2}].

$$D_O(\lambda,\varepsilon) = N_A \Gamma_O(t)\omega_O(\lambda,\varepsilon). \tag{A-39}$$

It is clear now that the concentration density function has units of [cm^{-2}eV^{-1}] as only surface states are involved. The concentration density function for the reduced species can be similarly deduced and is given by

$$D_R(\lambda,\varepsilon) = N_A \Gamma_R(t)\omega_R(\lambda,\varepsilon). \tag{A-40}$$

A.5.3 Formulation of the ET Rate Constant

The local rate of reduction is defined as the number of electrons that succeed the transition from occupied surface states to unoccupied solution states over the energy range of ε and $\varepsilon+d\varepsilon$ in time interval Δt. The actual local rate, $\mathcal{L}_{red}(\varepsilon)$ is then

$$\mathcal{L}_{red}(\varepsilon) = \frac{1}{\Delta t}\left[P_{red}(\varepsilon)\mathcal{A}f(\varepsilon)\mu(\varepsilon)d\varepsilon\right], \tag{A-41}$$

where $Af(\varepsilon)\mu(\varepsilon)$ is the number of electrons (states) available on the electrode, and $P_{red}(\varepsilon)$ is the probability of electronic transition. Intuitively, one can understand that the probability of the electronic transition $P_{red}(\varepsilon)$ must be directly proportional to the surface concentration D_O (or surface coverage) of the O species. We can then rewrite the local rate as

$$\mathcal{L}_{red}(\varepsilon) = \frac{1}{\Delta t}\left[\kappa_{red}(\varepsilon) D_o(\lambda,\varepsilon) Af(\varepsilon)\mu(\varepsilon) d\varepsilon\right], \tag{A-42}$$

where $\kappa_{red}(\varepsilon)$ is a proportionality function having units of [cm^{3}eV] for a diffusing species, or [cm^{2}eV] for a surface-bound species. The total rate of reduction is then an integral of the rates at each energy.

$$\begin{aligned}\rho &= \nu \int_{-\infty}^{+\infty} \kappa_{red}(\varepsilon) D_o(\lambda,\varepsilon) Af(\varepsilon)\mu(\varepsilon) d\varepsilon = \\ &= \nu A N_A \Gamma_O(t) \int_{-\infty}^{+\infty} \kappa_{red}(\varepsilon)\omega_O(\lambda,\varepsilon) f(\varepsilon)\mu(\varepsilon) d\varepsilon.\end{aligned} \tag{A-43}$$

Here the frequency factor $(1/\Delta t)$ has been replaced by the effective frequency for nuclear motion ν. ρ is the rate of ET expressed in molecules or electrons per second. By dividing ρ by $AN_A\Gamma_O(t)$ on obtains the usual heterogeneous rate constants,

$$\begin{aligned}k_+ &= \nu \int_{-\infty}^{+\infty} \kappa_{red}(\varepsilon)\omega_O(\lambda,\varepsilon) f(\varepsilon)\mu(\varepsilon) d\varepsilon \\ k_- &= \nu \int_{-\infty}^{+\infty} \kappa_{ox}(\varepsilon)\omega_R(\lambda,\varepsilon)[1-f(\varepsilon)]\mu(\varepsilon) d\varepsilon.\end{aligned} \tag{A-44}$$

The form of the solution states distribution can be easily recognized from the form of the electron transfer rate constant described by the classical transition state theory (A-14). One can see that this distribution can be written as

$$\omega \propto \exp\left[-\frac{\Delta G^*}{k_B T}\right]. \qquad \text{A-45}$$

An analytical form of the activation energy can be obtain from the Marcus macroscopic model for electron transfer reactions described by the diagram of the standard free energy as a function of the reaction coordinates. The analysis of the reaction surfaces leads to the determination of a very important expression for the activation energy:[22]

$$\Delta G^* = \frac{\lambda}{4}\left(1+\frac{\Delta G^0}{\lambda}\right)^2, \qquad \text{A-46}$$

where ΔG^0 is the driving force and λ is the reorganization energy. The key idea for the determination of an appropriate activation energy for an electrode reaction is that interfacial electron transfer can take place from any occupied state of energy ε to the Fermi level of the solution, ε_F^S. Then, the driving forces for a reduction or oxidation can be described, using (A-10), by

$$\Delta G_{\pm}^0 = \pm(\varepsilon_F^S - \varepsilon) = \pm(\varepsilon_F^W + nF(E-E^0) - \varepsilon) = \pm(\varepsilon_F^W + e\eta - \varepsilon). \qquad \text{A-47}$$

One has to notice that, in the case of a reduction, ΔG_{+}^{0} describes the electron transfer to empty states in solution ω_O; thus by combining (A-45), (A-46), and (A-47) and normalizing the distribution such that $\int \omega d\varepsilon = 1$, we obtain an explicit form for solution state probability distribution:

$$\omega_O(\lambda,\varepsilon) = \frac{1}{\sqrt{4\pi\lambda k_B T}} \exp\left[-\frac{(\lambda - (\varepsilon - \varepsilon_F^W) + e\eta)^2}{4\lambda k_B T} \right]$$
$$\omega_R(\lambda,\varepsilon) = \frac{1}{\sqrt{4\pi\lambda k_B T}} \exp\left[-\frac{(\lambda + (\varepsilon - \varepsilon_F^W) - e\eta)^2}{4\lambda k_B T} \right]. \qquad \text{A-48}$$

A schematic representation of the density of states is shown in Figure A-2.

Let us considerate a simple change of notation and rewrite the Fermi-Dirac distribution as

$$f_{\pm}(\varepsilon) = \left[1 + \exp\left(\pm \frac{\varepsilon - \varepsilon_F^W}{k_B T} \right) \right]^{-1}, \qquad \text{A-49}$$

where $f_{+}(\varepsilon) = f(\varepsilon)$ and $f_{-}(\varepsilon) = 1 - f(\varepsilon)$. The solution states can be expressed as

$$\omega_{\pm}(\lambda,\varepsilon) = \frac{1}{\sqrt{4\pi\lambda k_B T}} \exp\left[-\frac{[\lambda \mp (\varepsilon - \varepsilon_F^W - e\eta)]^2}{4\lambda k_B T} \right], \qquad \text{A-50}$$

where $\omega_{+}(\lambda,\varepsilon) = \omega_O(\lambda,\varepsilon)$ and $\omega_{-}(\lambda,\varepsilon) = \omega_R(\lambda,\varepsilon)$. Note the inversed sign in the exponential factor. Thus, the generalized expression of the rates becomes

$$k_{\pm} = \nu \int_{-\infty}^{+\infty} \kappa_{\pm}(\varepsilon)\omega_{\pm}(\lambda,\varepsilon) f_{\pm}(\varepsilon)\mu(\varepsilon)d\varepsilon, \qquad \text{A-51}$$

where $\kappa_{+}(\varepsilon) = \kappa_{red}$ and $\kappa_{-}(\varepsilon) = \kappa_{ox}$. Usually, ν is identified as the nuclear vibration frequency ν_n. It is important noticing that, because of the generality of this equation, it might be possible to account for variations of the rate constant caused by non ideal density of states. The proportionality factor κ is usually considered constant over the energy range of an experiment and is associated with the tunneling probability κ_{el}. Moreover, $\mu(\varepsilon)$ is also considered constant on a small energy range. All these factors compose the integral prefactor that often is used to account for kinetics effects. Ultimately, by combining equations (A-49), (A-50), and (A-51) the rates can be expressed by the well-known expression

$$k_{\pm} = \nu_{el}\kappa_{el}\sigma\mu\sqrt{\frac{k_B T}{4\pi\lambda}}\int_{-\infty}^{+\infty}\exp\left\{-\left[\theta - \frac{(\lambda \mp e\eta)}{k_B T}\right]^2 \frac{k_B T}{4\lambda}\right\}\left[1+\exp(\theta)\right]^{-1} d\theta, \qquad \text{A-52}$$

where here we have changed the variables ($\pm(\varepsilon - \varepsilon_F)/k_B T = \theta$).

A.6 References

1. Debye, P.; Huckel, E., The theory of electrolytes. I. Lowering of freezing point and related phenomena. *Zeitschrift für Physik und Chemie* **1923,** 24, 185-206.
2. Debye, P.; Huckel, E., Theory of electrolytes. II. The limiting law of electrical conductivity. *Zeitschrift für Physik und Chemie* **1923,** 24, 305-25.
3. Helmholtz, H. L. F. v., II. Uber einige Gesetze der Vertheilung elek-trischer Ströme in körperlichen Leitern mit Anwendung aufdie thierisch-elektrischen Versuche [Some laws concerning the distribution of electrical currents in conductors with applications to experiments on animal electricity]. *Annalen der Physik und Chemie* **1853,** 89, (6), 211-233.
4. Helmholtz, H. L. F. v., Studien über elektrische Grenzschichten. *Wiedemanns Ann Physik* **1879,** 7, 337.
5. Bard, A. J.; Faulkner, L. R., *Electrochemical Methods, Fundamental and Applications*. 2nd ed.: John Wiley and Sons, 2001.
6. Gileadi, E., *Electrode Kinetics for Chemists, Chemical Engineers, and Materials Scientists*. VCH: 1993.
7. Faraday, M., Experimental Researches in Electricity. *Philisophical Transactions of the Royal Society of London* **1832,** 122, 125.
8. Faraday, M., Experimental Researches in Electricity. Twentieth Series. *Philisophical Transactions of the Royal Society of London* **1846,** 136, 21.
9. Arrhenius, S. A., *Zeitschrift für Physik und Chemie* **1889,** 4, 226.
10. Chidsey, C. E. D., Free-Energy and Temperature-Dependence of Electron-Transfer at the Metal-Electrolyte Interface. *Science* **1991,** 251, (4996), 919-922.

11. Tender, L.; Carter, M. T.; Murray, R. W., Cyclic Voltammetric Analysis of Ferrocene Alkanethiol Monolayer Electrode-Kinetics Based on Marcus Theory. *Analytical Chemistry* **1994,** 66, (19), 3173-3181.

12. Randles, J. E. B., Kinetics of Rapid Electrode Reactions. *Discussions of the Faraday Society* **1947,** 1, 11-19.

13. Randles, J. E. B., Kinetics of Rapid Electrode Reactions .2. Rate Constants and Activation Energies of Electrode Reactions. *Transactions of the Faraday Society* **1952,** 48, (9), 828-832.

14. Randles, J. E. B.; Somerton, K. W., Kinetics of Rapid Electrode Reactions .4. Metal Ion Exchange Reaction at Amalgam Electrodes. *Transactions of the Faraday Society* **1952,** 48, (10), 951-955.

15. Randles, J. E. B.; Somerton, K. W., Kinetics of Rapid Electrode Reactions .3. Electron Exchange Reactions. *Transactions of the Faraday Society* **1952,** 48, (10), 937-950.

16. Laviron, E., Ac Polarography and Faradaic Impedance of Strongly Adsorbed Electroactive Species .1. Theoretical and Experimental-Study of a Quasi-Reversible Reaction in the Case of a Langmuir Isotherm. *Journal of Electroanalytical Chemistry* **1979,** 97, (2), 135-149.

17. Macdonald, J. R.; Potter, L. D., A Flexible Procedure for Analyzing Impedance Spectroscopy Results: Description and Illustrations. *Solid State Ionics* **1987,** 24, (1), 61-79.

18. Brug, G. J.; Vandeneeden, A. L. G.; Sluytersrehbach, M.; Sluyters, J. H., The Analysis of Electrode Impedances Complicated by the Presence of a Constant Phase Element. *Journal of Electroanalytical Chemistry* **1984,** 176, (1-2), 275-295.

19. Hurt, R. L.; Macdonald, J. R., Distributed Circuit Elements in Impedance Spectroscopy: A Unified Treatment of Conductive and Dielectric Systems. *Solid State Ionics* **1986,** 20, (2), 111-124.

20. Creager, S. E.; Wooster, T. T., A new way of using ac voltammetry to study redox kinetics in electroactive monolayers. *Analytical Chemistry* **1998,** 70, (20), 4257-4263.

21. Brevnov, D. A.; Finklea, H. O.; Van Ryswyk, H., Ac voltammetry studies of electron transfer kinetics for a redox couple attached via short alkanethiols to a gold electrode. *Journal of Electroanalytical Chemistry* **2001,** 500, (1-2), 100-107.

22. Marcus, R. A.; Sutin, N., Electron Transfers in Chemistry and Biology. *Biochimica et Biophysica Acta* **1985,** 811, (3), 265-322.